Thesis for Doctor Of Philosophy in Mechanical Engineering

# Modelling and Control of Coupled AFM Arrays For Parallel Imaging Verified Through A Macro Scale Experiment

Thesis Submitted in Partial Fulfilment
of the Degree of Doctor of Philosophy


Author:

Samuel Jackson

Supervisors:

Dr. Stefanie Gutschmidt
Prof. XiaoQi Chen


Date: 19/06/2017

*"Imagination is more important than knowledge. Knowledge is limited. Imagination encircles the world"*

–Albert Einstein, 1929

# Acknowledgements

I would first like to expresses my deepest gratitude to my supervisor, Dr. Stefanie Gutschmidt. Stefanie has provided insight and guidance through every step of my research. She has always been open to new ideas and thought provoking discussions, and has always encouraged my personal growth and learning. I would also like to thank Dennis Roeser, Prof. Thomas Sattel and Prof. Ivo Rangelow for supporting my research visits to the Technische Universität Ilmenau, and Arun Kumar for the productive discussions about the challenges we faced during our respective research work.

I would like to thank the technical staff at the University of Canterbury, without whom the experimental aspects of this thesis would not have been possible. I would especially like to thank Julian Murphy, for providing all required electronic components, Garry Cotton, for offering mechanical design advise for construction of the test equipment, and Gerry Kirk, for providing continuous advise and assistance for all aspects relating to electronics and software.

I would like to thank the visiting research assistants (VRAs) Tobias Posielek, Jonas Witschel, Guillaume Collura and Martin Raeder for their assistance with the design and construction of both macro scale test rigs, and for conducting preliminary experimental investigations.

Finally, I would like to thank my parents for their continuous support and encouragement throughout my PhD journey. I would not have been able to complete this thesis without their support.

# Abstract

Atomic Force Microscopy (AFM) is a mature imaging technology that is utilised in a wide range of applications for the purpose of obtaining high resolution images of sample topography and sample property measurements. Currently, AFM technology is centred around the use of single cantilevers to obtain data for one point on the sample at a time. There is currently a drive to extend AFM technology beyond the capabilities of established measurement techniques, including the ability to measure multiple sample points simultaneously, increase acquisition rate, increase measurement sensitivity to sample variations, and to obtain detailed, localised information about material properties. One possible way to address some of these issues is to use arrays of cantilevers instead of a single beam. Using multiple active sensing cantilevers in close proximity allows for true simultaneous data acquisition across multiple points of interest on a sample, as well as increasing measurement density. The main drawback is that cantilevers in a closely spaced array become mechanically coupled, altering the dynamic response of the system. To ensure reliable functionality, a full understanding of the coupled system dynamics is required, including how response is altered by nonlinear force interactions at each cantilever tip.

In this research, a detailed dynamic analysis is conducted for a set of fabricated micro-cantilever AFM arrays fabricated by our collaborators at the Technische Universität Ilmenau (TUI), for the purpose of understanding the system response during Amplitude Modulation operation (AM-AFM). A mathematical model was developed for an array of $M$ beams, each with nearest-neighbour mechanical coupling and individual nonlinear tip-sample force interaction terms. It is shown that this model is able to capture the system eigenmodes, and how the spatial shape of the eigenmodes is altered by tip-sample force interactions. To complement the model, an equivalent macro scale experimental setup was developed to mimic the response of the micro arrays. The macro scale test rig allows for easy and quick parameter variation to gain a better understanding of the micro system response. This approach provided insight into the micro scale dynamics and provided experimental validation of the mathematical model.

Using the developed model and macro scale experiment, the observed response of the micro arrays could be linked to the parameter space of the

system. This information has been used to determine the cause of observed nonlinear phenomena in the array response. Recommendations have been made as to how the array parameters may be optimised to avoid unwanted phenomena which may result in erroneous data. It is believed that this information will be valuable to our collaborators and will be a significant step towards commercialisation of their array technology for parallel throughput AFM. In addition, a new method of enhanced sensitivity AFM has been proposed, utilising the change in spatial mode shape as a measurement signal. This method utilises mechanical coupling as an advantage, as opposed to trying to eliminate coupling as a unwanted feature. The proposed concept has been validated through mathematical modelling and experimental investigation, and the preliminary steps required to implement the technology with the TUI arrays have been proposed.

# Publications

- Jackson, S., Gutschmidt, S., Roeser, D. et al. Development of a mathematical model and analytical solution of a coupled two-beam array with nonlinear tip forces for application to AFM. Nonlinear Dyn (2017) 87: 775. doi:10.1007/s11071-016-3076-7
- Jackson S, Gutschmidt S. Identification and Analysis of Artifacts in Amplitude Modulated Atomic Force Microscopy Array Operation. ASME. J. Comput. Nonlinear Dynam. 2017;12(5):051018-051018-7. doi:10.1115/1.4036520.
- Jackson, S., Gutschmidt, S., Journal of Vibration and Acoustics. Cantilever Array for Enhanced AFM Capabilities and Sensitivity (Prepared).

# Contents

# List of Figures

# List of Tables

# Nomenclature

| | |
|---|---|
| $x$ | Spatial position along the cantilever length |
| $t$ | Time |
| $N$ | Total number of modelled modes |
| $M$ | Total number of cantilevers in array |
| $n$ | Mode number |
| $m$ | Cantilever number |
| $L_{c_m}$ | Length of cantilever $m$ |
| $L_b$ | Length of shared base |
| $b_{c_m}$ | Cantilever width of cantilever $m$ |
| $b_g$ | Cantilever separation |
| $L_P$ | Point location of applied actuation |
| $\hat{m}_m$ | Tip mass applied to beam $m$ |
| $k_c$ | Coupling coefficient per unit length |
| $F_I$ | Nonlinear tip-sample interaction force |
| $d_{0_m}$ | Tip-sample separation of cantilever $m$ |
| $K_m$ | Coefficient of attractive component of nonlinear tip-sample force |
| $\bar{K}_m$ | Coefficient of repulsive component of nonlinear tip-sample force |
| $p_1$ | Exponent of attractive component of nonlinear tip-sample force |
| $p_2$ | Exponent of repulsive component of nonlinear tip-sample force |
| $w_{bm}$ | Displacement of base section $m$ as a function of time and space |

| | |
|---|---|
| $w_{cm}$ | Displacement of cantilever section $m$ as a function of time and space |
| $\rho$ | Material density |
| $A_m$ | Cross-sectional area of cantilever $m$ |
| $E$ | Young's Modulus |
| $I_m$ | Second moment of area of cantilever $m$ |
| $DC_m$ | Static offset actuation applied to beam $m$ |
| $AC_m$ | Amplitude of sinusoidal actuation applied to beam $m$ |
| $\Omega_m$ | Excitation frequency applied to beam $m$ |
| $\hat{x}$ | Nondimensional spatial position along the cantilever length $m$ |
| $\tau$ | Nondimensional time |
| $\hat{w}_{bm}$ | Nondimensional base section displacement $m$ |
| $\hat{w}_{cm}$ | Nondimensional cantilever section displacement $m$ |
| $\hat{L}_b$ | Nondimensional length of shared base |
| $\hat{L}_p$ | Nondimensional point location of applied actuation |
| $\hat{L}_{c_m}$ | Nondimensional length of cantilever $m$ |
| $\hat{k}_c$ | Nondimensional coupling coefficient per unit length |
| $\hat{DC}_m$ | Nondimensional static offset actuation applied to cantilever $m$ |
| $\hat{AC}_m$ | Nondimensional amplitude of sinusoidal actuation applied to cantilever $m$ |
| $\hat{\Omega}_m$ | Nondimensional excitation frequency applied to cantilever $m$ |
| $\mu_m$ | Nondimensional continuum stiffness for cantilever $m$ |
| $\hat{d}_{0_m}$ | Nondimensional tip-sample separation of cantilever $m$ |
| $\tau_m$ | Nondimensional coefficient of attractive component of nonlinear tip-sample force |

| | |
|---|---|
| $\bar{\tau}_m$ | Nondimensional coefficient of repulsive component of nonlinear tip-sample force |
| $\omega_n$ | Modal frequency of mode $n$ |
| $\hat{\omega}_n$ | Nondimensional modal frequency of mode $n$ |
| $W_{mn}$ | Nondimensional modal shape function of cantilever $m$ at mode $n$ |
| $\Phi_n$ | Temporal distribution function of mode $n$ |
| $\overline{W}_{mn}$ | Nondimensional modal tip displacement of cantilever $m$ at mode $n$ |
| $W_{kmn}$ | Nondimensional modal stiffness of cantilever $m$ at mode $n$ |
| $W_{cmn}$ | Nondimensional modal damping of cantilever $m$ at mode $n$ |
| $W_{NLmn}$ | Nondimensional modal nonlinear coefficient of cantilever $m$ at mode $n$ |
| $W_{Fmn}$ | Nondimensional modal actuation coefficient of cantilever $m$ at mode $n$ |
| $X_m$ | Time dependant tip displacement of cantilever $m$ |
| $\overline{W}_{kmn}$ | Nondimensional direct displacement stiffness of cantilever $m$ at mode $n$ |
| $\overline{W}_{cmn}$ | Nondimensional direct displacement damping of cantilever $m$ at mode $n$ |
| $\overline{W}_{NLmn}$ | Nondimensional direct displacement nonlinear coefficient of cantilever $m$ at mode $n$ |
| $\overline{W}_{Fmn}$ | Nondimensional direct displacement actuation coefficient of cantilever $m$ at mode $n$ |

CHAPTER 1

# Introduction

## 1.1 AFM Technology

The year 1982 saw the invention of the scanning tunnelling microscope [1] by Binnig and Rohrer, winning the inventors the nobel prize for physics in 1986 and lead to the development of the Atomic Force Microscope [2] by Binnig, Quate and Gerber in 1986. This technology is capable of measuring the topography of a sample surface with sub-nanometer scale resolution as well as various sample qualities, including surface stiffness, viscoelasticity and material damping [3]. In addition, the technology does not require any specific sample preparation, unlike other technologies, specifically electron microscopy. Due to its versatility, Atomic Force Microscopy (AFM) has been used for imaging a wide range of samples, primarily in the fields of material science and biological research.

The fundamental operating principle of AFM imaging involves scanning a cantilever beam with a sharp tip along the surface of a sample (Figure 1.1). The interaction between the tip and sample causes the cantilever to deflect and vibrate, which can be measured to interpolate information about the sample surface. The favoured method of tip deflection measurement for commercial AFM devices is the optical lever [4]. A laser is focused onto the free end of the cantilever and the position of the reflected point is detected by a split photo-diode, which corresponds to the tip deflection. There are currently three well developed modes of operation that are utilised in AFM. These operating modes are contact mode, intermittent contact mode (commonly called tapping mode) and noncontact mode [5]. Each method has unique advantages and disadvantages, and are employed based on the type of sample information required and the sample properties. A brief description of the three modes is provided below.

- **Contact mode:** AFM imaging was first implemented using contact mode. The method involves dragging the probe tip along the sample while the tip is in direct and continuous contact with the surface. A

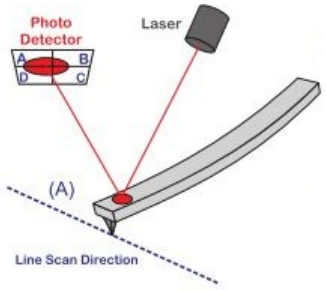


Figure 1.1: A NANOSENSORS™ AFM probe schematic including cantilever and tip. Image produced by Abramovitch et al. [5]

feedback loop displaces the sample vertically to drive the cantilever tip displacement towards a constant reference point, which is used to map the surface topography. Contact mode AFM requires relatively simple control algorithms and does not produce impact forces, as the tip is always in contact with the sample. While contact mode AFM has been extensively used, the high shear forces generated as the probe is dragged over the sample [6] can cause irreversible damage to both the sample and the probe tip. For this reason, its use is mostly limited to hard samples.

- **Intermittent Contact mode:** Commonly known as Amplitude Modulated AFM (AM-AFM) or tapping mode, this method was developed by Martin et al. as an alternative to contact mode imaging [7]. The method requires oscillating the cantilever near its resonant frequency such that the tip is in contact with the surface during only a small fraction of the oscillation cycle. By displacing the sample such that the response amplitude is driven to a predefined constant, the height of the sample at each measurement point can be determined. This method is widely used in favour of contact mode as the shear forces between tip and sample are greatly reduced due to the short contact time. However, the impact forces created by tapping mode can still damage very soft samples such as mammalian cells [8]. An additional advantage is that the nonlinear force gradient between tip and surface can provide information regarding sample material properties as well as the topography [9].

- **Noncontact mode:** In 1991 the first non-contact mode of AFM imaging was developed by IBM's research division [10], known as Frequency Modulated AFM (FM-AFM). This imaging mode involves os-

cillating the cantilever at its resonant frequency and measuring the shift in resonant frequency as the cantilever is influenced by long range atomic forces. The sensitivity of the frequency shift to sample topography is significantly greater than that of static displacment or amplitude, making noncontact mode ideally suited for obtaining high resolution images. Noncontact mode causes no damage or alteration to the sample due to the lack of contact, so is ideally suited for imaging soft, deformable samples. It is, however, highly susceptible to noise and hence requires careful tuning and calibration [3]. For this reason, the utilisation of FM-AFM is currently limited mostly to research applications.

This is a small introduction to the critical aspects AFM, which is too broad a topic to be explained in further detail. Several review papers exist in the literature which provide a more comprehensive overview of the history, theory and application of the technology. Abramovitch et al. have produced a simple and well written review detailing the basic operation of AFM and the fundamental theoretical principles needed for the technology to function [5]. The dynamic principles that specifically govern the micro cantilever critical for AFM operation is reviewed by Raman et al. [11]. The historical development and possible future trends of the technology since the invention of AFM, specifically in application to biology, is summarised by Parot et al. [9]. Finally, Jalili et al. go into detail about the application and theoretical understanding of AFM [12].

## 1.2 Future of AFM

Since its invention, AFM has advanced from a tool capable only of measuring surface topography in limited applications to one that can obtain a wide range of information about both surface and subsurface features of hard and soft samples. Advancing the capabilities of AFM to meet the needs of end users in both industry and academia is an area of active research. The technological developments and trends of AFM cover a very wide scope, too wide for this thesis. Only the research areas identified as having the most relevance to the scope of this thesis (detailed in section 1.6) are outlined in the following paragraphs. Questions relating to both the theoretical understanding and the application of technology are identified.

Of particular interest is the future of AFM in the field of biology. AFM techniques were first utilised in the biological community soon after its inception as a viable microscopy tool. The application of AFM to biology is evident by the continuously increasing amount of literature in which the

technology is utilised to measure biological phenomena within the first 10 years following its invention [13] and in the past 15 years [8]. It is likely that this trend will continue into the future as technological advances create the potential to measure biological processes with ever increasing precision and versatility. Existing AFM methods are now considered to be a mature technology, and there is a need to move beyond stand-alone, single cantilever measurement techniques to deliver new tools to meet the needs of biological research. A good summary of the possible future trends of AFM for biological applications was written by Casuso et al. [14]. Within the review paper by Casuso, as well as other sources [15, 16], a large range of desired applications and technological developments pertaining to AFM in biology are discussed. With the ability to gather, store and process ever larger quantities of data, arrays will become standard equipment in AFM applications, as opposed to a specialist tool. In particular, multi-probe AFM will become common in applications were there is a need to take measurements over a large surface area with true synchrony, for example when measuring chemical interactions occurring in large groups of cells. The versatility of arrays to be tuned for specific needs, such as parallel imaging, combined imaging and manipulation, and multi-modal AFM is a further positive attribute that can be utilised to meet the future needs of AFM. These aspects of multi-probe AFM will be discussed further in this chapter. Because the scope of biological AFM in the literature is so vast, it is not possible to identify and discuss all aspects in this thesis. Future trends that are of relevance to this thesis have been grouped into three open questions. The questions are; how to image samples with a scan rate sufficiently high to capture dynamic biological processes over a wide scan area; how to measure material properties of samples, including visco-elasticity, inter-molecular force gradients and adhesion in addition to topography; and how to detect and measure features below the sample surface to build up a 3D image of the sample, including material properties. These open questions will be discussed in more detail in the following paragraphs.

AFM research is currently heading towards imaging samples at high speeds. One of the major drawbacks of AFM is that scanning rates tend to be slow, often taking several minutes to produce a single image over a very small sample area [17]. Slow scanning speeds are unsuitable for imaging dynamic biological processes, which often occur in a time frame of milliseconds [18]. As a result, researchers have begun to develop high speed AFM techniques (HS-AFM) with the ultimate goal of producing video rate imaging. The development of HS-AFM has mostly focused on dynamic imaging modes using small cantilevers with very high bandwidths, and employing specialised electronics and software to measure small and rapid changes in

cantilever response. According to Ando, Olympus have developed AFM probes which are near the theoretical limits of cantilever bandwidth and measurement sensitivity, which are on the order of 6 µm in length [8]. Ando has demonstrated the versatility of dynamic HS-AFM in biological applications, and imaging of molecular interactions in aqueous solutions at frame rates of up to 15 fps is now possible [15]. The technology is reaching maturity, with small increments in single beam design and implementation still required to perfect the technique of HS-AFM, such as the recent developments by Ando and colleagues [19]. HS-AFM technology will soon be widely commercially available. Another development of interest in the field of HS-AFM is that of Picco et al., who have developed a contact method of HS-AFM, aimed at both material science and biological applications [20]. Due to the constant contact interaction between the tip and sample, this method is less susceptible to error due to transient response, and is capable of very high scan rates. The method can also be incorporated with contact resonance imaging for measurement of material properties [21]. It is clearly discusssed in the literature that HS-AFM, with imaging speeds of multiple fps, has been achieved over small areas in vacuum and air, and is nearing viability in liquids as well [8]. Still lacking is the ability to image at high speed over a large sample area within a reasonable time frame (seconds rather than hours). The current knowledge gaps are mostly technological, with the main requirements being the optimisation of cantilever parameters with regards to Q-factor and response time and the development of high speed electronics.

Much research is aimed at extending the capabilities of AFM to measure subsurface features. One of the key limitations of common AFM imaging techniques is that they provide no information about the sample beyond the immediate topographical features. This is a major drawback from the point of view of biological research, as much information about the sample lies below the surface due to the complex structure of biological systems. Several research groups have demonstrated the ability to map the location of subsurface nano-particles using AFM by measuring changes in visco-elasticity, surface damping and wave propagation of high frequency acoustics through the sample caused by the presence of such particles. There are multiple examples in the literature demonstrating the detection of gold nano-particles buried beneath a sample surface using AFM techniques. Shekhawat et al. passed ultrasound waves through a sample from the underside and used an oscillating AFM probe to detect the resulting signal. By measuring the interaction between the cantilever driving signal and the sample response, sub-surface features, including malaria parasites in red blood cells could be detected, which would distorted the transmission of the ultra-

sound waves [22]. This technique has achieved a spatial resolution on the scale of 10-100 nm. A similar technique was also demonstrated by Passian et al. [23] and Verbiest et. al. [24]. Passian et al. demonstrated a method to generate a multi layer image of impurities embedded in the sample by measuring multiple vibrational modes. Hu et al. used the interaction between a transmitted acoustic wave and cantilever eigenmodes to detect changes in localised sample elasticity [25], which could be extrapolated to the detection of subsurface defects. A recent development of interest is an experimental investigation performed by Ashino et al. [15], who were able to image fullerine balls that were embedded within carbon nano-tubes. This was done by measuring the damping ratio of the sample surface during nc-AFM imaging and using the information to infer the presence of fullerine balls within the carbon nanotube structure, using a-priori knowledge of how the fullerine balls would alter response. Atomic resolution of the damping properties of the sample and hence of the subsurface features was achieved. The papers discussed demonstrate the ability of AFM to detect the presence of subsurface features though indirect measurement of the mechanical properties of a sample. Subsurface measurement techniques are now well established in the literature, but are lacking in applicability. Measurement techniques are rapidly maturing, but the main challenge lies in the interpretation of measurement signals, specifically correlating feedback response to the material composition of subsurface features and the surrounding medium. Knowledge of the relation between damping and stiffness characteristics within multiple sample layers is required, in addition to the relation between the response of higher order eigenmodes and the interaction forces. This is a theoretical challenge requiring a mathematical modelling approach.

There is a drive to take AFM technology beyond imaging soley sample topography and to take it to a point where material and force properties can be measured with ease of use and with good reliability. Whilst many research groups have demonstrated the ability of AFM methods to measure material properties of specific samples, a general technology that is applicable to a wide variety of applications has not yet been realised. A technique that is commonly used is force spectroscopy, which involves measuring the deflection of a cantilever beam of known stiffness as it is brought towards the sample surface. By measuring the cantilever deflection during approach and retraction, the force gradient can be calculated, which provides information about the local stiffness, viscoelasticity and surface adhesion. A good example of the utilisation of this method and its application to biology is presented by Kuznetsova et al. [26]. Knowledge of the nano-mechanical properties of cells and other biological structures can provide a great deal of information about their chemical composition and functionality. There is

a wide range of applications to which localised material property measurement can be applied, particularly in the pursuit of personalised medicine, for which knowledge of individual cell behaviour is necessary. Several research groups have recognised the importance of AFM force spectroscopy for biological research and medical applications. Muller, for example, identifies the ability of AFM and force spectroscopy techniques to measure the properties of biological membranes [27]. In particular, Muller demonstrates how variations in chemical structure and molecular bonding can be mapped out. Similar conclusions are drawn by Alessandrini et al. with regards to the mapping of the chemical composition of biological samples based of material property measurements [28]. One of the major downsides of force spectroscopy is that it requires very sensitive deflection measurement and very soft cantilevers to obtain reliable force measurement with sufficient precision (surface forces can be as low as a few pico-Newtons at the molecular level). However, to achieve high force sensitivity with soft cantilevers, the bandwidth of the measurement is inevitably reduced, lowering the data acquisition rate. This drawback has prevented the wide spread use of force spectroscopy beyond fundamental research applications. An additional method of material property measurement is to use multiple modes and higher harmonics of a cantilever as a method of measuring the nonlinear tip-sample interaction force gradient. Different vibrational modes of a cantilever respond differently to the nonlinear force gradient, and harmonics of the excitation frequency are formed in the cantilever response. A review paper discussing the concepts behind multi-frequency AFM is presented by Garcia et al. [29]. Two distinct methodologies exist for the detection of higher modes. A typical AM-AFM imaging technique can be employed, where one mode is excited externally and the higher harmonics are measured using additional lock-in amplifiers. Hillenbrand et al. demonstrated early on the ability of AM-AFM to detect material contrast on relatively featureless surfaces, in this case by measuring the 13th harmonic of the cantilever [30]. The method has also been implemented in cell biology to obtain information about variations in chemical composition of the cell structure [31]. The main drawback of this AM-AFM technique is that the harmonic response tends to be very weak, making it susceptible to noise and reduced measurement precision. The other method of higher mode detection involves exciting multiple eigenmodes of the cantilever, most commonly the first two modes [32]. Due to the orthogonality of the cantilever eigenmodes, the first mode can be used for measuring topography, whilst another mode can be used to obtain information about the nonlinear force gradient. It is also possible to combine these two methods by designing cantilevers with higher order eigenmodes that are close to harmonics of the fundamental mode, as

demonstrated by Schuh et al. [33]. Whilst the concept of higher harmonic and multi-modal AFM has been well demonstrated in the literature for a variety of trial samples, it is not yet sufficiently reliable and user-friendly for commercial application. The main technological challenge is the design of probes with eigenmodes of specific frequency ratios. Higher eigenmodes often respond with very low amplitudes and hence have a poor signal-to-noise ratio (SNR), preventing high precision measurement. Tuning of cantilever modes can increase the response sensitivity of higher eigenmodes. This is an area of intense research activity. From a modelling viewpoint, it is necessary to understand how the system modes and harmonics interact with each other and the sample, with specific emphasis on how to maximise the SNR of the desired measurement signals. The link between higher harmonic/multi-mode response and the conservative/dissipative sample properties is also not yet fully understood, limiting the application of the technology to well understood test samples.

## 1.3 Micro-Cantilever Arrays

One concept that has been identified for meeting the future requirements of AFM is that of utilising multiple cantilevers in an array configuration. Using arrays of cantilevers would allow AFM technology to be applied in ways that are currently beyond the capabilities of single beam systems. Arrays offer two key advantages over a single beam; the potential to increase measurement speed and measurement sensitivity. Using multiple cantilevers allows multiple points on a sample to be imaged simultaneously, which would allow end users to obtain truly parallel information about separate points on a sample, as opposed to using serial acquisition with a single beam, which produces a small but non-negligible time delay that can add uncertainty to the acquired data. Simultaneous acquisition is of particular significance for biological measurement applications. Many naturally occurring bio-chemical processes are extremely complex, usually involving multiple chemical reactions simultaneously. The influence of bio-chemical reactions can spread rapidly over a large surface. Obtaining measurements from multiple points simultaneously can provide a better understanding of the large scale dynamics of such phenomena. The second advantage is that multiple, coupled cantilevers can be used to increase measurement sensitivity and selectivity, due to the additional degrees of freedom (DOF) present in the system. Each additional cantilever added to the array structure adds another DOF to the system, and the degree to which the cantilevers are mechanical coupled determines the level of interaction between the DOF. Each additional beam offers the opportunity to vary the selectivity and sensitivity of the system

to certain frequency bandwidths, and hence certain sample properties. By controlling the level of coupling between the available DOF, multiple feedback signals, including amplitude, phase and frequency can be measured simultaneously, increasing the amount of information that can be obtained in a single measurement. Adding DOF to traditional AFM systems and tuning the level of interaction between them has been demonstrated as a potentially useful technique in the literature. Nurul et al. recently demonstrated the use of a paddle embedded within the cantilever structure to add a tunable DOF to the system [34]. Similar devices have also been tested by Zeyen et al. [35] and Felts et al. [36]. Through precise mechanical design of the paddles, the modal shapes of the cantilever-paddle eigenmodes can be controlled, and by carefully selecting the frequency and damping characteristics of the cantilever-paddle system, the response of each mode can be enhanced/reduced at specific points on the structure. The technique can be used for example to magnify the response of higher harmonic components of the cantilever response, and to enhance the signal to noise ratio of selected eigenmodes, allowing for selectivity of desired sample properties. Arrays offer an alternative method to the paddle system for adding flexibility to a cantilever measurement system. Arrays have the advantage that many additional beams can be added, with the option to vary individual beam dimensions and allowing for greater bandwidth selectivity from the response signal.

Several research groups have already attempted to introduce arrays into AFM technology since the early 1990s. Various applications have been identified already for AFM arrays, including simultaneous sample measurement and manipulation [37], parallel imaging over a large surface [38] and even high density data storage [39]. All these applications take advantage of the ability of arrays to interact with the sample surface at multiple points in a parallel manor. As yet, no research group has utilised the advantages offered from additional DOF and parameter selectivity in array applications. A significant amount of research is aimed at sensor design for parallel readout. The standard optical level method cannot be easily extrapolated for multiple cantilevers, due to space and alignment constraints. Instead, other methods including interferometry, piezo-resistance and capacitance have been tried for sequential readout. Sensor design for AFM arrays is now a mature field of research, and major challenges needed to be overcome have been identified and addressed in detail in the literature. Another focus within the literature is the parallel systems operation and image processing of array feedback. There are already several examples in the literature of simple images formed using multiple cantilevers simultaneously, mostly with widely spaced cantilevers [37, 40, 41]. A key challenge in the acqui-

sition and processing of simultaneous signals is the design of high speed, truly parallel electronics. This challenge is tackled with bespoke electronic hardware utilising field programmable gate arrays (FPGA). This is an area of active research, but lies outside the scope of this work.

Micro-cantilever arrays have already been utilised for applications other than AFM in the literature, the most prominent of which is the detection and mass measurement of nano-particles and molecules. Mass detection and measurement can be enhanced by using array eigenmodes to increase sensitivity and decrease susceptibility to noise, and measurements in the regions of picograms have been achieved [42], by utilising the tunability of parameters within the array structure. The most common method involves designing the array with desirable mode shapes at desirable frequency bandwidths. The mode shapes and frequencies can be determined based on the mass and damping properties of the particles that are to be detected and measured. The system parameters can be tuned such that different beams/eigenmodes in the array respond to certain particles and properties of interest. In addition to this, the level of interaction between the eigenmodes can be controlled, also through careful parameter selection. Measurement of the interaction between eigenmodes through changes in response amplitude can produce very high measurement sensitivity [43]. These factors make cantilever arrays a versatile tool for mass detection and measurement, hence the research interest in the literature. The concepts discussed regarding arrays for mass sensing tie in closely with the concepts discussed above for AFM arrays, specifically the idea of utilising additional DOF for increased flexibility of parameter selection, which leads to enhanced selectivity and sensitivity of the measurement signal. Demonstration of this concept is severely lacking in the literature and offers a potential research opportunity.

## 1.4 Challenges Facing Array Technology

Several fundamental challenges must be overcome if the previously mentioned goals of AFM array technology are to be achieved. The most notable challenge facing the implementation of array technology is a lack of understanding of the fundamental system dynamics. The dynamics of single AFM cantilevers is now well understood, with a significant body of research present in the literature and a number of textbooks written on the subject, for example by Bhushan et al. [44]. The relationship between tip forces and cantilever response is also well understood. What is not well understood is how the three key elements of an AFM array combine; the known spatial and temporal response of an individual cantilever; mechanical coupling

between cantilevers; and the nonlinear interaction forces applied separately to each cantilever tip. Separately, all three of these concepts are studied extensively in the literature, however, there is a lack of knowledge as to how all three elements combine. In addition, there is a lack of understanding relating to the multiphysics interactions (mechanical, electrostatic, thermal and fluidic) that occur when multiple cantilevers are in close proximity as identified by Roeser et al. [45].

Several research groups have attempted to analyse the dynamics of AFM arrays. A detailed discussion of this is provided in the literature review. A common theme in the literature, however, is the lack of a fundamental, holistic approach to the mathematical modelling of array response. In most cases, modelling has focused solely on the elimination of coupling effects for parallel throughput, usually with a pre-determined array structure and often with low cantilever density. While the issue of reliable, parallel throughput is important, this approach can prematurely eliminate other avenues of investigation, which is an important reason for the lack of research aimed at developing arrays for enhanced AFM measurement through utilisation of the additional DOF and parameters available. What is needed is a detailed mathematical model that incorporates the three aforementioned elements and simulates the most significant phenomena that occur during AFM imaging. The phenomena that must be captured include; frequency, amplitude and phase bifurcations, which can occur due to nonlinear force interactions and can cause discontinuities to be observed in the system response; and synchronisation, which is influenced by the relative resonant frequencies of beams in the array and the strength of the coupling between them. The modelling needs to be done from a base-level approach and should ultimately drive array mechanical design. The modelling needs to be kept as simple as possible whilst capturing the key response characteristics that occur when tip forces and mechanical coupling are combined, which ensures that the model can be scaled for an arbitrarily sized array without the response calculations becoming excessively complex. The key characteristics that must be captured are the modal properties of the array eigenmodes, including spatial mode shape, frequency bandwidth and phase shift, the interaction between eigenmodes and the formation of higher harmonics.

As mentioned, a major aspect of AFM technology is the ability to interpret the components of system response to obtain information about material properties and sample topography simultaneously. The key challenge here is how to process the measured signals into usable data, and is an active area of research in the field of single cantilever and array AFM. Also of note is the selection of suitable sensors and actuators, which is still a major issue. Due to the complexity of the system and parallel nature of the

cantilevers, traditional piezo-stack actuators and the optical lever method are not suitable for arrays. Sensor and actuator selection is an area of ongoing research, and one that is taken from the perspective of design and fabrication, as cost and ease of manufacture/implementation are the key drivers. While both of these are important considerations, for these reasons they will not be included in the research scope, as stated in the next section.

## 1.5 Project Background

The wider project to which this thesis relates began with the formation of a research collaboration between the University of Canterbury (UC) and the Technische Universität Ilmeau (TUI) in Germany. The group lead by Prof. Rangelow at TUI have been designing and fabricating micro arrays for application to AFM. The research has been primarily focused on experimental investigation to determine what methods work best for parallel imaging for the purpose of improving scan speeds. The research team at UC were brought in to provide expertise in the field of mathematical modelling and dynamic analysis to compliment the experimental work conducted at TUI. As a result, the team at TUI continue to conduct experimental investigations and design new arrays, while modelling and simulation is carried out at UC, including a detailed analysis of the arrays already fabricated at TUI.

In addition, the research group at UC has been conducting experiments using an equivalent macro scale system of the micro cantilever arrays. The idea behind this is to simulate the fundamental dynamics of micro-fabricated arrays but on a larger scale. The purpose of using a macro scale experiment is two-fold; it is easy to visually observe response phenomena on the macro scale and the state of operation of the system, for example whether the cantilever tip is in contact with the sample; and it is easy and inexpensive to vary key parameters for investigative purposes, for example the individual cantilever dimensions and strength of the mechanical coupling. Simulating micro phenomena on the macro scale is possible as the physics governing cantilever motion are the same at both scales, and tip-sample interaction forces can be readily simulated, as is discussed in the literature review. The macro scale approach is used by UC in conjunction with mathematical modelling and experimental data provided by TUI, creating a more effective research collaboration. This thesis will build on that work by also utilising macro scale experimentation to simulate the performance of micro scale arrays.

Mathematical modelling pertaining to the TUI cantilevers has been conducted by Roeser et al. as part of the research collaboration [45–47]. The

research focuses on the multi-physics interactions that occur within a single, multi-layered TUI cantilever, containing a heater actuator and piezo-bridge sensor. The developed model takes into account the different material layers that make up a TUI cantilever to determine the resulting beam stiffness and spatial mode shapes, and has been demonstrate to match well to experimental data. Also investigated is the multi-physics coupling that occurs within a single TUI cantilever, specifically coupling between the sensor and actuator. It was demonstrated that the observed displacement signal was influenced by the heater output power, and was not constant. A mathematical model of the thermal, mechanical and electrostatic coupling between the actuator and sensor elements demonstrated this phenomena and has been validated through experimentation. The dynamics and multi-physics coupling within a single TUI array is hence now well understood. The combined influence of coupling between cantilevers and nonlinear interaction forces within an array has not yet been accounted for, which is the focus of this thesis. It will be possible to combine the outcomes of the research work of this thesis with the outcomes of Roeser et al. to produce a comprehensive understanding of the dynamic response of a TUI array.

The UC research group also investigates the interaction of arrays with a surrounding fluid medium. Understanding the influence of fluid dynamics on array response is an important aspect of the research project as many AFM applications, particularly in biology, favour imaging in liquid environments. The interaction between the motion of a closely spaced array and a fluid medium is extremely complex. The research work specific to this thesis does not incorporate the mechanism of fluidic coupling and instead focuses in detail on the observed phenomena that result from linear coupling. The two research streams individually provide vital information that together contributes to the understand of array dynamics in the context of AFM.

## 1.6 Research Scope

The possible future trends in AFM technology have been identified with emphasis on how cantilever arrays may be used to meet the requirements of end users. The challenges that must first be met have also been discussed, with the conclusion that a fundamental understanding of the dynamic response of arrays is required, specifically, how array response is influenced by system parameters and external factors. This fundamental knowledge is needed before mechanical design parameters can be set and before signal processing can be undertaken. In conclusion, the research will focus on fundamental dynamic analysis.

A majority of the research in the field of AFM over the last three decades

has focused on single beam measurement and imaging. There are still many research groups worldwide working on improving the speed, reliability and usability of single beam techniques as well as developing new AFM based systems to open new avenues into nano-scale measurement in biology and metrology. For these reasons, a detailed analysis of the dynamics of a single beam does not provide a significant original contribution to the body of reasearch and will not be included in the thesis. The thesis will instead focus solely on cantilever arrays and their application to AFM. The analysis of array dynamics will be done to address the two key issues that have been identified, the need to image multiple sample points simultaneously with high reliability and precision, and the need to measure sample properties and nonlinear force interactions with improved sensitivity. The analysis will be conducted for arrays with mechanical coupling only. Mechanical coupling will always be a factor when cantilevers share a common base and is relatively easy to model with precision. Fluid coupling has also been identified as a major source of interaction, especially when imaging biological samples in an aqueous environment [48], and is a key part of our group's research. The physics governing fluidic coupling can be extremely complex and is a major area of research on its own, and will not be included in the scope of this Thesis. Other forms of coupling have also been studied in the literature, including thermal, electrical and magnetic. These are often addressed through actuator/sensor design or through circuit design, neither of which are a focus of this thesis. It has been deemed more useful to study the general effects of coupling phenomena on cantilever arrays and how this can be applied to advance AFM technology. The specific impact of different types of coupling can be incorporated into the model at a later stage.

Within the scope of this work, the individual beams of the array are assumed to be linear, with nonlinearities deriving solely from the tip-sample interaction forces. In most imaging applications, the nonlinearities inherent to the micro cantilever play a minor role in the system response in comparison to the interaction forces. Assuming a linear beam model is hence a valid approach and will reduce the complexity of the array model. Additionally, only dynamic modes of AFM will be considered, with particular emphasis on tapping mode and noncontact mode. These methods provide the greatest opportunities for the utilisation of the extra DOF and available feedback signals available from array technology. Tapping mode is also the most widely used imaging method, used in both research and industrial applications. For these reasons, it is deemed advantageous to focus the research within the scope of well established forms of dynamic mode AFM.

Experimental results are obtained on both the micro scale and macro scale. Throughout this thesis, the micro scale is defined as $<1\,\mathrm{mm}$, and

the macro scale is everything larger than this. As will be discussed in the literature review, it has been conclusively shown in the literature that micro scale dynamic phenomena can be studied using an equivalent macro scale set up. The majority of the research in this thesis is performed using a macro scale test rig to validate mathematical simulations and obtain data. The micro scale is used predominantly for validation purposes of the macro scale system and for identifying the performance of arrays.

## 1.7 Contributions

This Thesis consists of a total of eight chapters. In Chapter 2, a review of the literature is given, which can be summarised into three distinct areas, a review of micro arrays focusing on fundamental dynamic studies, a review of AFM developments in regards to applications, and a review of macro scale experiments that have been used to gain an understanding of micro scale phenomena. In Chapter 3 experimental data gathered using micro cantilever arrays will be presented. The focus of this chapter will be to demonstrate the dynamic response that occurs in a base coupled array and how the response is altered when near a sample surface. The information creates the groundwork of the research by identifying the key issues that can adversely affect imaging feedback when using arrays for parallel imaging, as well as identifying alternative uses for arrays to improve the state of the art of existing AFM technolgy. In Chapter 4, the design and construction of the macro scale test rig is discussed. The focus of the discussion is on the functionality of the test rig to simulate the coupled and nonlinear phenomena that occur in micro AFM arrays and to vary the key parameters of coupling strength, cantilever stiffness and tip interaction force strength. Experimental results using the test rig will be presented for comparison with the TUI micro arrays and model simulations. This is for validation purposes, and experimental results for research outcomes will be presented in later chapters. In Chapter 5 the mathematical model of a base coupled array influenced by nonlinear tip forces is presented. The mathematical model is primarily used to perform numerical simulations to understand how the system parameters can alter system response, and how this influences the measurement process. The model is used specifically to determine how coupling strength, individual cantilever stiffness and tip interaction force strength can combine to produce reliable, parallel imaging and enhanced measurement. In Chapter 6, the dynamics of the TUI arrays will be analysed for the purpose of parallel imaging. The focus will be on ensuring that stable, reliable and precise measurements are possible with multiple beams simultaneously, without negative impact from coupling phenomena. The

coupling phenomena identified in Chapter 3 will be related to the system parameters and system response. Based on the analysis, suggestions will be made as to how to avoid or mitigate any detrimental effects resulting from the identified coupling phenomena. These outcomes will be backed up with mathematical simulations. Suggestions will include considerations for both mechanical design and operation. In Chapter 7, cantilever arrays will be studied for their ability to increase measurement sensitivity beyond that achievable with standard single beam methods. It will be shown that the parameter space of an array can be tuned such that steep changes in amplitude, phase and frequency for a given change in tip sample separation can be achieved without instabilities occurring. Mathematical simulations will be used to quantify the achievable sensitivity relative to an equivalent single beam system and to identify the required parameter constraints. Finally, in Chapter 8 the research findings are summarised and final conclusions are drawn. The discussion is focused on the impact of the research on the future of AFM. Specifically, the input of the results on the TUI array technology is discussed.

CHAPTER 2

# Literature Review

## 2.1 Introduction

The review will provide an overview of the research presented in the literature into arrays of coupled, micro-scale oscillators. Included is a review on generic micro devices for which a coupled, nonlinear response is observed, a discussion of the mathematical modelling that has been conducted for specific macro devices, and what experimental results have been obtained to back up theoretical findings. This Chapter will provide a frame work from which the original modelling, numerical simulation and experimental work of the thesis can be built. As well as discussing generic micro arrays, a review is presented for the specific application of arrays in AFM. Work performed by other research groups, both theoretically and experimentally, is reviewed and the gaps in the research are identified. Finally, a review of macro scale experiments used to simulate micro scale phenomena is presented to set out the framework for the design of the experimental methods used in this thesis and to justify the use of a macro scale system.

## 2.2 Micro-Cantilever Arrays, Theory and Experiment

Theoretical and experimental research has been carried out on micro arrays with differing mechanical structures and for differing applications. Of note is the experimental investigations conducted by Buks and Roukes on doubly clamped micro beam arrays [49], which was a pioneering experiment that demonstrated the complex response created when nonlinear oscillators are coupled together. In their paper, an array of clamped-clamped beams was used, and coupling was induced by applying a potential difference between the beams. The results showed that distinct eigenfrequencies were formed, and that the relative modal frequencies could be tightly controlled by ad-

justing the coupling parameter, which in this case was the DC potential between neighbouring beams. Following publication of the experimental findings, the dynamic behaviour of the array was studied analytically by Lifshitz and Cross [50]. Their work showed mathematically how the observed frequency response of the coupled system was affected by nonlinear stiffness and damping terms. A discrete model of the micro beam array was formulated assuming a duffing nonlinearity and parametric excitation terms. Numerical simulations demonstrated the formation of many stable/unstable solution branches, which accounted for the response phenomena observed by Buks and Roukes. This combined experimental and theoretical study is an early example of coupled micro oscillator analysis, and set the framework for much of the future research in the literature. The model successfully described the observed response qualitatively, but was unable to provide a quantitative match between response and parameter space, due to the lumped mass approximation used by Lifshitz and Cross. Another, similar example of a mathematical model for a clamped-clamped micro beam array is presented by Gutschmidt and Gottlieb [51]. The work utilises a continuum mechanics approach to model the micro beams, capturing the spatial mode shapes as well as output response. The advantages of using a continuum mechanics model are well demonstrated, as unlike the case for Lifshitz and Cross, the response can be directly linked to parameter space, without the need of independent identification for the nonlinear, coupling and parametric excitation parameters. The comparison between the two papers is a good demonstration of the relative merits and shortfalls of the lumped mass and continuum mechanics approaches.

The most common form of mathematical modelling for coupled micro-resonators utilises nearest neighbour coupling, where coupling terms are included only between adjoining elements, a concept employed by Lifshitz and Cross et al. in another publication [52]. The paper investigates an array of coupled nonlinear oscillators, and uses secular perturbation theory to find the system equilibria. The addition of coupling terms is shown to introduce very complex expressions linking the individual oscillators with overall system response. Using only nearest neighbour coupling prevents an excessive build-up of these coupling terms as the number of individual elements increases. The paper also demonstrates that nearest-neighbour coupling is sufficient to capture the full system response of a generic array of coupled oscillators with sufficient precision. Another good example demonstrating nearest neighbour coupling is the paper by Dick et al. [53], which models an array of coupled micro-resonators with cubic nonlinearity terms from first principles using discrete elements. This study in particular looks at the formation of Intrinsic Localised Modes (ILM) that form

within oscillator arrays. The results demonstrate that the model is able to capture the frequency and relative displacement properties of the system's eigenmodes, and specifically how they are altered by the cubic nonlinearity, the relative parameter values of the individual elements and the applied external excitation. However, the coupling between the eigenmodes is very susceptible to the nonlinear parameters, which must be selected carefully to ensure meaningful outcomes. Several other groups have also demonstrated the ability to model changes in modal properties when combining coupled oscillators with a source of nonlinearity [54, 55]. The large body of research on the subject suggests that it should be possible to model the combined effect of mechanical coupling and nonlinear tip-sample interactions for AFM arrays using a similar approach.

A prominent application of cantilever arrays that was discussed in the introduction was the detection and measurement of nano-particles and molecules. This is a practical application of the ILM phenomena, using the changes in eigenmode properties as a feedback signal. The method commonly employed requires weakly coupling arrays of near identical cantilevers. Adding a mass to one cantilever causes a single eigenmode of the system to become spatially localised at that specific cantilever and at a specific frequency, which can be identified by a sharp increase in modal amplitude. Spletzer et al. [56] demonstrated that eigenmode shifts in coupled arrays can be 2-3 orders of magnitude more sensitive than equivalent frequency and amplitude shifts of a single cantilever. The research utilised a discrete model to capture the system eigenmodes, and was able to map amplitude changes to mass changes at each sensing element. This is crucial information that is needed to accurately and precisely map the feedback signals from the sensing elements to the location and amount of added mass, and demonstrates the need for a good understanding of the fundamental system dynamics. Thiruvenkatanathan et al. [57] showed that the coupling strength parameter is extremely important in determining the measurement sensitivity and bandwidth of detection and Glean et al. [58] also showed the importance of parameter space with regards to setting bandwidth and sensitivity limits.

## 2.3 Cantilever Arrays for AFM

### 2.3.1 Design and Fabrication

In the scope of this review an array of AFM probes is identified as consisting of 2 or more individual cantilevers situated in close proximity to each other on a shared base. The design and fabrication of such arrays has been conducted by several groups since the mid 1990's [37, 59–63]. Initial work

began with the fabrication of small arrays. The first case of a fabricated AFM array found in the literature is a two beam array fabricated by Minne et al. in 1995 [37]. The work presented the idea that the imaging rate and scan size of AFM could be increased with the use of parallel data acquisition through multiple probes, and was a significant new approach to nano-imaging technology that has paved the way for the development of array based AFM. Minne et al. continued their work, eventually fabricating an array of 50 cantilevers in 1998 [64]. The project was discontinued soon after, and no further publications are present in the literature.

One of the key features of these early array designs was the large spacing between individual cantilevers (other examples can be seen in [40, 62, 65]), which has the advantage of eliminating interactions between the cantilevers, allowing well establish, single cantilever modelling and operation methods to be implemented. Despite offering a solution that is simple to implement, the large spacing reduces the potential scan rate of the array system. This is undesirable with regards to the goal of high speed AFM imaging. Several research groups have produced arrays with closely spaced cantilevers (tip to tip spacing less than three time the cantilever width) to better utilise their potential benefits. In 2007, Rangelow et al. presented the fabrication of a 2D array consisting of 128 (4×32) cantilevers [59,66] as part of the PRONANO project. To date, the group has developed the fabrication technology to produce larger arrays of up to 512 (8×64) beams [67]. In 2008 Ahn et al. developed arrays of 30 (1×30) and 104 (1×104) beams with specific emphasis on close spacing [61]. Zhang et al. have recently fabricated a 1×8 array [68]. The large number of varying array sizes indicates the breadth of research present in the literature with regards to fabricating closely spaced arrays, and demonstrates that it is an active area of research.

Major developments in the fabrication of micro-cantilever arrays have been made by IBM's research division as part of the 'Millipede' Project [39]. The Millipede project is focused on micro cantilever arrays with applications in data storage. The idea was to use micro cantilevers to read and write indentations on a polymer surface, representing binary data. The cantilevers tips are plunged into the surface to create indentations, then raster scanned over the surface in contact mode to read back the data. The small scale allows for high density storage and the high bandwidth for fast writing and reading. Despite the differing application, the technological developments are still relevant to AFM, in particular the advanced manufacturing techniques. The Millipede group was able to produce an array of 1024 individual V-shaped probes (32×32) [69], which is the largest fabricated AFM array system to date. Like many other groups discussed in this review, the Millipede group only fabricated arrays consisting of very widely spaced can-

tilevers. The project was ultimately discontinued due to the development of superior data storage technologies.

One of the key design issues of AFM arrays is the space restrictions for sensing and actuation. The optical lever method and piezo tube actuators traditionally used for single cantilever operation cannot be easily incorporated into arrays due to space constraints, alignment difficulties, and the need to control all cantilevers in the array individually. This has driven researchers to investigate other methods of tip deflection sensing and base excitation. Whilst AFM array research began roughly 20 years ago, there is currently no single, well established method for actuation or sensing in the literature. This is in contrast to single cantilever AFM, which heavily favours the well established optical lever and piezo tube actuator for sensing and actuation, respectively. This suggests that research into AFM arrays is sporadic, with a wide range of groups currently fabricating arrays with varying goals for both fundamental research and commercial application. There is a need to focus the research towards improving the capabilities of AFM technology, namely to image multiple points on a sample simultaneously and to improve the sensitivity and selectivity of AFM, and to achieve the goal of high throughput, non-evasive parallel imaging of a wide range of samples. A selection of some of the key methods of actuation and sensing are presented below with advantages and shortfalls of each.

- **Sensing:**
  - **Piezoresistive:** The piezoresistive sensor was first demonstrated with an AFM probe in 1991 [70] as an alternative to the optical lever. The key advantage of this technology is that the piezoresistor is fabricated directly into the cantilever, eliminating the need for bulky equipment external to the probe or for careful alignment. In addition, only simple signal processing is needed to convert the raw output into a usable signal. Piezoresistors have been used extensively by several research groups [37, 59, 62]. A major downside of this method is the complexity of fabrication to integrate the sensor into the cantilevers, increasing the cost of production. It has also been shown that piezoresistive sensors can be strongly affected by noise, depending on the sensor design and layout [71], limiting the achievable resolution.
  - **Interferometry:** Interferometry has been trialled for tip displacement sensing since the early days of AFM [7]. The working principle is to focus a laser beam into a line, which is directed at the cantilever tips in the array. Diffraction gratings are machined

into the cantilevers, which diffract the laser light into a fringe pattern. The pattern is detected by an array of photo-diodes and is used to determine the tip displacement of each cantilever. This technique was implemented by Minne et al. in 2001 [38] and has been used by several other research groups [72, 73]. Interferometry produces very good resolution and does not require the stringent alignment that plagues the optical lever method. It also avoids the issue of optical cross-talk as it is the fringe pattern, not the absolute position or magnitude of the reflected laser that produces the position signal. However, the set-up tends to be expensive, suffers from space issues with large arrays and does not illuminate all the probes with uniform intensity. The largest existing array with which interferometry has been implemented is 100 cantilevers (10×10) [73].

- **Actuation:**
  - **Piezoelectric:** Piezoelectric actuators are often used for MEMS devices as they have a very high bandwidth and good sensitivity. Piezoelectric actuators have been used by several groups, including the Zhang, Minne and Kim groups [37, 68, 74]. A major advantage is that it is possible to use the piezoelectric effect as a feedback signal as well as applying an actuation force. The result is that the actuator and sensor can be integrated into one element, reducing space requirements. Zhang et al. used this method to create an array of 8 cantilevers fabricated from PZT with individual sensing and actuating capabilities [68].
  - **Thermal:** Heating materials with different thermal expansion coefficients can be used to induce bending in a multi-layered cantilever. Due to the small size of the cantilevers, low power levels are suitable for adequate deflection, allowing for rapid actuation. This technique has been used extensively by the Rangelow group (as part of the PRONANO project), who have implemented the use of thermal actuation in their work [59, 67, 75] and have proved the feasibility of this method for large arrays. Other examples are presented in [60, 76, 77]. While this technique is inherently simple, it presents issues with thermal noise, which can be induced in the sensor, and thermal coupling between individual probes.
  - **Electrostatic:** Electrostatic actuation is one of the most commonly used actuation mechanisms for MEMS [78], and has been

employed as an actuation method for several AFM array designs [37, 61, 79]. The technology for fabricating micro electrostatic actuators is well developed and ideally suited to AFM cantilever base excitation, where micro-meter scale deflections are required. Despite its suitability, electrostatic actuation is problematic for AFM arrays due to high noise generation. Hundreds of volts are usually required to generate a sufficient amplitude, which creates both electrical and thermal (resistive heating) noise that introduces errors in the sensor signal (for an AFM cantilever the sensor and actuator are often in close proximity). Thermal and electrostatic coupling is also created due to the close proximity of individual probes.

### 2.3.2 Modelling and Control

In order to produce a clear, high resolution image using AFM technology, a firm understanding of the cantilever dynamics is required [11]. Several research groups have previously investigated the dynamic phenomena that occur within micro cantilevers subject to non-linear tip forces and produced mathematical models of AFM beams. A detailed review of single cantilever modelling is not included here. Instead, the focus is on array modelling.

When creating dense cantilever arrays with probes in close proximity, additional phenomena occur that alter the dynamics of individual beams, including mechanical, electrostatic, fluidic and thermal coupling. These phenomena must be understood through mathematical modelling in order to fully utilise the potential of AFM arrays and produce high resolution images with high throughput. The first publication of a model for coupled AFM cantilevers found in the literature was in 1999 by Napoli et al. [80]. This was an important piece of work as it is the first example of research moving away from a design and fabrication based approach towards a modelling approach to produce a usable AFM array system. It was also one of the first papers to identify the need to compensate for the effects of coupling. The cantilevers were modelled as simple spring-mass-damper systems along with a basic mechanical coupling matrix. The work of Napoli et al. progressed to a model of a pair of coupled electrostatically actuated cantilevers, incorporating both mechanical and electrical coupling [81]. This publication utilised coupled Mathieu equations to model the coupling between the two cantilevers. Whilst the modelling was fairly simplistic, this piece of work demonstrated mathematically that both mechanical and electrical coupling between cantilever probes in close proximity must be considered when studying system response.

Another group of particular note with regards to array modelling and control is Lenczner et al., who began work on AFM arrays in 2007 [82, 83]. The group has based their work on a two-scale model, which consists of an elastic base onto which an arbitrary number of cantilevers are attached. The cantilevers are assumed to be homogeneous and sufficiently thin to be modelled by the Love-Kirchhoff thin plate equation. The base is also assumed to be stiffer than the individual cantilevers. The model is simple and easily expandable to large arrays whilst keeping computational effort low. The model was later used to develop an optimal control method using a semi-decentralised strategy [84] where only nearest neighbour coupling was considered. The control strategy used the developed model to predict the error at each eigenmode between the coupled and equivalent uncoupled system and applied an appropriate input compensation. A simulation of this model was conducted using an array of 10 cantilevers excited at one particular mode [85]. Experimental verification of the model is not present in the literature.

The models described have been important for the development of viable AFM array systems for high throughput, parallel imaging and high sensitivity imaging. However, while these models have been validated through simulation, no detailed experimental validation has been conducted. None of the work discussed above has been used successfully to implement a viable AFM array system using closely spaced cantilevers.

## 2.4 The Gap Between Fabrication and Modelling

In the previous sections the research in the literature has been presented for two very distinct streams, namely the design/fabrication approach and the modelling/control approach. Both are vitally important for the progression of AFM array technology, however, the two research streams must be properly integrated to ensure the technology developed meets end user requirements. It is not possible to develop optimal measurement strategies and control algorithms without suitable hardware, and vice versa it is not possible to optimise the electro-mechanical design without understanding the system response. This integration is currently lacking in the literature.

The design and fabrication research groups have focused predominantly on arrays consisting of 8 or more cantilevers, with some research groups developing very large arrays consisting of hundreds of cantilevers. Large arrays are desirable for high throughput measurement, however, little consideration is given to the practicality or feasibility of such large arrays. Several

groups have fabricated cantilever arrays with integrated sensor and actuator elements but have shown little experimental validation, and only using controlled test sample to demonstrate imaging capability [59, 74, 76, 86]. This does not sufficiently demonstrate that the fabricated arrays can be used to image a variety of samples.

In contrast, research groups in the modelling stream have tended to focus on small sized arrays, usually consisting of 2-3 beams [81]. Larger models have tended to be highly simplified, with all beams assumed to be perfectly uniform and exactly identical [84]. This is in stark contrast to the properties of real arrays, which are mostly fabricated with a large number of beams, all of which have slightly varied dimensions and properties. Fundamental mathematical modelling has answered some of the fundamental questions about micro array dynamics, and while this information is important, detailed models incorporating real world conditions are also needed to ensure optimal operation in all conditions.

There is a need to bridge the gap between design and modelling research. Mathematical models need to be developed to analyse realistic arrays, specifically those with non-uniform and non-identical beams. Knowledge from this can be used to influence the design of AFM arrays, including the selection of optimal parameters to ensure high sensitivity, resolution, reliability and stability. The development of control algorithms that overcome some of the major obstacles facing AFM array development are also needed. The design of arrays should be focused on sensor/actuator selection and array layout/sizing for implementation with optimal control, whilst keeping the fabrication process simple and easily scalable.

## 2.5 Macro Scale Cantilever Experiments

Due to the small scale of micro arrays, it can be difficult to observe the system response and gain a full understanding of the dynamic phenomena present in the system. It can also be costly and time consuming to fabricate new micro devices, especially when multiple parameter sets need to be analysed. One possible solution to these problems is to study an equivalent macro scale system and use the knowledge gained to make inferences about the response of micro systems. Several research groups have used macro scale experiments previously as a way of gaining an understanding of the fundamental dynamics governing micro scale systems, as discussed in the following paragraphs.

Of particular note is the work performed by Balachandran et al.. In 2009, Balachandran et al. first suggested the use of a macro scale cantilever beam as a method of studying the dynamics that occur during tapping mode

AFM operation [87]. The work was focused on the nonlinear dynamics that occur in the event of zero velocity surface impacts during tapping mode operation. Magnets were used to simulate attractive forces and a compliant impact surface to simulate repulsive forces. The work demonstrated that the macro scale force interactions are qualitatively but not quantitatively similar to the micro scale. As the purpose of macro scale simulation is to capture the effects of nonlinear phenomena on system response, and not to predict exact response output, a qualitative match is sufficient. Balachandran et al. continued their work and presented a comparison between macro and micro scale results [88]. The work again focused on zero velocity impacts that can occur during tapping mode operation and proved there is good qualitative agreement with regards to nonlinear dynamic phenomena between the two scales.

There are several examples of other cantilever arrays that have been investigated on the macro scale. Hikihara et al. used a macro scale experiment to investigate mode localisation within an array of coupled cantilevers [89,90]. In these experiments, cantilevers were clamped to a common base and coupled using a flexible rod attached at a set distance from the clamp. Magnets were placed beneath the tip of each beam to provide nonlinear interaction forces. Experiments showed that localised modes were formed within the macro array and that a reasonable match was observed with localised modes that occur in an equivalent micro systems as studied by Sato et al. [91]. Mode localisation in macro scale arrays was also investigated by Yabuno et al. [92], with the focus on the application of high sensitivity mass sensing using micro cantilever arrays. A macro array of two cantilevers was fabricated from a single piece of material with a common base structure providing the coupling. Mode localisation was demonstrated in the array, however, poor resolution was observed due to the effects of air damping.

## 2.6 Summary

The review shows that a wide range of literature exists in the field of micro cantilever arrays for AFM measurement. As yet, no functioning AFM array beyond a few prototypes has been produced for the purpose of high throughput or high sensitivity imaging. The lack of a viable device can be summarised with two key reasons. Collaboration between research groups specialising in design and fabrication and those specialising in mathematical modelling is lacking. Both fields of research are vitally important to solve fundamental questions necessary to produce usable array technology and must be performed in tandem. There is also a lack of focus towards

an end goal in the literature. Many of the research groups discussed in Sections 2.3.1 and 2.3.2 offered new, fundamental sensing and control techniques without answering key technological questions, including how to use coupled array response as a feedback signal, how to control individual tip-sample separations when all cantilevers share a common base and how to design and implement arrays with maximum sensitivity to tip-sample forces as well as minimal noise sensitivity. These questions must be answered before AFM array technology can be implemented reliably and have the chance to become commercially viable.

CHAPTER 3

# Phenomena in Micro Arrays

## 3.1 Introduction

In this chapter, the dynamic performance of arrays fabricated at TUI are analysed and discussed to determine the presence of currently unexplained or unexpected phenomena. It is important to understand the characteristics of the arrays in order to give direction to the research and to ensure the outcomes of this thesis can provide useful information regarding the design of AFM arrays. The results from this chapter will tie into the content of the following chapters covering mathematical modelling and macro scale experimental investigations.

The research team at TUI have been fabricating arrays for 15 years for the purpose of increasing the measurement density of existing AFM technology. Successive arrays have been fabricated by the research team with ever decreasing spacing between the individual beams, increasing the number of points that can be measured simultaneously over a given surface area. Reducing the separation distance between cantilevers has introduced increased coupling, to the detriment of measurement reliability. Good quality topographic images have been achieved in parallel, but some images have been blurred and distorted, examples of which can be seen in Figure 3.1. The images shown were taken by two neighbouring beams in a four beam array. The white areas indicate points where images were not successfully formed from the cantilever response signal. It is believed that this error is predominantly due to mechanical coupling within the array. Currently, the onset of distortion and imaging artefacts is not predictable, which is problematic for the technology. The lack of imaging reliability is due to the fact that the dynamic response of the system has not been linked to the system parameters, and hence the conditions under which stable and unstable AM-AFM operation occurs is unknown.

The content of this chapter will be split into the following sections. In Section 3.2, the experimental equipment used to obtain data on the micro

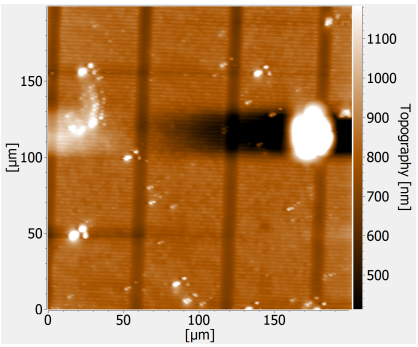


(a) Image of a silicon test grating formed with beam one of a four beam micro array.

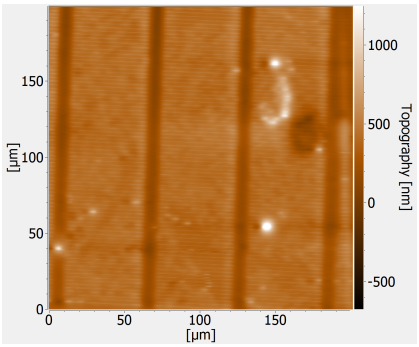


(b) Image of a silicon test grating formed with beam two of a four beam micro array.

Figure 3.1: Images formed in parallel using neighbouring beams in a TUI array. The white patches indicate areas that were not successfully imaged.

scale is described. In Section 3.3 the cantilever arrays utilised for experimental investigation are depicted and explained. In Section 3.4, the response of two different TUI array designs are investigated without the presence of tip sample forces, to determine how the individual beam frequency and separation distance parameters alter steady state response. In Section 3.5, the response of the most recently fabricated arrays are investigated under the influence of tip sample forces. The discrepancies that arise in the array response are discussed in relation to the response of a standard single beam.

## 3.2 Experimental Equipment

The experimental setup used to test the TUI arrays can be viewed in Figure 3.2. The experimental investigations were performed entirely at our collaborator's site using arrays fabricated in house. The test rig structure is predominantly fabricated from Aluminium. On the main structure, two piezo-stage actuators are mounted; a SmarAct stage, through which the height of the cantilevers and mounting can be adjusted; and a PX200 stage, through which the height of the test sample can be adjusted. The cantilever structure, and the electronics necessary to power the actuator, are mounted to the SmarAct stage through a custom designed 3D printed component, incorporated into which is a micrometer screw for adjusting the angle of the array relative to the sample surface. It is necessary to be able to adjust the angle ensure that all cantilever tips approach the surface simultaneously.

The equipment used to construct the experimental setup is listed below. Included is a description of the functionality of each item. The entire exper-

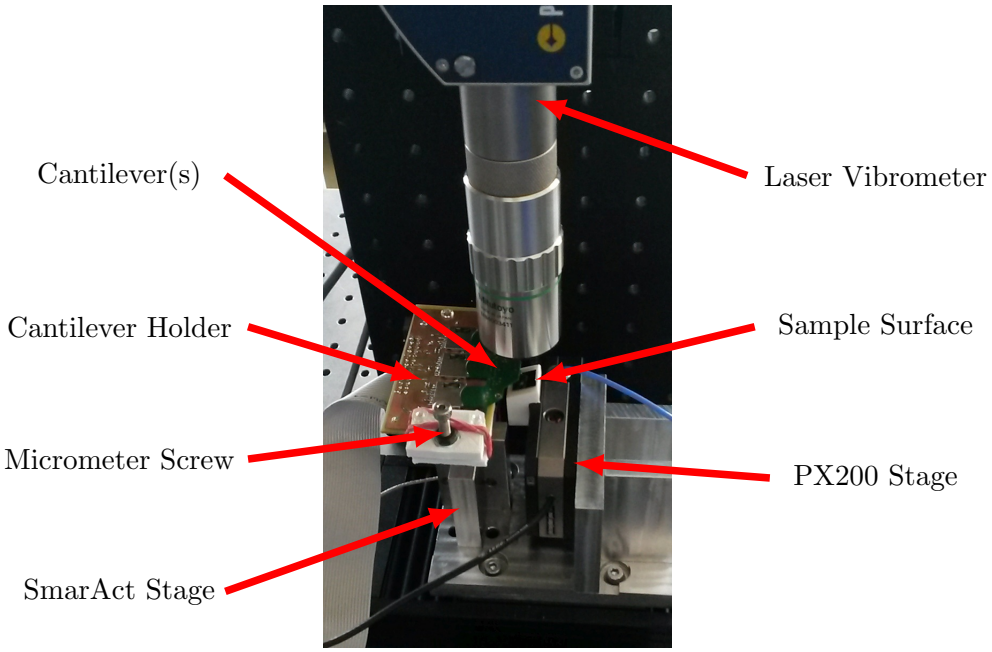


Figure 3.2: Micro scale test setup used for experimentation.

imental setup was operated from a desktop computer running Matlab® and Simulink®. The system inputs and outputs were controlled through either a digital oscilloscope or a dspace® control module depending on the specific experiment conducted as explained in the equipment list. BNC cables were used to connect all system components to the oscilloscope/dspace® modules.

- **Polytec OFV-534 Laser Vibrometer:** The laser vibrometer was used to measure the velocity of the cantilever tip. A Polytec OFV-5000 controller was used for signal processing. The amplification could be set from $1\,\mathrm{m\,s^{-1}\,V^{-1}}$ to $5\,\mathrm{mm\,s^{-1}\,V^{-1}}$. The laser vibrometer was used for all experiments instead of the piezo-resistive bridge sensors as it provided better measurement precision and reliability as discussed in Section 3.3.

- **Amplifying Circuit:** A custom built amplifying circuit was used to power the heater actuators and to prevent current overloads, which would result in destruction of the actuator.

- **TiePie HS5 Digital Oscilloscope:** The TiePie HS5 oscilloscope was used for signal generation and data acquisition, and was controlled with Matlab®. The oscilloscope is capable of signal generation and acquisition at a rate of up to 50 MHz, but with limited data

storage (approximately 1 second worth of data at 1 MHz acquisition). Continuous generation/acquisition is not possible.

- **dSpace:** A dSpace® system was used for signal generation and data acquisition when longer experimental runs and continuous control loops were required than was possible with the Tie Pie HS5. A DS2102 DAC module was used for signal generation and a DS2004 ADC module was used for data acquisition. The limitations of the hardware meant that the maximum generation and acquisition rate was 500kHz, limiting the maximum control bandwidth.

- **SmarAct SLC 2430 S Lindear Positioning Stage:** This piezo-position stage has a range of 16 mm of motion with sub-nanometer resolution. The stage was used for rough adjustment of the cantilever tip height above a sample.

- **Piezosystem Jena PX200 Positioning Stage:** Te PX200 is a high speed positioning stage with 200 µm range of motion, sub-nanometer accuracy and built-in feedback control. This stage was used for fine tuning the cantilever height above the sample surface, specifically for producing the approach curves that are discussed in Section 3.5.

## 3.3 Array Hardware

The outcome of the research efforts of the TUI team can be viewed in Figure 3.3, which depicts the latest two successive array designs with a noticeable decreasing gap size. Each individual cantilever is fabricated with a bi-morph heater actuator and a piezo-resistive sensor, providing individual excitation and displacement measurement for each probe. The actuator uses resistive heating to deflect the cantilever through thermal expansion, which is achieved by constructing the cantilevers with layers of different materials, each with a different thermal expansion coefficient. The thermal energy generated, and hence the amount of deflection, is directly proportional to the voltage applied across the actuator. It is important to note that the actuator can only provide a force in one direction, as a negative thermal energy transfer cannot be achieved. Actuation must be applied about an equilibrium position that is offset from the neutral position, such that the input voltage is always positive. If the input voltage crosses the zero axis, harmonic forcing terms are generated due to the inability to apply a force in the opposing direction. It is necessary to apply an input offset term equal to or greater than the input amplitude applied to the actuator.

The in-built sensor takes the form of a piezo-resistive Wheatstone bridge located at the base of each cantilever. Measurement of the base strain is used to infer the amplitude of oscillation at the tip, preventing the need to use a laser vibrometer or optical lever for each cantilever. Due to the low levels of strain that occur during operation, the bridge sensor requires significant signal amplification and filtering to obtain reliable readings. Development of the necessary electronic hardware to operate the bridge sensors reliably is an area of ongoing research for TUI group, and for this reason it was not utilised for displacement sensing within the scope of this thesis. The focus of the research in this thesis is on the fundamental dynamic response of the array structure, which can be sufficiently captured using a laser vibrometer.

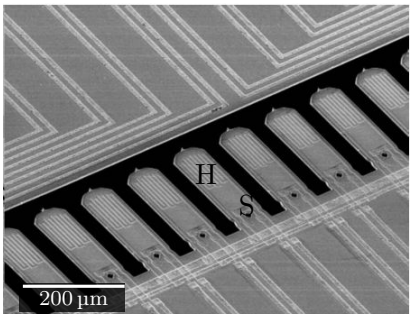


(a) An older TUI array showing spacing between cantilevers of roughly 50 µm. The spacing is still relatively small in comparison to most of the arrays discussed in the literature review.

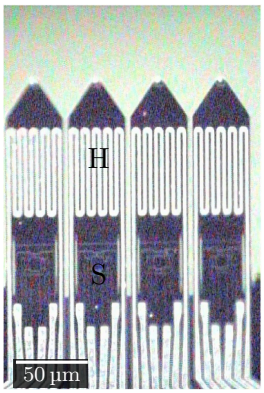


(b) An example of the most recent TUI arrays with small spacing between cantilevers. The gap is just 5 µm, compared to the cantilever width of 40 µm.

Figure 3.3: A comparison of TUI arrays showing the decreasing gap size between cantilevers. The array in (a) was fabricated in 2008 and the array in (b) was fabricated in 2016. The heater actuator is labelled H and the piezo-resistive sensor is labelled S.

## 3.4 Coupled Response - Far Field

Initially, the time and frequency response of the fabricated arrays is measured without external force interactions to isolate the mechanical coupling between beams, which can be well approximated with linear terms. The linear coupling is linked to the parameter space of the system, and specifically to beam spacing and relative beam frequency.

The effect of cantilever separation is first compared using the two array designs introduced in Figure 3.3. The arrays used are a 17 beam array with 50 µm spacing and a 4 beam array with 5 µm spacing. These array

sizes were readily available from the research team at TUI, hence their usage. The exact number of beams in the array is not critical for studying response qualitatively, as it is the mechanism by which coupling occurs, and the extent to which individual beams are coupled that needs to be identified. To quantify the coupling phenomena, a single beam in each array was actuated using the in-built heater actuator. A frequency sweep was used to obtain the response of the system. The sweep was performed within a suitably wide frequency range to ensure that the resonant frequency of all individual beams was captured, with only the first bending mode of each beam considered. Performing a sweep response for each beam separately was also used to estimate the uncoupled first resonant frequency of each individual cantilever. The input amplitude and linear offset to the actuator was kept constant for all beams to allow for direct comparison. The input amplitude in all cases was 0.5 V and the offset was 0.5 V. The frequency sweep results can be viewed in Figures 3.4 (17 beam array) and 3.5 (4 beam array).

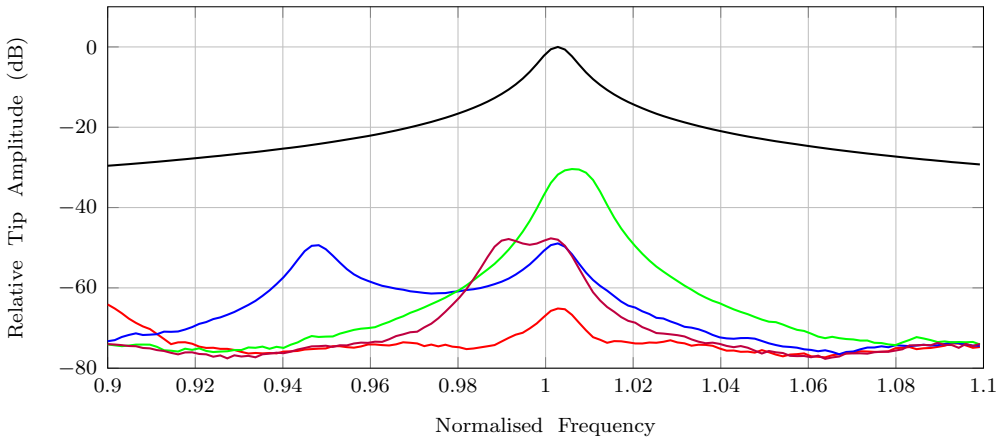


Figure 3.4: Experimental sweep response on the micro scale of a seventeen beam array of the type depicted in 3.3a (cantilever space of 50 µm) with beam 9 actuated only. The response of neighbouring beams due to coupling is apparent from the formation of multiple peaks. The noise floor is at approximately −80 dB. Red - Beam 7, Blue - Beam 8, Black - Beam 9, Green - Beam 10, Purple - Beam 11.

It can be clearly seen from comparison of the frequency sweeps that the reduction in gap size has a significant effect on the relative coupling observed in the frequency response, with an order of magnitude increase in response observed in all neighbouring beams when the gap size was reduced from 50 µm to 5 µm. This is a good demonstration as to why a significant number of the arrays discussed in the literature review had wide spacing, and why close proximity, high throughput arrays are yet to be made viable

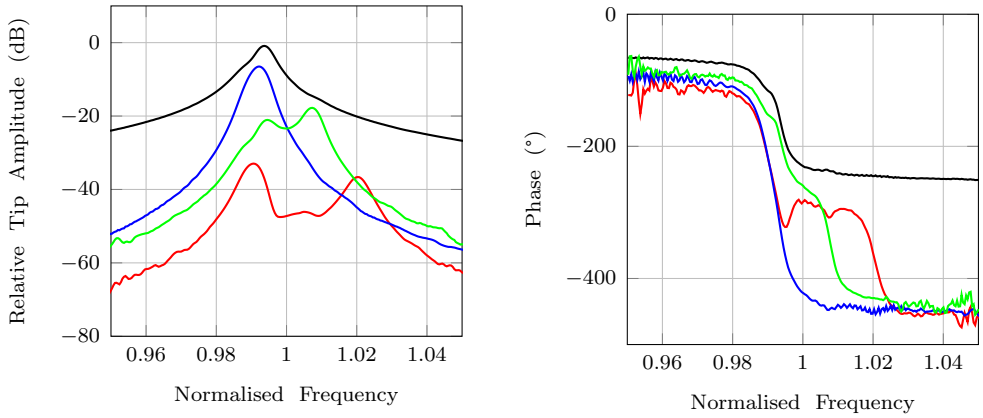


(a) Amplitude Response.

(b) Phase Response.

Figure 3.5: Experimental sweep response on the micro scale of a four beam array of the type depicted in 3.3b (cantilever space of 5 µm) with beam 3 actuated only. Coupling of significantly greater magnitude compared to Figure 3.4 is observed due to the reduced distance between cantilevers. The noise floor is at approximately −80 dB. Red - Beam 1, Blue - Beam 2, Black - Beam 3, Green - Beam 4.

for commercial AFM use.

Both results also clearly demonstrate the influence of individual beam resonant frequency on the observed coupled response. Beams with a first resonant frequency close to that of the actuated beam show significantly higher output amplitudes than beams with relatively higher or lower first resonant frequencies. The observation is consistent with linear vibration theory, as the energy output will be greater when the actuation frequency is close to a resonant frequency of any particular beam.

The observed coupling in the sweep response of the closely spaced array (Figure 3.5) demonstrates relatively weak coupling. That is, the response shows a single, dominant resonant peak for the actuated beam. The formation of phase-governed array modes is not apparent, with the phase transition of beam 3 predominantly following the path expected for single beam response. A detailed discussion on the regions of coupling will be presented in Chapters 4 and 5, but it can be stated here that the closely spaced micro array demonstrates a response in the weak to transition coupling region.

To demonstrate the relative influence of beam separation and resonant frequency gap, a comparison was made between four different arrays of the type in Figure 3.3b. Each array was fabricated in a different batch and all had been used previously for experimental investigations by the research team at TUI. The combination of fabrication tolerances and wear through

Table 3.1: Individual cantilever estimated first resonant frequencies for 4 different four beam arrays.

| | **Beam Frequencies (kHz)** | | | |
|---|---|---|---|---|
| | **Array 1** | **Array 2** | **Array 3** | **Array 4** |
| **Beam 1** | 121.22 | 116.04 | 37.75 | 116.02 |
| **Beam 2** | 120.05 | 116.02 | 36.62 | 114.12 |
| **Beam 3** | 118.70 | 115.84 | 36.76 | 112.54 |
| **Beam 4** | 119.19 | 115.78 | 37.28 | 114.13 |

use had resulted in each array having different frequency characteristics, which could be directly compared. The estimated resonant frequencies of the individual cantilevers in the four beam arrays are provided in Table 3.1. The individual beam frequencies were assumed to be the frequencies at which peak amplitude was observed when each cantilever was actuated individually. The assumption is reasonable to make as the micro arrays are dominated by weak coupling, where phase governed, synchronised modes are not present in the response as can be seen in Figure 3.5b. Sweep responses were performed using the same experimental procedure as stated above in this section. Each beam in each of the four available arrays was actuated in turn. The amplitude magnitude of all four beams was measured at the point of peak amplitude of the actuated beam. The raw experimental data can be viewed in Figure 3.6. The Pearson correlation coefficient was used to determine the relative impact of frequency gap and separation distance between the actuated and measured beams. The Pearson correlation coefficient $R$ is defined by (3.1). The dependent variable A was separation distance between beams and frequency gap, and the independent variable B was amplitude magnitude.

$$R(A,B) = \frac{\mathrm{Cov}(A,B)}{\sigma_A \sigma_B} \tag{3.1}$$

Where $A$ and $B$ are the data sets of the dependent and independent variable, $\mathrm{Cov}(A,B)$ is the covariance of the data sets, $\sigma_A$ is the mean value of data set $A$ and $\sigma_B$ is the mean value of data set $B$. The correlation coefficients are given in Table 3.2.

The correlation coefficients demonstrate that the observed coupled response is influenced by the two control parameters in almost equal magnitudes, which suggests that it is equally important to consider the resonant frequencies of individual beams as well as the physical spacing between

Table 3.2: Correlation coefficients for beam separation and resonant frequency gap.

| Coefficient | Value |
|---|---|
| $R_{beam\ separation}$ | -0.5568 |
| $R_{resonant\ frequency\ gap}$ | -0.5673 |

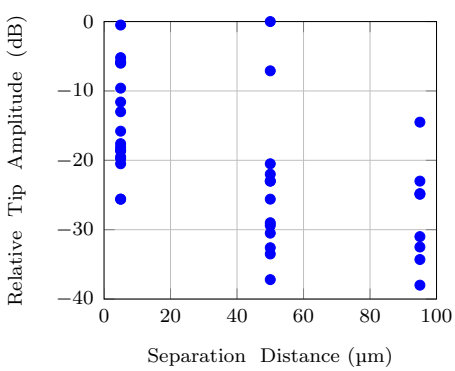


(a) Relative amplitude response due to coupling as a function of the physical gap between cantilevers.

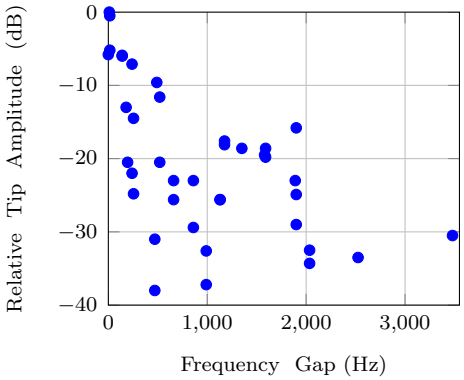


(b) Relative amplitude response due to coupling as a function of the frequency gap between cantilevers.

Figure 3.6: Experimental data on the micro scale comparing the influence of cantilever separation and frequency gap on the transfer of energy between beams. The relative amplitude is the measured amplitude difference in dB between the actuated beam and its neighbouring beams at the resonant frequency of the actuated beam.

them. This phenomenon is not well accounted for in the literature, and as discussed in the literature review, the majority of modelling research considers all cantilevers in an array to be identical. The results presented here demonstrate that the identical beam assumption is not valid in the scope of this research. Further discussion of the relative influence of frequency gap and separation distance will be presented in Section 6.6.

In addition to the discussed sweep response, the time responses of selected beams in both the 17 and 4 beam arrays are depicted in Figures 3.7 and 3.8. In all cases, two neighbouring beams in the array were actuated at their own resonant frequencies at an equal amplitude of 0.5 V to the heater. The response of one of the actuated beams was then measured using a laser vibrometer. The combination of the two input signals results in a clear beating response due to interference between the forcing term from the heater actuator and the forcing term from the neighbouring beam through the mechanical base coupling. As expected, a decrease in cantilever

separation and frequency gap generates a larger amplitude variation during one cycle of the combined beating frequency (comparison of Figures 3.7a and 3.8b). The effect of multiple frequencies in the time response can be easily filtered out during operation using a lock-in amplifier in the context of control. For this reason the presence of a strong beating phenomenon is not a consideration with regards to feedback control and data processing. The phenomenon, however, will alter the physical interaction between the tip and sample, which cannot be filtered out in software. In particular, an irregular amplitude can result in large variations in the peak force applied to the sample by the tip, leading to a loss of measurement precision and potentially damaging the sample. The issue was identified by Solares et al. [93]. A conclusion of this paper was that in the case of multiple external excitation frequencies, the frequency gap between multiple actuation terms should be kept large to smooth out the peak force applied by the beam tip. This same principle applies to closely spaced AFM arrays.

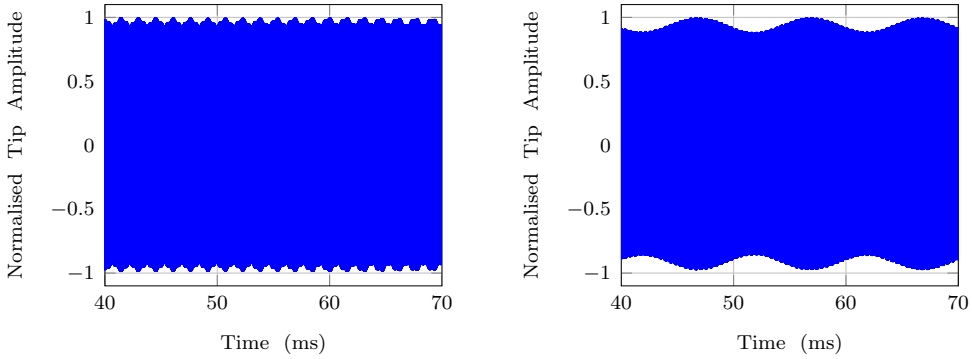


(a) Time response of beam 10 in a 17 beam array with beams 9 and 10 actuated at resonance. The difference in resonance frequency is 650Hz.

(b) Time response of beam 15 in a 17 beam array with beams 15 and 16 actuated at resonance. The difference in resonance frequency is 100Hz.

Figure 3.7: Experimental time response signals of individually actuated beams within a 17 beam array on the micro scale. The effect of the frequency gap between cantilevers creates a noticeable beating phenomena. The larger beating amplitude and lower beating frequency for the case of a larger frequency gap is consistent with standard vibration theory [94].

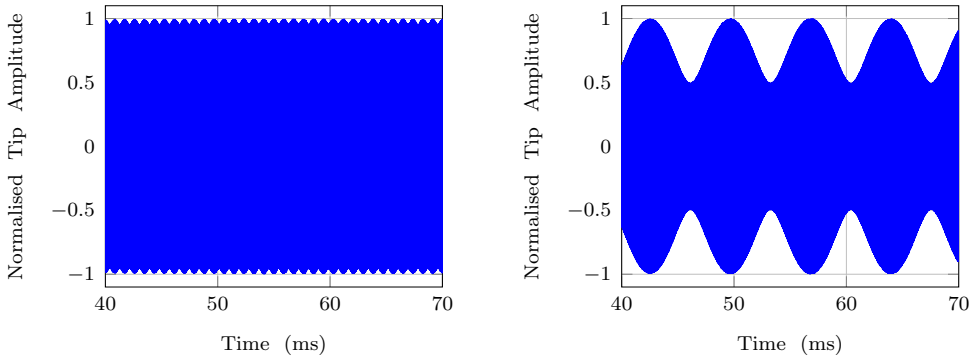


(a) Time response of beam 1 in a 4 beam array with beams 1 and 2 actuated at resonance. The difference in resonance frequency is 1130Hz.

(b) Time response of beam 2 in a 4 beam array with beams 2 and 3 actuated at resonance. The difference in resonance frequency is 140Hz.

Figure 3.8: Experimental time response signals of individually actuated beams within a 4 beam array on the micro scale. The effect of the frequency gap between cantilevers creates a noticeable beating phenomena. The larger beating amplitude and lower beating frequency for the case of a larger frequency gap is consistent with standard vibration theory [94]. It can also be seen in comparison to Figure 3.7 that the beating amplitude is increased significantly when the cantilevers are located closer together on a shared base.

## 3.5 Coupled Response - Near Surface

Once the characteristics of the fabricated arrays are studied at far field, the influence of tip-sample force interactions on the system response must also be analysed to effectively understand array response in the context of AFM. The method of measurement that is used to identify the influence of force interactions will be termed the approach curve for the remainder of this thesis. Approach curves represent the functional relationship between cantilever response (amplitude, frequency and/or phase) and the tip-sample separation distance ($d_0$) when the amplitude of actuation is held constant. In this section, a constant input frequency and amplitude is used, allowing the approach curve data to be directly related to AM-AFM, which is the designed application of the TUI arrays. This technique also isolates the influence of interaction forces during dynamic operation from the controllable inputs, allowing for direct analysis of system parameter space.

The following methodology is applied to collect the data necessary to form the approach curves. The raw time response of the cantilevers is measured whilst the cantilever tips are lowered towards the test sample. The rate at which the cantilevers are brought towards the surface is several

orders of magnitude slower than the response time of the beams. This is done to ensure that the beams remain close to steady state (quasi-static) at all times so that accurate measurements can be made. The cantilever height above the sample is varied from far-field (negligible force interactions) to the point of jump-to-contact, which is defined as the point where the tip remains permanently in contact with the sample and oscillations became negligible. This range of motion captures the cantilever response during all possible operation states (including all possible measurement set heights and short term tip-sample separation changes due to sample topography), ensuring the necessary dynamic information is obtained. The measured data is post-processed to extract amplitude and phase data.

Initially, the approach curve of a single cantilever was measured as a reference signal against which the array approach curves can be compared. An input amplitude and offset of 0.7V was applied to the heater actuator at a frequency of 99.79kHz (the far-field resonant frequency of the cantilever used). The amplitude approach curve for the single beam can be viewed in Figure 3.9.

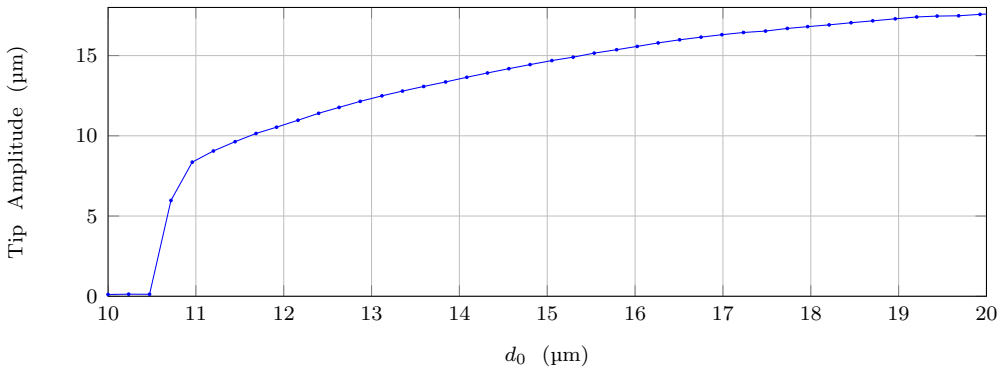


Figure 3.9: Experimental amplitude approach curve of a micro single beam. The beam is actuated with a constant amplitude at its resonant frequency.

The single beam approach curve depicts a smooth, continuous decrease in amplitude as the cantilever tip interacts with the surface. The qualitative shape of this curve is consistent with the expected shape of a commercial AM-AFM cantilever [44], where the continuous, monotonic decrease in amplitude is used as a control signal for holding the cantilever tip at a constant height above the surface. The approach curve is a validation of the TUI single beam design for use in AFM applications.

The approach curves of a TUI array are studied following validation of the single beam. For this section, array number 3 from Table 3.1 is used (a 4 beam array). The same experimental procedure is applied as for the single beam with minor modifications. Initially, the array was held above the test

sample and levelled, using a micrometer screw to adjust the angle of the array relative to the surface. To do this, all beams were actuated with a small, equal amplitude of 0.05 V and the height at which each beam in the array jumped to contact and oscillations became negligible was measured. The angle of the array was adjusted until the jump-to-contact phenomena occurred at all four beams within a height displacement range of 10 µm. A greater accuracy could not be achieved due to the precision limit of the equipment used. To obtain the approach curves, each beam was actuated in turn at its own resonant frequency and an amplitude of 0.7 V, and the array was brought towards the surface to a point where at all four beams were in contact with the surface. The response was recorded for the actuated beam only using the laser vibrometer. This process was repeated for all beams in the array. In addition to the amplitude approach curves depicted in Figure 3.10, the phase shift between the input signal and beam response is depicted in Figure 3.11.

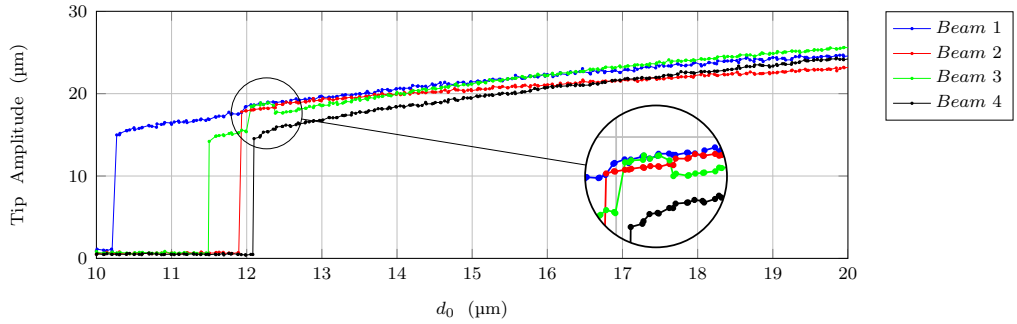


Figure 3.10: Experimental amplitude approach curve of a four beam micro array. Each beam is actuated individually with a constant amplitude at its resonant frequency. The approach curves for each beam are measured during separate experimental runs. The resonant frequencies are 37.75kHz for beam 1, 36.62kHz for beam 2, 36.76kHz for beam 3 and 37.28kHz for beam 4.

It is clear from the comparison between Figures 3.9 and 3.10 that there are significant differences between the smooth, single beam approach curve and the array approach curves. Sudden Changes in amplitude, both increasing and decreasing, are observed in the response of the array cantilevers. Of particular note is the approach curve of beam three, where an upward jump in amplitude is observed to occur at a height of approximately 2.4 µm, which is followed by a downward jump at a height of approximately 2 µm. This phenomenon is not observed in the single beam approach curve, and as will be discussed in Chapter 6, can be shown to result from the combination of nonlinear force terms and mechanical coupling between cantilevers. The array approach curves demonstrate two main issues that may prohibit the

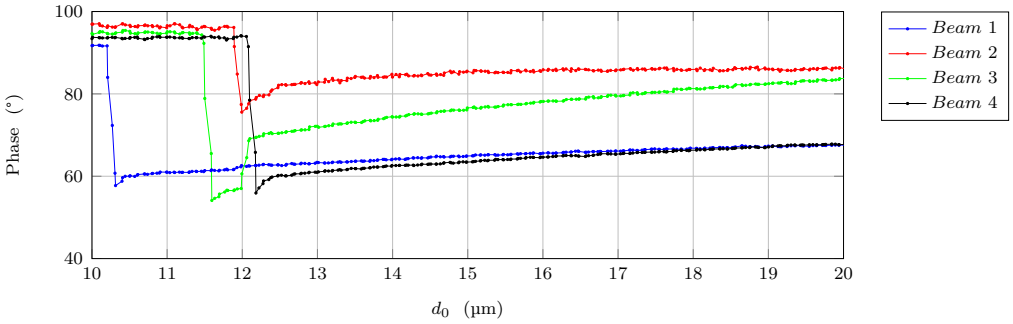


Figure 3.11: Experimental phase approach curve of a four beam micro array. Each beam is actuated individually with a constant amplitude at its resonant frequency. The approach curves for each beam are measured during separate experimental runs. The resonant frequencies are 37.75kHz for beam 1, 36.62kHz for beam 2, 36.76kHz for beam 3 and 37.28kHz for beam 4.

acquisition of reliable data in parallel. The first issue is that the lack of a monotonic trend, which would appear as artefacts in the final topography image. If the set point amplitude can be met with multiple separation distances, rather than a unique point, the control software may switch between equilibrium points depending on the direction from which the discontinuity is approached during the scan process. Because it would not be possible to distinguish between multiple equilibrium points using standard AM-AFM techniques, it would not be possible to distinguish between true surface features and imaging artefacts. The second issue is the possible lack of stability that could result from a significant change in the approach curve gradient as well as the presence of discontinuous jumps. If significant changes in the system dynamics are not accounted for in control, it is possible that a loss of stability can occur, which would result in jump-to-contact occurring at one or multiple beams in the array. Once this has occurred, useful data acquisition is lost until stability can be restored, eliminating the speed benefits of parallel imaging.

The results in Figures 3.10 and 3.11 were obtained by actuating beams individually. During true AFM operation, all beams would be actuated together. Included is the same experimental data obtained by actuating all beams during each run, not just the measured beam (Figure 3.12 and 3.13). The purpose of these figures is to demonstrate that the same jump phenomena occurs in the case of all beams actuated together, which is how the array would be operated for parallel imaging. As will be seen in Chapter 6, macro experimental and mathematical simulation investigations will be conducted with the assumption of one beam actuated at a time. Single beam actuation reduces the complexity of the response single and makes

it easier to link response phenomena to parameter space. The qualitative similarities of Figures 3.10 and 3.12 and Figures 3.11 and 3.13 demonstrate that this approach is valid.

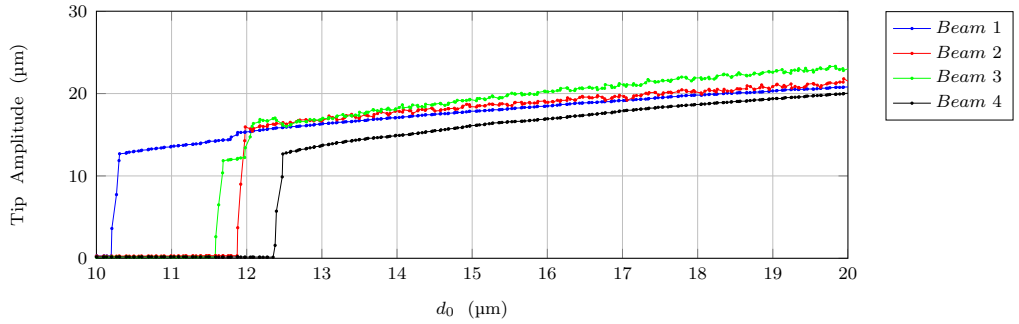


Figure 3.12: Experimental amplitude approach curve of a four beam micro array. All beams are actuated together with a constant, equal amplitude at their individual resonant frequencies. The approach curves for each beam are measured during separate experimental runs. The resonant frequencies are 37.75kHz for beam 1, 36.62kHz for beam 2, 36.76kHz for beam 3 and 37.28kHz for beam 4.

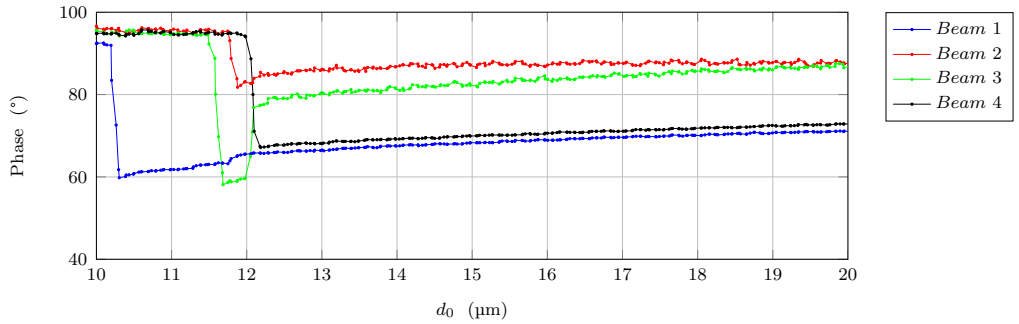


Figure 3.13: Experimental phase approach curve of a four beam micro array. All beams are actuated together with a constant, equal amplitude at their individual resonant frequencies. The approach curves for each beam are measured during separate experimental runs. The resonant frequencies are 37.75kHz for beam 1, 36.62kHz for beam 2, 36.76kHz for beam 3 and 37.28kHz for beam 4.

## 3.6 Conclusion

In this chapter, the dynamic response of micro cantilever arrays designed for high throughput AFM have been experimentally investigated. The experimental investigations were performed at our collaborations site using

the two most recent array design iterations. Frequency sweeps were performed on both array designs, which demonstrated that reducing the gap width between cantilevers increased the observed coupled response. Experimental data collected from four different arrays of equivalent design was used to correlate the influence of cantilever separation and relative resonant frequency gap to observed coupling strength, which demonstrated that both factors influence the transfer of energy between beams by an equal amount. Using the most recent array design, the influence of tip-sample interaction forces on array response was measured. The approach curves, which depict the relationship between observed amplitude/phase and the tip-sample separation distance, for a single beam and an array were compared. The outcome of this section was that coupling effects resulted in discontinuous jumps in the array approach curves. I has been established in the literature that nonlinear discontinuities in an AFM approach curve can be stabilised, and used to produce images with good reliability [95]. However, before this or another solution can be achieved, the nature of the nonlinear phenomena and the underlying causes must be fully understood. The findings in this chapter set a framework for the research, and will tie into the content of the later Chapters in this thesis.

CHAPTER 4

# Macro Scale Test Rig

## 4.1 Purpose

In this chapter, the design, fabrication and validation of the macro scale experimental test rig will be discussed, which included a total of two design iterations. The content presented here will provide a framework for the experimental investigations that form the later chapters of the thesis and will tie into their content.

The work conducted in this thesis focuses on the underlying principles that govern the response of arrays in the context of AFM, how these principles relate to the output signals of fabricated arrays used for imaging, and how any adverse response phenomena may be eliminated or mitigated. With this in mind, it is desirable to test array response over a large, relevant range of parameter space to validate findings obtained through mathematical simulation, including the relative influence of nonlinear tip forces and coupling strength on observed response, and in what parameters space nonlinear or unstable response is observed. An equivalent macro scale test rig is far more capable of accommodating this requirement as opposed to the micro system. Fabricating arrays with varying dimensions, mass properties and coupling strength can be done quickly and cheaply using standard macro-machining techniques, as well as 3D printing technology. The other consideration is the ability to visually observe dynamic response on the macro scale, which is difficult to achieve on the micro scale due to the small size and high operating bandwidth. Visual observation of the state of operation is desirable (when possible) if the fundamental principles governing system response are not fully understood, as is the case with the TUI arrays. When operating on the macro scale, it is possible to observe directly what state the system is in, specifically if it is in non-contact, intermittent contact or in continuous contact with the surface, which must be inferred indirectly on the micro scale. It should be noted that the purpose of the test rig is to help understand the underlying physics that are present on both

the macro and micro scales qualitatively, and not to provide precise quantitative agreement. Properties that are unique to scale, such as the exact force profile of electrostatic forces on the micro scale, are not matched.

It is necessary to justify the ability of such a system to provide results that are meaningful in the context of the micro array system. In scaling up from micro to macro, the physical laws governing cantilever motion do not change qualitatively. While it is not intended to quantitatively match the measured outputs on both scales, it is sufficient to gain a qualitative understanding of how system parameters affect system response. The most pressing issue is to accurately simulate the tip-sample interaction forces on the macro scale qualitatively, as this is a crucial aspect of AFM, and will be discussed in Section 4.2. As was discussed in the literature review, several other research groups have independently performed macro scale experimental investigations and have been able to draw conclusions about micro scale phenomena successfully [87–90]. This provides further justification.

## 4.2 Required Test Rig Functionality

It is necessary to determine an appropriate scaling factor from the micro to the macro system. Abramovitch shows that typical dimensions for commercially available rectangular AFM cantilevers are 90-460 µm in length, 25-60 µm in width and 0.7-7.5 µm in thickness [5], though cantilevers as small as 6 µm in length have been fabricated [8]. The range at which atomic interaction forces between tip and sample are significant is on the order of 1 nm from the sample surface [11] and cantilever oscillation amplitudes tend to range from a few nm up to a few µm. Using a scaling factor of 1000× (µm to mm) would result in cantilevers on the order of 90-460 mm in length, which is acceptable for the macro scale as visual observation at this size would be possible without requiring an excessively large test rig. However, with this scaling factor cantilever amplitudes would be on the order of 1-1000 µm and the interaction force range would be on the order of 1 µm. This scale would require very high precision measurement to acquire usable data. It is therefore proposed that while cantilever dimensions be scaled on the order of 1000×, cantilever amplitudes and interaction force range be scaled to a range of 1-5 mm, which ensures that good quality data can be obtained in the presence of measurement noise and error. Provided that the underlying physics governing the observed system response on the macro scale remain equivalent to the micro scale system, this assumption should provide qualitatively comparable results, which is the desired outcome.

Creating a test rig that could successfully mimic the conditions of AFM operation proved to be challenging, consisting of several layers of functional

requirement based on the research scope proposed in Chapter 1. The main purpose is to simulate the operation of a generic AFM array, consisting of multiple, actively actuated cantilevers interacting with a surface through a nonlinear force gradient at the tip. The system also has to simulate specific features of the TUI arrays, including actuators and sensors built into each cantilever capable of independent actuation and indirect measurement of tip displacement. As the main goal of the thesis is to study and to understand the system response for a wide range of relevant parameter space, it must be possible to modify all identified parameters of interest. The overall functionality can be broken down into the five key aspects listed below, and the relation between these aspects is visualised with the diagram in Figure 4.1.

- The system must be centred around an array of cantilevers clamped to a solid structure. This is the basis of the TUI arrays.
- The test rig must qualitatively simulate the interaction forces between sample and cantilever tip that occur on the micro scale, including the ability to change the distance between cantilever tip and sample. The tip-sample separation distance must be fully controllable.
- Each cantilever must have its own actuator and sensor that can be used independently. This is equivalent to the mechanical design of the TUI arrays.
- The system must have sufficient flexibility to alter key parameters, which are individual beam stiffness and mass properties, coupling strength and tip-sample separation so that a wide range of parameter space can be tested.
- It must be possible to attach a concentrated mass to each cantilever tip. The mass simulates the presence of an AFM tip, and provides a simple method of varying the frequency properties of the cantilever.

For the test rig to have relevance to AFM research, it is necessary to implement a suitable method of simulating the tip-sample interaction forces that occur on the micro scale. Two independent types of interaction occur on the micro scale, long range attractive and short range repulsive electrostatic forces, and repulsion due to contact stiffness when the tip impacts into the sample. As will be discussed in Section 5.2, contact mechanics are not incorporated into the mathematical model, and hence are not replicated on the macro scale. The focus will instead be on simulating the contactless electrostatic forces. Magnets offer a simple way of creating an

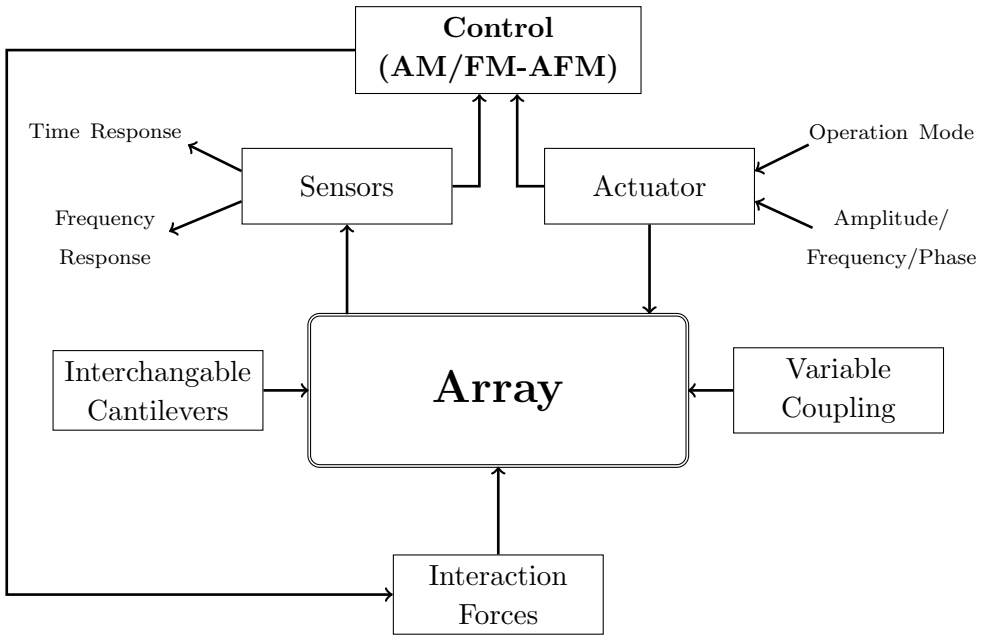


Figure 4.1: Diagram depicting the key functionality requirements and their integration.

attractive nonlinear force that is mathematically equivalent to the attractive tip forces of AFM, as both phenomena derive from the same fundamental electromagnet force. As was discussed in the literature, Balachandran et al. also employed magnets to simulate AFM tip interaction forces with success [87]. It is reasonable to use the same proven method. The electrostatic repulsion force that occurs on the micro scale due to Pauli exclusion cannot be easily replicated on the macro scale. The influence of electrostatic repulsion occurs over a very small range close to the sample surface and in the context of AFM does not have as significant an effect of cantilever response as electrostatic attraction or impact forces. It is reasonable to neglect this force on the macro scale. Despite not simulating contact forces, the macro scale test rig can still be used to draw qualitative conclusions regarding cantilever response. This is because both electrostatic and contact forces have the same basic effect on response, namely that the resonant frequency is lowered and a softening behaviour is observed.

While most features of the test rig were custom built, several key components were purchased off the shelf, most importantly the cantilever actuators and sensors. These components were used for both test rig designs and are described here.

- **Actuators**

Piezo-electric film actuators were selected as the best method for exciting the cantilevers. Piezo actuators are capable of providing a wide bandwidth of actuation with a high force capacity relative to size. In addition they are small and light weight, allowing them to be attached directly to the cantilevers without significantly altering system response. The specific actuators used are the qp10n series produced by MIDE, which run on a ±200 V excitation signal. The qp10n actuators have a maximum output strain of 500 μϵ over an active element length of 46 mm and can produce a maximum force of 125 N. The level of actuation was controlled by applying a sinusoidal voltage with amplitude between 0 V and 200 V.

- **Sensors**

  Stain gauges were used to measure cantilever response, with four strain gauges mounted at each cantilever base in a full Wheatstone bridge configuration. Measurement of the strain at the cantilever base is used as a measurement of the time response of the tip displacement equivalent to the TUI arrays. The gauges used had Aluminium active elements, with a gauge length of 3 mm and nominal gauge resistance of 119.8 Ω

## 4.3 Test Rig Design

Two design iterations were conducted to produce the final test rig, which is used for the majority of experimental investigations in this thesis, except for the proof of concept experiments, which were conducted with the first design (Section 4.4.1). Both design iterations were centred around an arch structure machined from Aluminium, which formed a rigid clamp to which the cantilevers could be secured. The arch was designed to be of greater stiffness than the cantilevers to ensure its first resonant frequency was significantly greater than the measurement frequencies of interest. A large slot was machined into the upper block of the arch structure, forming the clamp into which cantilevers were inserted. In all cases, cantilevers were laser cut from 1.5 mm thick Aluminium sheet. On each cantilever, the sensors and actuators were mounted using a high strength epoxy resin to bond both the sensors and actuators to the forward facing cantilever surfaces.

### 4.3.1 First Iteration

A solid model depiction of the first design iteration is given in Figure 4.2. The cantilevers were fabricated as a whole array unit, with up to five can-

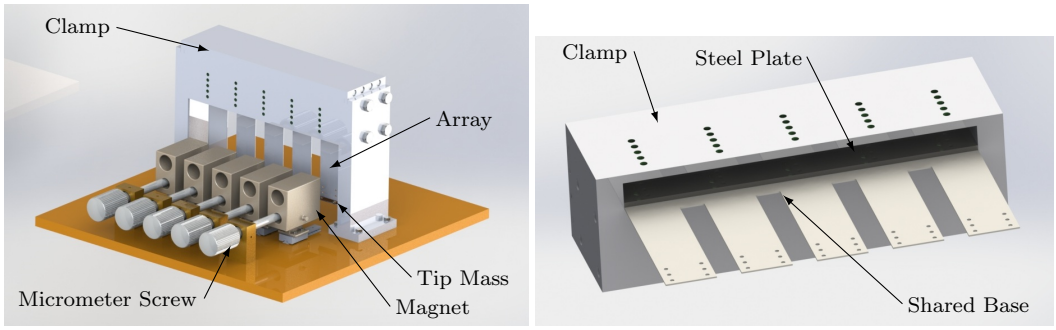


(a) Oblique view of the entire test rig.

(b) An array structure within the clamping block. A steel plate is located between the array and the grub screws to improve the quality of the clamp.

Figure 4.2: Graphical rendering of the first test rig.

tilevers in each array. The individual beams are 105 mm in length and 29 mm in width, and are connected through a shared base structure. As the array was fabricated as a single unit, the gap distance between beams was fixed during fabrication and was set to a value of 10 mm. To clamp the array in place, the shared base was slotted into the clamping structure. A steel plate was also placed within the clamping slot above the array and fastened in place using M5 grub screws threaded into holes machined into the front face of the clamp. The level of coupling could then be adjusted by altering the length of shared base material that protruded from the lower face of the clamping structure. A strip of 4 mm $\times$ 4 mm key steel was fastened to the tip of each cantilever, acting as a tip mass. By varying the length of the steel, the masses, and hence the frequency properties of the individual beams could be varied. This was done in lieu of changing the cantilever lengths/widths, which were set during the laser cutting process.

National Instruments LabVIEW® modules were used to read sensor data and send input signals to the actuators. A standard PC was used to run the electronic system using the LabVIEW® System Design Software. The program was designed to supply sinusoidal signals to the actuators whilst simultaneously acquiring data from the strain gauge sensors. User controls were included in the program for the voltage amplitude and frequency of the actuator signals. The actuator signals were run through a custom built amplifier, which consisted of PA340U high voltage power amplifiers. These amplifiers have a power bandwidth of 35 kHz at a nominal peak-to-peak test voltage of 280 V. Experimental data was saved to the PC disk through user controlled commands.

Several observational conclusions were made regarding the functionality of the first design iteration and the observed weaknesses were incorporated into the second design iteration. The ability to vary the coupling level was

demonstrated to work well, however, varying the amount of base coupling material required increasing the distance between the clamped edge of the array and the cantilever tips. The change of intrinsic cantilever length had the undesirable effect of changing the fundamental resonant frequencies of the uncoupled cantilevers. The consequence was that experimental data acquired at different coupling levels can not be directly compared, which is undesirable when analysing the response of arrays under the influence of tip-sample forces at varying levels of coupling as is done in Chapters 6 and 7. To properly compare response phenomena with different levels of coupling, it is necessary to separate the coupling and cantilever frequency parameters as much as possible.

Several weaknesses were also noted during experimentation. The array was clamped in place using grub screws, which were tightened by hand. It was found that slight changes in the torque used to tighten the grub screws resulted in noticeable changes in the observed resonant frequencies of the cantilevers. It is necessary to ensure that the clamping condition remained consistent between experiments, as clamping was not a parameter of interest to the experimental investigation. The inability to ensure consistent clamping between experiments is detrimental. Finally, the wires connecting the piezo actuators and strain gauge sensors were noted to randomly alter the array response, specifically by altering the measured Q factor. The reason for the change in Q factor is that the wires hung loose from the actuator and sensor terminals and could become excited during operation, taking energy away from the system. It is necessary to remove the influence of wiring on the array dynamics as much as possible to ensure consistent response.

### 4.3.2 Final Iteration

The second design built upon the experiences gained from operating the first test rig to create a system better suited to studying array dynamics in varying parameter space. The design of the second test rig maintained the basic layout and functionality depicted in Figure 4.1, whilst incorporating full active control of tip-sample separation and improvements to address the identified weaknesses of the first test rig. As well as an improved mechanical design, a National Instruments CompactRio (cRio) micro controller platform was incorporated into the system. National Instruments Modules were used within the cRio platform to control the piezo actuators and tip-sample separation whilst simultaneously acquiring data from the strain gauge sensors. The cRio was programmed using LabVIEW®.

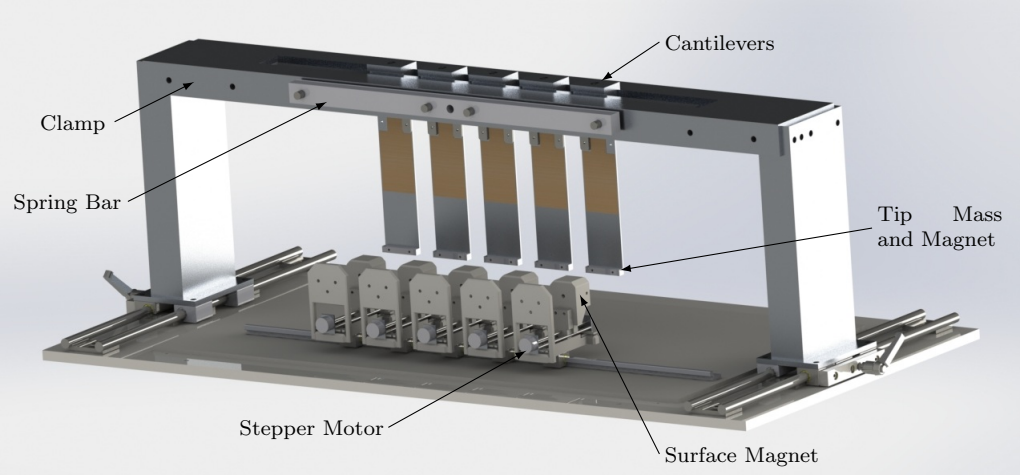


Figure 4.3: Graphical rendering of the second test rig.

### 4.3.3 Mechanical Design

A solid model rendering of the second test rig can be viewed in Figure 4.3 and an image of the completed system is shown in Figure 4.5. The main structure of the system is the clamping bridge, which is taken from the first design. T-shaped Aluminium blocks were attached to the base of the cantilevers, allowing them to be placed through the slot and located on upper surface of the bridge such that the position in the clamp remained consistent. Instead of grub screws, compression springs were used to press the cantilevers against the clamping structure to secure them in place. The cantilevers could be released by pulling back the springs using the spring bar depicted in the solid model. Locating the cantilevers on a machined surface and using the springs to provide the clamping force ensured that the clamping condition was repeatable between experiments, removing the error that was observed in the first test rig design.

As the new clamping mechanism required that the cantilevers be located in the same position each time, it was not possible to alter the coupling strength by varying the protrusion of shared base material from the clamp. Instead, cantilevers were laser cut individually and separate coupling elements were also laser cut from the same Aluminium sheet with varying lengths. The coupling pieces were secured to the cantilevers with M3 screws at the point of protrusion from the clamping structure to form a section of shared base, an example of which can be seen in Figure 4.4. Using separate coupling pieces allowed for the creation of adjustable mechanical coupling through a shared base equivalent to the micro scale system, but without significantly altering the individual cantilever frequency response.

Coupling could be adjusted by changing either the separation between cantilevers, or by adjusting the width of the coupling piece, altering the amount of shared base material. This mechanism allowed for reliable comparison between data from arrays with differing levels of coupling. The basic dimensions of the cantilevers are 160 mm in length and 40 mm in width. Tip masses in the form of small steel masses were again secured to the tips of the cantilevers.

To provide tip-sample separation adjustment, an actuator system was purchased that combined a stepper motor unit, rail guides and threaded bar to convert the stepper motor motion into a linear motion. The purchased stepper motor system was originally designed for use in home-built 3D printers. The stepper motor is a two phase, 4-6 V/300 mA unit with a holding torque of 5 N m and step angle of 1.8°. The threaded bar is 90 mm in length with a screw pitch of 0.5 mm. These dimensions result in linear motion step resolution of 2.5 µm, which is an order of magnitude below the tip-sample force range. This should be sufficient for the application. 2.5 µm is also well below the dimensional tolerances of the test rig structure, and as such smaller discrete steps would not add to the precision of the overall system.

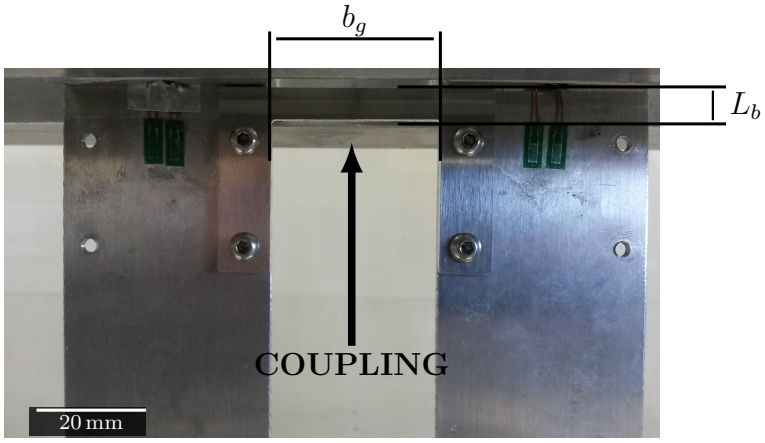


Figure 4.4: Depiction of a coupling element between two cantilevers, which simulates a section of shared base material. Sections with different widths ($L_b$) and separation distances ($b_g$) can be selected to alter the coupling strength.

During the first design iteration, an electromagnet was trialled to simulate attractive tip-sample interaction forces. Because the core of the electromagnet was 15 mm in length, the well established inverse square relationship governing magnetic attraction between two bodies did not hold well when the displacement was taken to be the distance between the surfaces of the electromagnet and the cantilever tip. To successfully model the magnetic

force profile of a magnet with a long core length, an offset parameter needs to be introduced, setting the point from which separation is measured effectively inside the magnet core. This was not desirable from an experimental perspective as a significant portion of the attractive force gradient curve was rendered unusable (as it was effectively within the magnet core). To overcome this issue, small Neodymium permanent magnets were utilised for the second test rig design. The magnets used were 2 mm in diameter and 1 mm thick. The short core length meant that the magnetic force profile could be modelled with good accuracy using an inverse square function with greater precision than an electromagnet. A magnet was placed on a mounting block on each stepper motor assembly as well as on the tip of each cantilever, with opposite poles facing towards each other.

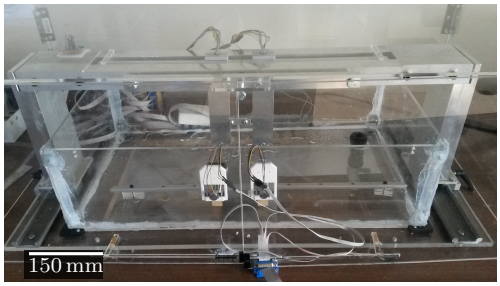


(a) Wide angle view of the second test rig showing clamping structure, cantilevers and stepper motors.

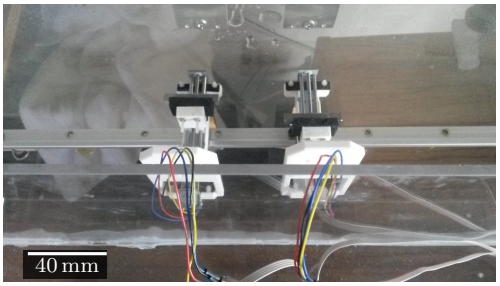


(b) Close up view depicting the stepper motors that control the distance between the simulated sample surface and cantilever tips.

Figure 4.5: Depiction of the second macro array test rig.

### 4.3.4 Electronics and Software

The second test rig system is operated using a National Instruments cRio micro controller running National Instruments LabVIEW® software. Four National instruments modules were used in the micro controller to run the electronic systems; an NI9263 analog output module; an NI9239 analog input module; an NI9237 analog input with Wheatstone bridge; and an NI9401 digital input/output module. The utilisation of the modules in relation to the electronic systems is described in the following list.

- **NI9263 analog output:** This module was used to run the piezo actuators independently, outputting up to four user defined voltage signals with up to 10 V amplitude each. The signals are passed through a bespoke amplifier that upped the voltage by a factor of 20. The amplified signals were then routed to the actuators.

- **NI9239 analog input:** This module was used to directly measure the true, post amplified signals sent to the piezo actuators. The signals were passed through voltage divider circuits to reduce the signals to within ±10 V to be read by the module.

- **NI9237 analog input with bridge:** This module was used to read the raw signals from the four strain gauges mounted to each cantilever. The module contains a built in, self calibrated Wheatstone bridge to convert the strain gauge voltage output into a usable signal.

- **NI9401 digital input/output:** This module was used to run the stepper motors to adjust tip-sample separation. Digital output pulses are sent to a stepper motor control circuit which operates the motor coils. Additional digital outputs controlled the direction of motion of the stepper motors.

The cRio controller contains a programmable FPGA chip that writes to/reads from the inserted modules directly. The FPGA chip is able to run at a maximum rate of 40 MHz. The high speed and precise timing of the FPGA chip makes it ideally suited for continuous data acquisition/signal output with controlled timing. A LabVIEW® program is written onto the FPGA chip to perform the fundamental reading and writing tasks necessary to operate the physical system. The program consists of multiple functions that run independently and simultaneously, including functions to operate each stepper motor, a function to read all measured signals from the strain gauge sensors and piezo actuators, and a function to output the user defined sinusoidal signals to each piezo actuator. All input signals were acquired within a single function to achieve true simultaneous acquisition for accurate signal processing. The input signal function was run at a speed of 10 kHz. Likewise, all actuator signals were outputted within a single function to achieve simultaneous actuation, which was also run at a rate of 10 kHz. The FPGA code can be viewed in Appendix C.

As well as the FPGA program, a high level control program is written to the cRio controller. The high level program is used to run the experimental procedures, allow the user to specify inputs to the system, and to record and save data. The high level program communicates with the FPGA program through first-in-first-out (FIFO) memory buffers as well as direct inputs. The FIFO buffers are used to account for the fact that the high level and FPGA programs are not synchronised. Two FIFO buffers are utilised, one to transfer strain gauge data from the FPGA to the high level program, and one to transfer actuator data. Direct inputs are used to transfer stepper motor inputs to the FPGA program as well as to control the amplitude, phase

and frequency of the actuator outputs. The high level program is written based on the specific experimental procedures to be carried out, and communication between the program and user is possible through connection to a standard PC. Experimental data is stored by the high level program on the internal memory of the cRio and can be transferred to an external memory device as commanded by the user. The control architecture is depicted in Figure 4.6 for visualisation of the communication between the user, software and physical test rig.

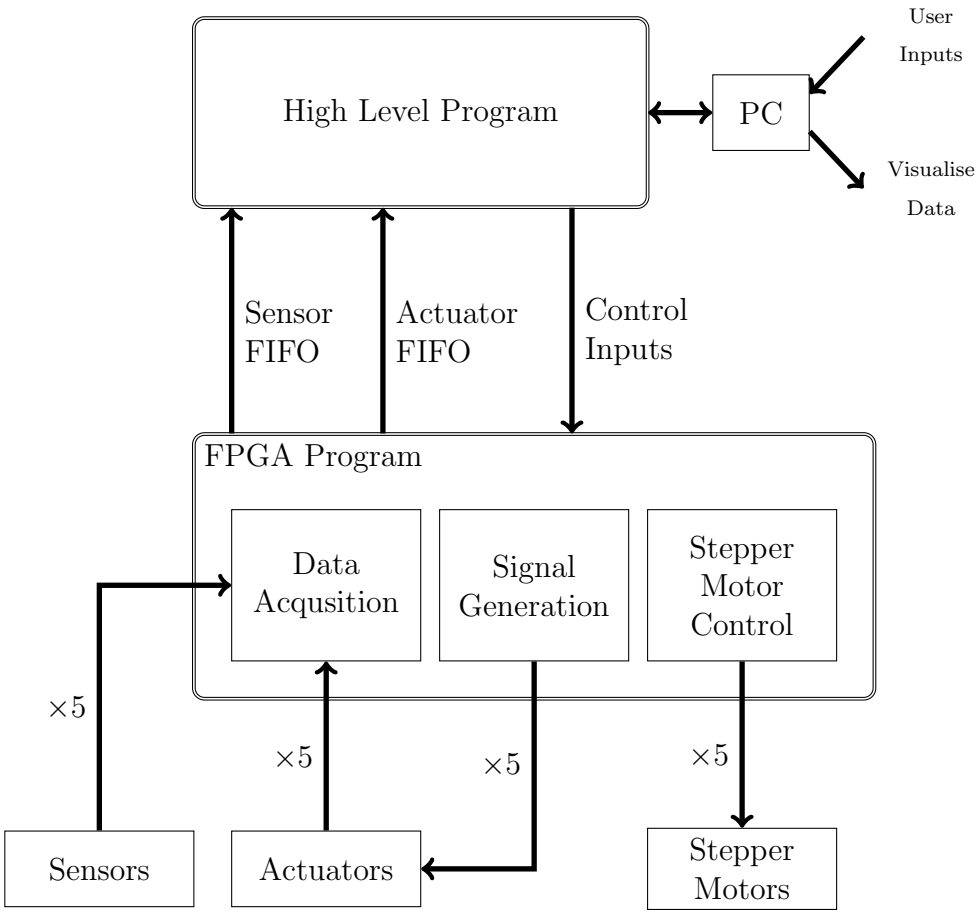


Figure 4.6: Depiction of the control architecture used to run the the second test rig.

## 4.4 Design Performance

In this section, the ability of the final design to meet the functionality requirements is presented. The first test rig design is used to validate the

fundamental functionality of the macro scale concept, specifically the ability to simulate micro scale AFM cantilever response, vary coupling strength and vary individual cantilever frequency response. The mechanical structure of the second test rig design is fundamentally unchanged from the first, Due to the functional similarity, it is sufficient to confirm fundamental functionality with the first design only. Parameter identification of the system and the ability to conduct feedback control are established using the final design.

### 4.4.1 Proof of Concept

The main functionality test of the first test rig was to confirm that the physical principles governing the micro array could be successfully simulated. Qualitative comparison of experimental data would verify the ability of a macro array system to simulate the dynamic phenomena of the micro AFM arrays. Initially, a single cantilever was tested on both scales, the dimensions for which can be found in Table 4.1. Two properties of the systems were compared, the Q factor (damping) and the intrinsic nonlinearity. As both systems are operated in an air environment and are governed by the same physical laws, both properties should be comparable. The experimental data is shown in Figure 4.7 in the form of a frequency response and transfer function curve.

It can be observed from the single beam responses that both systems behave in a highly linear fashion within the tested range, demonstrating negligible nonlinearity. The range of experimental data corresponds to a maximum tip deflection amplitude of 27 µm on the micro scale with an actuation amplitude of 1.2 V and of 5.8 mm on the macro scale with an actuation amplitude of 20 V. This observation is backed up by the transfer functions, which do not change within the measured range of actuation amplitudes. The calculated Q factors of the transfer functions is 220 on the micro scale and 110 on the macro scale, which are both within the same order of magnitude as expected for equivalent atmospheric conditions. The results demonstrate that the macro system is a good representation of the micro system for a single cantilever.

It is also necessary to confirm that the level of coupling within the array can be varied successfully to capture both individual cantilever and array modes. A full five beam array was utilised for this test. As discussed, the dimensions of each cantilever were the same, but different tip masses were used to vary the individual cantilever resonant frequencies. The relevant dimensions of the array can be found in Table 4.2. To identify the cantilever/array modes, an impulse response was performed on the array, with the impulse provided by striking the clamping structure. Coupling was varied across

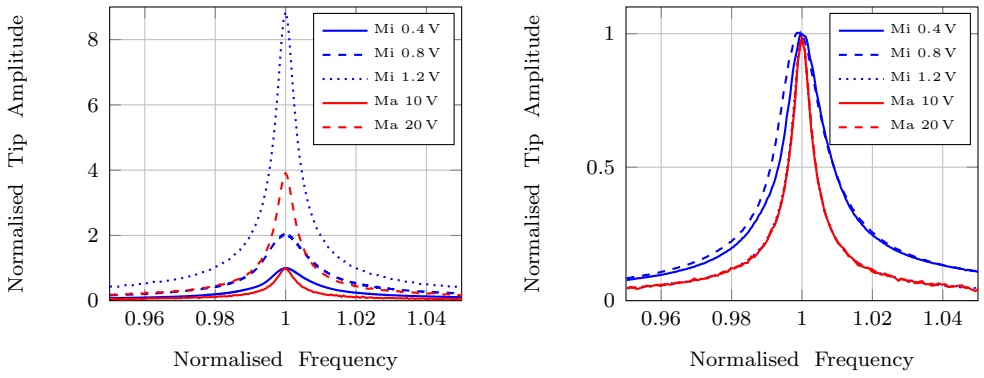


(a) Normalised response spectrum of the tip amplitude of a micro and macro single cantilever.

(b) Normalised transfer function of a micro and macro single cantilever.

Figure 4.7: Experimental frequency response comparison between the macro (Ma) and micro (Mi) scale. The voltages correspond to the amplitude of the input signal. The frequency is normalised by the resonant frequency at each scale. The amplitude is normalised by the amplitude at resonance with an input of Mi 0.4 V and Ma 10 V.

three regions of interest, which are as follows; weak coupling, where each cantilever has a single, dominating peak and the phase between beams is not a factor; strong coupling, where each beam exhibits multiple peaks of similar magnitude and the output response is highly dependant on the phase between cantilevers; and transition coupling, where each cantilever has a single, dominant peak but with smaller, secondary peaks beginning to form. These three regions of interest were found to occur with the following base structure protrusions from the clamp; 5 mm for weak coupling; 10 mm for transition coupling; and 15 mm for strong coupling. The experimental data can be viewed in Figures 4.8, 4.9 and 4.10.

It can be seen that the three coupling levels are clearly distinguishable across the range of shared base material tested. The ratios of the individual cantilever resonant frequencies relative to each other observed in Figure 4.8 were also as expected for the tip masses used. The results confirm the ability to capture the transformation of the array response from unsynchronised to synchronised response by using a shared base structure of varying length. The results also demonstrate the practicality of varying the tip masses as a method of simulating the small differences in cantilever frequency response observed with fabricated micro AFM arrays. The demonstrated coupling regions can be compared with the micro scale sweep response that was performed in Chapter 3 (Figure 3.5). Examination of the phase response suggests that the tested micro array resembles the phase transitions observed in Figures 4.8b and 4.9b. This backs up the statement made in Section 3.4

Table 4.1: Cantilever Parameters comparing a macro and micro single cantilever. The scaling factor from micro to macro is included for each parameter.

| | Macro | Micro | Scaling |
|---|---|---|---|
| Cantilever Length | 105 mm | 320 µm | 330 |
| Cantilever Width | 29 mm | 111 µm | 260 |
| Cantilever Thickness | 1.5 mm | 4.6 µm | 330 |
| Tip Mass | 3.5 g | N/A | N/A |
| First Resonance Frequency | 47.8 Hz | 99.79 kHz | 0.0005 |

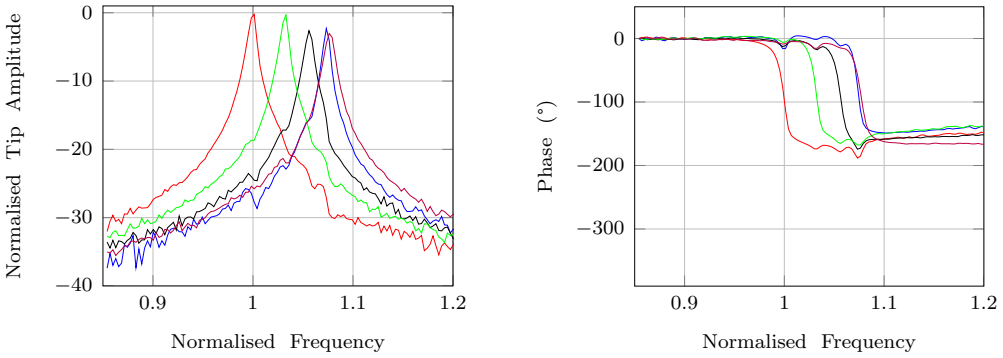


(a) Amplitude Response.

(b) Phase Response.

Figure 4.8: Experimental impulse responses of a macro five beam array with weak coupling (5 mm shared base material). Amplitude is normalised by the maximum measured amplitude and frequency is normalised by the frequency at which the first peak occurs. Red - Beam 1, Blue - Beam 2, Black - Beam 3, Green - Beam 4, Purple - Beam 5.

that the micro arrays exhibit coupling in the weak/transition region, with individual beam resonant frequencies dominating over phase-governed array modes.

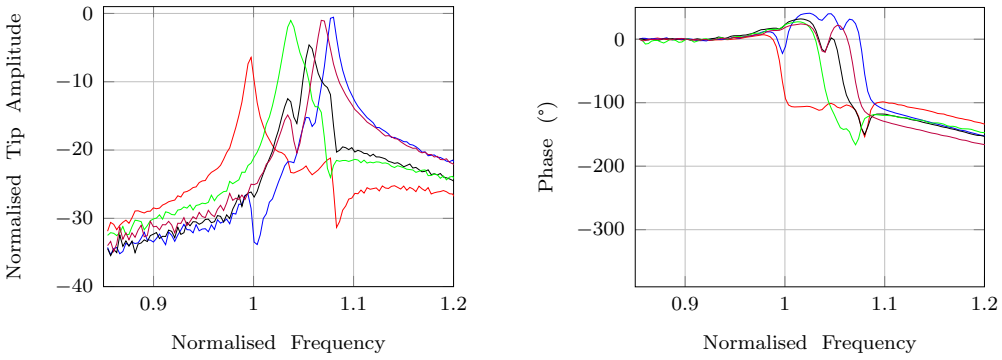


(a) Amplitude Response.

(b) Phase Response.

Figure 4.9: Experimental impulse responses of a macro five beam array with transition coupling (10 mm shared base material). Amplitude is normalised by the maximum measured amplitude and frequency is normalised by the frequency at which the first peak occurs. Red - Beam 1, Blue - Beam 2, Black - Beam 3, Green - Beam 4, Purple - Beam 5.

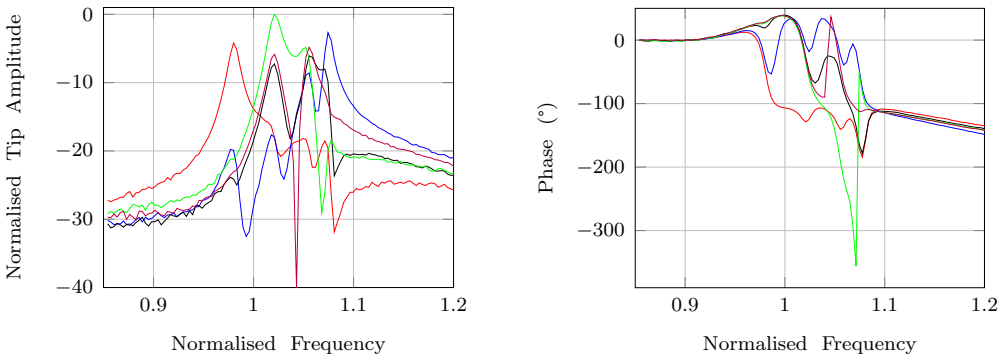


(a) Amplitude Response.

(b) Phase Response.

Figure 4.10: Experimental impulse responses of a macro five beam array with strong coupling (15 mm shared base material). Amplitude is normalised by the maximum measured amplitude and frequency is normalised by the frequency at which the first peak occurs. Red - Beam 1, Blue - Beam 2, Black - Beam 3, Green - Beam 4, Purple - Beam 5.

Table 4.2: Key Parameter of the 5 beam array used to conduct the impulse responses.

| | Beam 1 | Beam 2 | Beam 3 | Beam 4 | Beam 5 |
|---|---|---|---|---|---|
| Cantilever Length | 105 mm | | | | |
| Cantilever Width | 29 mm | | | | |
| Cantilever Thickness | 1.5 mm | | | | |
| Tip Mass | 3.9 g | 3.5 g | 3.6 g | 3.7 g | 3.5 g |

### 4.4.2 Parameter Identification

It is necessary to calibrate the strain gauge sensors, so that measured strain can be converted into mm of tip displacement, which is the measurement of interest. The NI9237 module contains built in calibration software to convert the raw voltage measurements across the Wheatstone bridge into a strain measurement. To calibrate the strain gauges, a linear variable differential transformer (LVDT) was used to directly measure the displacement of the cantilever tip from the neutral axis. The LVDT used was a DS15 of the Orbit3 series purchased from Solartron Metrology. The DS15 has a measurement range of 15 mm and maximum error of 50 µm. As the test rig is designed to operate with tip amplitudes in the region of 1-5 mm, an error of 50 µm is sufficiently small for calibration of the strain gauges. LabVIEW® was used to simultaneously read the strain gauge signal and LVDT measurements for static deflection and for one beam at a time. The acquired data is presented in Figure 4.11.

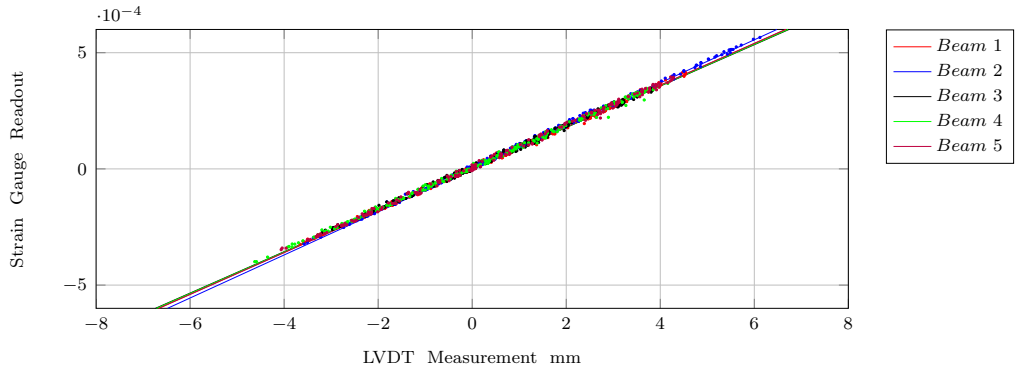


Figure 4.11: Strain gauge calibration data and linear fit for five beams of the second macro test rig.

It can be clearly seen from Figure 4.11 that a linear relationship can be found between true tip displacement and the strain gauge readings. This is the expected outcome for small tip displacements, where linear Euler-Bernoulli beam theory applies. The linear fit coefficient and R-squared values for all five beams are shown in Table 4.3. All R-squared values are in excess of 99%, suggesting a good fit to the data. As the dimensions of each cantilever are identical, it is expected that all linear coefficients be equivalent. It can be seen that there is a small amount of variance in the coefficient values, which will be due predominantly to small disparates in the precise mounting location of the strain gauges. Other potential sources of error include the strength of the epoxy glue bond between strain gauge and cantilever and the dimensional tolerances of the cantilevers.

Table 4.3: Strain gauge calibration coefficients for five beams including R-squared goodness of fit values.

| | Linear Coefficient | R-squared Value |
|---|---|---|
| Beam 1 | 11129 | 0.9982 |
| Beam 2 | 10801 | 0.9980 |
| Beam 3 | 11228 | 0.9959 |
| Beam 4 | 11194 | 0.9976 |
| Beam 5 | 11104 | 0.9974 |

The force coefficient of the magnets used to simulate the tip-sample interaction forces was calculated empirically for the permanent magnets used on the second test rig. The coefficient was found by measuring cantilever deflection due to magnetic attraction as the magnet position was varied. A curve fit using the experimental data could then be applied to the equilibrium equation, which is derived from the EOM of a single cantilever system. The derivation of the EOM can be found in Chapter 5 along with all definitions. Here, the EOM of the form of (5.25) in Section 5.3 is reduced to a static single beam equation (all functions of time and derivatives set to zero). This produces the following equation that is used to calculate the nondimensionalised magnet force coefficient $\tau_m$. $\overline{W}_{11}$ is the spatial mode displacement of the cantilever tip, $W_{k11}$ is modal stiffness and $W_{NL11}$ is the nonlinear force coefficient.

$$W_{k11}\Phi_1 - \frac{W_{NL11}\tau_m}{(\hat{d}_{01} - \overline{W}_{11}\Phi_1)^2} = 0 \tag{4.1}$$

The temporal mode function $\Phi_1$ and nondimensionalised separation distance $\hat{d}_{01}$ in (4.1) can be related to tip deflection ($w_1$) and tip-sample separation ($d_{01}$) respectively using the following relationships.

$$\Phi_1 = \frac{w_1}{\overline{W}_{11}L_{c_1}}, \tag{4.2}$$

$$\hat{d}_{01} = \frac{d_{01}}{L_{c_1}}, \tag{4.3}$$

where $L_c$ is the cantilever length. Upon calculating the nondimensional coefficient $\tau_m$, the dimensional magnet force coefficient $K_m$ can be calculated

using the following relationship, which is taken from the nondimensional definitions of (5.9) in Chapter 5.

$$K_m = \tau_m \rho A (L_{c_1} + L_b)^4 \omega_1^2 \tag{4.4}$$

To obtain the required data, the surface magnet was brought towards the cantilever at a continuous rate using the stepper motor whilst the static tip displacement and separation distance was recorded. Zero separation is defined as the point at which the surface magnet was in contact with the tip magnet and the cantilever deflection was equal to zero. Experimental data was converted into the appropriate form using (4.2) and (4.3), and $\tau_m$ was determined by minimising the sum of squared errors of (4.1) as defined in the following equation.

$$\min_{\tau_m \in \mathbb{R}} \sum_{i=1}^{N} \left( W_{k11}\Phi_{1_i} - \frac{W_{NL11}\tau_m}{(\hat{d}_{01_i} - \overline{W}_{11}\Phi_{1_i})^2} \right)^2 \tag{4.5}$$

The experimental data and curve fit is depicted in Figure 4.12 and the equation parameters and calculated magnet force constant are given in Table 4.4. It can be seen that the R-squared value is close to one, suggesting the calculated parameter is a good fit to the experimental data.

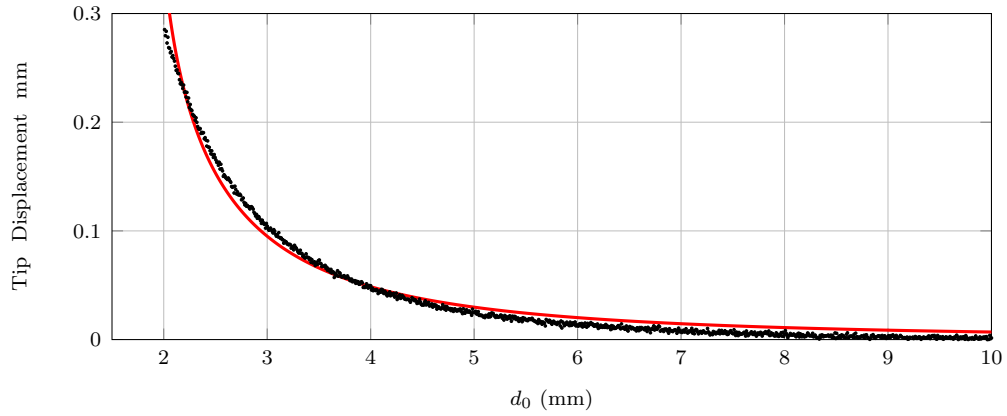


Figure 4.12: Static tip displacement measurements due to magnetic attraction. The black dots represent data points and the red lin is the minimised curve fit.

The final parameter that must be determined is the damping coefficient. Damping can be obtained by measuring the amplitude decay of a cantilever impulse response. The EOM of the form in (5.25) from Chapter 5 is again used, this time with damping included and external forcing terms set to zero, producing the following single beam equation.

Table 4.4: Magnet calibration parameters including R-squared goodness of fit value.

| Parameter | Value |
|---|---|
| $\overline{W}_{11}$ | 1 |
| $W_{NL11}$ | $-0.02$ |
| $W_{k11}$ | $-1$ |
| $K_m$ | $6.00\text{e}^{-5}$ |
| R-squared | 0.982 |

$$\ddot{\Phi} + W_{c11}\dot{\Phi} + W_{k11}\Phi = 0 \tag{4.6}$$

The damping term can be found from the normal form solution of (4.6), which takes on the following form,

$$\Phi = \hat{\Phi}\text{e}^{-\zeta\omega\tau}\sin(\sqrt{W_{k11}}\sqrt{1-\zeta^2}\tau + \varphi), \tag{4.7}$$

where $\hat{\Phi}$ and $\varphi$ are constants of integration, $\zeta$ is the damping ratio and $\omega$ is the undamped natural frequency. $\Phi$ can be related to experimental data using (4.2) and $\tau$ is nondimensionalised time of the form $\tau = t\omega$. The damping ratio and undamped natural frequency are found experimentally by minimising the sum of squared errors of (4.7).

$$\min_{\zeta,\omega\in\mathbb{R}} \sum_{i=1}^{N} \left( \hat{\Phi}\text{e}^{-\zeta\omega\tau_i}\sin(\omega\sqrt{1-\zeta^2}\tau_i + \varphi) - \Phi_i \right)^2 \tag{4.8}$$

Finally, the damping coefficient can be calculated as $W_{c11} = 2\zeta\omega$. Utilising (4.8) for experimental data for all five macro scale beams gives the damping coefficients seen in Table 4.5.

Table 4.5: Damping coefficients for five beams including R-squared goodness of fit values.

| | Damping Coefficient | R-squared Value |
|---|---|---|
| Beam 1 | 0.0068 | 0.9952 |
| Beam 2 | 0.0075 | 0.9987 |
| Beam 3 | 0.0073 | 0.9994 |
| Beam 4 | 0.0070 | 0.9995 |
| Beam 5 | 0.0071 | 0.9963 |

### 4.4.3 Feedback Control

It is necessary to verify ability to simulate tip-sample interaction forces and to vary the separation distance between cantilever tip and sample magnet. The test rig is designed such that the magnets simulating the sample surface can be moved, whilst the cantilevers remain fixed in position. This is equivalent to moving the sample whilst holding the cantilever in a fixed position on the micro scale as is done with standard AFM techniques. To demonstrate the ability to control tip-sample displacement, it is necessary to demonstrate the ability to control the magnet position such that it can be related to system parameters.

To demonstrate the ability of the test rig to be used with feedback control, AM-AFM and FM-AFM based control is implemented for a single cantilever with a 0.35 g tip mass. For AM-AFM control, the cantilever is driven at its far field resonance frequency with a constant input amplitude. The magnet is brought into close proximity with the cantilever tip ($\approx 1.5\,\text{mm}$) using the stepper motor and the resulting amplitude response is recorded as the amplitude set point. For FM-AFM, the same procedure is followed except the cantilever is continually excited at its resonance (90° phase shift). When in close proximity, the resulting frequency response is recorded as the frequency set point. A simple PID controller is implemented using LabVIEW® to hold the cantilever at the set point by adjusting the magnet position. The control gains and system parameters used can be found in Table 4.6. The Solartron LVDT sensor is used to accurately measure the position of the magnet in relation to the location of the set point. At set intervals, the magnet position is abruptly changed by applying a manual input within the control code, simulating changes in sample topography. The magnet position is continually monitored as it deviates from and returns to the set point through feedback control as can be seen in

Figure 4.15 for AM-AFM and Figure 4.17 for FM-AFM. The signal flow diagrams are presented in Figures 4.13 (AM-AFM) and 4.14 (FM-AFM). The corresponding gain values used for the control loops are give in Table 4.7. The cantilever amplitude and resonant frequency is also measured during the experimental run to further demonstrate the ability of the system to converge to a defined fixed point. The measured amplitude during AM-AFM is shown in Figure 4.16 and the measured resonant frequency during FM-AFM is shown in Figure 4.18.

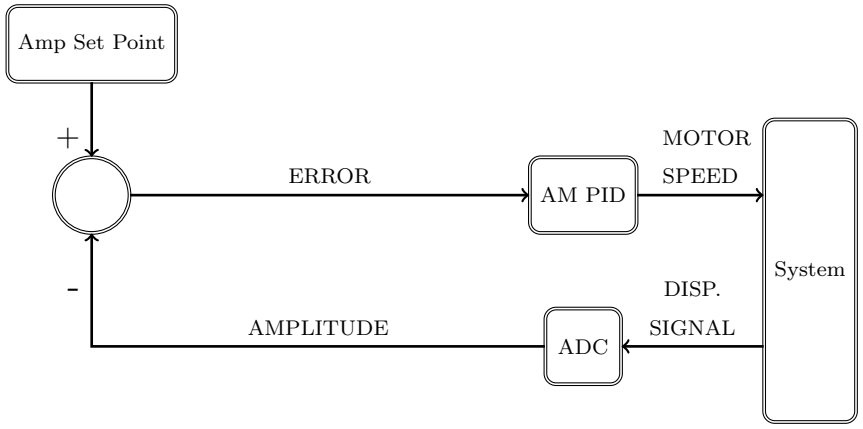


Figure 4.13: Signal diagram for AM-AFM control used on the macro scale test rig.

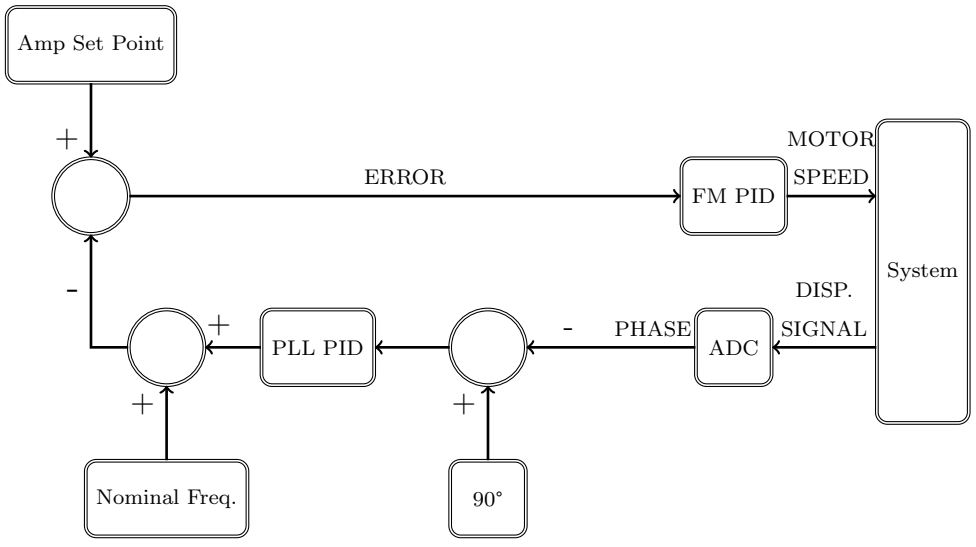


Figure 4.14: Signal diagram for FM-AFM control used on the macro scale test rig.

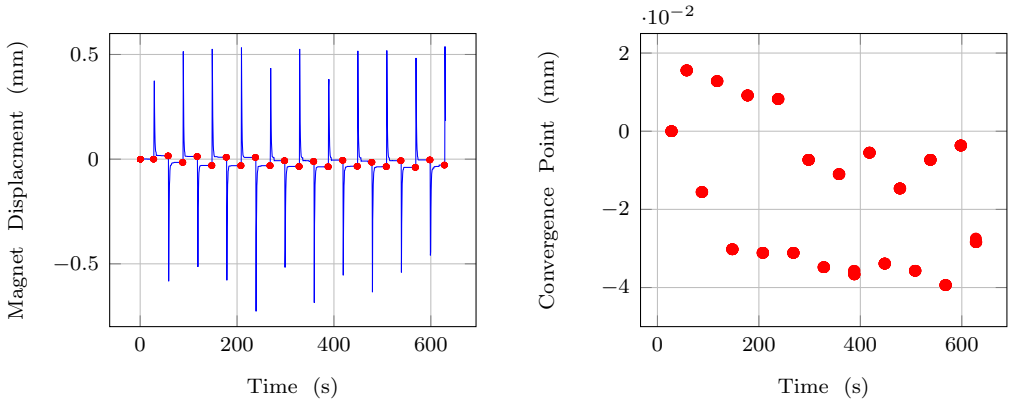


(a) Magnet displacement during AM-AFM operation. The red dots indicate the convergence points.

(b) Close up of the convergence points only.

Figure 4.15: Magnet displacement during experimental AM-AFM operation on the macro scale.

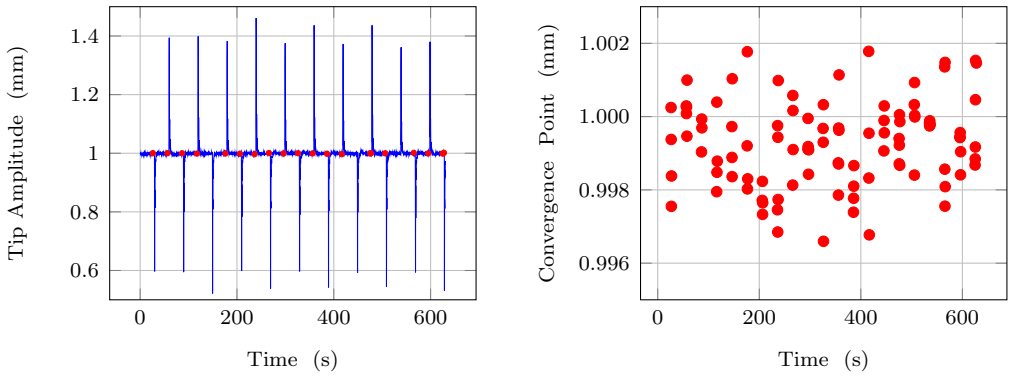


(a) Measured tip amplitude during AM-AFM operation. The red dots indicate the convergence points.

(b) Close up of the convergence points only.

Figure 4.16: Tip amplitude during Experimental AM-AFM operation on the macro scale.

It can be seen from Figures 4.15a and 4.17a that the system is able to track both a predefined amplitude and frequency set point and maintain a constant magnet position. There is, however, a small amount of steady state error at the point of convergence when multiple step inputs are applied for both AM-AFM and FM-AFM, as can be seen in Figures 4.15b and 4.17b. The convergence point was found by giving the system sufficient time to approach a steady state value before applying another adjustment to the magnet position. Steady state was deemed to have been reached when the variation in magnet position remained within 0.01 mm for at least 70 data points at a sampling rate of 40 Hz. The statistical analysis of the observed

steady state error is presented in Table 4.8. The mean steady state error is several orders of magnitude lower than the total applied motion of the magnet structure and of the cantilever tip amplitude. Standard deviation is 10× higher than position resolution of the stepper motor, so this is not the primary source of error. The high precision demonstrates the ability of the test rig to track a chosen amplitude or frequency set point using standard AFM control techniques. It should be noted that the standard deviation for the measured amplitude/resonant frequency at steady state is several times lower than the standard deviation of the measured magnet position. The difference between the two is an indicator of the measurement precision achievable with the macro scale AFM system using a single cantilever, as despite converging to the set point within very tight tolerances, measurement error was still present in the tip-sample separation.

Careful examination of both Figures 4.15a and 4.17a shows that there is a small deadband error that is dependent on the direction of the applied adjustment to the magnet position. The deadband error is most likely due to backlash in the stepper motor gearing and also in the connection between the LVDT probe and the magnet holding block. The hysteresis error is small and within a similar range to the observed steady state error, as can be seen in Figures 4.15b and 4.17b. The deadband error is an unavoidable feature of the utilised stepper motor and LVDT system.

Table 4.6: Parameters and control gains for the single beam AM-AFM and FM-AFM experiments.

| Parameters | Value | |
|---|---|---|
| | AM-AFM | FM-AFM |
| Input Amplitude | 0.7 V | 0.7 V |
| Input Frequency | 47.2 Hz | N/A |
| Far Field Amplitude | 2.7 mm | 2.7 mm |
| Set Amplitude | 1 mm | N/A |
| Set Frequency | N/A | 46 Hz |

The results presented here demonstrate that the test rig design is a true simulation of the basic operation of AFM on the micro scale. The achievable resolution and measurement precision has been demonstrated for a single beam, which will be used as a reference in the following chapters to demonstrate the potential performance improvements achievable with arrays. The controllability of multiple cantilevers using the test rig will also

Table 4.7: Parameters and control gains for the single beam AM-AFM and FM-AFM experiments.

| Parameters | Value | | |
|---|---|---|---|
| | AM PID | FM PID | PLL PID |
| P Gain ($K_p$) | 2 | 1 | 1 |
| I Gain ($K_I$) | 0.005 | 0.00001 | 0.00001 |
| D Gain ($K_d$) | 0 | 0.0001 | 0.0001 |

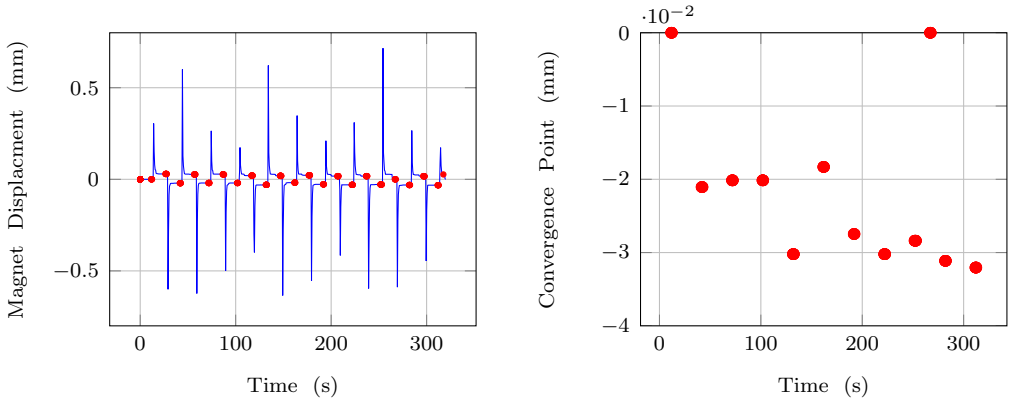


(a) Magnet displacement during FM-AFM operation. The red dots indicate the convergence points.

(b) Close up of the convergence points only.

Figure 4.17: Magnet displacement during experimental FM-AFM operation on the macro scale.

Table 4.8: Mean and standard deviation of the steady state error at the set point for AM-AFM and FM-AFM.

| | No. Data Points | Mean | Standard Dev. |
|---|---|---|---|
| AM-AFM Disp | 293 | −0.0152 mm | 0.0177 mm |
| AM-AFM Amp | 96 | 0.9993 mm | 0.0012 mm |
| FM-AFM Disp | 207 | −0.0015 mm | 0.0235 mm |
| FM-AFM Freq | 442 | 44.3078 Hz | 0.0130 Hz |

be demonstrated in Chapter 7.

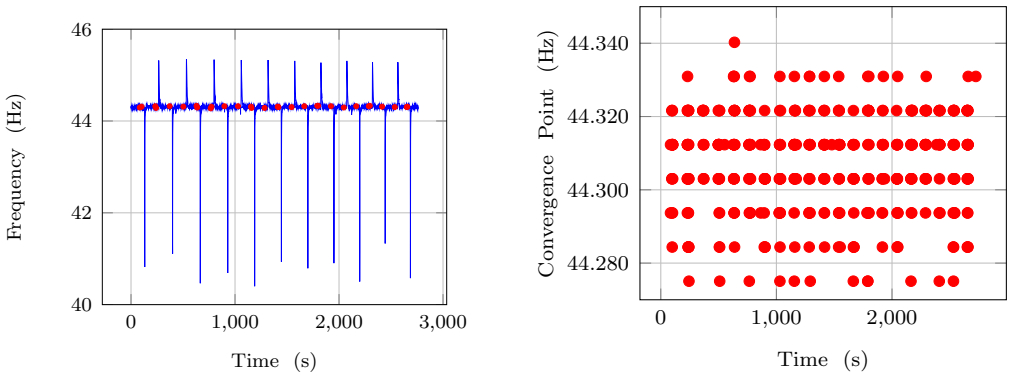


(a) Measured resonant frequency during FM-AFM operation. The red dots indicate the convergence points.

(b) Close up of the convergence points only.

Figure 4.18: Measured resonant frequency during experimental FM-AFM operation on the macro scale.

## 4.5 Conclusion

In this chapter, the design and validation of a macro scale test rig simulating micro scale AFM operation has been successfully completed. The macro scale test rig can be used as a novel tool to gain a better understanding of the dynamics that govern the response of micro cantilever arrays in the context of AFM. The advantages of the macro scale system is that key parameters can be easily varied and that the state of response can be visually observed, neither of which is possible on the micro scale. This makes the developed test rig a powerful tool for fundamental dynamic research. Several examples of equivalent macro scale test rigs exist in the literature, however, none have been designed to study the response of arrays in the context of AFM. The final test rig design can utilise arrays with up to five cantilevers, with varying levels of mechanical coupling and with attractive tip interaction forces that simulate the interaction between cantilever tip and sample during AFM operation. In total, two design iterations were constructed. The first design was built as a proof of concept, specifically to demonstrate that the response of a micro cantilever is qualitatively similar to the macro scale, specifically with regards to damping and nonlinearity, and that key parameters can be altered, namely coupling strength. The second design was built to conduct experiments pertinent to the outcomes of this thesis, and includes fully controllable tip-sample distance adjustment. One major drawback of the final test rig design is the inability to simulate repulsive interaction forces that occur the micro scale, both from electrostatic forces and from impact with the sample. Only attractive forces

have been simulated. The objective of this thesis is to gain a qualitative understanding of micro array dynamics in the presence of mechanical coupling and nonlinear tip forces. Precise quantitative results are not possible and not desired. Both the attractive and repulsive force interactions act to reduce the system resonant frequencies, and as such, simulating only the attractive force gradient and how it alters the eigenmodes of the array is sufficient at this stage of the research.

This chapter has presented the creation of the final test rig and experimental validation. It can be used to drawn qualitative conclusions about the response of micro arrays. Data pertaining to the novel research outcomes of this thesis, however, are presented in later chapters, specifically Chapters 6 and 7.

CHAPTER 5

# Mathematical Modelling

## 5.1 Introduction

In this chapter, a mathematical model of an array of cantilevers mechanically coupled through a shared base is formulated. The model is vitally important for understanding the dynamics of an array in the context of AFM. Several aims are identified that must be fulfilled through modelling and simulation, including; replication of the observed micro-array phenomena so that system parameters and inputs can be linked to response; prediction of expected response under AFM operating conditions; validation of the macro scale experimental setup and its ability to mimic the TUI arrays; identification of nonlinear phenomena and their classification, particularly in cases where unstable solution branches are present; and the testing of proposed concepts for enhancing measurement sensitivity. In relation to these aims, the model must serve two key purposes; it must be able to capture the observed dynamics of the TUI micro arrays (Chapter 3) and it must be possible to compare mathematical simulation results with macro scale experimental results (Chapter 4). As the fundamental mechanics governing both systems are qualitatively similar, this is achievable with a single, nondimensionalised model.

For the model to meet the required objectives, it must have certain properties. As discussed in the literature review, AFM arrays have been fabricated with large variations in the number of beams (from 2 up to hundreds), resulting in different response phenomena depending on the scale of the array. For this reason, the number of cantilevers incorporated into the model must be fully variable. As well as the number of beams, it is important to consider the properties of individual cantilevers within the array. As arrays are fabricated from a single block of material (usually crystalline silicon or corresponding nitrides/oxides), the material properties of each beam should be identical, however, it is typical for the mechanical parameters to vary, namely length, width and thickness, through both fabrication toler-

ances and design. Due to the fact that etching processes are carried out on the whole array structure, the layer thickness tends to be uniform across the whole structure, however, the length and width can be easily varied during the fabrication process. The model is therefore developed such that each beam has unique spacial dimensions and hence response properties. As previously discussed, this feature is not well incorporated in existing studies in the literature. A further consideration is that the mathematical model must capture the modal shapes and frequencies of the array structure. Capturing the modal components that make up the response of each beam, and particularly the change in both relative displacement and frequency of the modal components, is necessary to fully understand how observed system response is linked to system parameters.

Two major modelling approaches exist for beam structures, both generally and in the context of AFM. These are the lumped mass approach and the continuum mechanics approach. The lumped mass approach is commonly used due to its simplicity and ability to capture the system response with sufficient accuracy for most applications. However, one of the key drawbacks is that a lumped mass model does not resolve the spatial variations of the modes of a coupled system, as the distribution of mass throughout the system is not considered. As such, a lumped mass model would not meet the goal of capturing the interactions between array modes, and how the combined interactions relate to individual beam response due to applied nonlinear forces. A continuum mechanics model should therefore be used to capture the spatial distribution of the array modes. The model formulation in this chapter will be based on the methods laid out by Hagedorn and DasGupta [96], which provides a good overview of the basic principles for deriving the equations of motion for a system with distributed mass and external forces. Hamilton's method is utilised specifically. The equations of motion are formulated through an energy summation across the entire array, including all cantilevers and the base structure through which the beams are coupled.

## 5.2 Assumptions and Model Setup

The physical construction of the model is determined from which the energy balance can be formulated. Included are the assumptions required to produce a usable model that meets the objectives discussed above. A physical representation of the mathematical layout of the array system is presented in Figure 5.1 and is analogous to both the macro and micro scale.

This depiction represents beams $m-1$, $m$ and $m+1$ in an $M$ beam array. The basic premise of the model derivation splits the array structure into two

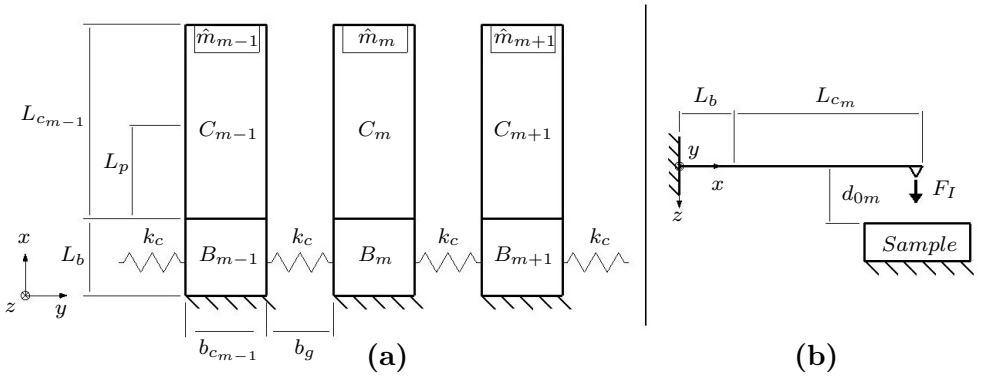


Figure 5.1: Diagram depicting the boundary conditions and coupling method used for the mathematical model with a top view (a) and a side view (b).

sub-components; individual cantilever beams ($C$), which are isolated from each other; and a shared base structure ($B$), through which mechanical coupling occurs. On the micro scale, the base section represents the base material that forms the clamping structure, but in which non-negligible motion is still present during operation. The point at which motion in the clamp structure becomes negligible is defined as the origin of the $x$ coordinate, and it is reasonable to apply standard clamping conditions (zero deflection and slope). The coupling assumptions is presented pictorially in Figure 5.2, which demonstrates how the base section length $L_b$ is set. From the origin, the base section has length $L_b$ and the cantilever sections have length $L_{c_m}$. This approach produces a mathematically simple way of capturing the mechanical coupling of the system and keeps the complexity of the energy balance equations low. To capture the mechanical coupling, it is assumed that the material located between cantilevers in the base section can be modelled as a distributed linear spring with a stiffness coefficient $k_c$. The relative displacement in the z-direction at the base section is small in comparison to that at the cantilever tips, and hence a linear approximation is reasonable. This spring is assumed to be distributed across the entire base section adjoining each pair of cantilevers, and hence must be given in units of $\mathrm{N\,m^{-2}}$. The base material between cantilevers effectively acts as a short cantilever structure itself, and hence the spring constant can be approximated using the well known cantilever stiffness equation (5.1).

$$k_c = \frac{EI}{b_g}, \tag{5.1}$$

where $E$ is the Young's Modulus of the base material, $b_g$ is the length of the effective cantilever structure between coupled base elements and $I$ is the second moment of area per unit width for unit consistency ($\frac{h^3}{12}$ where $h$ is the

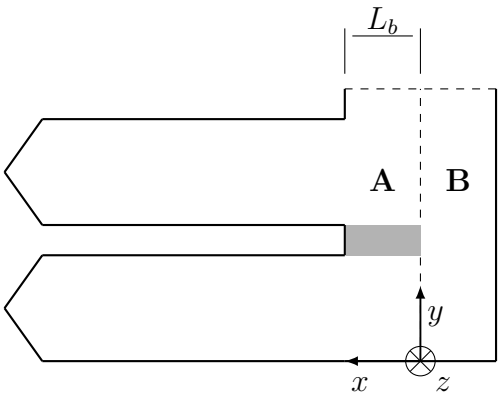


Figure 5.2: Pictorial of coupling model. Section **A** is the base material through which non-negligible coupling can occur and section **B** is the base material through which coupling is negligible and perfect clamping conditions can be assumed. The grey shaded area is the coupling material represented by the distributed spring element $k_c$.

thickness of the base material between adjoining cantilevers). For simplicity, the base coupling spring coefficient is assumed to be the same between all adjoining cantilevers. This is a reasonable assumption as material thickness is uniform and the cantilevers are evenly spaced.

The cantilevers, along with the base material, are fabricated from the same material, and hence the material properties throughout the structure are assumed to be constant. Thickness is also considered uniform, as it is difficult to vary the thickness across a structure with standard microfabrication techniques. The cantilever lengths $L_{c_m}$ and widths $b_{c_m}$ however, are variable to account for variations in frequency response due to fabrication tolerances and design specifications. In addition, each cantilever is assumed to have a small mass $\hat{m}_m$ at its free end which is also variable. On the micro scale this mass represents the tip used for interacting with the sample surface and on the macro scale this mass represents the magnetic material used to simulate interaction forces (with further details in Chapter 4).

The final consideration is the need to incorporate external forces into the model, namely the applied actuation force and the tip-sample interaction force to each beam. Both forces are assumed to act as point forces, with the interaction forces $F_I$ acting at point $x = L_{c_m}$ and the actuation force acting at point $x = L_p$. This is a good assumption for the interaction forces as the surface area of the tip is very small compared to the surface area of the cantilever. The location of the point is assumed to be at the free end edge of the cantilever. With true AFM cantilevers, the tip is located a non-zero

distance away from the free end edge, however, the free edge approximation is reasonable. The true force profile generated by the heater actuator is not well represented as a point force. However, it is not within the scope of this research to accurately model the functional relationship between input voltage and output force. Of interest is how the cantilevers respond to a given sinusoidal input, and particularly how the response is altered by external forces and mechanical coupling. Therefore, it is reasonable, in the scope of this work, to assume the actuation input is a sinusoidal signal applied as a point force and neglect the exact relationship between input voltage and output force. The functional relationship of the heater actuator used on the TUI arrays has been studied in detail by Roeser [47], as discussed in Chapter 1. In the model, $L_p$ is set to be at the cantilever tip.

It is necessary to define the mathematical form of the tip-sample interaction forces. As discussed, the basic form of the model is required to be compatible with both the macro and micro scale systems. The most commonly used model of interaction forces used in AFM is the Lennard-Jones force curve [97]. The Lennard-Jones model takes into account attractive electrostatic forces between molecules as well as repulsion due to the Pauli exclusion principle. This model takes the following form,

$$F_{I_{micro}}(r) = 4\epsilon\left[\frac{\sigma^6}{d_{0m}^7} - 2\frac{\sigma^{12}}{d_{0m}^{13}}\right], \tag{5.2}$$

where $d_{0m}$ is the separation distance between tip and sample, $\sigma$ is the distance at which the potential between tip and sample is zero, and $\epsilon$ is the potential well depth and is dependant on the cantilever tip geometry and material properties. This model only accounts for noncontact forces, and does not take into account contact forces that occur when the tip is pressed into the sample. Multiple contact models have been utilised in the context of AFM, the most common of which include the Hertz model, Derjaguin-Müller-Toporov (DMT) model and the Johnson-Kendall-Roberts (JKR) model [98]. Contact forces in AFM are dependent on a number of factors, including material stiffness, viscoelasticity and surface adhesion, and hence a large amount of research is dedicated to formulating contact models for AFM. Due to the breadth and complexity of contact modelling, it will not be included in this thesis. The focus of the thesis is on the influence of long-distance forces on array response.

As explained in Chapter 4, magnets are used to simulate attractive electrostatic forces, while repulsive and contact forces are not simulated. It is well established that the force gradient of magnetic attraction can be modelled as being proportional to the inverse square of the distance between two

surfaces [99]. This model is qualitatively similar to the attractive component of the Lennard-Jones Potential in that the force is inversely proportional to separation distance. The force gradient for the macro scale system takes on the following form,

$$F_{I_{macro}}(r) = \frac{f_a}{d_{0m}^2}, \tag{5.3}$$

where $f_a$ is a magnetic field constant. The force constant of the attractive term is calculated empirically in Chapter 4. As (5.2) and (5.3) are of an equivalent form, it is possible to formulate a generalised force gradient model that can be applied to both the macro and micro scale using interchangeable parameters. This model is of the form,

$$F_I(r) = \frac{K_m}{d_{0m}^{p_1}} - \frac{\bar{K}_m}{d_{0m}^{p_2}}, \tag{5.4}$$

where $K_m$, $\bar{K}_m$, $p_1$ and $p_2$ are constants that can be set to match either (5.2) or (5.3). A comparison of the force curves for both the micro and macro scale system are given in Figure 5.3. The curves give a qualitative representation of the relative force-distance relationship for both scales, as well as depicting the relative cantilever tip operating range. To provide qualitatively comparable results, the values used to produce the curves using (5.4) are $K_m = 0.075$, $\bar{K}_m = 0.0023$, $p_1 = 7$ and $p_2 = 13$ for the micro scale curve and $K_m = 1.2$, $\bar{K}_m = 0$ and $p_1 = 2$ for the macro scale curve.

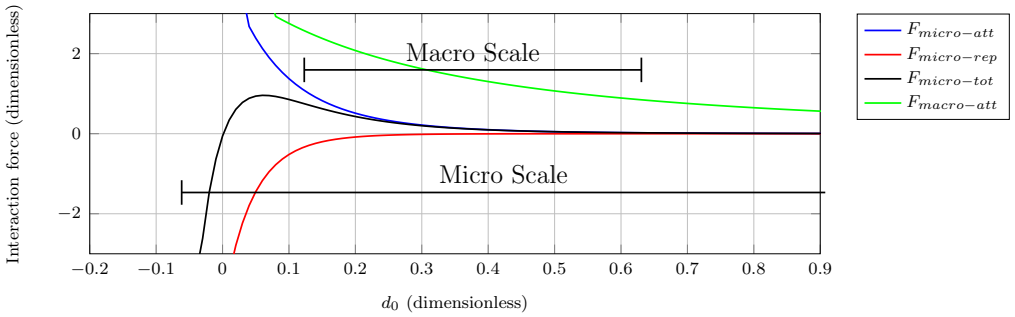


Figure 5.3: Force distance curve relationships for the micro Lennard-Jones force and magnetic attraction force. The depicted forces curves are scaled such that the Lennard-Jones force has a peak of 1 and crosses the zero axis at $d_0 = 0$. The magnetic attraction force curve is scaled to allow for comparison between the two force curves. The figure allows for qualitative comparison of the force curves, and parameters do not match the quantitative values of the macro and micro scale systems.

## 5.3 Continuum Mechanics Formulation

To begin formulating the equations of motion for a base coupled array, the energy balance of the entire system is equated using the layout presented in Figure 5.1. Damping terms are not included in the continuum mechanics formulation and are added as discrete coefficients into the final ODE. The focus of this research is on how the physical parameters of a coupled array affect response, and detailed modelling of damping is not included. The formulation will be done in the context of the macro scale system, using the empirically determined constants for the tip-force interaction model from (5.4) as the model is predominantly used in tandem with experimental data from the macro scale. For the macro scale, the displacement term of the nonlinear function ($r$ in (5.4)) is the distance between the sample surface and array structure ($d_{0m}$) minus the cantilever tip displacement ($w_{cm}$). The kinetic energy $T$, potential energy $U$ and nonlinear tip forces plus external actuation $F$ are formulated to be (neglecting damping at this stage),

$$T = \sum_{m=1}^{M} \left[ \frac{1}{2} \int_0^{L_b} \rho A_m \dot{w}_{bm}^2(x,t)\,\mathrm{d}x + \frac{1}{2} \int_0^{L_{cm}} \rho A_m \dot{w}_{cm}^2(x,t)\,\mathrm{d}x \right], \tag{5.5}$$

$$U = \sum_{m=1}^{M} \left[ \frac{1}{2} \int_0^{L_b} EI_m w''^2_{bm}(x,t)\,\mathrm{d}x + \frac{1}{2} \int_0^{L_{c_m}} EI_m w''^2_{cm}(x,t)\,\mathrm{d}x \right] + \sum_{m=1}^{M-1} \left[ \frac{1}{2} \int_0^{L_b} k_c (w_{bm}(x,t) - w_{b(m+1)}(x,t))^2\,\mathrm{d}x \right], \tag{5.6}$$

$$F = \sum_{m=1}^{M} \left[ \left( \frac{K_m}{(d_{0m} - w_{cm}(x,t))^{p_1}} - \frac{\bar{K}_m}{(d_{0m} - w_{cm}(x,t))^{p_2}} \right) \delta(x - (L_{c_m} + L_b)) + (DC_m + AC_m \cos(\Omega_m t)) \delta(x - (L_p + L_b)) \right], \tag{5.7}$$

where $\rho$ and $A_m$ in (5.5) are the material density and cross-section area of beam $m$, $E$ and $I_m$ in (5.6) are the Young's Modulus and second moment of area of beam $m$, $\Omega_m$, $DC_m$, $AC_m$, $K_m$, and $d_{0m}$ in (5.7) are the forcing frequency, the linear offset and sinusoidal constants of actuation applied at a point $x = L_p + L_b$ on the beam, the force constant of the nonlinear term applied at the tip ($x = L_{c_m} + L_b$) of beam $m$ and the separation distance between the array structure and sample surface, respectively. $w_m(x,t)$ is the displacement of beam $m$ at position $x$ in the $z$ direction and at time $t$. Displacement towards the surface is defined as positive, which ensures consistency in the energy balance and in the physical representation of the system. The equation of motion as a function of space and time is formulated in the following non-dimensional form and is done using Hamilton's principle, following the methodology in [96].

$$\ddot{\hat{w}}_{cm} + \mu_m \hat{w}^{IV}_{cm} - \left( \frac{\tau_m}{(\hat{d}_{0m} - w_{cm})^{p_1}} - \frac{\bar{\tau}_m}{(\hat{d}_{0m} - w_{cm})^{p_2}} \right) \delta(\hat{x} - (\hat{L}_{c_m} + \hat{L}_b)) - (\widehat{DC}_m + \widehat{AC}_m \cos(\hat{\Omega}\tau)) \delta(\hat{x} - (\hat{L}_p + \hat{L}_b)) = 0, \tag{5.8}$$

$$\ddot{\hat{w}}_{bm} + \mu_m \hat{w}^{IV}_{bm} + \hat{k}_c \hat{w}_{bm} - \hat{k}_c \hat{w}_{b(m+1)} = 0. \tag{5.9}$$

The system is equated in a non-dimensional form to ensure consistency. The following non-dimensional definitions are applied.

$$\hat{x} = \frac{x}{L_{c_1} + L_b}, \quad \hat{w}_m = \frac{w_m}{L_{c_1} + L_b}, \quad \hat{L}_b = \frac{L_b}{L_{c_1} + L_b}, \quad \tau = \omega_1 t,$$

$$\hat{d}_{0m} = \frac{d_{0m}}{L_{c_1} + L_b}, \quad \hat{L}_p = \frac{L_p}{L_{c_1} + L_b}, \quad \hat{\Omega}_m = \frac{\Omega_m}{\omega_1},$$

$$\mu_m = \frac{EI_m}{\rho A (L_{c_1} + L_b)^4 \omega_1^2}, \quad \hat{k}_c = \frac{k_c}{\rho A (L_{c_1} + L_b) \omega_1^2},$$

$$\widehat{AC}_m = \frac{AC_m}{\rho A \omega_1^2 (L_{c_1} + L_b)}, \quad \widehat{DC}_m = \frac{DC_m}{\rho A \omega_1^2 (L_{c_1} + L_b)},$$

$$\tau_m = \frac{K_m}{\rho A (L_{c_1} + L_b)^4 \omega_1^2}, \quad \bar{\tau}_m = \frac{\bar{K}_m}{\rho A (L_{c_1} + L_b)^4 \omega_1^2}, \quad \hat{L}_{c_m} = \frac{L_{c_m}}{L_{c_1} + L_b}$$

In the above definitions, $\omega_1$ represents the frequency of the array mode with the lowest frequency (nominally the first array mode). In accordance with the defined model assumptions, the base sections are assumed to be perfectly clamped at $\hat{x} = 0$ and the cantilever sections are assumed to be free at $\hat{x} = \hat{L}_{cm} + \hat{L}_b$. The cantilever and base sections in the model are bonded at the meeting point to produce a smooth transition to represent the physical system. The resulting boundary and transition conditions are written as follows.

$$\begin{aligned}
&w_{bm}(0,\tau) = 0, \quad w_{bm}^{'}(0,\tau) = 0, \quad w_{cm}^{''}(\hat{L}_{c_m},\tau) = 0, \\
&w_{cm}^{'''}(\hat{L}_{c_m},\tau) = \frac{\hat{m}_m L_{c_m}^3}{EI_m} \ddot{w}_{cm}(\hat{L}_{c_m},\tau), \\
&w_{bm}(\hat{L}_b,\tau) = w_{cm}(\hat{L}_b,\tau), \quad w_{bm}^{'}(\hat{L}_b,\tau) = w_{cm}^{'}(\hat{L}_b,\tau), \\
&w_{bm}^{''}(\hat{L}_b,\tau) = w_{cm}^{''}(\hat{L}_b,\tau), \quad w_{bm}^{'''}(\hat{L}_b,\tau) = w_{cm}^{'''}(\hat{L}_b,\tau).
\end{aligned} \tag{5.10}$$

The spatially dependent system is solved by applying the associated boundary conditions (5.10) to determine the modal shape distribution function. This is done for the special case where external forces are zero ($\widehat{DC}_m = \widehat{AC}_m = 0; \tau_m = \bar{\tau}_m = 0$). External forces are incorporated back into the model along with damping terms after the derivation of the free vibration modes. It is assumed that the displacement is periodic in time such that the solution can be defined in the following form.

$$\hat{w}_m(\hat{x},\tau) = W_m(\hat{x}) \mathrm{e}^{-i\hat{\omega}_n \tau} \tag{5.11}$$

In (5.11), $W_m$ represents the modal shape of the combined cantilever and base structure of beam $m$ as a function of $\hat{x}$ and is of the form $W_m =$

$W_{bm} + W_{cm}$. $\omega_n$ represents the as yet undefined natural frequency of the $n_{th}$ mode of the array and is normalised in the form $\hat{\omega}_n = \omega_n/\omega_1$. The set of governing equations ((5.8) and (5.9)) are 4th order in space, thus the equations can be reformulated into 4 first order equations. Applying (5.11) to (5.8) and (5.9), the system can be written in the following matrix form.

$$\bar{\mathbf{W}}^{'\mathbf{T}} = \mathbf{A}^{*}\bar{\mathbf{W}}^{\mathbf{T}}, \tag{5.12}$$

where $\bar{\mathbf{W}}$ is a $1 \times 8M$ row vector containing all $\hat{w}_{cm}$ and $\hat{w}_{bm}$ functions as well as their first three spatial derivatives. $\bar{\mathbf{A}}$ is the state space matrix of the system of size $8M \times 8M$ that defines the equations of motion of the system. The matrix equation consists of the following components in the following form.

$$\begin{bmatrix}\bar{\mathbf{W}}_{\mathbf{1}} & \bar{\mathbf{W}}_{\mathbf{2}} & \cdots & \bar{\mathbf{W}}_{\mathbf{M}}\end{bmatrix}^{'T} = \mathbf{A}^{*}\begin{bmatrix}\bar{\mathbf{W}}_{\mathbf{1}} & \bar{\mathbf{W}}_{\mathbf{2}} & \cdots & \bar{\mathbf{W}}_{\mathbf{M}}\end{bmatrix}^{T}, \tag{5.13}$$

$$\mathbf{A}^{*} = \begin{bmatrix}\bar{\mathbf{A}}_{\mathbf{1}} & \bar{\mathbf{G}}_{\mathbf{1}} & \bar{\mathbf{O}}_{\mathbf{8}} & \cdots & \bar{\mathbf{O}}_{\mathbf{8}} \\ \bar{\mathbf{O}}_{\mathbf{8}} & \bar{\mathbf{A}}_{\mathbf{2}} & \bar{\mathbf{G}}_{\mathbf{2}} & \cdots & \bar{\mathbf{O}}_{\mathbf{8}} \\ \bar{\mathbf{O}}_{\mathbf{8}} & \bar{\mathbf{O}}_{\mathbf{8}} & \bar{\mathbf{A}}_{\mathbf{3}} & \cdots & \bar{\mathbf{O}}_{\mathbf{8}} \\ \vdots & \vdots & \vdots & \ddots & \vdots \\ \bar{\mathbf{O}}_{\mathbf{8}} & \bar{\mathbf{O}}_{\mathbf{8}} & \bar{\mathbf{O}}_{\mathbf{8}} & \cdots & \bar{\mathbf{A}}_{\mathbf{M}}\end{bmatrix}, \tag{5.14}$$

$$\bar{\mathbf{W}}_{\mathbf{m}} = \begin{bmatrix}\hat{w}_{cm} & \hat{w}'_{cm} & \hat{w}''_{cm} & \hat{w}'''_{cm} & \hat{w}_{bm} & \hat{w}'_{bm} & \hat{w}''_{bm} & \hat{w}'''_{bm}\end{bmatrix}, \tag{5.15}$$

$$\bar{\mathbf{A}}_{\mathbf{m}} = \begin{bmatrix}\hat{\mathbf{A}}_{\mathbf{m}} & \bar{\mathbf{O}}_{\mathbf{4}} \\ \bar{\mathbf{O}}_{\mathbf{4}} & \hat{\mathbf{A}}_{\mathbf{m}}\end{bmatrix}, \tag{5.16}$$

$$\bar{\mathbf{G}}_{\mathbf{m}} = \begin{bmatrix}\bar{\mathbf{O}}_{\mathbf{4}} & \bar{\mathbf{O}}_{\mathbf{4}} \\ \bar{\mathbf{O}}_{\mathbf{4}} & \hat{\mathbf{G}}_{\mathbf{m}}\end{bmatrix}, \tag{5.17}$$

$$\hat{\mathbf{A}}_{\mathbf{m}} = \begin{bmatrix} 0 & 1 & 0 & 0 \\ 0 & 0 & 1 & 0 \\ 0 & 0 & 0 & 1 \\ \dfrac{\hat{\omega}_n^2}{\mu_m} - \dfrac{\hat{k}_c}{\mu_m} & 0 & 0 & 0 \end{bmatrix}, \tag{5.18}$$

$$\hat{\mathbf{G}}_{\mathbf{m}} = \begin{bmatrix} 0 & 1 & 0 & 0 \\ 0 & 0 & 1 & 0 \\ 0 & 0 & 0 & 1 \\ \dfrac{\hat{k}_c}{\mu_m} & 0 & 0 & 0 \end{bmatrix}. \tag{5.19}$$

In (5.13), (5.16) and (5.17), $\bar{\mathbf{O}}_{\mathbf{4}}$ is a $4 \times 4$ matrix of zeros and $\bar{\mathbf{O}}_{\mathbf{8}}$ is an $8 \times 8$ matrix of zeros. The system described by (5.13) is solved by finding the orthogonal eigenmodes of the state space matrix. The solution can be written in the following form.

$$\bar{\mathbf{W}}^{\mathbf{T}} = \mathbf{V}\mathrm{e}^{\mathbf{\Lambda}\hat{x}}\mathbf{V}^{-\mathbf{1}}\mathbf{D}^{\mathbf{T}}, \tag{5.20}$$

where $\mathbf{V}$ is a matrix whose columns consist of the right eigenvectors of $\bar{\mathbf{A}}$ and $\mathbf{\Lambda}$ is a diagonal matrix whose elements consist of the eigenvalues of $\bar{\mathbf{A}}$. $\mathbf{D}$ is a row vector consisting of the constants of integration. To find the natural frequency of the modes within the array ($\hat{\omega}_n$), it is necessary to solve for the condition where the determinant of the solution matrix ($\mathbf{V}\mathrm{e}^{\mathbf{\Lambda}\hat{x}}\mathbf{V}^{-\mathbf{1}}$) is zero for the given boundary conditions (5.10). With this condition, there does not exist a unique solution for $\mathbf{D}$, as the solution matrix is rank deficient by 1. As a result, any single element of $\mathbf{D}$ can be defined arbitrarily and the remaining elements determined from the boundary conditions for each mode $\hat{\omega}_n$. The resulting vectors represent the modal shape in space for each array mode ($W_n$). The vector is a non-dimensional scaling factor and the absolute values are not significant, only the ratio between elements.

The method of separation of variables [96] is applied to the equations of motion (5.8) and (5.9) to divide the system into separate functions of space and time. The solution is in the form of a summation of the modal shape functions derived in (5.20) multiplied by a temporal distribution function.

$$\hat{w}_m(\hat{x}, \tau) = \sum_{n=1}^{N} W_{mn}(\hat{x})\Phi_n(\tau), \tag{5.21}$$

where $W_{mn}$ is the modal shape function of beam $m$ at mode $n$ found from (5.20) and is a function of $\hat{x}$ only and $\Phi_n$ is the temporal distribution function of mode $n$ and is a function of $\tau$ only. Note that each beam has a unique spatial function for each mode, whilst the temporal function

applies to the entire array. The number of modes includes both array modes (which relate to the phase angle between individual cantilevers) and intrinsic bending modes of the cantilevers themselves. The number of array modes will always be equal to the number of beams, while the number of bending modes incorporated into the model can be selected freely. If the number of bending modes incorporated into the model is $\hat{n}$, the total number of modes is $N = \hat{n} \times m$. Applying the separation of variables condition (5.21) to (5.8) and (5.9) results in the following equation of motion.

$$\sum_{n=1}^{N}(W_{mn}\ddot{\Phi}_n) + \sum_{n=1}^{N}((\mu W_{mn}^{IV} + \hat{k}_c W_{mn} - \hat{k}_c W_{(m+1)n})\Phi_n)$$
$$- \left(\frac{\tau_m}{(\hat{d}_{0m} - \sum_{n=1}^{N}(\overline{W}_{mn}\Phi_n))^{p_1}} - \frac{\bar{\tau}_m}{(\hat{d}_{0m} - \sum_{n=1}^{N}(\overline{W}_{mn}\Phi_n))^{p_2}}\right)$$
$$\times \delta(\hat{x} - (\hat{L}_{c_m} + \hat{L}_b)) - (\widehat{DC}_m + \widehat{AC}_m \cos(\Omega\tau))\delta(\hat{x} - (\hat{L}_p + \hat{L}_b)) = 0, \tag{5.22}$$

where $\overline{W}_{mn}$ is used to represent the tip displacement of a specific beam and specific mode shape ($\overline{W}_{mn} = W_{mn}(\hat{x} = \hat{L}_b + \hat{L}_{c_m})$). Equation (5.22) can be written in the following matrix form for all beams 1 to $M$.

$$\hat{\mathbf{W}}\ddot{\mathbf{\Phi}} + \hat{\mathbf{W}}_{\hat{\mathbf{k}}}\mathbf{\Phi} - \hat{\mathbf{W}}_{\hat{\mathbf{F}}}\mathbf{F} - \hat{\mathbf{W}}_{\hat{\mathbf{NL}}}\mathbf{NL} = \mathbf{0} \tag{5.23}$$

$\hat{\mathbf{W}}$ is an M×N matrix whose columns contain the spatial mode shape functions for each beam $m$ at mode $n$. $\mathbf{\Phi}$ is a 1×N column vector consisting of the temporal distribution functions. $\hat{\mathbf{W}}_{\hat{\mathbf{F}}}$ and $\hat{\mathbf{W}}_{\hat{\mathbf{NL}}}$ are both M×N identity matrices representing the forcing terms and nonlinear tip force interaction terms, respectively, and are multiplied by their corresponding dirac delta functions. $\mathbf{F}$ is a column vector consisting of the AC and DC actuation terms for each beam and $\mathbf{NL}$ is a column vector consisting of the nonlinear tip force terms.

The Galerkin method [96] can be used to spatially discretise (5.23) into $N$ sets of ODEs varying in time only. The discretisation is formulated as follows.

$$\int_0^1 \hat{\mathbf{W}}^{\mathbf{T}}(\hat{\mathbf{W}}\ddot{\mathbf{\Phi}} + \hat{\mathbf{W}}_{\mathbf{k}}\mathbf{\Phi} - \hat{\mathbf{W}}_{\mathbf{F}}\mathbf{F} - \hat{\mathbf{W}}_{\mathbf{NL}}\mathbf{NL})dx = \mathbf{0} \tag{5.24}$$

The spatial mode shapes are scaled such that $\int_0^1 \hat{\mathbf{W}}^{\mathbf{T}}\hat{\mathbf{W}}dx = 1$ to standardise the equations [96]. At this stage, damping is also introduced into

the system in the form of a linear coefficient for each mode. The damping coefficients are found from experimental data using parameter identification on both the macro and micro scale. Theoretical modelling of damping terms was deemed unnecessary as any nonlinear damping would originate predominantly from fluidic interaction, and as stated in Chapter 1 this was not within the thesis scope. Finally, the system can be written in the following form.

$$\ddot{\mathbf{\Phi}} + \mathbf{W_c}\dot{\mathbf{\Phi}} + \mathbf{W_k}\mathbf{\Phi} - \mathbf{W_F}\mathbf{F} - \mathbf{W_{NL}}\mathbf{NL} = \mathbf{0}, \tag{5.25}$$

where $\mathbf{W_c}$ and $\mathbf{W_k}$ are diagonal matrices containing the damping and stiffness coefficients respectively for each mode and $\mathbf{W_F}\mathbf{F}$ and $\mathbf{W_{NL}}\mathbf{NL}$ contain the terms that represent the actuation and tip force coupling between modes. The terms of the matrix equation take on the following expanded forms.

$$\mathbf{\Phi} = \begin{bmatrix} \Phi_1 \\ \Phi_2 \\ \vdots \\ \Phi_N \end{bmatrix}, \qquad \mathbf{F} = \begin{bmatrix} \widehat{DC}_1 + \widehat{AC}_1\cos(\Omega\tau) \\ \widehat{DC}_2 + \widehat{AC}_2\cos(\Omega\tau) \\ \vdots \\ \widehat{DC}_m + \widehat{AC}_m\cos(\Omega\tau) \end{bmatrix},$$

$$\mathbf{NL} = \begin{bmatrix} \dfrac{\tau_m}{(\hat{d}_{01} - \sum_{n=1}^{N}(\overline{W}_{1n}\Phi_n))^{p_1}} - \dfrac{\bar{\tau}_m}{(\hat{d}_{01} - \sum_{n=1}^{N}(\overline{W}_{1n}\Phi_n))^{p_2}} \\ \dfrac{\tau_m}{(\hat{d}_{02} - \sum_{n=1}^{N}(\overline{W}_{2n}\Phi_n))^{p_1}} - \dfrac{\bar{\tau}_m}{(\hat{d}_{02} - \sum_{n=1}^{N}(\overline{W}_{2n}\Phi_n))^{p_2}} \\ \vdots \\ \dfrac{\tau_m}{(\hat{d}_{0m} - \sum_{n=1}^{N}(\overline{W}_{mn}\Phi_n))^{p_1}} - \dfrac{\bar{\tau}_m}{(\hat{d}_{0m} - \sum_{n=1}^{N}(\overline{W}_{mn}\Phi_n))^{p_2}} \end{bmatrix},$$

$$\mathbf{W_c} = \begin{bmatrix} W_{c11} & 0 & \cdots & 0 \\ 0 & W_{c22} & \cdots & 0 \\ \vdots & \vdots & \ddots & \vdots \\ 0 & 0 & \vdots & W_{cMN} \end{bmatrix}, \qquad \mathbf{W_k} = \begin{bmatrix} W_{k11} & 0 & \cdots & 0 \\ 0 & W_{k22} & \cdots & 0 \\ \vdots & \vdots & \ddots & \vdots \\ 0 & 0 & \vdots & W_{kMN} \end{bmatrix},$$

$$\mathbf{W_F} = \begin{bmatrix} W_{F11} & W_{F12} & \cdots & W_{F1N} \\ W_{F21} & W_{F22} & \cdots & W_{F2N} \\ \vdots & \vdots & \ddots & \vdots \\ W_{FM1} & W_{FM2} & \vdots & W_{FMN} \end{bmatrix},$$

$$\mathbf{W_{NL}} = \begin{bmatrix} W_{NL11} & W_{NL12} & \cdots & W_{NL1N} \\ W_{NL21} & W_{NL22} & \cdots & W_{NL2N} \\ \vdots & \vdots & \ddots & \vdots \\ W_{NLM1} & W_{NLM2} & \vdots & W_{NLMN} \end{bmatrix}.$$

The form of (5.25) is the modal form, whereby the temporal functions of each mode can be solved and recombined with the spatial mode functions to calculate the displacement of each cantilever. The system can also be rewritten in direct displacement form by applying the following transformation,

$$\mathbf{X} = \overline{\mathbf{W}}\mathbf{\Phi}, \tag{5.26}$$

where $\mathbf{X}$ is a vector of the time dependent tip displacement terms $X_m$ for each beam $m$. The $M \times N$ transformation matrix $\overline{\mathbf{W}}$ contains the tip displacement of the modal shape functions $\overline{W}_{mn}$ for each beam $m$ and each mode $n$. Applying the transformation (5.26) to (5.25) and again normalising the inertial term of the ODE, the direct displacement equations can be written in the following matrix form.

$$\ddot{\mathbf{X}} + \overline{\mathbf{W}}_{\mathbf{c}}\dot{\mathbf{X}} + \overline{\mathbf{W}}_{\mathbf{k}}\mathbf{X} - \overline{\mathbf{W}}_{\mathbf{F}}\overline{\mathbf{F}} - \overline{\mathbf{W}}_{\mathbf{NL}}\overline{\mathbf{NL}} = \mathbf{0}, \tag{5.27}$$

where $\overline{\mathbf{W}}_{\mathbf{c}} = \overline{\mathbf{W}}\mathbf{W}_{\mathbf{c}}\overline{\mathbf{W}}^{-\mathbf{1}}$, $\overline{\mathbf{W}}_{\mathbf{k}} = \overline{\mathbf{W}}\mathbf{W}_{\mathbf{k}}\overline{\mathbf{W}}^{-\mathbf{1}}$, $\overline{\mathbf{W}}_{\mathbf{F}} = \overline{\mathbf{W}}\mathbf{W}_{\mathbf{F}}\overline{\mathbf{W}}^{-\mathbf{1}}$ and $\overline{\mathbf{W}}_{\mathbf{NL}} = \overline{\mathbf{W}}\mathbf{W}_{\mathbf{NL}}\overline{\mathbf{W}}^{-\mathbf{1}}$. The terms of the matrix equation take on the following expanded forms.

$$\mathbf{X} = \begin{bmatrix} X_1 \\ X_2 \\ \vdots \\ X_N \end{bmatrix}, \qquad \overline{\mathbf{F}} = \begin{bmatrix} \widehat{DC}_1 + \widehat{AC}_1\cos(\Omega\tau) \\ \widehat{DC}_2 + \widehat{AC}_2\cos(\Omega\tau) \\ \vdots \\ \widehat{DC}_m + \widehat{AC}_m\cos(\Omega\tau) \end{bmatrix},$$

$$\overline{\mathbf{NL}} = \begin{bmatrix} \dfrac{\tau_m}{(\hat{d}_{01} - X_1)^{p_1}} - \dfrac{\bar{\tau}_m}{(\hat{d}_{01} - X_1)^{p_2}} \\ \dfrac{\tau_m}{(\hat{d}_{02} - X_2)^{p_1}} - \dfrac{\bar{\tau}_m}{(\hat{d}_{02} - X_2)^{p_2}} \\ \vdots \\ \dfrac{\tau_m}{(\hat{d}_{0m} - X_M)^{p_1}} - \dfrac{\bar{\tau}_m}{(\hat{d}_{0m} - X_M)^{p_2}} \end{bmatrix},$$

$$\overline{\mathbf{W}}_{\mathbf{c}} = \begin{bmatrix} \overline{W}_{c11} & \overline{W}_{c12} & \cdots & \overline{W}_{c1N} \\ \overline{W}_{c21} & \overline{W}_{c22} & \cdots & \overline{W}_{c2N} \\ \vdots & \vdots & \ddots & \vdots \\ \overline{W}_{cM1} & \overline{W}_{cM2} & \vdots & \overline{W}_{cMN} \end{bmatrix},$$

$$\overline{\mathbf{W}}_{\mathbf{k}} = \begin{bmatrix} \overline{W}_{k11} & \overline{W}_{k12} & \cdots & \overline{W}_{k1N} \\ \overline{W}_{k21} & \overline{W}_{k22} & \cdots & \overline{W}_{k2N} \\ \vdots & \vdots & \ddots & \vdots \\ \overline{W}_{kM1} & \overline{W}_{kM2} & \vdots & \overline{W}_{kMN} \end{bmatrix},$$

$$\overline{\mathbf{W}}_{\mathbf{F}} = \begin{bmatrix} \overline{W}_{F11} & \overline{W}_{F12} & \cdots & \overline{W}_{F1N} \\ \overline{W}_{F21} & \overline{W}_{F22} & \cdots & \overline{W}_{F2N} \\ \vdots & \vdots & \ddots & \vdots \\ \overline{W}_{FM1} & \overline{W}_{FM2} & \vdots & \overline{W}_{FMN} \end{bmatrix},$$

$$\overline{\mathbf{W}}_{\mathbf{NL}} = \begin{bmatrix} \overline{W}_{NL11} & \overline{W}_{NL12} & \cdots & \overline{W}_{NL1N} \\ \overline{W}_{NL21} & \overline{W}_{NL22} & \cdots & \overline{W}_{NL2N} \\ \vdots & \vdots & \ddots & \vdots \\ \overline{W}_{NLM1} & \overline{W}_{NLM2} & \vdots & \overline{W}_{NLMN} \end{bmatrix}.$$

Either (5.25) or (5.27) can be used to model the system depending on whether the information of interest is the modal time response or the tip displacement time response.

## 5.4 Model Validation

Following the derivation of the mathematical model, it is necessary to demonstrate its validity by comparison of simulations with experimental data. In Chapter 4, the macro scale setup was compared against micro scale results, which demonstrated that they are qualitatively similar. It is therefore reasonable to validate the mathematical model against macro scale experimental results only. Macro scale validation is done to take advantage of the ease of changing array coupling and cantilever frequency properties so that a wide range of parameters can be tested. Validation will be done for two cases; far field (without tip forces) to demonstrate the ability to capture mode shape distributions when cantilever frequency properties and coupling strength are varied; and near field (with tip forces) to demonstrate the ability to capture array eigenmode changes and relate them to

output amplitude, phase and resonant frequency. All mathematical simulations in this thesis are conducted using MathWorks MATLAB® software. The Matlab® code used to form the equations of motion can be viewed in Appendix A. In most cases, numerical simulations were conducted using nonlinear Runge-Kutta based solvers, most notably the well know ode45 function. In addition to standard MATLAB® functions, the Computational Continuation Core (COCO) software framework is used to perform continuation simulations using the mathematical model. The COCO software framework contains functions designed to perform numerical continuation with user defined equations and was developed by Dankowicz and Schilder [100]. COCO was used predominantly to map the periodic orbits of the equation of motion as tip-sample separation and coupling strength were varied.

### 5.4.1 Far Field

There are two far field phenomena that should be adequately captured by the mathematical model, these are the spatial mode shape distributions within the array and the frequency response of the individual cantilevers. Knowledge of the array modes are necessary to understand the relative displacement and phase shifts between beams and link them back to the material properties and physical dimensions of the system. In particular, it is important to know when the array is in a synchronised state, such that cantilever displacement is heavily dependent on its neighbours, or when it is in an unsynchronised, state such that cantilever response is largely independent. Frequency response is useful as this can be easily compared to experimental data.

Initially, the spatial array modes were simulated for three different coupling levels, which are defined in Section 4.4. The spatial mode shapes were calculated using (5.20) and all relevant definitions. The simulated modal shapes for the three coupling regions of a five beam array are depicted in Figure 5.4. The cantilevers were of equal dimensions but with varying tip masses. The dimensions of the five cantilevers and tip masses are equivalent to the arrays used with the first macro test rig for comparison against the results presented in Section 4.4, and the relevant dimensions are provided in Table 4.2.

It can be seen from Figure 5.4 that the model is able to capture the transition from unsynchronised cantilever modes to synchronised array modes when the amount of shared base material is changed and when each cantilever has a different uncoupled resonant frequency. With strong coupling, the first mode approaches a state where the cantilevers are perfectly in-

Table 5.1: Normalised modal frequencies of a five beam array. Frequencies are normalised by the first mode.

| | **Weak Coupling** | **Transition Coupling** | **Strong Coupling** |
|---|---|---|---|
| **Mode 1** | 1.000 | 1.000 | 1.000 |
| **Mode 2** | 1.037 | 1.039 | 1.040 |
| **Mode 3** | 1.056 | 1.060 | 1.109 |
| **Mode 4** | 1.072 | 1.079 | 1.154 |
| **Mode 5** | 1.085 | 1.083 | 1.182 |

phase (exactly 0° phase difference), whilst the fifth mode approaches a state where the cantilevers are perfectly out-of-phase (exactly 180° phase difference). These are the ideal mode shapes expected for identical, perfectly synchronised coupled oscillators [101]. The differences in tip mass, and hence uncoupled resonant frequency, account for the phase shifts away from the idealised mode shapes.

Simulated impulse responses were used to test the ability of the model to capture the frequency response of a coupled array. The simulations were performed such that they can be directly compared to the impulse response experiments presented in Section 4.4 (Figures 4.8, 4.9 and 4.10) using the same cantilever parameters. In addition, the simulations were performed to determine which shared base lengths best demonstrate weak, transition and strong coupling in the context of the mathematical model. The simulations were performed using the MATLAB® ode45 nonlinear solver. The impulse was generated by giving each cantilever an initial nondimensionalised displacement of 1 unit. The amplitude and phase response for the three coupling levels can be seen in Figures 5.5, 5.6 and 5.7.

It is shown that there is a very good qualitative agreement between the experimentally obtained impulse responses in Section 4.4 and the numerically obtained impulse responses of Figures 5.5, 5.6 and 5.7. The weak, transition and coupling regions are clearly visible from both results, indicating that the mathematical model is a good representation of the macro scale cantilever array. There is a good agreement between the location of the three coupling regions with regards to coupling strength for the experimental and numerical results. The shared base lengths of 5 mm for weak coupling, 10 mm for transition coupling and 15 mm for strong coupling will be used as reference points for the remainder of the thesis.

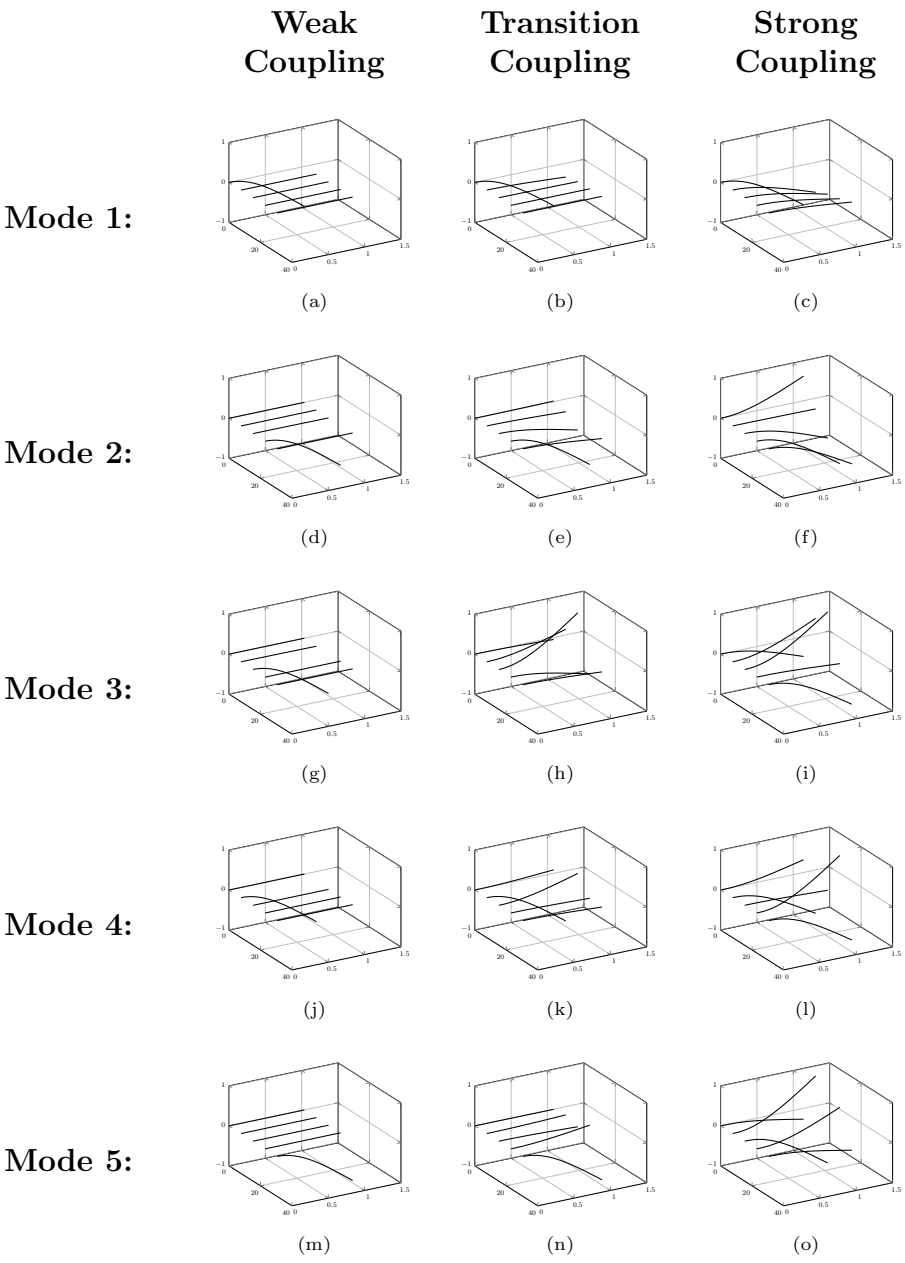


Figure 5.4: Simulated modal shapes of a 5 beam array for both weak coupling (5 mm shared base), transition coupling (10 mm shared base) and strong coupling (15 mm shared base).

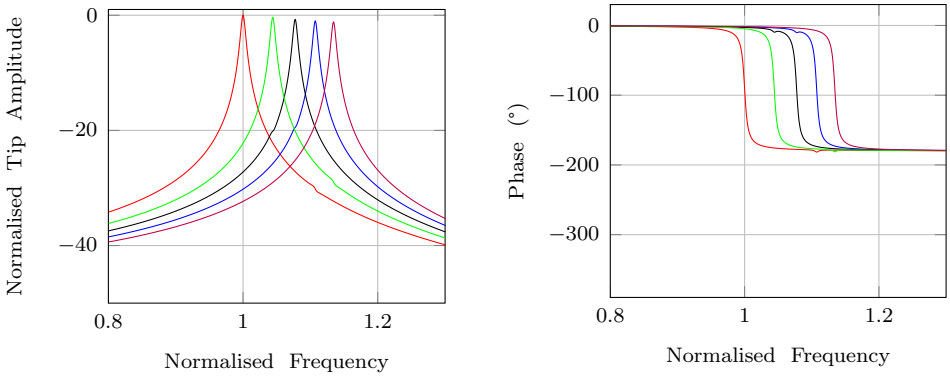


(a) Amplitude Response.

(b) Phase Response.

Figure 5.5: Simulated impulse responses of a five beam array with weak coupling (5 mm shared base material). Red - Beam 1, Blue - Beam 2, Black - Beam 3, Green - Beam 4, Purple - Beam 5.

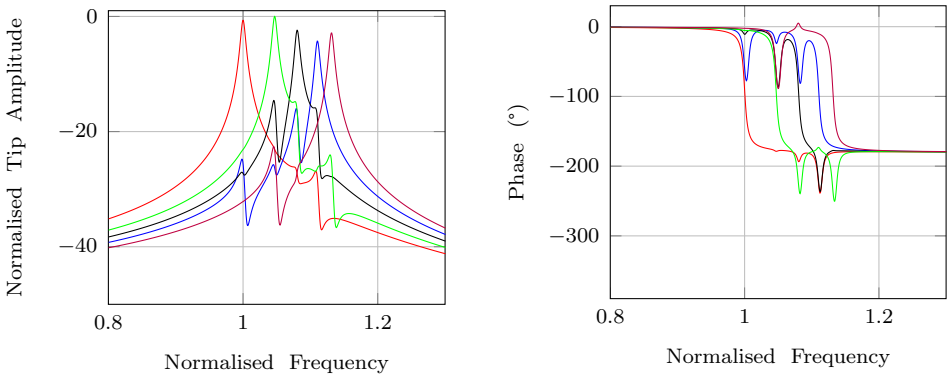


(a) Amplitude Response.

(b) Phase Response.

Figure 5.6: Simulated impulse responses of a five beam array with transition coupling (10 mm shared base material). Red - Beam 1, Blue - Beam 2, Black - Beam 3, Green - Beam 4, Purple - Beam 5.

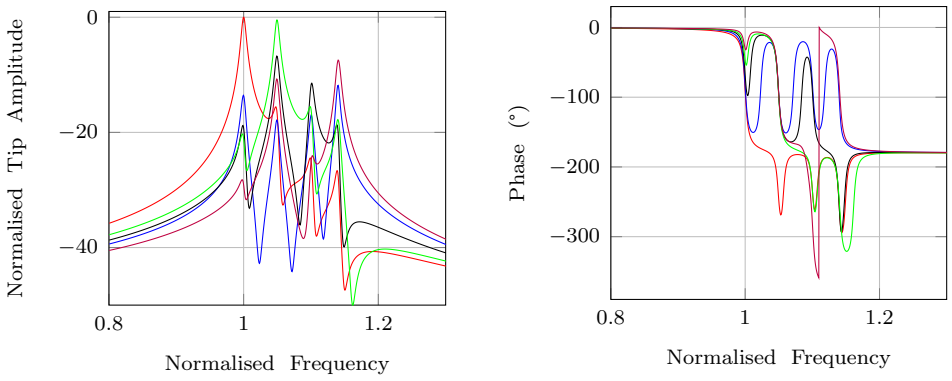


(a) Amplitude Response.

(b) Phase Response.

Figure 5.7: Simulated impulse responses of a five beam array with strong coupling (15 mm shared base material). Red - Beam 1, Blue - Beam 2, Black - Beam 3, Green - Beam 4, Purple - Beam 5.

### 5.4.2 Nearest Neighbour Coupling Validation

A series of simulations were conducted to demonstrate the validity of the nearest neighbour coupling assumption. The model was reformulated with additional coupling terms by re-writing (5.14) in the following form.

$$\mathbf{A}^* = \begin{bmatrix} \bar{\mathbf{A}}_\mathbf{1} & \bar{\mathbf{G}}_\mathbf{12} & \bar{\mathbf{G}}_\mathbf{13} & \cdots & \bar{\mathbf{G}}_\mathbf{1N} \\ \bar{\mathbf{O}}_\mathbf{8} & \bar{\mathbf{A}}_\mathbf{2} & \bar{\mathbf{G}}_\mathbf{23} & \cdots & \bar{\mathbf{G}}_\mathbf{2N} \\ \bar{\mathbf{O}}_\mathbf{8} & \bar{\mathbf{O}}_\mathbf{8} & \bar{\mathbf{A}}_\mathbf{3} & \cdots & \bar{\mathbf{G}}_\mathbf{3N} \\ \vdots & \vdots & \vdots & \ddots & \vdots \\ \bar{\mathbf{O}}_\mathbf{8} & \bar{\mathbf{O}}_\mathbf{8} & \bar{\mathbf{O}}_\mathbf{8} & \cdots & \bar{\mathbf{A}}_\mathbf{M} \end{bmatrix}, \tag{5.28}$$

$$\bar{\mathbf{G}}_\mathbf{mn} = \begin{bmatrix} \bar{\mathbf{O}}_\mathbf{4} & \bar{\mathbf{O}}_\mathbf{4} \\ \bar{\mathbf{O}}_\mathbf{4} & \hat{\mathbf{G}}_\mathbf{mn} \end{bmatrix}, \tag{5.29}$$

$$\hat{\mathbf{G}}_\mathbf{mn} = \begin{bmatrix} 0 & 1 & 0 & 0 \\ 0 & 0 & 1 & 0 \\ 0 & 0 & 0 & 1 \\ \dfrac{\hat{k}_{c_{n-m}}}{\mu_m} & 0 & 0 & 0 \end{bmatrix}. \tag{5.30}$$

The value of $\hat{k}_{c_{n-m}}$ is calculated again from (5.1) and using the same nondimensionalising. In each case, the value of $L$ in (5.1) is the distance between the closest edges of cantilevers to which the coupling term applies. (5.28), (5.29) and (5.30) are substituted in place of (5.14), (5.17) and (5.19) and the same derivation is followed.

The model with additional coupling terms is used to simulate the modal frequencies of an array of 5 identical cantilevers with strong coupling (15 mm shared base) using the dimensions given in Table 4.2. The simulations are performed with nearest neighbour coupling and up to the case of all beams coupled to each other. The simulated modal frequencies are presented in Table 5.2.

The results show that relatively insignificant changes in the nondimensional modal frequencies occur due to the addition of extra coupling terms. This demonstrates the validity of the nearest neighbour coupling assumption, which is used for the remainder of this thesis. The maximum percentage change in modal frequency due to the addition of extra coupling terms if 0.14 % (mode 3 nondimensional frequency). The main reason for the lack of influence of the additional coupling terms is that the coupling

Table 5.2: Normalised modal frequencies of a five beam array with different coupling assumptions

| | **Nearest Neighbour** | **2nd-Nearest Neighbour** | **3rd-Nearest Neighbour** | **4th-Nearest Neighbour** |
|---|---|---|---|---|
| **Mode 1** | 1.0000 | 1.0000 | 1.0000 | 1.0000 |
| **Mode 2** | 1.0400 | 1.0406 | 1.0407 | 1.0408 |
| **Mode 3** | 1.1088 | 1.1103 | 1.1104 | 1.1103 |
| **Mode 4** | 1.1544 | 1.1548 | 1.1548 | 1.1547 |
| **Mode 5** | 1.1817 | 1.1816 | 1.1815 | 1.1815 |

stiffness drops significantly for cantilevers that are not direct neighbours. This is because of the coupling stiffness term is inversely proportional to the cantilever separation $L$ from (5.1). $L$ remains small for direct neighbours in a closely spaced array as it is equal to separation distance, but increases significantly for non-neighbouring cantilevers, as $L$ will include at least one cantilever width. For the TUI arrays, cantilever width is significantly greater than the separation distance. It is possible that for arrays were the separation distance between cantilevers and the cantilever width are roughly equal, additional coupling terms will have a more significant impact on simulated modal response.

### 5.4.3 Near Field

The mathematical model has been demonstrated to perform well for arrays with different coupling strength and for cantilevers with different uncoupled frequency responses. It is necessary to test the performance of the mathematical modelling when nonlinear tip interaction forces are included. Initially, simulated frequency sweeps were performed and compared to equivalent experimental data obtained using the macro scale test rig. Comparison between experimental data and simulated results is necessary for model validation.

To perform both the simulations and the experiments, a three beam array was utilised so as to capture multiple array modes whilst keeping the complexity of the array at a minimum. The array was coupled using 15 mm of shared base material and a gap width of 10 mm to create a strongly coupled response. Strong coupling was used to ensure multiple array modes could be observed in the response. A tip mass of 0.35 g was attached to all

three cantilever tips, (the tip magnet). Beam 2 only was actuated with an input voltage of 0.4 V, which corresponded to a maximum far field amplitude of approximately 1 mm. Actuating beam 2 allowed the first and third array modes to be observed and tracked as tip forces were applied. It should be noted that the second array mode would not show in the response at far field as beam 2 lies on a nodal line at the second mode due to the symmetry of the array. In addition to actuation, tip forces were applied to the tip of beam 2 only at controlled separation distances. The frequency response of both simulated and experimental data were measured and compared, specifically, the location of the modal peaks in the frequency domain were tracked as the tip force gradient was altered. The results are presented in Figure 5.8.

The results in Figure 5.8, demonstrates a reasonable match between the experimental data and the model simulations. Specifically, the qualitative match of the location of the modal frequencies is good as well as the relative change in modal amplitudes. At small separation distances (Figures 5.8g and 5.8h in particular), the level of agreement between experiment and simulation is significantly reduced. It is likely that the reason for the lack of agreement is due to the discrepancy between the true force gradient and the modelled force gradient at small separation distances. This conclusion can be confirmed from examination of Figure 4.12 in Section 4.4. Close to the pull-in instability point, the empirically fitted magnet force function is a less good approximation of the measured data points then at larger separation distances. In addition, the steep gradient of the force curve close to the instability point means small discrepancies between true and measured tip-sample separation results in a large discrepancy in applied tip force and hence a significant shift in modal frequency and shape. These two sources of error are the likely reasons for the observed discrepancies in the frequency responses. A final point to make is that a distinct softening behaviour is observed in the simulated response in Figures 5.8g and 5.8h. It should be noted that the experimentally obtained response in Figure 5.8h also demonstrates a slight softening behaviour, suggesting that qualitative shape of the simulated response is representative of the true system, and not merely an artefact of the model. The quantitative discrepancy is likely caused by the same sources of error already discussed. It was not possible to accurately measure the sweep response on the macro scale at smaller tip-sample separations without going past the pull-in instability.

The final feature of the model that will be presented is its ability to capture changes in eigenmodes, in terms of both amplitude, frequency and mode shape, to changes in tip sample forces. Simulations only will be performed, as the model has already been validated against experimental data

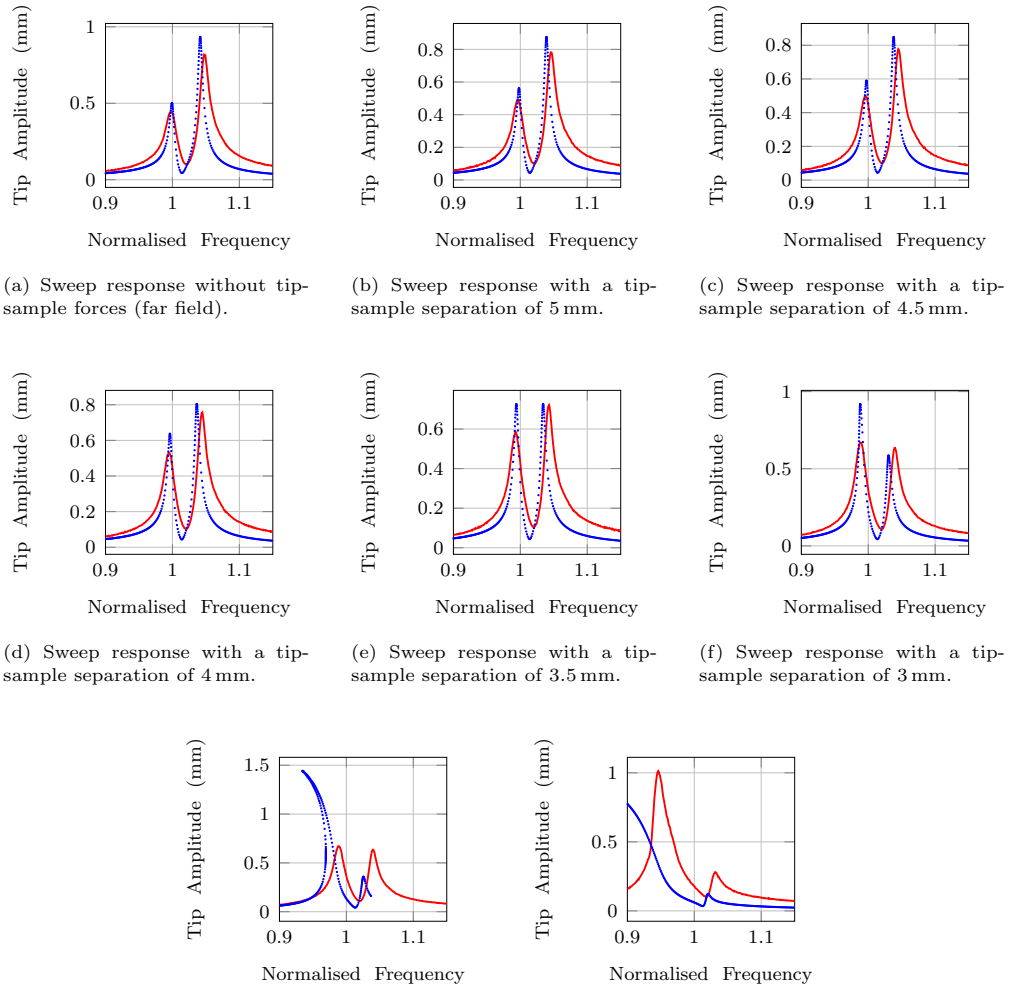


(a) Sweep response without tip-sample forces (far field).

(b) Sweep response with a tip-sample separation of 5 mm.

(c) Sweep response with a tip-sample separation of 4.5 mm.

(d) Sweep response with a tip-sample separation of 4 mm.

(e) Sweep response with a tip-sample separation of 3.5 mm.

(f) Sweep response with a tip-sample separation of 3 mm.

(g) Sweep response with a tip-sample separation of 2.5 mm.

(h) Sweep response with a tip-sample separation of 2 mm.

Figure 5.8: Simulated sweep response (blue) in comparison to equivalent experimental data on the macro scale (red) of beam 2 only in a strongly coupled three beam array. External actuation and tip forces are applied to beam 2 only. The shift of both modes one and three can be clearly seen. The frequency sweep was from low to high.

with tip forces present in Figure 5.8 and the accompanying discussion. A 3 beam array was again used for the simulations to demonstrate the model's ability to track multiple eigenmodes in a complex, coupled system and to demonstrate the creation/destruction of models as tip forces are varied. The beams are again assumed to be identical so that a simple, predictable pattern of eigenmodes is produced when tip-forces are negligible. Strong coupling (15 mm of shared base material) is used so that multiple spatial

mode shapes could be captured. The dimensions of the cantilevers are based on the second macro scale test rig cantilevers, and each beam has a tip mass of 0.35 g, equivalent to the tip magnets used for experimentation. Beam 2 in the array is actuated only, and in addition, the tip-sample distance ($d_0$) is varied for beam 3 only. The eigenmodes are found at discrete points of separation distance by locating the amplitude peaks that appear in the frequency response of the actuated beam (beam 2). The change in system eigenmodes for the strongly coupled 3 beam array are presented in Figure 5.9.

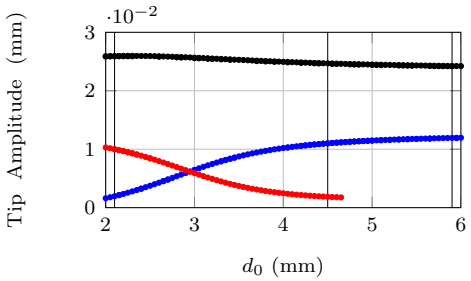


(a) Eigenmode amplitude changes. Blue - beam 2 amplitude at mode 1. Red - beam 2 amplitude at mode 2. Black - beam 2 amplitude at mode 3.

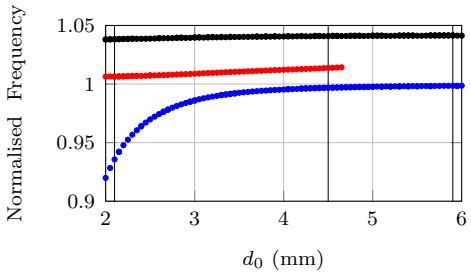


(b) Eigenmode frequency changes with weak coupling. Blue - mode 1 frequency. Red - mode 2 frequency. Black - mode 3 frequency.

Figure 5.9: Resonant frequency changes in a three beam array due to the combined influence of mechanical coupling and nonlinear tip forces. Simulations were performed with beam 2 only actuated and tip forces applied to beam 3 only. The vertical lines indicate the points where mode shapes are given in Figure 5.10.

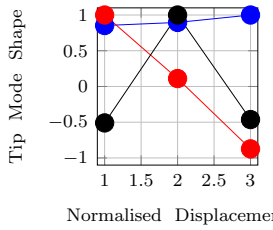


(a) Mode shapes at 5.9mm separation.

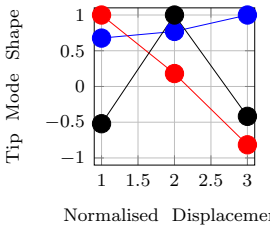


(b) Mode shapes at 4.5mm separation.

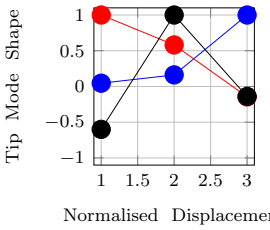


(c) Mode shapes at 2.1mm separation.

Figure 5.10: Simulated mode shapes of the three beam simulation from Figure 5.9 at three distinct separation distances. The transition from the expected array modes of a three beam system to individual cantilever modes is demonstrated.

It can be seen in Figure 5.9 that at large separation distances, the response approaches that of the far field response (negligible tip forces). In

particular, at a separation distance of 5.9 mm, two distinct modal peaks appear, which are the first and third mode, which can be distinguished by their frequencies (Figure 5.9b). As mentioned, it is the middle beam that is excited and measured, which lies on a nodal line at the second modes when the beams are identical due to the symmetry of the array. This is apparent from 5.10a, which depicts the array mode shapes when separation distance is relatively large. As the tip sample distance is reduced (force gradient increased), an additional modal peak appears in the response at a separation distance of roughly 4.6 mm. At this distance, the frequency properties of beam 3 have been altered sufficiently due to force interactions that the array looses its symmetrical properties. At this point, beam 2 no longer lies close to a nodal line at mode 2, as seen in Figure 5.10b, and it appears as a peak in the frequency response. As the separation distance is reduced, the frequency properties of beam 3 are further altered and the resonant frequency of mode 1 is reduced. At a separation distance of 2.1 mm, the modes have transitioned towards individual beam modes, specifically with mode 1 localising at beam 3 (Figure 5.10c). This is the expected result as the resonant frequencies of the cantilevers are moved apart and synchronisation is lost. It is therefore demonstrated that the model can be used to track qualitative changes in eigenmodes due to the influence of tip sample forces, and that the resulting eigenmodes agree with expected outcomes.

## 5.5 Conclusion

In this chapter, the mathematical model of a coupled array of AFM cantilevers has been formulated. Three key features are incorporated into the model; mechanical coupling, which is the results of the cantilevers being mounted on a common base; an individual actuation term applied to each beam; and a nonlinear force applied to the tip of each beam to simulate the interaction between cantilever tip and sample that occurs during AFM operation. In addition, the model was formulated with variable mass and stiffness properties for each cantilever, rather than assuming identical beams, to capture the properties of a true fabricated array. A mathematical model of an AFM array that includes mechanical base coupling, individual tip interaction forces and variable mass/stiffness properties in each beam as not be formulated previously in the literature. Validation experiments and simulations have been conducted to compare the simulated response of the model to the macro scale test rig. The results have demonstrated that the model is able to capture the three regions of coupling (weak, transition and strong) with a good qualitative match to experiment. It has also been demonstrated that the model can capture changes in array eigenmodes due

to an applied tip-sample forces, and that this is also a reasonable qualitative match to experimental data. As the model has been sufficiently validated, it can be used to examine the underlying causes of the observed micro scale results, and draw conclusions as to why reliable, precise parallel imaging is not currently achievable with the fabricated TUI arrays.

This chapter has presented a novel mathematical model, and validated it against experimental data. A model is a necessary tool for understanding dynamic response and will be used in conjunction with the macro scale test rig to meet the research outcomes of this thesis and draw conclusions about the response of micro AFM arrays. Simulations pertaining to the core research outcomes of this thesis will be presented in Chapters 6 and 7.

CHAPTER 6

# Arrays for Parallel Imaging

## 6.1 Introduction

So far in this thesis, the dynamic response of AFM arrays fabricated by the TUI team have been analysed. Experimental investigations both with and without tip sample interactions have been conducted to demonstrate how individual cantilever response is altered due to mechanical coupling, and to identify the response phenomena that could adversely affect imaging reliability and precision (see Chapter 3). In addition, the tools necessary to analyse the underlying causes of the identified coupled phenomena have been established, in the form of an equivalent macro scale experiment (Chapter 4) and a mathematical model for simulation (Chapter 5). The main focus of this chapter is to answer the open questions regarding the link between system response and parameter space that were raised in Chapter 3, specifically what is the cause of the observed discontinuous amplitude jumps and how can a monotonic trend in output response be assured in the presence of coupling. The established tools are utilised to determine the likely causes of the observed response on the micro scale and to offer possible solutions for the implementation of the technology.

To begin the analysis, the approach curves obtained using the latest TUI arrays that were presented in Section 3.5 are replicated using the macro scale test rig. The purpose of the replication is to gain an understanding as to what parameter space resulted in the micro scale response through visual observations. A range of parameters are tested using the macro scale test rig, providing insight as to the probable causes of the discontinuous jumps observed on the micro scale. Following experimental replication of the approach curves, numerical simulations are conducted with the model to validate and further analyse the conclusions drawn regarding the link between parameter space and observed response. The model is capable of capturing both stable and unstable solution branches, and parameter space can be exactly controlled. In addition to the analysis of the approach

curves, the outcome regarding the relative importance of frequency gap and separation distance between beams (Section 3.4) is investigated and validated through simulation, which was not possible with the pre-fabricated micro arrays. The influence of the amount of shared base material is also discussed. Finally, the outcomes of this chapter are summarised in the context of the implications to array technology, specifically the commercial implementation of arrays for parallel imaging.

## 6.2 Replication of Approach Curves

To further investigate the approach curves of the micro arrays with the macro scale experiment, a two beam array is used on the macro scale. The purpose of using two beams is to isolate the coupling between a single, excited cantilever and a single, passive cantilever so that only one energy transfer path is available through the structure. Providing a single energy transfer path reduces the complexity of comparing response in different parameter space. The fundamental physics governing the coupled response is the same for an array of any size. As such, it should be possible to study the response of a two beam array and extrapolate the conclusions to larger arrays. The same basic experimental method for generating approach curves on the micro scale was applied to the macro test rig. Beam 1 was actuated at its own far field resonant frequency with a constant amplitude of 0.7 V, whilst the magnets were brought slowly towards the tips of both cantilevers simultaneously such that cantilever response remained quasi-static. Varying tip masses were applied to the cantilevers to produce different resonant frequencies, but in all cases the resonant frequency of beam 1 was kept below that of beam 2. The tip-sample separation of the passive beam was deliberately kept 0.3 mm smaller than the tip-sample separation of the active beam. The purpose of this discrepancy was to ensure that the instability points of each beam were reached at different points during the experimental run, the reason for which will become apparent in the discussion of the experimental results. The raw time signals of both beams are recorded using the strain gauge sensors and post processing was used to determine the amplitude, static deflection and tip-sample separation. The separation distance $d_0$ is extrapolated from the movement commands sent to the stepper motors. A reference point of $d_0 = 0$ was found by moving the stepper motor to a position at which the cantilever tip was in contact with the surface magnet and the measured tip deflection was zero.

By varying the resonant frequency of the individual cantilevers and the amount of shared base material, the response of the system could be determined for a range of parameter values. The amplitude approach curves for

four slightly varying beams can be viewed in Figure 6.1 and the corresponding deflection curves can be viewed in Figure 6.2. The far field resonant frequencies of the cantilevers used for each experiment are between 40 and 60 Hz, and exact values are provided in the figures. These parameter sets were chosen to clearly demonstrate the effects of both a large and small resonant frequency gap and both strong and weak coupling on the amplitude approach curves.

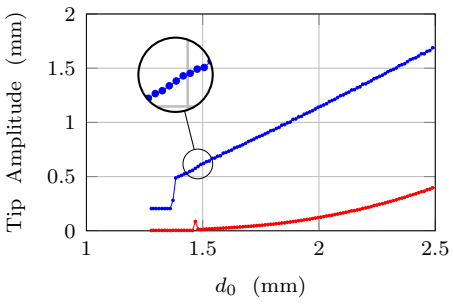


(a) Frequencies close together (47.50 Hz and 48.51 Hz). 6 mm of coupling material.

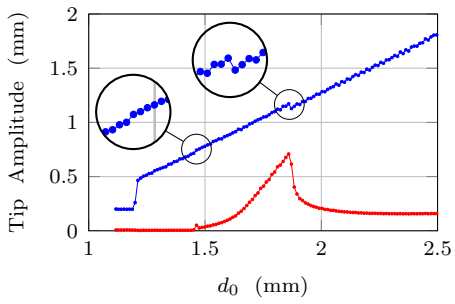


(b) Frequencies far apart (41.85 Hz and 48.56 Hz). 6 mm of coupling material.

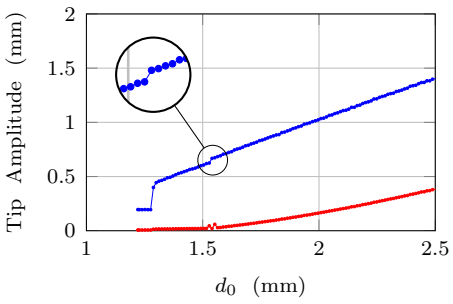


(c) Frequencies close together (47.50 Hz and 48.51 Hz). 12 mm of coupling material.

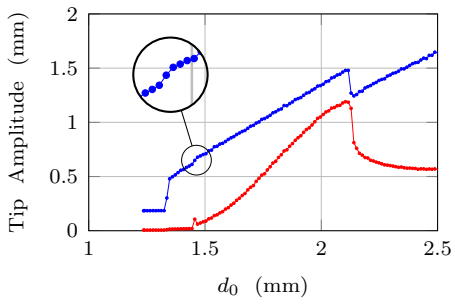


(d) Frequencies far apart (41.85 Hz and 48.56 Hz). 12 mm of coupling material.

Figure 6.1: Macro experimental amplitude approach curves of a macro scale two beam array. Only beam 1 is actuated in all cases. Blue - Beam 1, Red - Beam 2.

A comparison of Figures 3.10 and 6.1 demonstrates that the macro scale experiments produced both upward and downward jumps in amplitude, similar to that observed on the micro scale. Zoomed sections are included to make the small jumps easier to see. The similarity in the approach curves of both systems suggests similar underlying physics are responsible for the observed curve shape, and that the macro scale results can be used to draw conclusions about the micro scale dynamics. It can be seen through comparison between Figures 6.1 and 6.2 that the location of jumps in amplitude correspond directly to jumps in static deflection with regards to $d_0$ values, and vice versa. The static deflection of the cantilever directly influences the

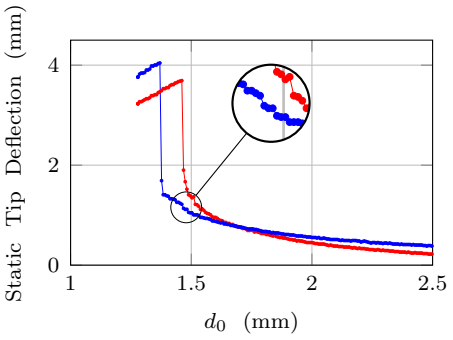


(a) Frequencies close together (47.50 Hz and 48.51 Hz). 6 mm of coupled material.

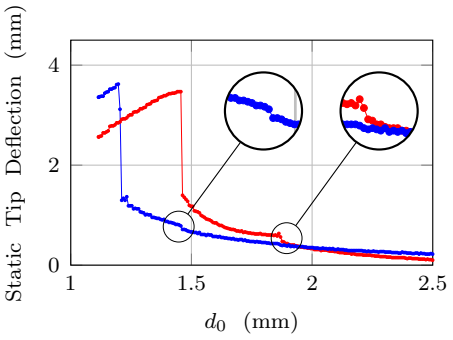


(b) Frequencies far apart (41.85 Hz and 48.56 Hz). 6 mm of coupled material.

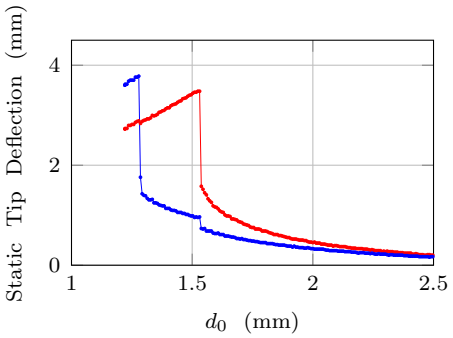


(c) Frequencies close together (47.50 Hz and 48.51 Hz). 12 mm of coupled material.

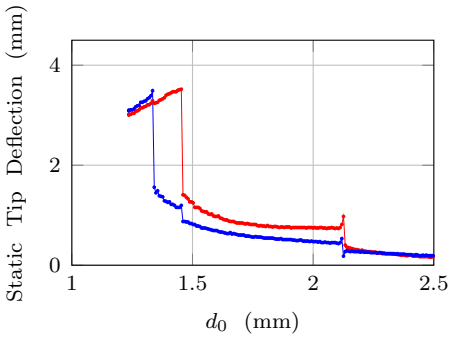


(d) Frequencies far apart (41.85 Hz and 48.56 Hz). 12 mm of coupled material.

Figure 6.2: Macro experimental deflection approach curves of a macro scale two beam array. Only beam 1 is actuated in all cases. Blue - Beam 1, Red - Beam 2.

force gradient applied to the tip during each oscillation because of the direct correlation between deflection and tip-sample separation. It is expected that an increased deflection towards the sample would lower the resonant frequency of the system due to the increased force gradient, which would appear as a reduction in output amplitude for a constant excitation signal.

It is observed that when one beam passes the instability point and jumps into contact, the neighbouring beam is also deflected towards the surface due to a transfer of strain through the base structure, resulting in a decrease in the resonant frequency and hence an observed drop in amplitude (jumps at $d_0 \approx 1.5$ mm). Comparing the jumps in relation to parameter space, it can be seen that this phenomenon is strongly influenced by the base coupling strength between the beams, but is not affected by the size of the resonant frequency gap. This is expected as deflection is a zero-frequency phenomenon. It is likely that the same phenomenon is the cause of the

downward jump in the beam 3 approach curve of Figure 3.10 in Section 3.5, which coincides with the point of jump-to-contact of beam 4. On both scales, not all beams passed the instability point at the same moment resulting in the sudden increase in deflection of the neighbouring beam without resulting in contact. On the micro scale, this was due to alignment errors between the array and the surface as well as other uncontrollable sources of error, including non-flat features on the silicon sample, tip height discrepancies and wear, and the possible presence of a fluid layer and other contaminants. On the macro scale, the differences in the location of instability point are due predominantly to the aforementioned discrepancy in tip-sample separation between the actuated and passive beams that was deliberately created. The reason for the deliberate discrepancy is to measure the effect on response when one beam passes the instability point, and to confirm that strain transfer through the shared base at the point of jump-to-contact is a likely cause of the observed amplitude jump phenomenon on the micro scale.

Figure 6.1b shows a sudden increase in amplitude at a height of $d_0 \approx 1.8\,\text{mm}$ for the case of beam 2 having a higher far field resonant frequency than that of beam 1, which a corresponding increase is deflection (The right-hand zoomed regions in Figures 6.1b and 6.2b). Due to the influence of the nonlinear force applied by the magnet surface, the first resonant frequency of beam 2 is reduced and approaches that of the excitation signal applied to beam 1. As resonance is approached, the energy transfer from the actuator through the actuated beam to the passive beam increases. The resulting increase in total system energy leads to an increase in output amplitude, which is accompanied by an increased static deflection of both beams towards the surface as the tips penetrate deeper into the force potential (Figure 6.2d). The point at which this phenomenon occurs is termed the frequency cross-over point, which is defined as a point in parameter space at which the resonant frequency of one cantilever in the array approaches and crosses the resonant frequency of another beam, or the frequency of the excitation signal. The phenomenon is equivalent to internal resonance between the multiple degrees of freedom of the system. The most probable reason that the same phenomenon is not observed in Figures 6.1a or 6.1c is that the measurement region is already below the frequency cross-over point. The frequency cross-over point is heavily dependent on the frequency gap of the beams, and will only be observed for specific ratios between the nominal height above the sample of the two beams ($d_0$). The presence of the discontinuous jump suggests nonlinear behaviour and the existence of multiple stable and unstable solution branches at this point in parameter space.

## 6.3 Simulated Approach Curves

### 6.3.1 Two Beam Numeric Simulations

The results of the experimental investigation are verified by simulating the response of a two beam array using the modal form of the mathematical model (type (5.25) from Section 5.3). The two beam modal model takes the form of (6.1). The model was used to map the solution branches within the vicinity of the frequency cross-over point to find all periodic orbit solution branches, specifically for the cases where discontinuous jumps in amplitude were observed to occur. Periodic orbit solution branches were mapped using the COCO continuation solver [100] with $d_0$ as the control variable. The simulation was run so as to mimic the experimental methodology used to obtain the approach curves in Section 6.2. The tip masses applied to each beam were selected such that frequency cross-over would occur at a suitable separation distance of a few mm. Actuation was applied to beam 1 only at a constant amplitude and frequency. An equal separation value for $d_0$ was applied to the entire array. The cantilevers were sized to match those of the macro scale test rig. The relevant parameters of the simulation are given in Table 6.1 and the simulation results with different levels of coupling are presented in Figure 6.3.

$$\begin{aligned}
&\begin{bmatrix}\ddot{\Phi}_1\\ \ddot{\Phi}_2\end{bmatrix} + \begin{bmatrix}W_{c11} & 0\\ 0 & W_{c22}\end{bmatrix}\begin{bmatrix}\dot{\Phi}_1\\ \dot{\Phi}_2\end{bmatrix} + \begin{bmatrix}W_{k11} & 0\\ 0 & W_{k22}\end{bmatrix}\begin{bmatrix}\Phi_1\\ \Phi_2\end{bmatrix}\\
&\quad - \begin{bmatrix}W_{F11} & W_{F12}\\ W_{F21} & W_{F22}\end{bmatrix}\begin{bmatrix}\widehat{AC}_1\cos(\Omega\tau)\\ \widehat{AC}_2\cos(\Omega\tau)\end{bmatrix}\\
&\quad - \begin{bmatrix}W_{NL11} & W_{NL12}\\ W_{NL21} & W_{NL22}\end{bmatrix}\begin{bmatrix}\dfrac{\tau_m}{\left(\hat{d}_{01} - \overline{W}_{11}\Phi_1 - \overline{W}_{12}\Phi_2\right)^2}\\ \dfrac{\tau_m}{\left(\hat{d}_{02} - \overline{W}_{21}\Phi_1 - \overline{W}_{22}\Phi_2\right)^2}\end{bmatrix} = \begin{bmatrix}0\\0\end{bmatrix},
\end{aligned} \tag{6.1}$$

The simulations show that multiple solution branches are indeed formed within the vicinity of the frequency cross-over point for the case of strong coupling. The combined effect of nonlinear tip forces and mechanical coupling result in a pair of saddle node bifurcations joined by two fixed points, which creates a set of unstable periodic orbits near the point of frequency cross-over. Following the approach curves in Figure 6.3 in the direction of decreasing separation distance, it can be observed that transition at the fixed point from one solution branch to the other would result in discontinuous jumps from one stable solution branch to another, and that the jumps would be qualitatively similar to those observed in the experimentally obtained approach curves in Figures 6.1 and 6.2. This suggests it is

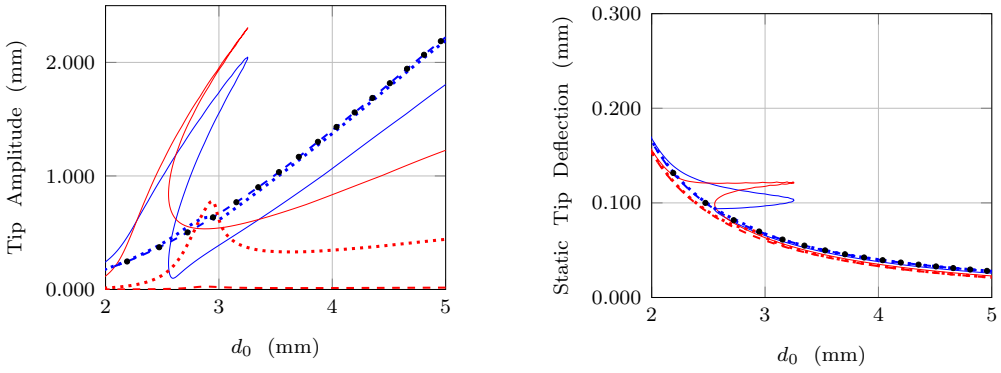


(a) Amplitude approach curves.

(b) Deflection approach curves.

Figure 6.3: Simulated approach curves of a 2 beam array (beam 1 - blue, beam 2 - red) in the vicinity of the frequency cross over point. The simulations are performed with strong coupling (15 mm, solid), transition coupling (10 mm, dotted) and weak coupling (5 mm, dashed). The black dots represent the location of the approach curve for an equivalent single beam.

a bifurcation event creating a pair of stable and unstable solution branches that is responsible for the discontinuities observed experimentally. Looking retrospectively at the experimental results obtained on the micro scale, the observed jump phenomena show a strong qualitative resemblance to the macro scale results, suggesting that the same underlying cause is responsible. For a similar causality for the dynamic amplitude jumps to be plausible, a frequency cross-over event is necessary. For the results in Figure 3.10 in Section 3.4, it can be seen that beam 3 has a larger far field resonant frequency than beam 2 of a few hundred Hz, which can plausibly lead to a frequency cross-over event. It is in the approach curves of these beams that upward discontinuous jumps in amplitude are observed (clearly resolved for beam 2 in the insert, less well resolved but still visible for beam 3), which is again qualitatively similar to the macro scale results. It logically follows that frequency cross-over between beams 2 and 3 is the cause for the observed discontinuities on the micro scale for the case of increasing amplitude. The implications of this outcome will be discussed in further detail in Section 6.7.

It is noted that the onset of bifurcation is highly dependent on the coupling level within the system. The approach curve for the weakly coupled case is nearly indistinguishable from the approach curve of an equivalent single beam system, also shown in Figure 6.3. To demonstrate the relationship between the onset of bifurcation, tip-sample separation and coupling strength, the evolution of the approach curves from weakly coupled

Table 6.1: Parameters used for the 2 beam approach curve simulations.

| Parameter | Value | |
|---|---|---|
| | Beam 1 | Beam 2 |
| Tip mass | 0.68 g | 0.35 g |
| Actuation Term ($AC_1$) | $1e^{-2}$ | 0 |
| Normalised Far Field Resonant Frequency | 1 | 1.025 |
| Shared Base (weak coupling) | 5 mm | |
| Shared Base (transition coupling) | 10 mm | |
| Shared Base (strong coupling) | 15 mm | |

to strongly coupled is analysed. The same cantilever dimensions and parameters (Table 6.1) are utilised for the simulations. The evolution of the amplitude approach curves are presented in Figure 6.4 and the evolution of the deflection approach curves are presented in Figure 6.5. The depictions in Figures 6.4 and 6.5 make clear the transition from a monotonic decrease in amplitude/increase in deflection to the creation of multiple solution branches. The observed shape of the surface plots suggest that a catastrophe bifurcation event [102] occurs at a critical coupling value, above which discontinuous jumps in the approach curves will occur.

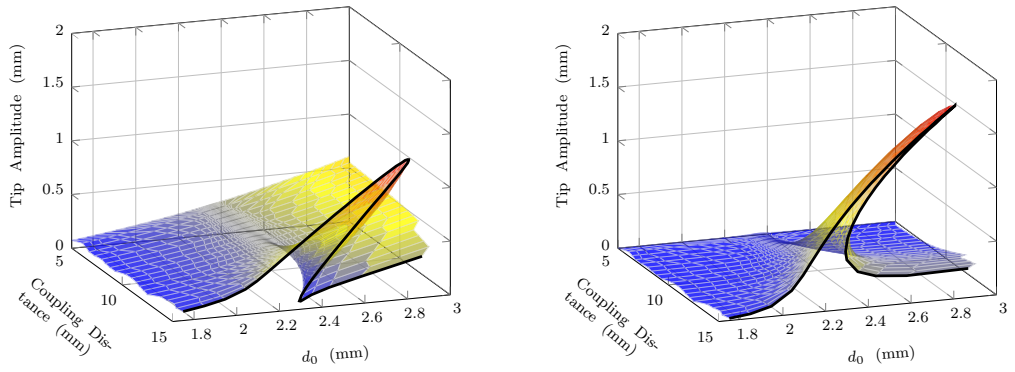


(a) Beam 1.

(b) Beam 2.

Figure 6.4: Simulated amplitude surface plot in a two beam array in relation to tip-sample separation and coupling strength.

The discussion in this section has so far been focused on the response

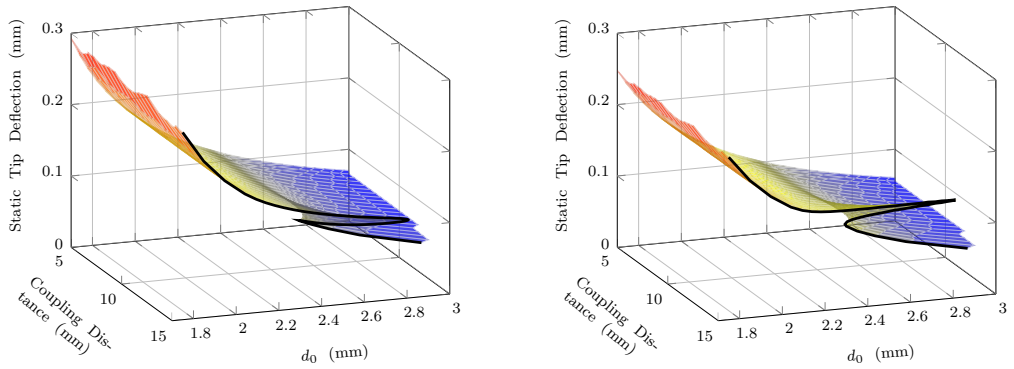


(a) Beam 1.

(b) Beam 2.

Figure 6.5: Simulated deflection surface plot in a two beam array in relation to tip-sample separation and coupling strength.

phenomena that occur at the frequency cross-over point. It is necessary to show the shape of the approach curves within a coupled array when frequency cross-over is not approached. To avoid frequency cross-over, simulations are performed with cantilevers that have a large frequency gap, which is achieved by applying a very large tip mass to beam 1 only, reducing its resonant frequency well below beam 2. Beam dimensions are again set to that of the second macro scale test rig, and the same parameters in Table 6.1 are used, except for the tip mass of beam 1, which is set to 6.95 g. The result is a normalised far field resonant frequency of 1.00 for beam 1 and of 1.43 for beam 2. The approach curves for this simulation are presented in Figure 6.6.

When frequency cross-over is avoided, monotonic amplitude decrease/ deflection increase is observed even for strong coupling. With a very large frequency gap, as is the case in Figure 6.6, the approach curve is very similar to that expected from an equivalent single beam system. The simulation demonstrates the importance of considering the relative frequency gap when operation the cantilevers within an array individually. The result demonstrates that the most significant unwanted dynamic phenomena can be avoided if the frequency cross-over point is avoided, regardless of the strength of the mechanical coupling. The implications of avoiding frequency cross-over will be further discussed in Section 6.7.

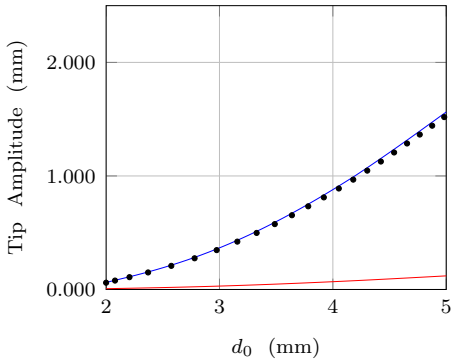


(a) Amplitude approach curves.

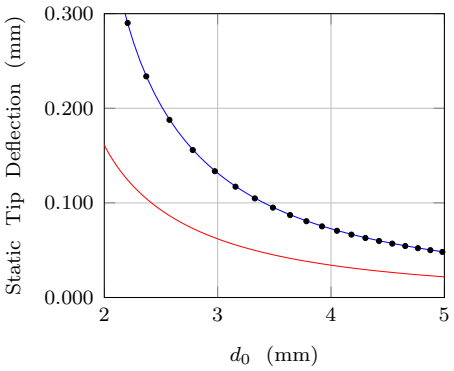


(b) Deflection approach curves.

Figure 6.6: Simulated approach curves of a strongly coupled (15 mm) 2 beam array (beam 1 - blue, beam 2 - red) with a large frequency gap between cantilevers. The black dots represent location of the approach curve on an equivalent single beam.

### 6.3.2 Multi-beam Numeric Simulations

So far the simulations have been limited to the analysis of a two beam array, where energy transfer is confined to a single path. It can be shown that multiple frequency cross-over points in an array larger than 2 beams can result in additional bifurcation points, which is demonstrated in Figure 6.7. The figure depicts the approach curves of a 5 beam array with beam 3 actuated only at its far field resonant frequency. Each beam has a tip mass selected so that multiple frequency cross-over events occur during the simulation. The relevant parameters of the simulation are given in Table 6.2. It can be seen that multiple inflection points as well as saddle node bifurcations are present in the approach curves of all 5 beams. The response is exceedingly complex, but demonstrates that the addition of multiple beams can influence approach curve shape, not just neighbouring beams. The result demonstrates that array design for parallel AFM imaging must factor in the entire system dynamics, particularly frequency cross-over points, as well as considering the response of each individual cantilever.

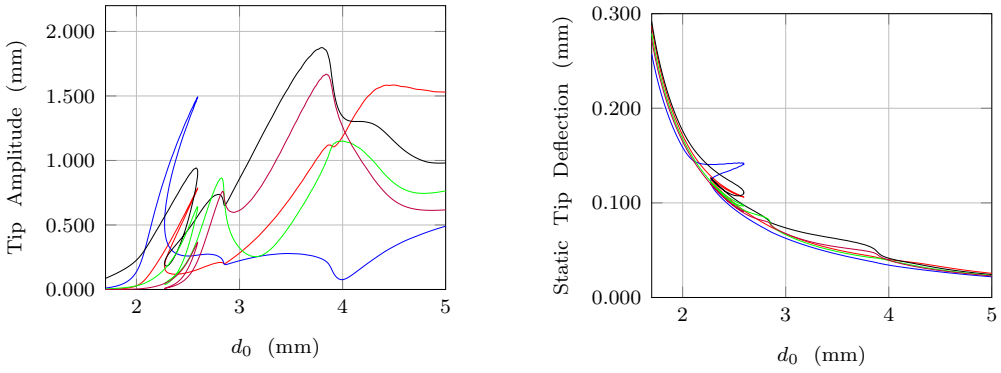


(a) Amplitude approach curves.

(b) Deflection approach curves.

Figure 6.7: Simulated approach curves of a strongly coupled (15 mm) 5 beam array. Significant deviations from a monotonic relationship between amplitude/deflection and tip-sample separation is apparent in the approach curves for all beams. Red - Beam 1, Blue - Beam 2, Black - Beam 3, Green - Beam 4, Purple - Beam 5.

Table 6.2: Parameters used for the 5 beam approach curve simulations.

| Parameter | Value | | | | |
|---|---|---|---|---|---|
| | Beam 1 | Beam 2 | Beam 3 | Beam 4 | Beam 5 |
| Tip mass | 0.91 g | 0.35 g | 1.01 g | 0.78 g | 0.58 g |
| Actuation ($AC_1$) | 0 | 0 | $1e^{-2}$ | 0 | 0 |
| Far Field Resonant Frequency | 1.015 | 1.140 | 1.000 | 1.062 | 1.027 |

## 6.4 Approach Curve Parameter Space

It has been demonstrated in this chapter how a combination of nonlinear tip forces and mechanical coupling can result in a saddle node bifurcation, which leads to undesirable nonlinear jumps in cantilever responses. Mathematical simulations have captured multiple solution branches that can form due to bifurcation events, and macro scale experiments have linked the observed discontinuities in the micro array approach curves to the simulation analysis. There remains an open requestion regarding the link between the micro scale results and the macro scale data/simulation results. In this chapter, the results presented have all shown discontinuous jumps due to frequency cross-over to occur only in the strong coupling region, however, it has been

previously concluded that the far field response of the TUI arrays depict weak or transition coupling. A link must be found between the two results to explain this observed discrepancy and relate it back to parameter space.

The influence of other model parameters with regards to the onset of bifurcation can be analysed, namely damping, excitation amplitude and order of the force gradient term. Using the same basic parameteric set in Table 6.1 and varying the damping, excitation and force gradient parameters, it can be demonstrated that a saddle node bifurcation will occur in the transition coupling region (10 mm shared base material) where it did not occur previously. Linking to the micro scale, it has been demonstrated previously that the measured level of damping is comparable to that of the macro scale test rig and is likely not a major factor. The input amplitude utilised when obtaining the micro scale approach curves was, however, relatively high (tens of µm compared to a typical AM-AFM amplitude range of a few µm down to tens of nm). In addition, the force gradient on the micro scale due to electrostatic attraction/repulsion is of a higher order than the magnetic force potential used to simulation tip-sample forces on the macro scale. It is likely that the relative values of these two parameters are the underlying reason for the presence of discontinuities in a different coupling region compared to the macro scale experiments/simulations.

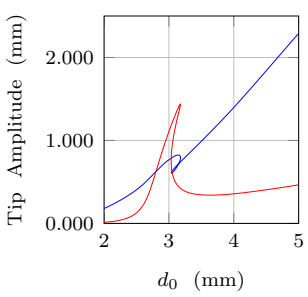


(a) Damping coefficient reduced from 0.007 to 0.0035. Excitation amplitude $AC_1$ of $1e^{-2}$, nonlinear force power $p_1$ of 2 and magnet coefficient $\tau_m$ of $-6.00e^{-5}$.

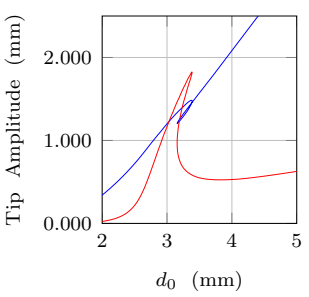


(b) Excitation amplitude $AC_1$ increased $1e^{-2}$ to $2e^{-2}$. Damping coefficient of 0.007, nonlinear force power $p_1$ of 2 and magnet coefficient $\tau_m$ of $-6.00e^{-5}$.

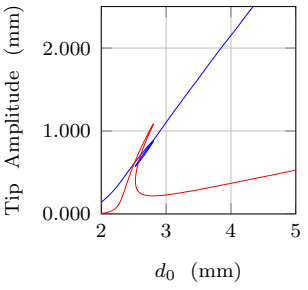


(c) Nonlinear force power $p_1$ increased from 2 to 6 and magnet coefficient $\tau_m$ reduced from $-6.00e^{-5}$ to $-6.00e^{-13}$. Damping coefficient of 0.007 and excitation amplitude $AC_1$ of $1e^{-2}$.

Figure 6.8: Simulation of multiple solution branches in the approach curves of a 2 beam array with transition coupling (10 mm shared base) with decreased damping, increased excitation amplitude and higher order nonlinear term. Blue - Beam 1, red - Beam 2.

The nonlinear force gradient is not a parameter that can be controlled, and is dependent on the tip material/geometry and the material of the sample surface. Both the input amplitude and damping can, however, be

user controlled (to an extent). In most applications, the amplitude of oscillation is tuned by the user performing the imaging process. A number of factors influence the selection of a suitable amplitude, including tip geometry, sample material properties and desired measurement information. Tuning of the excitation signal is a skill normally acquired through years of practice [5], and a wide range of amplitudes can be employed depending on the specific application [3]. It is therefore not a desirable solution to limit the range of excitation amplitudes available to the operator as a method of avoiding adverse nonlinear effects. Damping is another parameter of interest that can be shifted into a range that would prevent discontinuity at the frequency cross-over point. A simple method of adjusting system damping is known as active Q-control [103]. Q control utilised feedback control to alter the frequency spectrum of the cantilever system, effectively changing the damping coefficient. Q control is achieved by feeding the tip deflection signal through a 90° phase shifter and adding it to the user defined actuation signal. The system damping can be lowered to improve measurement sensitivity, or raised to reduce error caused by transient oscillations and to increase the achievable measurement speed whilst maintaining high precision. In applications where a fast response time is required, Q control could be used with the added advantage of preventing nonlinear discontinuities from arising in a situation where a frequency cross-over point could be approached. Another major factor when considering damping in AFM in the medium in which the sample is imaged. In a liquid environment, the damping is greatly increased, resulting in a drop in Q factor of at least an order of magnitude in comparison to operating in air. It is possible that when operating in a liquid environment, such as when imaging certain biological samples, the added damping would prevent bifurcation at the cross-over point, which would prevent response discontinuity from affecting system stability. This will be true provided that the impact of any added fluidic coupling is less than the influence of reduced damping on the approach curves.

## 6.5 Two Beam Perturbation Analysis

The influence of parameter space on the approach curves of a two beam array has been thoroughly tested through numerical simulations, and it has been demonstrated that excitation amplitude, damping and coupling strength can affect the onset of nonlinear response through a catastrophe bifurcation. So far, the link between the underlying physics (corresponding to the terms of the mathematical model) and the observed bifurcation events have not been identified. Perturbation analysis can be used to assess the underlying

reasons why the aforementioned parameters cause a bifurcation event, and how discontinuity can be predicted. In this section, a perturbation of the equation of motion of a two beam array system is conducted, using the direct displacement form of the model (type (5.27) from Section 5.3). The model for a two beam system takes on the following form

$$\begin{aligned}
&\begin{bmatrix}\ddot{X}_1\\ \ddot{X}_2\end{bmatrix} + \begin{bmatrix}\overline{W}_{c11} & \overline{W}_{c12}\\ \overline{W}_{c21} & \overline{W}_{c22}\end{bmatrix}\begin{bmatrix}\dot{X}_1\\ \dot{X}_2\end{bmatrix} + \begin{bmatrix}\overline{W}_{k11} & \overline{W}_{k12}\\ \overline{W}_{k21} & \overline{W}_{k22}\end{bmatrix}\begin{bmatrix}X_1\\ X_2\end{bmatrix}\\
&\quad - \begin{bmatrix}\overline{W}_{F11} & \overline{W}_{F12}\\ \overline{W}_{F21} & \overline{W}_{F22}\end{bmatrix}\begin{bmatrix}\widehat{AC}_1\cos(\Omega\tau)\\ \widehat{AC}_2\cos(\Omega\tau)\end{bmatrix}\\
&\quad - \begin{bmatrix}\overline{W}_{NL11} & \overline{W}_{NL12}\\ \overline{W}_{NL21} & \overline{W}_{NL22}\end{bmatrix}\begin{bmatrix}\dfrac{\tau_m}{(\hat{d}_{01}-X_1)^2}\\ \dfrac{\tau_m}{(\hat{d}_{02}-X_2)^2}\end{bmatrix} = \begin{bmatrix}0\\0\end{bmatrix},
\end{aligned} \tag{6.2}$$

where all definitions are provided in Section 5.3. The model derivation is performed for the macro scale case, as was used for the numeric simulations. $p_1$ takes on a value of 2 to represent the force profile of the magnet. The tip displacement terms $X_m$ are separated into a static offset term $\overline{X}_m$ plus an oscillatory term $\hat{X}_m$ such that $X_m = \overline{X}_m + \hat{X}_m$. Separating the static and oscillatory terms reduces the complexity of the perturbed nonlinearities by reducing the number of secular terms at successive perturbation orders. The nonlinear terms are expanded about $\overline{X}_m$ in a Maclaurin series up to the third power. The multiple scales method of perturbation is utilised for this section [102], expanding the oscillatory terms about a small term $\epsilon$. The expansion is taken up to the first order of $\epsilon$, which requires two time scales, a fast time scale $\tau_a = \tau$ and a slow time scale $\tau_b = \epsilon\tau$. Due to the coupled nature of the equation, higher orders of $\epsilon$ quickly become very lengthy. We wish to study particular terms and their influence on the system behaviour, and the excessive number of higher order secular terms make it impractical to consider more than the first two terms of $\epsilon$. The expansion of the oscillatory terms are

$$\hat{X}_m = \hat{X}_{m0} + \epsilon\hat{X}_{m1}, \tag{6.3}$$

with the following time derivatives

$$\begin{gathered}
\tfrac{\mathrm{d}}{\mathrm{d}\tau} = D_0 + \epsilon D_1, \qquad \tfrac{\mathrm{d}^2}{\mathrm{d}\tau^2} = D_0^2 + \epsilon 2 D_0 D_1,\\
D_0 = \frac{\mathrm{d}}{\mathrm{d}\tau_a} \qquad D_1 = \frac{\mathrm{d}}{\mathrm{d}\tau_b}.
\end{gathered}$$

The damping and excitation terms are placed at the first order of $\epsilon$, along with the nonlinear terms resulting from the Maclaurin expansions.

Substituting (6.3) into (6.2) along with the time derivatives and expanding up to $\mathcal{O}(\epsilon)$ gives the following expression.

$$\begin{aligned}
&\begin{bmatrix}(D_0^2+\epsilon(2D_0D_1))(\hat{X}_{10}+\epsilon\hat{X}_{11})\\(D_0^2+\epsilon(2D_0D_1))(\hat{X}_{20}+\epsilon\hat{X}_{21})\end{bmatrix}+\epsilon\begin{bmatrix}\overline{W}_{c11}&\overline{W}_{c12}\\\overline{W}_{c21}&\overline{W}_{c22}\end{bmatrix}\begin{bmatrix}D_0\hat{X}_{10}\\D_0\hat{X}_{20}\end{bmatrix}\\
&\quad+\begin{bmatrix}\overline{W}_{k11}&\overline{W}_{k12}\\\overline{W}_{k21}&\overline{W}_{k22}\end{bmatrix}\begin{bmatrix}\hat{X}_{10}+\epsilon\hat{X}_{11}\\\hat{X}_{20}+\epsilon\hat{X}_{21}\end{bmatrix}-\epsilon\begin{bmatrix}\overline{W}_{F11}&\overline{W}_{F12}\\\overline{W}_{F21}&\overline{W}_{F22}\end{bmatrix}\begin{bmatrix}\widehat{AC}_1\cos(\Omega\tau)\\\widehat{AC}_2\cos(\Omega\tau)\end{bmatrix}\\
&\quad-\begin{bmatrix}\overline{W}_{NL11}&\overline{W}_{NL12}\\\overline{W}_{NL21}&\overline{W}_{NL22}\end{bmatrix}\begin{bmatrix}\dfrac{\tau_m}{(\hat{d}_{01}-\overline{X}_1)^2}+\dfrac{2\tau_m}{(\hat{d}_{01}-\overline{X}_1)^3}(\hat{X}_{10}+\epsilon\hat{X}_{11})\\\dfrac{\tau_m}{(\hat{d}_{02}-\overline{X}_2)^2}+\dfrac{2\tau_m}{(\hat{d}_{02}-\overline{X}_2)^3}(\hat{X}_{20}+\epsilon\hat{X}_{21})\end{bmatrix}\\
&\qquad+\begin{bmatrix}+\epsilon\dfrac{3\tau_m}{(\hat{d}_{01}-\overline{X}_1)^4}(\hat{X}_{10})^2+\epsilon\dfrac{4\tau_m}{(\hat{d}_{01}-\overline{X}_1)^5}(\hat{X}_{10})^3\\+\epsilon\dfrac{3\tau_m}{(\hat{d}_{02}-\overline{X}_2)^4}(\hat{X}_{20})^2+\epsilon\dfrac{4\tau_m}{(\hat{d}_{02}-\overline{X}_2)^5}(\hat{X}_{20})^3\end{bmatrix}=\begin{bmatrix}0\\0\end{bmatrix}
\end{aligned}\tag{6.4}$$

It can be seen from (6.4) that the growth of the expanded nonlinear terms grow proportionally to the oscillatory term $\hat{X}_m$ and inversely proportional to the absolute tip sample separation term $d_{0m}-\overline{X}_m$. A Maclaurin series is a reasonable approximation of the nonlinear term provided the oscillatory term remains smaller than the tip sample separation term, which will drive higher order terms to zero. The simulations presented in Section 6.3.1 all comply with this requirement. The terms of (6.4) are separated into orders of $\epsilon$, which are solved in sequence beginning with $\epsilon^0$

$$\begin{aligned}
\mathcal{O}(\epsilon^0):\quad&\begin{bmatrix}D_0^2\hat{X}_{10}\\D_0^2\hat{X}_{20}\end{bmatrix}+\begin{bmatrix}V_1&V_2\\V_3&V_4\end{bmatrix}\begin{bmatrix}\hat{X}_{10}\\\hat{X}_{20}\end{bmatrix}\\
&+\begin{bmatrix}\overline{W}_{NL11}&\overline{W}_{NL12}\\\overline{W}_{NL21}&\overline{W}_{NL22}\end{bmatrix}\begin{bmatrix}\dfrac{\tau_m}{(\hat{d}_{01}-\overline{X}_1)^2}\\\dfrac{\tau_m}{(\hat{d}_{02}-\overline{X}_2)^2}\end{bmatrix}=\begin{bmatrix}0\\0\end{bmatrix},
\end{aligned}\tag{6.5}$$

with the following simplifications made for the perturbed stiffness matrix terms.

$$\begin{aligned}
V_1&=\overline{W}_{k11}+\frac{2\tau_m\overline{W}_{NL11}}{(\hat{d}_{01}-\overline{X}_1)^3},\\
V_2&=\overline{W}_{k12}+\frac{2\tau_m\overline{W}_{NL12}}{(\hat{d}_{02}-\overline{X}_2)^3},\\
V_3&=\overline{W}_{k21}+\frac{2\tau_m\overline{W}_{NL21}}{(\hat{d}_{01}-\overline{X}_1)^3},\\
V_4&=\overline{W}_{k22}+\frac{2\tau_m\overline{W}_{NL22}}{(\hat{d}_{02}-\overline{X}_2)^3}.
\end{aligned}$$

The static deflection terms $\overline{X}_m$ have been eliminated, leaving only oscillatory terms. The solutions for $\hat{X}_{m0}$ are of the following form.

$$\begin{bmatrix}\hat{X}_{10}\\ \hat{X}_{20}\end{bmatrix} = \vec{z}_1(A_1 \mathrm{e}^{ir_1\tau_a} + cc.) + \vec{z}_2(A_2 \mathrm{e}^{ir_2\tau_a} + cc.), \tag{6.6}$$

where

$$A_1 = a_1 \mathrm{e}^{ib_1}, \quad \overline{A}_1 = a_1 \mathrm{e}^{-ib_1}, \quad A_2 = a_2 \mathrm{e}^{ib_2}, \quad \overline{A}_2 = a_2 \mathrm{e}^{-ib_2},$$

$$\vec{z}_1 = \begin{bmatrix} z_{11}\\ z_{21}\end{bmatrix}, \quad \vec{z}_2 = \begin{bmatrix} z_{12}\\ z_{22}\end{bmatrix},$$

and where $r_1$ and $r_2$ are the square roots of the eigenvalues of the stiffness matrix in (6.5) and $\vec{z}_1$ and $\vec{z}_2$ are the corresponding normalised eigenvectors. *cc.* represents the complex conjugate. The presence of two modal frequencies in the first order solution is equivalent to the array modes that form within the coupled system, consistent with the results demonstrated throughout this thesis. The level to which the modes interact is governed by the ratio of the eigenvectors, whilst the level to which each mode is excited is determined by the magnitude of $a_1$ and $a_2$. The constants of integration $a_1$, $a_2$, $b_1$ and $b_2$ are found through elimination of secular terms at the next order of $\epsilon$.

$$\begin{aligned}\mathcal{O}(\epsilon^1): \quad & \begin{bmatrix} D_0^2\hat{X}_{11}\\ D_0^2\hat{X}_{21}\end{bmatrix} + \begin{bmatrix} V_1 & V_2\\ V_3 & V_4\end{bmatrix}\begin{bmatrix}\hat{X}_{11}\\ \hat{X}_{21}\end{bmatrix} + \begin{bmatrix} 2D_0D_1\hat{X}_{10}\\ 2D_0D_1\hat{X}_{20}\end{bmatrix} + \begin{bmatrix}\overline{W}_{c11} & \overline{W}_{c12}\\ \overline{W}_{c21} & \overline{W}_{c22}\end{bmatrix}\begin{bmatrix} D_0\hat{X}_{10}\\ D_0\hat{X}_{20}\end{bmatrix}\\ & + \begin{bmatrix}\overline{W}_{F11} & \overline{W}_{F12}\\ \overline{W}_{F21} & \overline{W}_{F22}\end{bmatrix}\begin{bmatrix}\widehat{AC}_1\\ \widehat{AC}_2\end{bmatrix}(\mathrm{e}^{i\Omega\tau_1} + cc.)\\ & + \begin{bmatrix}\overline{W}_{NL11} & \overline{W}_{NL12}\\ \overline{W}_{NL21} & \overline{W}_{NL22}\end{bmatrix}\begin{bmatrix}\dfrac{3\tau_m}{(\hat{d}_{01}-\overline{X}_1)^4}(\hat{X}_{10})^2 + \dfrac{4\tau_m}{(\hat{d}_{01}-\overline{X}_1)^5}(\hat{X}_{10})^3\\ \dfrac{3\tau_m}{(\hat{d}_{02}-\overline{X}_2)^4}(\hat{X}_{20})^2 + \dfrac{4\tau_m}{(\hat{d}_{02}-\overline{X}_2)^5}(\hat{X}_{20})^3\end{bmatrix} = \begin{bmatrix}0\\0\end{bmatrix}.\end{aligned} \tag{6.7}$$

The $\mathcal{O}(\epsilon^1)$ equation can be simplified by grouping secular (terms of $\mathrm{e}^{ir_1\tau_a}$ and $\mathrm{e}^{ir_2\tau_a}$) and non-secular terms together and defining new new parameters. Due to the orthogonality of the modes of $r_1$ and $r_2$, the secular terms must go to zero individually, which makes it possible to multiply all $r_1$ terms through by the conjugate $\mathrm{e}^{-ib_1}$ and all $r_2$ terms through by the conjugate $\mathrm{e}^{-ib_2}$ to eliminate $b_1$ and $b_2$ terms. The excitation frequency $\Omega$ is expanded about the modal frequencies and new terms $\gamma_1$ and $\gamma_2$ are defined. These terms represent the phase shift between the excitation signal at frequency $\Omega$ and the response. The simplified set of equations is

$$\mathcal{O}(\epsilon^1): \quad \begin{bmatrix} D_0^2\hat{X}_{11} \\ D_0^2\hat{X}_{21} \end{bmatrix} + \begin{bmatrix} V_1 & V_2 \\ V_3 & V_4 \end{bmatrix} \begin{bmatrix} \hat{X}_{11} \\ \hat{X}_{21} \end{bmatrix} + \begin{bmatrix} ST_1 & ST_2 \\ ST_3 & ST_4 \end{bmatrix} \begin{bmatrix} \mathrm{e}^{ir_1\tau_1} \\ \mathrm{e}^{ir_2\tau_1} \end{bmatrix} + \begin{bmatrix} NST_1 \\ NST_2 \end{bmatrix} = \begin{bmatrix} 0 \\ 0 \end{bmatrix}. \quad (6.8)$$

In (6.8), $ST$ stands for secular term and $NST$ stands for non-secular term. The secular terms are defined as follows.

$$\begin{aligned} ST_1 &= 2ir_1z_{11}D_1a_1 + iP_1a_1 + Q_1\mathrm{e}^{i\gamma_1} + R_1a_1^3 + S_1a_1a_2^2, \\ ST_2 &= 2ir_2z_{12}D_1a_2 + iP_2a_2 + Q_2\mathrm{e}^{i\gamma_2} + R_2a_2^3 + S_2a_1^2a_2, \\ ST_3 &= 2ir_1z_{21}D_1a_1 + iP_3a_1 + Q_3\mathrm{e}^{i\gamma_1} + R_3a_1^3 + S_3a_1a_2^2, \\ ST_4 &= 2ir_2z_{22}D_1a_2 + iP_4a_2 + Q_4\mathrm{e}^{i\gamma_2} + R_4a_2^3 + S_4a_1^2a_2, \end{aligned}$$

with $P$, $Q$, $R$ and $S$ defined below. $P$ is used to represent terms that are a function of damping, $Q$ for terms that are a function of applied excitation, $R$ for uncoupled nonlinear terms and $S$ for coupled nonlinear terms.

$$\begin{gathered} \Omega = r_1 + \epsilon\sigma_1 = r_2 + \epsilon\sigma_2, \\ \gamma_1 = \sigma_1\tau_b - b_1, \quad \gamma_2 = \sigma_2\tau_b - b_2, \end{gathered}$$

$$\begin{gathered} P_1 = W_{c11}r_1z_{11} + W_{c12}r_1z_{21}, \quad Q_1 = W_{F11}AC_1 + W_{F12}AC_2, \\ R_1 = \frac{4\tau_m W_{NL11}}{(\hat{d}_{01} - \overline{X}_1)^5}(3z_{11}^3) + \frac{4\tau_m W_{NL12}}{(\hat{d}_{02} - \overline{X}_2)^5}(3z_{21}^3), \\ S_1 = \frac{4\tau_m W_{NL11}}{(\hat{d}_{01} - \overline{X}_1)^5}(2z_{11}z_{12}^2) + \frac{4\tau_m W_{NL12}}{(\hat{d}_{02} - \overline{X}_2)^5}(2z_{21}z_{22}^2), \end{gathered}$$

$$\begin{gathered} P_2 = W_{c11}r_2z_{12} + W_{c12}r_2z_{22}, \quad Q_2 = W_{F11}AC_1 + W_{F12}AC_2, \\ R_2 = \frac{4\tau_m W_{NL11}}{(\hat{d}_{01} - \overline{X}_1)^5}(3z_{12}^3) + \frac{4\tau_m W_{NL12}}{(\hat{d}_{02} - \overline{X}_2)^5}(3z_{22}^3), \\ S_2 = \frac{4\tau_m W_{NL11}}{(\hat{d}_{01} - \overline{X}_1)^5}(2z_{11}^2z_{12}) + \frac{4\tau_m W_{NL12}}{(\hat{d}_{02} - \overline{X}_2)^5}(2z_{21}^2z_{22}), \end{gathered}$$

$$\begin{gathered} P_3 = W_{c21}r_1z_{11} + W_{c22}r_1z_{21}, \quad Q_3 = W_{F21}AC_1 + W_{F22}AC_2, \\ R_3 = \frac{4\tau_m W_{NL21}}{(\hat{d}_{01} - \overline{X}_1)^5}(3z_{11}^3) + \frac{4\tau_m W_{NL22}}{(\hat{d}_{02} - \overline{X}_2)^5}(3z_{21}^3), \\ S_3 = \frac{4\tau_m W_{NL21}}{(\hat{d}_{01} - \overline{X}_1)^5}(2z_{11}z_{12}^2) + \frac{4\tau_m W_{NL22}}{(\hat{d}_{02} - \overline{X}_2)^5}(2z_{21}z_{22}^2), \end{gathered}$$

$$P_4 = W_{c21} r_2 z_{12} + W_{c22} r_2 z_{22}, \qquad Q_4 = W_{F21} AC_1 + W_{F22} AC_2,$$
$$R_4 = \frac{4\tau_m W_{NL21}}{(\hat{d}_{01} - \overline{X}_1)^5}(3z_{12}^3) + \frac{4\tau_m W_{NL22}}{(\hat{d}_{02} - \overline{X}_2)^5}(3z_{22}^3),$$
$$S_4 = \frac{4\tau_m W_{NL21}}{(\hat{d}_{01} - \overline{X}_1)^5}(2z_{11}^2 z_{12}) + \frac{4\tau_m W_{NL22}}{(\hat{d}_{02} - \overline{X}_2)^5}(2z_{21}^2 z_{22}).$$

The secular terms of (6.8) can be eliminated by solving for the variation in amplitude $a_1$ and $a_2$ on the slow time scale. To define the slow amplitude variation for the elimination of secular terms, we apply solvability conditions as proposed by Nayfeh [104] to reduce the number of constraint equations to equal the number of unknowns (which in this case is four). Upon elimination of secular terms, we require the solutions of the $\mathcal{O}(\epsilon^1)$ equation to be in the following form.

$$\begin{bmatrix} \hat{X}_{12} \\ \hat{X}_{22} \end{bmatrix} = \begin{bmatrix} A_{11}^* & A_{12}^* \\ A_{21}^* & A_{22}^* \end{bmatrix} \begin{bmatrix} e^{ir_1\tau_a} \\ e^{ir_2\tau_a}. \end{bmatrix} \tag{6.9}$$

Substituting equation (6.9) into (6.8) and neglecting all non-secular terms yields

$$\begin{bmatrix} -r_1^2 A_{11}^* + V_1 A_{11}^* + V_2 A_{21}^* & -r_2^2 A_{12}^* + V_1 A_{12}^* + V_2 A_{22}^* \\ -r_1^2 A_{12}^* + V_4 A_{12}^* + V_3 A_{11}^* & -r_2^2 A_{22}^* + V_4 A_{22}^* + V_3 A_{21}^* \end{bmatrix} \begin{matrix} e^{ir_1\tau_a} \\ e^{ir_2\tau_a} \end{matrix}$$
$$+ \begin{bmatrix} ST_1 & ST_2 \\ ST_3 & ST_4 \end{bmatrix} \begin{matrix} e^{ir_1\tau_a} \\ e^{ir_2\tau_a} \end{matrix} = \begin{bmatrix} 0 \\ 0 \end{bmatrix} \tag{6.10}$$

For non-trivial solutions of the homogeneous equations, one of the following matrix conditions must be satisfied:

$$\begin{vmatrix} V_1 - r_1^2 & V_2 \\ V_3 & V_4 - r_1^2 \end{vmatrix} = 0 \tag{6.11}$$

or

$$\begin{vmatrix} V_1 - r_2^2 & V_2 \\ V_3 & V_4 - r_2^2 \end{vmatrix} = 0. \tag{6.12}$$

Following the method by Nayfeh [104], the solvability condition can be written in the following forms. These forms are chosen to avoid the $V_1^2 - r_1^2$ and $V_4^2 - r_2^2$ terms, which go to zero when coupling is weak or when tip-sample separation is large, which can create numerical errors.

$$\begin{vmatrix} -ST_1 & V_2 \\ -ST_3 & V_4 - r_1^2 \end{vmatrix} = 0 \tag{6.13}$$

and

$$\begin{vmatrix} V_1 - r_2^2 & -ST_2 \\ V_3 & -ST_4 \end{vmatrix} = 0. \tag{6.14}$$

The determinant equations of (6.13) and (6.14) can be used to solve for the slow evolution of of the amplitude terms. As we are interested in steady state solutions, we want to find the case where the steady state amplitudes are unchanging on the slow time scale. This is done by solving for the case where $D_1 a_1 = D_1 a_2 = 0$.

$$\begin{aligned} D_1 a_1 = & \frac{-(V_4 - r_1^2)(P_1 a_1 - iR_1 a_1^3 - iS_1 a_1 a_2^2 - iQ_1 \mathrm{e}^{i\gamma_1})}{2(V_4 - r_1^2) r_1 z_{11} + 2V_2 r_1 z_{21}} \\ & - \frac{V_2(P_3 a_1 - iR_3 a_1^3 - iS_3 a_1 a_2^2 - iQ_3 \mathrm{e}^{i\gamma_1})}{2(V_4 - r_1^2) r_1 z_{11} + 2V_2 r_1 z_{21}} = 0 \end{aligned} \tag{6.15}$$

$$\begin{aligned} D_1 a_2 = & \frac{-(V_1 - r_2^2)(P_4 a_2 - iR_4 a_2^3 - iS_4 a_1^2 a_2 - iQ_4 \mathrm{e}^{i\gamma_2})}{2(V_1 - r_2^2) r_2 z_{12} + 2V_3 r_2 z_{22}} \\ & - \frac{V_3(P_2 a_2 - iR_2 a_2^3 - iS_2 a_1^2 a^2 - iQ_2 \mathrm{e}^{i\gamma_2})}{2(V_1 - r_2^2) r_2 z_{12} + 2V_3 r_2 z_{22}} = 0 \end{aligned} \tag{6.16}$$

We separate equations (6.15) and (6.16) into real and imaginary parts and solve for the steady state amplitude ($\dot{a}_1$, $\dot{a}_2$) modulations and phase ($\dot{\gamma}_1$, $\dot{\gamma}_2$) modulations:

$$\dot{a}_1 = (V_4 - r_1^2)(P_1 a_1 + Q_1 \sin(\gamma_1)) + V_2(P_3 a_1 + Q_3 \sin(\gamma_1)) = 0, \tag{6.17}$$

$$\dot{a}_2 = (V_1 - r_2^2)(P_4 a_2 + Q_4 \sin(\gamma_2)) + V_3(P_2 a_2 + Q_2 \sin(\gamma_2)) = 0, \tag{6.18}$$

$$\begin{aligned} \dot{\gamma}_1 = & \sigma_1 a_1 \Big( 2(V_4 - r_1^2) r_1 z_{11} + 2V_2 r_1 z_{21} \Big) + (V_4 - r_1^2) \Big( R_1 a_1^3 + S_1 a_1 a_2^2 + Q_1 \cos(\gamma_1) \Big) \\ & + V_2 \Big( R_3 a_1^3 + S_3 a_1 a_2^2 + Q_3 \cos(\gamma_1) \Big) = 0, \end{aligned} \tag{6.19}$$

$$\dot{\gamma}_2 = \sigma_2 a_2 \Big( 2(V_1 - r_2^2) r_2 z_{12} + 2V_3 r_2 z_{22} \Big) + (V_1 - r_2^2) \Big( R_4 a_2^3 + S_4 a_1^2 a_2 + Q_4 \cos(\gamma_2) \Big) + V_3 \Big( R_2 a_2^3 + S_2 a_1^2 a_2 + Q_2 \cos(\gamma_2) \Big) = 0. \tag{6.20}$$

The phase terms $\gamma_1$ and $\gamma_2$ can be eliminated through utilisation of the Pythagorean trigonometric identity $\sin^2(\gamma)+\cos^2(\gamma) = 1$ to substitute (6.17) and (6.18) into (6.19) and (6.20), respectively. By again defining new terms for compactness, the characteristic equations containing $a_1$ and $a_2$ are

$$\boldsymbol{B_{11}} a_1^6 + (\boldsymbol{B_{12}} a_2^2 + \boldsymbol{B_{13}}) a_1^4 + (\boldsymbol{B_{14}} a_2^4 + \boldsymbol{B_{15}} a_2^2 + \boldsymbol{B_{16}}) a_1^2 + \boldsymbol{B_{17}} = 0, \tag{6.21}$$

and

$$\boldsymbol{B_{21}} a_2^6 + (\boldsymbol{B_{22}} a_1^2 + \boldsymbol{B_{23}}) a_2^4 + (\boldsymbol{B_{24}} a_1^4 + \boldsymbol{B_{25}} a_1^2 + \boldsymbol{B_{26}}) a_2^2 + \boldsymbol{B_{27}} = 0, \tag{6.22}$$

The full definitions of the values $\boldsymbol{B_{11}}$ to $\boldsymbol{B_{27}}$ are given in Appendix D. Here, the values are presented as functions of $P$, $Q$, $R$ and $S$ for the analysis presented in this section.

$$\boldsymbol{B_{11}} = f(R_1, R_3), \quad \boldsymbol{B_{12}} = f(R_1, R_3, S_1, S_3), \quad \boldsymbol{B_{13}} = f(R_1, R_3),$$

$$\boldsymbol{B_{14}} = f(S_1, S_3), \quad \boldsymbol{B_{15}} = f(S_1, S_3), \quad \boldsymbol{B_{16}} = f(P_1, P_3), \quad \boldsymbol{B_{17}} = f(Q_1, Q_3),$$

$$\boldsymbol{B_{21}} = f(R_2, R_4), \quad \boldsymbol{B_{22}} = f(R_2, R_4, S_2, S_4), \quad \boldsymbol{B_{23}} = f(R_2, R_4),$$

$$\boldsymbol{B_{24}} = f(S_2, S_4), \quad \boldsymbol{B_{25}} = f(S_2, S_4), \quad \boldsymbol{B_{26}} = f(P_2, P_4), \quad \boldsymbol{B_{27}} = f(Q_2, Q_4),$$

Secular terms can be eliminated by solving (6.21) and (6.22) to find the amplitude terms $a_1$ and $a_2$. It can be seen that both equations are sextic polynomials, which are symmetric about the zero axis due to the lack of odd power terms. The symmetry results from the squaring of terms to eliminate $\gamma_1$ and $\gamma_2$ using the Pythagorean identity. This means that $a_1$ and $a_2$ both have up to three real, positive solutions, each with a corresponding negative conjugate. The presence of three solutions from the perturbation analysis accounts for the three solution branches observed in the experimental and simulation results presented in Sections 6.2 and 6.3.1. It is possible to use both equaitons (6.21) and (6.22) to predict when multiple solution branches will form in the response of an array, and how this is linked to parameter space.

First, the perfectly uncoupled case can be considered for reference, which is analogous to two single AFM cantilevers operating independently. In the uncoupled case, all off diagonal terms in (6.2) go to zero ($W_{c12} = W_{c21} = W_{k12} = W_{k21} = W_{NL12} = W_{NL21} = W_{F12} = W_{F21} = 0$). Following through the perturbation sequence it follows that $z_{12} = z_{21} = S_1 = S_2 = S_3 = S_4 = R_2 = R_3 = 0$ for the uncoupled case. This means that $\boldsymbol{B_{12}}$, $\boldsymbol{B_{14}}$, $\boldsymbol{B_{15}}$, $\boldsymbol{B_{22}}$, $\boldsymbol{B_{24}}$ and $\boldsymbol{B_{25}}$ all go to zero, decoupling the solutions of $a_1$ and $a_2$. Therefore, it is still possible for multiple solution branches to form depending on the relative magnitudes of $\boldsymbol{B_{13}}$, $\boldsymbol{B_{16}}$ and $\boldsymbol{B_{17}}$ and$\boldsymbol{B_{23}}$, $\boldsymbol{B_{26}}$ and $\boldsymbol{B_{27}}$. It can be seen that these coefficients are related to the excitation amplitude and damping terms, as well as the difference between excitation frequency and modal frequency $\sigma$. The presence of these terms in the coupled sextic equations demonstrates why multiple solution branches can also be formed when the input amplitude is high or when damping is low when only weak coupling is applied, as was demonstrated in Section 6.4, and also why multiple solution branches only occur at certain perturbed resonant frequencies (or conversely at certain actuation frequencies).

Considering coupling terms in (6.21) and (6.22) effectively perturbs the quartic and quadratic terms of the sextic equations as a function of the amplitude of the opposing mode. At the frequency cross-over point, the amplitude of the passive beam increases due to the onset of resonance, in turn increasing the modal amplitudes $a_n$. This leads to a perturbation of the coefficients of sextic equations away from the uncoupled case, which can cause multiple solutions to appear where none exist for the equivalent uncoupled system. This explains the presence of the cusp catastrophe as a function of coupling strength that was observed in Figures 6.4 and 6.5 and why the catastrophe occurs within the vicinity of the frequency cross-over point.

## 6.6 Frequency Gap - Beam Separation Comparison

In Section 3.4 it was demonstrated that their appeared to be an equal correlation between the observed level of coupling in the TUI micro arrays and both the physical separation gap and resonant frequency gap between cantilevers. In this section, controlled simulations will be conducted to verify or otherwise explain this micro scale observation and to link the observations to the technological implications for parallel imaging with arrays. Experimentally, multiple beams in a large array were used with different resonant frequencies and separation distances. For the simulations, a two

beam array model is used to ensure only a single energy transfer path is available between cantilevers so that coupling strength can be easily correlated. The cantilever tip masses (which define frequency gap) and physical separation distances are varied individually to measure the influence of each. The procedure used on the micro scale is utilised for the simulations. A sweep response was performed by providing actuation to beam 1 only and the point of maximum amplitude was found. The amplitude of beam 2 was then recorded at that point and the ratio of the two amplitudes was taken, representing a measure of the coupling in the system. The results are depicted in the following Figures, relationship between frequency gap and observed coupling with different shared base lengths (Figure 6.9a) and damping coefficients (Figure 6.10a) and relationship between separation distance and observed coupling with different shared base lengths (Figure 6.9b) and damping coefficients (Figure 6.10b).

The starting parameter regions of the simulations were chosen to be very small, with an initial separation gap of 1 mm (compared to a cantilever width of 40 mm) and an initial frequency gap of near zero (nearly identical beams). This initial parameter region results in strong initial coupling with a near 1:1 ratio of beam amplitudes. The reason for choosing this start point is to best represent the range of parameter space of the TUI micro arrays, which are closely spaced (5 µm separation for a beam width of 40 µm) and close to identical (Observed frequency gaps ranging from 100 Hz to 3000 Hz from cantilevers with a first resonant frequency in the region of 115 kHz, or 37 kHz in the case of array number three).

From the simulation results the relative influence of frequency gap and separation distance over the simulation range can be analysed. It can be seen in both Figures 6.9 and 6.10 that by increasing the separation distance the influence of coupling can be reduced to a greater extent than by increasing the frequency gap in all cases tested. This result directly contradicts the conclusion drawn previously in Section 3.4, which was that frequency gap and separation distance are equally significant. The simulations do demonstrate, however, the advantage of placing beams far apart to remove coupling, as is done by the vast majority of research groups.

Close inspection of Figures 6.9 and 6.10 shows that in regions where both the cantilever separation and frequency gap are small, the functional relationship between both parameters and observed coupling is similar in magnitude. When beginning from the stand point of closely spaced and near identical cantilevers, it can be concluded that increasing either frequency gap or cantilever separation will produce quantitatively similar reductions in observed coupling, but beyond a certain region in parameter space, the reduction in coupling is significantly amplified by increasing separation dis-

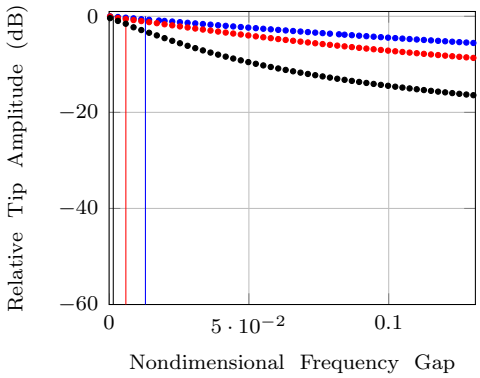


(a) Change in observed coupling strength as a function of frequency gap. The separation distance is set at 1 mm.

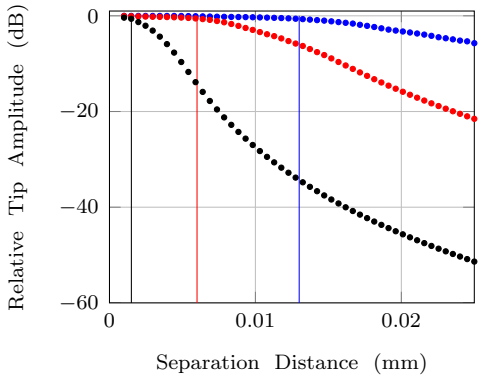


(b) Change in observed coupling strength as a function of cantilever separation distance. The nondimensional frequency gap is set at 0.00039.

Figure 6.9: Simulated functional relationship between frequency gap/separation distance and observed coupling strength for a two beam array (simulated with macro scale test rig dimensions). Blue - 15 mm shared base, red - 10 mm shared base, black - 5 mm shared base. The damping coefficient is set at 0.007.

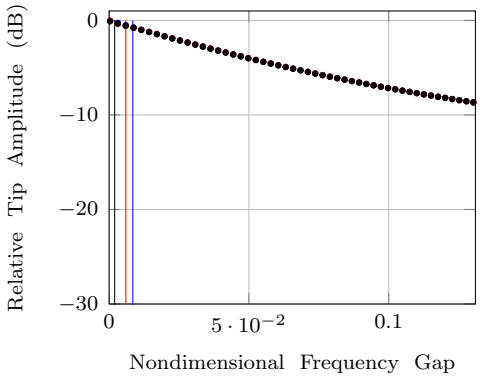


(a) Change in observed coupling strength as a function of frequency gap. The separation distance is set at 1 mm.

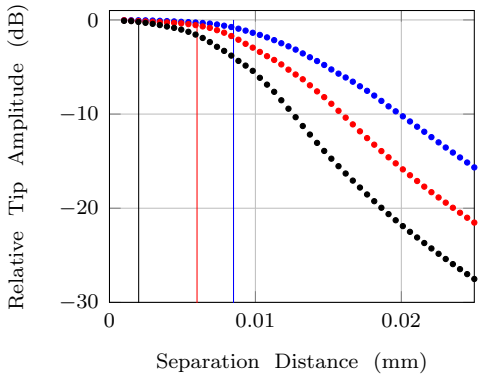


(b) Change in observed coupling strength as a function of cantilever separation distance. The frequency gap is set at 0.00039.

Figure 6.10: Simulated functional relationship between frequency gap/separation distance and observed coupling strength for a two beam array (simulated with macro scale test rig dimensions). Blue - damping coefficient 0.0035, red - damping coefficient 0.007, black - damping coefficient 0.014. The shared base material is set to 10 mm

tance. The boundaries between the two regions are marked by the vertical lines in Figures 6.9 and 6.10. The conclusion is now consistent with the observation of an equivalent correlation to both control variables from the

micro scale data (Figure 3.6), where the arrays utilised have small separation distances and frequency gaps. The outcomes of this section further demonstrate that relative frequency is an important factor that should be considered when designing and fabricating arrays for parallel AFM measurement with high measurement density, in addition to the strength of mechanical coupling. Increasing the frequency gap has been demonstrated to be a viable alternative to increasing separation distance for the TUI arrays, or trying to further minimise the amount of shared base material.

## 6.7 Technological Implications

So far in this chapter, some of the key reasons for the lack of reliable imaging feedback from the TUI arrays have been identified and analysed using a combination of mathematical modelling and experimental investigations. The conclusions drawn in the previous sections must be linked to the practical aspects of the technology so that viable solutions can be found for the problems resulting from fundamental dynamic response.

The data presented has shown that significant nonlinear phenomena can occur in the vicinity of the frequency cross-over point, and that the level of observed nonlinearity is highly dependent on the parameter space. Due to the discussed detrimental effects of frequency cross-over, it is desirable to avoid the frequency cross-over region if possible, which for closely spaced arrays can be achieved by controlling the individual cantilever resonant frequencies through careful parameter selection. Due to the nonlinearity of the force interactions that dominate the AFM process, the region in which stable operation can be achieved within the nonlinear force gradient is limited by the location of the pull-in instability point. As the region of stable operation is bounded, the maximum expected resonant frequency shift of any beam is also bounded. It can be stated that provided the frequency gap between any two cantilevers is larger than the maximum expected resonant frequency shift, frequency cross-over will not occur. Resonant frequency shifts during the imaging process is dependent on a number of factors, including cantilever material/geometry, surface material properties, response amplitude and operating mode (examples of different theoretical and experimental frequency shifts observed in AFM systems can be seen in [3, 105, 106]). Within the scope of AFM imaging, the above parameters are varied significantly, usually tuned by the operator, which means the range of expected maximum frequency shift is large, however, a survey of several AFM imaging parameters demonstrates that maximum expected frequency shifts do not exceed 2 kHz [3, 105, 106]. Using this frequency range, the extent to which cantilever parameters need to be varied to avoid frequency cross-over can

be studied through mathematical modelling.

Two parameters are immediately identified as viable candidates that can be varied during the fabrication process, which are the cantilever length and tip mass. The link between these parameters and resonant frequency are well understood, and can be varied and tightly controlled without the need for specialised or expensive fabrication techniques. The material properties of the cantilevers are fixed, based on the fabrication requirements of the actuator and sensor, as well as of the structure itself. It is also difficult to vary the thickness of individual cantilevers, as the etching process is conducted for the entire array at once. There are other possible options that can be investigated for resonant frequency variation, such as the targeted removal of material from specific cantilevers [107]. The selection of an optimal method of varying individual cantilever resonant frequencies should be conducted by the TUI research team, who have the specialist knowledge required. In this thesis, simulations are performed to demonstrate the degree to which cantilever length and tip mass would need to be varied in order to avoid frequency cross-over as discussed above. To perform the simulations, the mathematical model is derived from (5.5), (5.6) and (5.7) in Section 5.3 using parameters pertaining to the TUI arrays. The cantilevers are assumed to be homogeneous to comply with the derived model. The relation between resonant frequency gap and cantilever length is presented in Table 6.3 and the relationship to applied tip mass is presented in Table 6.4 (Parameters are also given in the tables).

Table 6.3: Uncoupled frequency gaps for cantilevers with different lengths. The additional parameters are used based on the TUI arrays. Tip mass - 0 ng. Cantilever width - 40 µm. Cantilever thickness - 4.5 µm. Material - Silicon.

| Parameter | Value | | | | |
|---|---|---|---|---|---|
| **Beam 1 length** (µm) | 352 | 354 | 356 | 358 | 360 |
| **Beam 2 length** (µm) | 350 | 350 | 350 | 350 | 350 |
| **Beam 1 Res. Freq.** (kHz) | 38.62 | 38.18 | 37.75 | 37.33 | 36.92 |
| **Beam 2 Res. Freq.** (kHz) | 39.06 | 39.06 | 39.06 | 39.06 | 39.06 |
| **Freq. Gap** (Hz) | 440 | 880 | 1310 | 1730 | 2140 |

A difference in length of just 10 µm between adjacent cantilevers can produce a frequency gap of more than 2 kHz for the parameters of the TUI cantilevers. This is a relatively small length difference required to prevent frequency crossing occurring between two cantilevers, but would become impractical for larger arrays (for a 4 beam array, a total length

Table 6.4: Uncoupled frequency gaps for cantilevers with different tip masses. The additional parameters are used based on the TUI arrays. Cantilever length - 350 µm. Cantilever width - 40 µm. Cantilever thickness - 4.5 µm. Material - Silicon

| Parameter | Value | | | | |
|---|---|---|---|---|---|
| **Beam 1 tip mass** (ng) | 3 | 6 | 9 | 12 | 15 |
| **Beam 2 tip mass** (ng) | 0 | 0 | 0 | 0 | 0 |
| **Beam 1 Res. Freq.** (kHz) | 38.58 | 38.11 | 37.67 | 37.24 | 36.82 |
| **Beam 2 Res. Freq.** (kHz) | 39.06 | 39.06 | 39.06 | 39.06 | 39.06 |
| **Freq. Gap** (Hz) | 480 | 950 | 1390 | 1820 | 2240 |

range of 40 µm would be required, which is 10 % of the nominal length). An equivalent frequency gap can be achieved with a tip mass variation of 15 ng. This mass is equivalent to a gold sphere 6 µm in diameter. On the basis of size, it could be practical to use gold micro-particles or similar to tune the individual cantilevers to prevent frequency cross-over. It is also viable to use a combination of cantilever length and tip mass variation to ensure frequency separation for larger arrays. It should be noted that the imaging bandwidth of an array with cantilever of varying frequency will be limited to the bandwidth of the cantilever with the lowest resonant frequency. As the difference in frequency is small relative to the absolute resonant frequency value, this shouldn't be an issue.

Several considerations must be taken into account before utilising either of the above methods to vary cantilever resonant frequency. It is necessary to know the expected error margin for each of the cantilever parameters that will have a significant effect on observed resonant frequency (including length, width, thickness, material stiffness, mass distribution and uniformity of the silicon crystal). With knowledge of the repeatability of the above factors, a normal distribution of the expected natural frequency of individual cantilevers can be calculated. To successfully and reliably separate cantilever resonant frequencies, the applied frequency gaps must be significantly greater than the standard deviation of expected resonant frequency. Parameter tolerance is a consideration that ties into the design and fabrication of arrays, and as this aspect of the research project is conducted by our collaborations it will not be investigated within the scope of this thesis.

The final implication to discuss relates to the transfer of static strain through the base structure, which can result in one cantilever being de-

flected due to an applied offset at a neighbouring cantilever. As AFM operates on the principle of driving the system to a known reference position, any unexpected added tip displacement would result in an offset that is unknown to the feedback controller, and would be interpreted as a change in sample topography. As this is a zero frequency phenomenon, adjusting the relative resonant frequencies of the cantilevers in an array will not provide a solution. It is possible to eliminate the phenomenon of static strain transfer by reducing mechanical coupling stiffness, either through an increasing in cantilever separation or a decrease in the length of shared base material. As has been discussed at length previously, it is undesirable to increase separation distance as measurement density is reduced, and it is not practically possible to completely eliminate coupling through a shared base structure. It is therefore necessary to minimise the influence of static strain transfer on imaging reliability. It was noted from Figure 6.2 that strain transfer was significant only for the case when one cantilever jumped into contact, which created a large tip displacement. Jump-to-contact is an undesirable phenomenon that is avoided during operation, but can occur if the control system looses stability. It is important that end users of the array technology are aware that a loss of stability at one cantilever, causing jump-to-contact, will result in a loss of measurement precision in other beams in the array. In conclusion, data acquired by multiple cantilevers in an array cannot be reliably used while one or more cantilevers are in contact with the sample surface during AM-AFM or FM-AFM operation. Stability must be restored to the whole array before continuing the measurement process, or artefacts are likely to appear in the final image.

## 6.8 Conclusion

In this chapter, the phenomena of amplitude jumps that was presented in Chapter 3 has been analysed and discussed. The jump phenomena that were observed in the response of the TUI micro arrays were successfully replicated on the macro scale. Through observation of the array response, it was possible to categorise the jump phenomena into two causes; zero-frequency coupling, which is influenced predominantly by the strength of the mechanical coupling; and dynamic coupling, which is influenced predominantly by the difference in uncoupled resonant frequency of the beams and occurs at the point of frequency cross-over. Simulations using the mathematical model were used to confirm the conclusions drawn from the experimental results. In addition, an analytical solution to the equations of motion, formed using perturbation theory, was used to link the parameters of the system to the onset of bifurcation and discontinuous jumps in amplitude. It was

shown that excitation amplitude, system damping and coupling strength all influence the onset of bifurcation. Also in this chapter, the relative influence of separation distance between cantilevers and resonant frequency gap has been investigated. It was shown that when cantilevers are closely spaced, the influence of increasing the resonant frequency gap and reducing the amount of shared base material were equally effective at reducing the transfer of energy between beams. This backed up the results from Section 3.4.

CHAPTER 7

# Arrays for Enhanced Measurement

## 7.1 Introduction

For the majority of this thesis, the focus has been on the analysis of coupled array dynamics for the purpose of parallel AFM imaging using all cantilevers simultaneously as individual sensors. This is the primary use for which the TUI arrays have been designed, as parallel imaging is desired to increase measurement speed and to allow for simultaneous acquisition of data at multiple points on a sample. Dynamic phenomena that are likely responsible for the lack of imaging reliability currently achievable with the TUI arrays have been identified, and ways to mitigate adverse phenomena have been identified. In this chapter, the alternative approach is taken, which is to identify how coupled dynamic phenomena could be utilised to enhance the capabilities of single point AFM imaging beyond that achievable with single cantilever technology. Specifically, the transition of array response from unsynchronised cantilever modes to synchronised array modes resulting from applied nonlinear tip forces is studied for the purpose of increasing AFM measurement sensitivity. As was discussed in the literature review (Section 2.2), eigenmode changes in coupled oscillators have been identified as a potential tool for achieving very high precision measurement on the nano scale. So far, the main application of this principle has been ultra-sensitive mass detection, which utilises the phenomenon of mode localisation when mass is added to the tip of a cantilever in an array. It is possible to apply a similar method to AFM, using tip-sample forces to induce eigenmode shifts which can be used as a measurement signal.

The focus of this chapter will be solely on enhancing the sensitivity of non-contact FM-AFM using a two beam array. The developed mathematical model (Section 5.3) is used to demonstrate how changes in individual cantilever frequency properties can cause sharp changes in modal response, which can be utilised for high precision sensing. Mathematical simulations are used to demonstrate the principle behind increased sensitivity and how

it is affected by the parameter space. The COCO toolbox is again used. Simulations are compared with experimental data on the macro scale to validate the proposed measurement principle as an alternative to current single beam techniques. Finally, technological implications are discussed, including the mechanical functionality required for enhanced imaging to be implemented practically, and the precision required for key system parameters to ensure reliable functionality.

## 7.2 Working Principle

The concept of sensitivity enhancement is directly related to the functional relationship that exists between the control parameter (in this case resonant frequency) and the observed parameter (in this case tip-sample separation). If the gradient of the functional relationship between the control parameter and observed parameter can be increased, there is the potential to detect sample surface features with finer resolution. It was demonstrated in Section 5.4.3 (Figures 5.9 and 5.10) that changing the uncoupled resonant frequencies of individual cantilevers in an array will result in a change in the observed spatial array mode shapes. As was discussed in the literature review (Section 2.2), the sensitivity of spatial mode shapes due to external influences can be an order of magnitude greater than the equivalent resonant frequency shift of a single DOF system [56]. It should be possible to combine these two phenomena with standard FM-AFM imaging techniques to enhance imaging sensitivity.

The proposed method focuses on the frequency cross-over region, which has been discussed previously in Section 6.2 and is defined as the point where the uncoupled resonant frequencies of two cantilevers approach and cross each other due to external force interactions. It is within this region that transitions in modal response occur and functional gradient can be maximised. The proposed FM-AFM method utilises two cantilevers with slightly varying uncoupled resonant frequencies (on the order of 1-2 Hz on the macro scale). The cantilever with the larger uncoupled resonant frequency is actuated (active cantilever) and brought into proximity with the sample surface, whilst the the other cantilever is left passive and at far field (which can be achieved through static deflection away from the surface or removal of the AFM tip). Excitation of the passive beam is only through mechanical coupling from the actuated beam. Actuation is applied such that the phase shift between the excitation signal and the response of the active beam is held at 90°, as is done for standard FM-AFM techniques. During measurement, the tip-sample displacement will be held at the point where frequency cross-over occurs, ensuring maximum

frequency sensitivity to changes in sample topography. This means that the height of imaging is set by the array parameters, and is not selected by the user. The implications of this will be discussed further in a later section.

## 7.3 Modelling and Simulation

The working principle of increasing the functional gradient between tip-sample separation and resonant frequency using array response is demonstrated through mathematical simulations, which are conducted in the framework of FM-AFM using the model developed in Chapter 5. The model is used in the form of (5.25) from Section 5.3 and is reduced to a two beam array. Simulations are again scaled for the macro scale system, to allow for comparison with experimental data in the next section. The model takes on the following form, with definitions from Section 5.3.

$$\begin{aligned}
&\begin{bmatrix}\ddot{X}_1\\ \ddot{X}_2\end{bmatrix} + \begin{bmatrix}\overline{W}_{c11} & \overline{W}_{c12}\\ \overline{W}_{c21} & \overline{W}_{c22}\end{bmatrix}\begin{bmatrix}\dot{X}_1\\ \dot{X}_2\end{bmatrix} + \begin{bmatrix}\overline{W}_{k11} & \overline{W}_{k12}\\ \overline{W}_{k21} & \overline{W}_{k22}\end{bmatrix}\begin{bmatrix}X_1\\ X_2\end{bmatrix}\\
&\quad - \begin{bmatrix}\overline{W}_{F11} & \overline{W}_{F12}\\ \overline{W}_{F21} & \overline{W}_{F22}\end{bmatrix}\begin{bmatrix}\widehat{AC}_1 F_{ext}\\ \widehat{AC}_2 F_{ext}\end{bmatrix}\\
&\quad - \begin{bmatrix}\overline{W}_{NL11} & \overline{W}_{NL12}\\ \overline{W}_{NL21} & \overline{W}_{NL22}\end{bmatrix}\begin{bmatrix}\dfrac{\tau_m}{(\hat{d}_{01}-X_1)^2}\\ \dfrac{\tau_m}{(\hat{d}_{02}-X_2)^2}\end{bmatrix} = \begin{bmatrix}0\\ 0\end{bmatrix},
\end{aligned} \tag{7.1}$$

The forcing function $F_{ext}$ is the nondimensional oscillatory component of the excitation signal, with the dimensional amplitude applied to beams 1 and 2 defined by $\widehat{AC}_1$ and $\widehat{AC}_2$, respectively. For FM-AFM, $F_{ext}$ needs to be defined such that the excitation signal is sinusoidal with a phase lead of 90° over the measured output signal, which in this case will be the tip displacement of beam 1. For the practical application of FM-AFM, the tip displacement signal is measured, phase shifted and the used as the excitation signal in a feedback loop. For simulations using the COCO toolbox, feedback control is not available, and a closed form function is required for the excitation signal. It is known that response velocity will have a 90° phase lag from the corresponding displacement signal, which means the inverse of the response velocity signal will have the required 90° phase lead. The output velocity is a state variable of the model, and can be used to define $F_{ext}$. To ensure the magnitude of the excitation signal remains bounded, the velocity signal must be normalised by the vector length of the oscillatory displacement and velocity signals, forming a unit circle in state-space. The displacement signal must be separated into oscillatory and static offset components using $X_m = \overline{X}_m + \hat{X}_m$, where $\overline{X}_m$ is the offset term and $\hat{X}_m$

is the oscillatory term. The excitation feedback signal is hence defined as follows.

$$F_{ext} = \frac{-\dot{\hat{X}}_1}{\sqrt{\dot{\hat{X}}_1^2 + \hat{X}_1^2}} \tag{7.2}$$

The excitation signal (7.2) is substituted into the EOM (7.1), along with the separation of the oscillatory and static offset terms and gives

$$\begin{aligned} &\begin{bmatrix} \ddot{\hat{X}}_1 \\ \ddot{\hat{X}}_2 \end{bmatrix} + \begin{bmatrix} \overline{W}_{c11} & \overline{W}_{c12} \\ \overline{W}_{c21} & \overline{W}_{c22} \end{bmatrix} \begin{bmatrix} \dot{\hat{X}}_1 \\ \dot{\hat{X}}_2 \end{bmatrix} + \begin{bmatrix} \overline{W}_{k11} & \overline{W}_{k12} \\ \overline{W}_{k21} & \overline{W}_{k22} \end{bmatrix} \begin{bmatrix} \overline{X}_1 + \hat{X}_1 \\ \overline{X}_2 + \hat{X}_2 \end{bmatrix} \\ &- \begin{bmatrix} \overline{W}_{F11} & \overline{W}_{F12} \\ \overline{W}_{F21} & \overline{W}_{F22} \end{bmatrix} \begin{bmatrix} \widehat{AC}_1 \\ \widehat{AC}_2 \end{bmatrix} \left( \frac{-\dot{\hat{X}}_1}{\sqrt{\dot{\hat{X}}_1^2 + \hat{X}_1^2}} \right) \\ &- \begin{bmatrix} \overline{W}_{NL11} & \overline{W}_{NL12} \\ \overline{W}_{NL21} & \overline{W}_{NL22} \end{bmatrix} \begin{bmatrix} \dfrac{\tau_m}{(\hat{d}_{01} - \overline{X}_1 - \hat{X}_1)^2} \\ \dfrac{\tau_m}{(\hat{d}_{02} - \overline{X}_2 - \hat{X}_2)^2} \end{bmatrix} = \begin{bmatrix} 0 \\ 0 \end{bmatrix}. \end{aligned} \tag{7.3}$$

The resulting periodic response of the system as a function of tip-sample separation $d_0$ is found using the COCO continuation toolbox with MATLAB® [100]. To perform the simulations, a two beam array system was used with 16 mm separation between cantilevers. A tip mass of 0.35 g was added to beam 1 and 0.68 g was added to beam 2, creating an uncoupled frequency gap of 1.12 Hz (which corresponds to a normalised frequency gap of to 0.025). Excitation actuation and tip forces are applied to beam 1 only, lowering its resonant frequency to approach that of beam 2 as tip-sample separation distance is reduced. A damping coefficient of 0.007 was applied to each beam and the actuation term $\widehat{AC}_1$ was set to 0.01, which corresponds to a far field amplitude of 1.35 mm for the uncoupled system. The simulations are performed in the vicinity of the frequency cross-over point, which is where maximum sensitivity is expected to occur. Varying lengths of shared base material are simulated to demonstrate the influence of coupling on the achievable increase in sensitivity. Enhanced sensitivity is demonstrated by simulating the frequency approach curve for the described two beam array and comparing it to the frequency approach curve of an equivalent single beam in Figure 7.1.

The blue line in Figure 7.1 represents the functional relationship between resonant frequency output and tip-sample separation for a standard single beam system. A steady, monotonic decrement in resonant frequency is observed, which is expected of a single cantilever subjected to long range attractive tip forces [3]. In comparison, it can be seen that the addition of

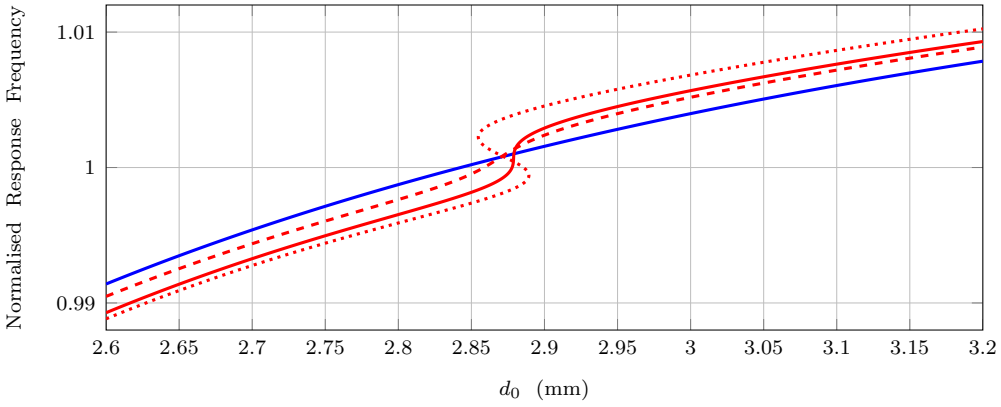


Figure 7.1: Simulated frequency approach curves for a two beam array (red) and a single beam (blue). The solid red line represents an array with 9.5 mm of shared base material, which is close to the boundary of bifurcation in the approach curve. The dashed line represents an array with 9 mm of shared base material and the dotted line represents an array with 10 mm of shared base material.

mechanical coupling between two cantilevers of differing mass and stiffness properties can induce significant deviations from the smooth trend at the point of frequency cross-over, which for the simulation parameters used is at a $d_0$ value of 2.84 mm. It can be seen that a significant increase in functional gradient can be achieved with the array compared to the single cantilever, which can be utilised for enhanced sensitivity imaging. In the figure, the approach curves of three array systems are presented, each with a different coupling parameter. As coupling is increased, two saddle-node bifurcation points occur and multiple solution branches appear (as was shown in Chapter 6), with an area of increased functional gradient between the saddle-nodes. This means that sensitivity increase can be achieved by using either the stable frequency branch below the point of bifurcation, or the unstable frequency branch between the two saddle nodes above the point of bifurcation. The results presented with 9.5 mm of shared base material are in the region of maximum achievable sensitivity increase. It is evident from the frequency approach curves that the hypothesis that enhanced sensitivity can be achieved utilising array response is confirmed, and has promising potential. Simulations were performed over a range of coupling parameters, and the key relationships between output sensitivity and coupling strength are presented in Figure 7.2.

The results presented in Figure 7.2a show that a peak in increased sensitivity occurs with approximately 9.5 mm of shared base material, and that at its peak the theoretical increase in functional gradient is up to two orders of magnitude. The curve represents the maximum sensitivity increase

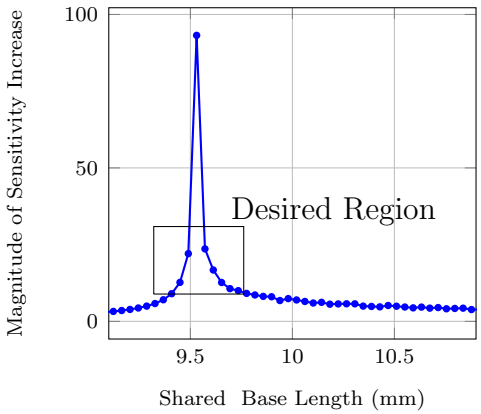


(a) Magnitude of the maximum measured frequency increase using a two beam array over an equivalent single beam in FM-AFM as a function of the coupling strength (amount of shared base material).

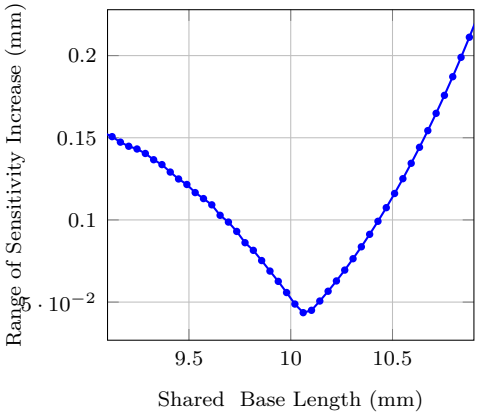


(b) Range of tip-sample separation over which a sensitivity increase of at least 10 % is measured using a two beam array over an equivalent single beam in FM-AFM as a function of the coupling strength (amount of shared base material).

Figure 7.2: Key relationships between achievable sensitivity parameters and the coupling parameter (shared base length) for a two beam array using FM-AFM.

observed as a ratio between the two beam response gradient and the single beam response gradient at an equal separation distance. It should be noted that in cases where a saddle node bifurcation occurs, the gradient at the bifurcation point is not included, as it approaches infinity and is not usable practically. It is apparent that an optimal coupling strength exists for maximum sensitivity, but that achievable sensitivity increases are highly dependent on coupling strength, requiring tight parameter control. The implications of this will be discussed further in Section 7.5. It is clear that sensitivity increase can be achieved by operating either above or below the point of bifurcation. In Figure 7.2b, the tip-sample separation distance range over which sensitivity increase occurs is presented. This represents the total separation distance range over which a functional gradient at least 10 % greater than that of the single beam system is observed. There is a roughly inverse relationship between achievable maximum sensitivity increase and the range over which a sensitivity increase is observed. A trade-off is evident from the simulations between these two parameters. The desirable region is highlighted in Figure 7.2a. This is the location at which significant increases in sensitivity can be achieved, but without approaching too close to the point of singularity where the theoretical gradient approaches infinity.

The principle of functional gradient increase has been successfully demonstrated, however, the phenomenon has not yet been linked to the modal response. The mathematical simulations can be used to assess the under-

lying dynamic principles behind the observed frequency approach curves. To do this, the amplitude of both beams as well as the spatial shape of the modal response are analysed. The simulations were performed with a constant actuation amplitude, and automatic gain control (AGC) providing a constant output amplitude was not implemented. For this reason, the simulated amplitude response is not constant for the actuated beam, as would be expected for conventional FM-AFM. The spatial mode shapes at the cantilever tips are presented in Figure 7.3 and the amplitude response is presented in Figure 7.4.

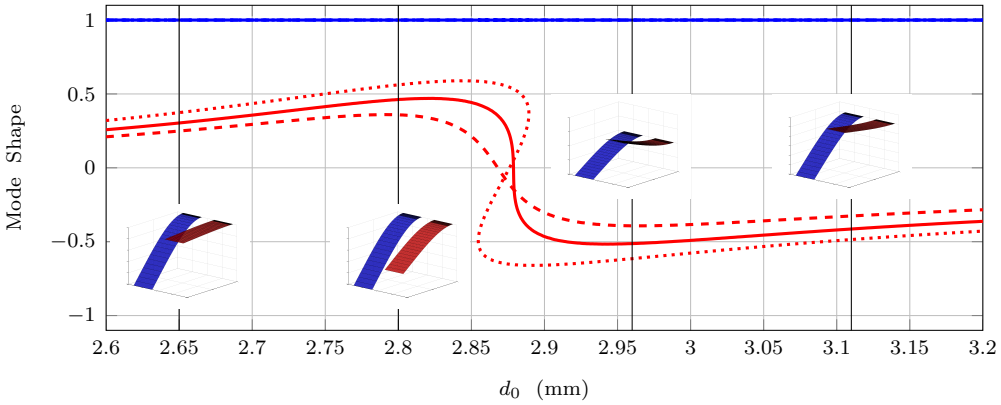


Figure 7.3: Simulated mode shapes of a two beam array during FM-AFM operation in normalised units of displacement. A mode shape of 1 and 1 represents perfectly in-phase response and a mode shape of 1 and −1 represents perfectly out-of-phase response. The solid line represents an array with 9.5 mm of shared base material, the dashed line represents an array with 9 mm of shared base material and the dotted line represents an array with 10 mm of shared base material. The inserts are a visual representation of the mode shapes at the points represented by the vertical lines. Blue - Beam 1, Red - Beam 2.

To confirm the hypothesis of this chapter, it should be possible to link the frequency approach curve observations to the principle of eigenmode shifts. The shift in modal response is apparent in Figure 7.3, which depicts the mode shapes of the cantilever tip displacements for the three aforementioned coupling levels. In addition, a visual depiction of the mode shapes at specific points in parameter space are shown. Above the frequency cross-over point, the modal response is out-of-phase and dominated by the actuated beam due to the disparity in far field resonant frequency. As the resonant frequencies of the two beams approach due to tip forces, the modal response transitions from single beam dominated to a two beam array mode. At frequency cross-over, the dominant mode (at which the system is excited) switches from out-of-phase (nominally array mode 2) to in-phase (nominally array mode

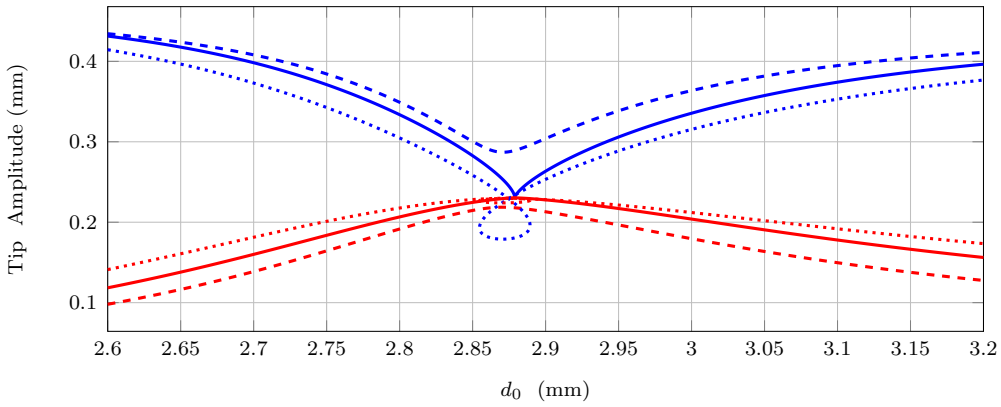


Figure 7.4: Simulated amplitude response of the two beam array (blue - beam 1, actuated, red - beam 2, passive) during FM-AFM operation. The solid line represents an array with 9.5 mm of shared base material, the dashed line represents an array with 9 mm of shared base material and the dotted line represents an array with 10 mm of shared base material.

1). This transition of array mode response accounts for the observed sharp transition in actuation frequency. As the tip-sample separation distance is further reduced, the cantilever resonant frequencies move apart, and the system again reverts to a single beam dominant mode. This confirms the presumption that it is a shift in the type of modal response of the system that is responsible for the increase in functional gradient.

From the amplitude response curve in Figure 7.4, a drop in amplitude of the actuated beam is observed, coupled with a rise in the amplitude of the passive beam in the vicinity of frequency cross-over. This phenomena is a result of the increased transfer of energy to the passive beam as resonance is approached. In addition, the change in amplitude at frequency cross-over increases for stronger coupling, again due to increased energy transfer as a result of the added stiffness created by added coupling material. The amplitude response can be used to relate the observe eigenmode shifts to the mathematical model by again utilising the perturbed analytical solution that was derived in Section 6.5. The final equations are repeated here for reference. The definitions of $B_{11}$ to $B_{27}$ and their derivations can be found in Appendix D, $a_1$ represents the amplitude of mode 1 and $a_2$ represents the amplitude of mode 2.

$$\boldsymbol{B_{11}}a_1^6 + (\boldsymbol{B_{12}}a_2^2 + \boldsymbol{B_{13}})a_1^4 + (\boldsymbol{B_{14}}a_2^4 + \boldsymbol{B_{15}}a_2^2 + \boldsymbol{B_{16}})a_1^2 + \boldsymbol{B_{17}} = 0, \quad (7.4)$$

$$\boldsymbol{B_{21}}a_2^6 + (\boldsymbol{B_{22}}a_1^2 + \boldsymbol{B_{23}})a_2^4 + (\boldsymbol{B_{24}}a_1^4 + \boldsymbol{B_{25}}a_1^2 + \boldsymbol{B_{26}})a_2^2 + \boldsymbol{B_{27}} = 0, \quad (7.5)$$

It can be seen that as the response amplitude of the passive beam increases (dominanted by the first modal amplitude, $a_1$), the coefficients of the quartic and quadratic terms of (7.5) are altered significantly, resulting in a rapid change in the roots of the equation, which corresponds to the observed shift in spatial mode shape and resonant frequency. It follows that the rate of change of the modal shape functions are linked to excitation amplitude and system damping as well as coupling strength, and a unique point in parameter space does not exist that produces a maximum sensitivity increase, but instead is dependent on all three parameters. To confirm this inference the impact of excitation amplitude in particular is analysed through simulation, tracking the maximum functional gradient increase over an equivalent single beam system as the input amplitude to beam 1 ($AC_1$) is varied from 0.002 to 0.015. The simulations are performed using the previously found optimal coupling strength, which occurred at 9.5 mm of shared base material. The functional relationship between input amplitude and maximum sensitivity increase can be viewed in Figure 7.5.

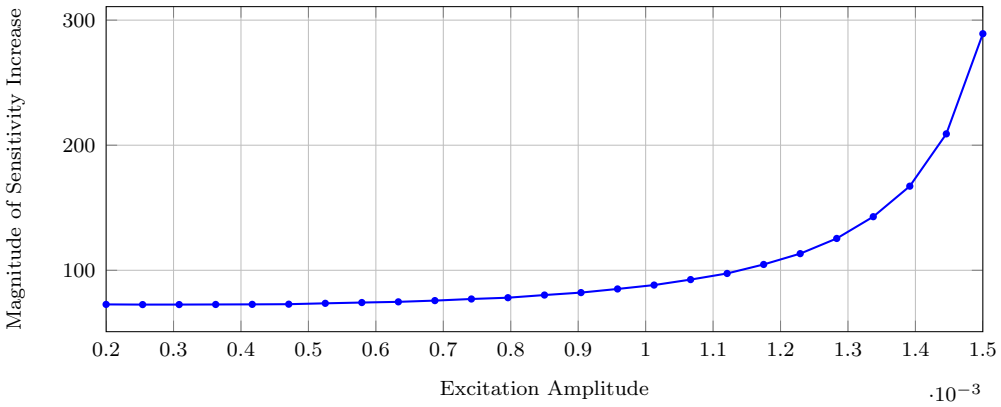


Figure 7.5: Simulated magnitude of the maximum measured frequency increase using a two beam array with 9.5 mm of shared base material over an equivalent single beam in FM-AFM as a function of the excitation amplitude.

It can be seen from Figure 7.5 that by tuning the applied excitation amplitude, the magnitude of sensitivity increase can be increased from a the previous level of 90 with an excitation term of 0.01 to 300 with an excitation term of 0.015. This demonstrates that achievable sensitivity is a function of multiple parameters, and that a single optimal point does not exist. The result also demonstrates that while coupling strength can be tuned during fabrication to maximise achievable sensitivity, the excitation amplitude can be tuned during operation to adjust sensitivity, the implications of which are discussed in Section 7.5.

## 7.4 Experimental Investigation

To validate the proposed method of sensitivity enhancement and the results of the mathematical simulations, experimental investigations are conducted using the macro scale test rig. A replication of the frequency approach curves is first conducted as a proof of concept and as a comparison to Figure 7.1. To conduct the experiment, a two beam array was used with coupling of 9 mm of shared base material and a separation distance of 16 mm between the beams. This was found to be a suitable level of coupling to ensure a frequency gradient increase was achieved at the point of frequency cross-over without without inducing a saddle node bifurcation. Coupling level was not optimised as the purpose of the experiments was proof of concept only. Tip forces and excitation were applied to beam 1 only (active beam) and beam 2 was left passive. A tip magnet with mass 0.35 g was applied to both cantilevers, and an additional mass of 0.33 g was applied to the passive cantilever. This produced a frequency gap between the cantilever far field resonant frequencies of 2 Hz. The experimental parameters are presented in Table 7.1 and the frequency approach curves are depicted in Figure 7.6.

Table 7.1: Operating parameters used to generate the frequency approach curves in Figure 7.6.

| | Array Beam 1 | Array Beam 2 | Single Beam |
|---|---|---|---|
| Input Amplitude | 0.7 V | 0 | 0.7 V |
| Far Field Amplitude | 3.0 mm | 0.25 mm | 2.7 mm |
| Tip Mass | 0.35 g | 0.68 g | 0.35 g |
| Far Field Frequency | 47.4 Hz | 45.5 Hz | 46.4 Hz |
| Shared Base Length | 8 mm | 8 mm | N/A |
| Separation Distance | 16 mm | 16 mm | N/A |

It can be clearly seen in Figure 7.6 that a distinct increase in the gradient of the frequency approach curve is observed for the two beam array at the point of frequency crossing (magnified in the figure). The gradient at this separation distance is observably greater than the gradient of the single beam frequency curve at a comparable separation distance. No significant difference was noted when using 7 mm or 8 mm of shared base material, whilst above 10 mm there appeared to be a hysteresis in the approach curve due to bifurcation events, which complies qualitatively with the results from the simulations. The lack of a clear distinction between 7 and 8 mm is in

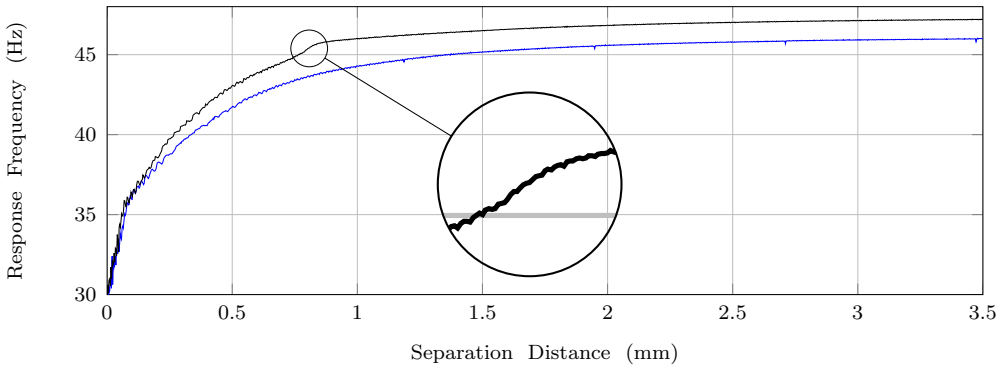


Figure 7.6: Macro experimental frequency approach curves of a single cantilever (blue) and a two beam array (black). The coupling strength and far field resonant frequencies of the array are set so as to achieve a functional gradient increase at the point of frequency cross-over (magnified).

contrast to the simulation results, and is likely due to the precision limits of the test equipment. Despite these discrepancies, the depicted approach curves demonstrate that the simulation results are replicable in experiment and that the sensitivity enhancement concept has potential in practical applications.

To demonstrate the potential benefits of utilising the eigenmode shifts at the frequency cross-over point in a two beam array, experiments were conducted using feedback control to hold the active cantilever at a user defined set point. The results are directly comparable to those presented in Section 4.4.3, which demonstrated the ability of the macro test rig to perform feedback control and showed the precision achievable with a single cantilever. The same control program and experimental procedure is used here with both the single cantilever and two beam array with the parameters in Table 7.1. The control gains used in Section 4.4.3 (Table 4.6) are used again for the array. A user defined frequency set point was tracked using feedback control whilst the magnet displacement was measured. Offsets were added to the magnet position at set intervals through a manual input in the control program, and the precision with which the system would return to the set point was measured. The frequency set point of the two beam array was defined as 45.4 Hz, which is the point of frequency cross-over and the identified point of maximum sensitivity from Figure 7.6. The set point of the single beam was defined as 44.3 Hz, which was the resonant frequency of the single cantilever at an equivalent tip-sample separation distance to the location of frequency cross-over of the array. An equivalent tip-sample separation was chosen for both systems so that the results could be comparable, as sensitivity is also a function of separation distance. This is evident

from Figure 7.6, which demonstrates that the frequency gradient increases as the tip approaches the surface due to the increasing force gradient from the magnet. The displacement tracking results are presented in Figure 7.7 and the frequency tracking results are presented in Figure 7.8.

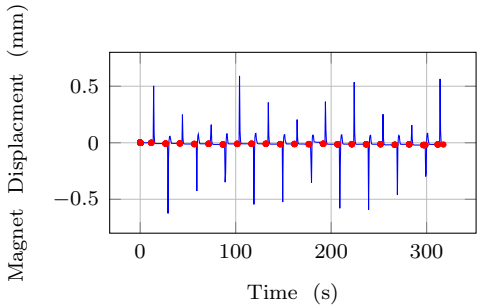


(a) Magnet displacement during FM-AFM operation with the two beam array. The red dots indicate the convergence points.

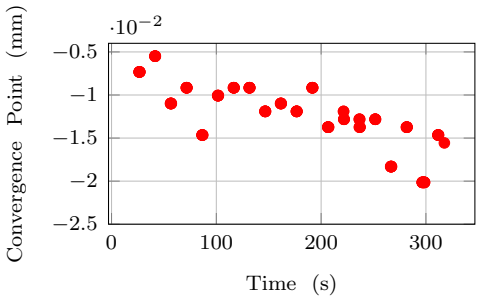


(b) Close up of the convergence points only for the two beam array.

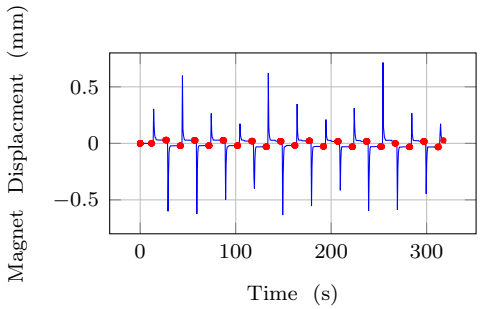


(c) Magnet displacement during FM-AFM operation with the single beam. The red dots indicate the convergence points.

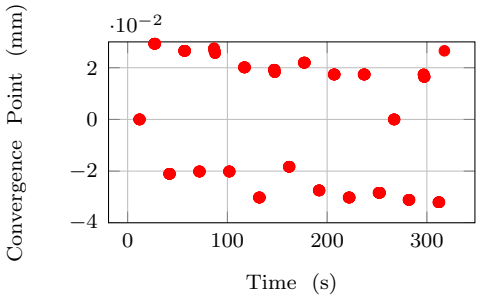


(d) Close up of the convergence points only for the single beam.

Figure 7.7: Magnet displacement during experimental FM-AFM operation on the macro scale with both a single beam and a two beam array.

Tracking of the user defined frequency set point was achieved with both the single cantilever and the two beam array, with both systems producing repeatable results. The convergence points presented in Figures 7.7b, 7.7d, 7.8b and 7.8d are the displacement/frequency values that the system converges to after each manually applied offset, and offer a representation of the measurement precision that can be achieved with each setup. The key statistics of the convergence points are presented in Table 7.2.

It can be seen that a near order of magnitude drop in measurement standard deviation is achieved using the two beam array at the frequency cross-over point over that of an equivalent single beam system. A significant decrease in the total range of the data points is also achieved with the array.

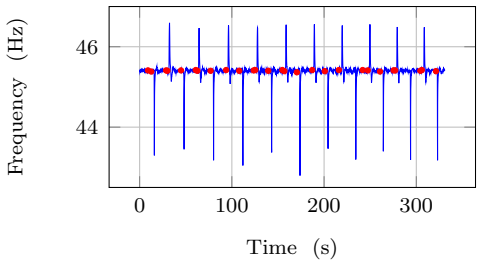


(a) Measured resonant frequency during FM-AFM operation with the two beam array. The red dots indicate the convergence points.

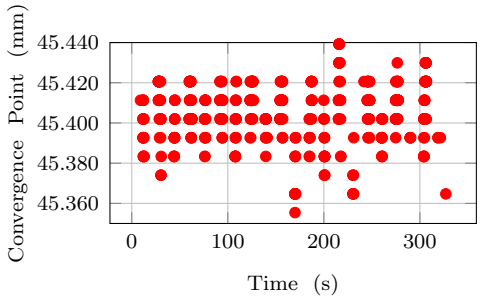


(b) Close up of the convergence points only for the two beam arrays.

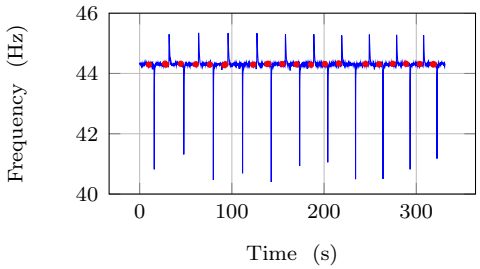


(c) Measured resonant frequency during FM-AFM operation with the singe beam. The red dots indicate the convergence points.

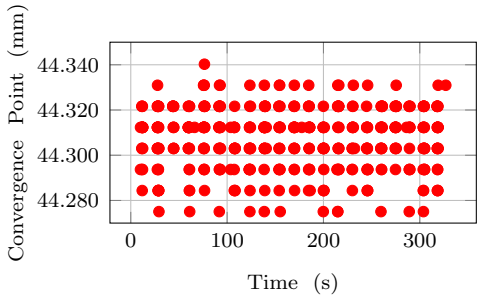


(d) Close up of the convergence points only for the single beam.

Figure 7.8: Measured resonant frequency during experimental FM-AFM operation on the macro scale.

The standard deviation of frequency error is little changed between the array and the single beam. This is to be expected, as the resonant frequency is the measured feedback parameter and measurement error is due to the precision of the sensor hardware, which is independent of the dynamic properties of the system. The results are promising, further suggesting the feasibility of the proposed method of sensitivity enhancement. It should, however, be noted that a significant deadband error is present in the response of the single beam, which is dependent on the manually applied error signal being positive or negative. This error was also identified in Section 4.4.3, where it was concluded that backlash in the magnet actuator gearing and surface structure was the cause. The same error is not present for the two beam array, which is likely due to the oscillatory motion present in the frequency response signal prior to convergence (seen in Figure 7.11). It is possible that the oscillatory motion about the set point reduces the contrast due to backlash in the actuator/magnet system. When deadband error is removed from Figure 7.7d, the upper data points have a mean of 0.0217 and

Table 7.2: Key statics for the displacement and frequency steady state error of the single beam and two beam systems during FM-AFM operation.

| | Two Beam | | Single Beam | |
|---|---|---|---|---|
| | Disp. | Freq. | Disp. | Freq. |
| Data Points | 135 | 522 | 207 | 442 |
| Mean | −0.0124 mm | 45.4050 Hz | −0.0015 mm | 44.3077 Hz |
| Std. Dev. | 0.0037 mm | 0.0147 Hz | 0.0235 mm | 0.0130 Hz |
| Range | 0.0146 mm | 0.0838 Hz | 0.0613 mm | 0.0652 Hz |

a standard deviation of 0.0045, while the lower data points have a mean of -0.0262 and a standard deviation of 0.0050. The convergence statistics of the two beam system are still an improvement over the single beam with deadband error removed, but the improvement in measurement standard deviation is greatly reduced. More precise data could not be obtained due to the measurement tolerance limitations of the experimental equipment. Further improvements to the test rig are required to reduce measurement variance and better verify the sensitivity enhancement capable with the two beam system.

The performance of the two beam array can be further analysed by looking at the control input and frequency error required to hold the active cantilever tip at the defined set point, and compare it to the equivalent single beam. It is expected that steady state error would be reduced, as smaller fluctuations in frequency can be detected and corrected by the controller due to the increased functional gradient. To test this hypothesis, the same experimental parameters were again used (Table 7.1) with both a single cantilever and two beam array. Both systems were held at their respective set points and both the control input sent to the magnet actuator and the measured resonant frequency were recorded. The control error is presented in Figure 7.9 and the frequency error is presented in Figure 7.10.

It is evident from the figures that there is a measurable drop in both the control error required to hold the system at the set point and the error in measured frequency when using the two beam array. This conclusion is backed up by the statistics presented in Table 7.3, which show a 45 % reduction in the standard deviation and range of data points for both the control and frequency error. Above a certain threshold of sample displacement error, a frequency shift above the measurement noise threshold will be detected by the controller, depending on the functional gradient between the measured variable (frequency) and the control variable (sample displace-

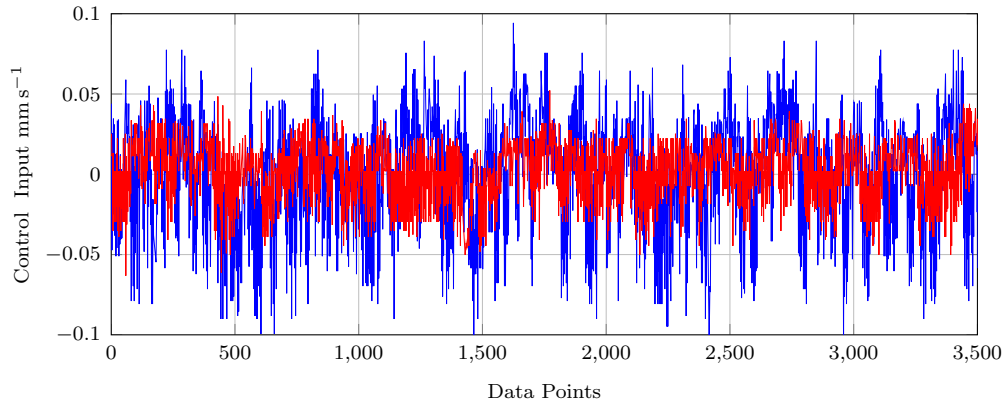


Figure 7.9: Experimental instantaneous control input to the magnet actuator on the macro scale (control input is actuator velocity in units of mm s$^{-1}$) whilst the system is held at the set point. The blue data points represent the single beam and the red data points represent the two beam array.

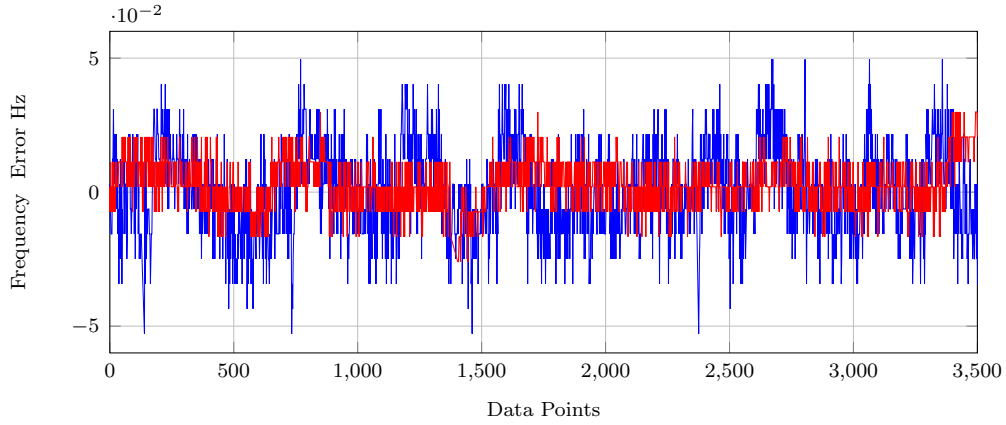


Figure 7.10: Experimental instantaneous frequency measured at the active cantilever on the macro scale whilst the system is held at the set point. The blue data points represent the single beam and the red data points represent the two beam array.

ment). This will generate a control input to restore the system to the user defined set point. It holds that as the functional gradient is greater for the array, the displacement threshold above which a statistically significant frequency shift is detected is lower for the two beam system than that of the single beam. The reduction in measured control error is suggestive of a reduced displacement error threshold, as the controller is able to maintain a close tracking of the set point, reducing the maximum control input required to restore the system to equilibrium. This result further backs up the hypothesis that eigenmode changes in an array can be used to in-

crease the measurement sensitivity of AFM. The data, however, is subject to the same sources of error and measurement limitations as have been discussed previously. Whilst the conclusions drawn are valid, it is suggested that greater measurement and sample displacement precision are required to fully validate the experimental findings.

Table 7.3: Key statics for the measured control input and frequency error of the single beam and two beam systems during FM-AFM operation.

| | Two Beam | | Single Beam | |
|---|---|---|---|---|
| | Cntr. Err. | Freq. Err. | Cntr. Err. | Freq. Err. |
| Mean | 0.0033 | 0.0033 | -0.00075 | -0.00048 |
| Std. Dev. | 0.0202 | 0.0098 | 0.0362 | 0.0178 |
| Data Range | 0.1323 | 0.0559 | 0.1990 | 0.1024 |

As was mentioned previously, the frequency response signal of the two beam array depicts a greater settling time in comparison to the single beam system (Figure 7.11). The settling time was defined as the time taken for all measured frequency points to be within 0.1 % of the defined set point, as is marked on Figure 7.11. The single beam settling time was 2.2 s and the two beam settling time was 7.8 s, an increase of 3.5 times. Due to the coupling between the cantilever in the array, energy transfer occurs. The transfer of energy between beams requires a greater amount of time than the transfer of energy from the actuator to the actuated beam. This increase in energy transfer time results in a longer time period for transients to die out and for steady state to be reached. The increase in time at which transient terms are significant in the array response is the likely reason for the increased settling time observed in the controlled experiments. The increase in settling time would result in a reduced maximum imaging speed in comparison to a standard single beam system, which is a disadvantage. The same feedback control loop and control gains were used for both the single beam and the array, to ensure a direct comparison of sensitivity could be made. It is possible that optimisation of the feedback control gains specifically for the array system could be used to reduce the settling time. It is also possible that enhanced sensitivity imaging would only be necessary for imaging small areas of interest on a sample, such that the loss of imaging speed is not a major drawback in comparison to the advantage of greater imaging resolution. The emphasis of this chapter is on the proof of principle of enhanced sensitivity measurement, and hence optimisation of the control system is not included.

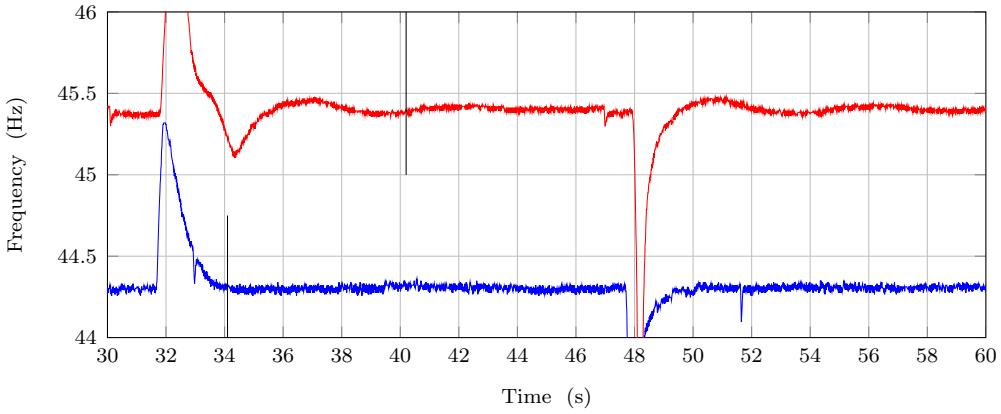


Figure 7.11: Experimental instantaneous excitation frequency during FM-AFM operation on the macro scale as the system convergences to the set point. The vertical black lines indicate the estimated location at which the system has settled to within 0.1 % of the defined set point.

## 7.5 Technological Implications

It is necessary to consider the practicality of implementing the proposed method of sensitivity enhancement as well as the hardware requirements and constraints needed for effective implementation. These considerations are related to the design and fabrication of cantilever arrays, and providing solutions to the discussed issues is outside the scope of this thesis. The purpose of this section is to discuss the required parameter values and tolerances necessary for the proposed technology to function, as well as to highlight advantageous design features that could be incorporated into the TUI array design. The implementation of features discussed here can be incorporated into the research work conducted by the TUI team (which will be further discussed as part of the future research in Section 8.2).

The most important consideration with regards to the practical fabrication of arrays for enhanced sensitivity is the dimensional tolerances required to produce the necessary dynamic properties. As was shown in Section 7.3, the increase in frequency gradient is highly sensitive to the level of coupling in the system in relation to the length of shared base material. A significant change in maximum sensitivity increase was observed with a change in shared base material length of only 0.1 % of the cantilever length (0.2 mm change in base length in Figure 7.2a in comparison to a cantilever length of 160 mm). For the reliable implementation of the technology, it is necessary to ensure that the designed sensitivity can be achieved repeatedly using fabrication techniques that can be scaled for high quantity manufac-

ture without excessive cost. If a minimum sensitivity threshold cannot be achieved reliably, or if the cost of manufacturing with this tolerance level is significantly greater than existing single cantilever systems, the technology would not be feasible for real world applications. This is a critical consideration that should be investigated before proceeding further with the proposed application of the array technology. In addition to coupling level, the frequency gap between the cantilevers is another crucial parameter that must be tightly controlled, as this parameter determines the location of the frequency cross-over point and hence the height above the sample at which maximum sensitivity will be achieved. The frequency shift expected due to tip-forces from standard single beam FM-AFM techniques is on the order of 10s to 100s of Hz [108], which is the frequency gap that must be designed into the TUI arrays. To create a change in resonant frequency of 10 Hz requires changing the cantilever length by 50 nm (0.014 % for a nominal length of 350 µm) or else changing the tip mass by an amount of 0.075 ng (equivalent to a gold sphere with diameter 1 µm. These are the mass and length tolerances that must be achievable for the proposed method of enhanced sensitivity to be practically implemented. It is necessary that the variance in frequency gap be kept low to ensure that the frequency cross-over point will not occur too far above the sample, which would reduce measurement resolution, or else will not occur after the pull-in instability point, which would render it unusable. Another promising method of frequency tuning has been presented by Schuh et. al. [107], who used micro-milling techniques to remove mass from a cantilever to tune the resonant frequency.

An important aspect of the AFM measurement process is the influence of imaging height above the surface in relation to the achievable resolution. To maximise the influence of the tip-sample interaction forces on cantilever response, it is desirable to excite the cantilever tip with a low amplitude close to the sample surface, to ensure the tip remains far within the potential well. This concept is well described by the single beam frequency approach curve (Figure 7.6), which shows how the rate of change of frequency shift increases significantly as the beam tip approaches the sample surface. The issue is that the tip is close to the point of instability where jump-to-contact can occur. If the instability point is crossed the imaging process is disrupted and the sample and beam tip can be damaged. As a result there is a trade-off that must be made between maximising image resolution and reducing the risk of entering the region of instability. The two beam array offers an improvement as the system can be designed such that a point of high functional gradient is located away from the instability point by selection of the cantilever frequency gap.

Using existing array designs and fabrication techniques, arrays for en-

hanced sensitivity would be created with coupling strength and frequency gap fixed following fabrication. As frequency cross-over occurs at a unique height above the sample, the separation distance at which maximum sensitivity occurs will be pre-determined by the design parameters, and not adjustable by the end user. This may be a significant drawback of the technology, as the optimal separation distance used for imaging with FM-AFM is almost always tuned by the end user. It would be advantageous in particular if the individual cantilever frequency properties could be adjusted (with certain limits) by the end user. This would ensure the ability to adjust the height above the sample at which measurements can be taken is maintained by allowing the user to control the location of the frequency cross-over point. Publications are present in the literature relating to the in-situ tunability of cantilever stiffness (and hence resonant frequency), including a publication by the Tamayo group [109], where the authors investigates applying small transverse curvatures to a cantilever structure as a way of adjusting stiffness properties. Such a technique could be applied to the cantilevers in the TUI arrays, providing the end user with a mechanism by which the frequency gap could be adjusted. In addition to the location of the cross-over point, it has been shown that the achievable sensitivity increase as a function of coupling strength is fixed following fabrication. It would be desirable to be able to tune the sensitivity of the system using controllable system inputs. This can be achieved by adjusting the amplitude of excitation applied to the active beam, as has been demonstrated through simulation. This feature of the system response gives the end user the ability to just system sensitivity within limits, depending on the application and desired output image parameters. As an alternative view, it is possible to look at the lack of flexibility in excitation amplitude selection as an advantage for ease-of-use. The required excitation amplitude for optimal sensitivity can be pre-defined within the AFM system, meaning a skilled user is not required to tune the excitation amplitude. Further investigation would be required to determine the suitability of this method.

## 7.6 Conclusion

In this chapter, a method of increasing the sensitivity of FM-AFM measurement using the modal response of a coupled array has been presented and validated. The method is based on the idea that eigenmode shifts occur within the array system at the point of frequency cross-over, which can result in an orders of magnitude increase in the functional gradient of the frequency response relative to the tip-sample separation distance. The functional gradient increase was demonstrated numerically using the

mathematical model, which showed that achievable sensitivity increase was highly dependent on the level of coupling in the system, and that a sensitivity increase over an equivalent single beam system of orders of magnitude was possible by varying the coupling strength (Figure 7.2a). Furthermore, numerical simulations were used to demonstrate the transition of the system from an out-of-phase to an in-phase array mode, which was the cause of the observed frequency gradient increase, confirming the hypothesis that eigenmode shifts could be used to increase the sensitivity of the system to changes in tip-sample separation.

An experimental investigation was conducted using the macro scale test rig to confirm the results of the numerical simulations. Frequency approach curves were measured for a two beam array, which clearly demonstrated an increase in functional gradient at the cross-over point qualitatively similar to the simulated approach curves. The two beam array was used to track a user defined frequency set point, which was defined at the point of cross-over. The measurement error was compared to an equivalent single beam system at an equivalent height above the sample, and an increase in measurement precision was demonstrated. The achievable increase in measurement precision was limited by the resolution of the stepper motors used to move the sample surface and the rigidity of the test rig. Improvements to these aspects of the test rig should be considered to improve the quality of data acquired, which will be further discussed in Section 8.2.

Finally, the technological implications of the proposed measurement method were discussed, focusing on the required fabrication tolerances and functionality of the TUI arrays. This discussion presents the challenges that must be overcome with regards to the array design and fabrication aspects of the research project.

CHAPTER 8

# Conclusions and Future Outlook

## 8.1 Summary and Conclusions

AFM has been a useful tool for scientists and engineers for the past ≈30 years, producing high resolution images of sample surfaces down to the molecular level. AFM has found many applications, and in particular has been used extensively in the fields of biology and material science. The technology is used to image sample topography and measure material properties with extremely high precision in a non-invasive and non-destructive manor. Since its inception in 1986, many research groups have worked towards improving the capabilities of AFM. The areas of research can be organised into the following categories; increasing the rate at which information about the sample surface can be acquired; acquiring additional information about the sample material properties as well as topography; and enhancing the precision and reliability with which data can be obtained. The research presented in this thesis is inspired by the work conducted by the Rangelow group at the Technische Universität Ilmenau in Germany, who have constructed arrays of AFM cantilevers for the purpose of increasing imaging speed and measurement density, allowing multiple points on a sample to be measured in true synchrony.

It was shown that a wide range of AFM arrays already exist in the literature for the purpose of parallel measurement going back to the early 90s. The vast majority of the arrays identified all had the same drawback, which was that the beams were widely spaced, greatly reducing the potential increase in measurement density that could be achieved. The TUI arrays overcome this issue by placing cantilevers in close proximity (spacing less than 10 % of the cantilever width) to maximise the number of points that can be measured simultaneously over a given area. This method introduces non-negligible mechanical coupling between the individual cantilevers through the shared base structure, which when combined with the nonlinear force gradient resulting from interaction between the cantilever tip and

sample introduces complex nonlinear response characteristics to the system. The coupled, nonlinear response of the arrays, and how it relates to parameter space, is currently not fully understood. This prevents the application of the technology due to a lack of imaging reliability. The main purpose of this thesis has been to use a combination of experimental investigation and mathematical modelling to understand how the cantilevers of the TUI arrays are interacting, how the interactions influence the response observed, the relationship between the physical parameters of the system and the observed response, and to suggest how adverse dynamic phenomena resulting from nonlinear interactions can be eliminated or mitigated. In addition, speculative research has been conducted to determine if mechanically coupled cantilever arrays can be utilised to address other open questions in the field of AFM research, specifically the question of how to enhance measurement precision and reliability.

To produce the novel research outcomes of this thesis, three distinct tools were utilised. An experimental test rig was used to measure the response of the TUI arrays, which was done at our collaborators site. This test rig was first used to determine the type of modal response of the TUI arrays, specifically to determine if the system was weakly coupled, with modal response dominated by single cantilevers, or strongly coupled, with modal response dominated by the phase between cantilevers. The type of modal response was linked to cantilever spacing and resonant frequency gap. Once the response without tip-sample interaction forces had been analysed, the array was brought into close proximity with a silicon test surface to measure the combined influence of mechanical coupling and tip-sample forces. The experiments were used to identify the dynamic phenomena that could be responsible for the lack of imaging reliability, to provide the focus point for the research. The second tool used was a mathematical model of the cantilever array. The model was developed to find the modal response of an array with varying levels of coupling through a shared base, and to determine how modal response was altered by the influence of tip-sample forces. This was done through numerical simulations as well as analytical perturbation methods. The main use of the model was to link design parameters to output response so that adverse phenomena could be avoided and advantageous phenomena could be utilised. The final tool developed was a macro scale test rig that mimicked the dynamics of the TUI micro arrays at a length scale 500$\times$ greater. The macro scale test rig allowed for visual observation of the state of response when in close proximity to a simulated sample surface, and allowed for quick and low cost adjustments to key parameters to be made. The purpose of the macro scale test rig was to test array response over a large range of parameters, particularly the amount of

shared base material, for validation of the mathematical model and to gain a better understanding of how the parameter space results in the observed array response.

To ensure that the research conducted for this thesis produced outcomes that were relevant to AFM array technology, it was necessary to gain an understanding of the response characteristics of the fabricated TUI arrays. This work is presented in Chapter 3. Experiments were conducted at our collaborators site to gain an understanding of the type of coupled response resulting from mechanical base coupling, and how the type of coupled response was altered by the addition of interaction forces between the cantilever tips and a sample surface. Initially a single cantilever was tested to determine the Q factor of the system in air and the amount of intrinsic nonlinearity in the cantilever. The single TUI cantilever was found to have a Q factor of 220, which is within the range expected for operation in air, and negligible intrinsic nonlinearity. The single cantilever results were used for comparison with the macro scale test rig to ensure similar levels of damping and nonlinearity, which was achieved. Initially, the arrays were tested at far field using frequency sweeps to find the modal resonant frequencies and to identify the qualitative level of coupling. The measured responses demonstrated weak coupling in the array, with the response of each mode dominated by a single cantilever. It was also shown that the individual cantilever resonant frequencies and the physical separation between beams had a near equal influence on the transfer of energy between beams. This result suggested that the influence of coupling could be altered by adjusting the individual cantilever resonant frequencies, rather than trying to further limit the amount of shared base material through which energy transfer could occur. The array response was also measured in the presence of tip sample forces, which was done by actuating individual beams in the array at a fixed frequency and amplitude and lowering the entire array towards a flat silicon test surface. The data displayed was output amplitude as a function of the array height above the sample. This display style was termed the amplitude approach curve. The results depicted discontinuous jumps in amplitude at specific locations in the amplitude approach curve which did not occur in the response of a single cantilever subjected to the same experimental procedure. It was hypothesised that the presence of discontinuous jumps was a primary cause of the TUI array's lack of imaging reliability, and could be linked to nonlinear phenomena resulting from the combination of mechanical base coupling and tip-sample interaction forces. The thesis was directed to confirming that weak coupling was responsible for the observed far-field array response, identifying how both cantilever separation and frequency gap influenced the transfer of energy between beams, and understanding

why discontinuous jumps were observed in the amplitude approach curves and how the nonlinear response links to the parameter space.

In Chapter 4, the development of the macro scale test rig mimicking the dynamics of the micro scale arrays is discussed. The test rig is used to measure array response in a wide range of parameter space. It incorporates both mechanical base coupling and nonlinear tip forces in the form of permanent magnets, creating a system that is qualitatively similar to the TUI arrays. The developed macro scale test rig is a novel tool, and similar systems have not been used previously in the literature for studying micro scale dynamics in the context of coupled AFM arrays in close proximity to a surface. The test rig was capable of capturing both weakly and strongly coupled phenomena at far field, with good agreement between experimental data and mathematical simulations. The test rig was successfully used to directly observe the state of response of a cantilever array in a range of parameter space. Specifically, the test rig allowed for easy visual observation of where each tip was in relation to the corresponding surface magnet.

The mathematical model of a base coupled array of cantilevers subjected to nonlinear tip forces was derived in Chapter 5. The purpose of the model is to understand the influence of parameter space on system response. The model was developed from a continuum mechanics approach utilising Galerkin's method for spatial discretisation. Mechanical coupling was incorporated into the model through a shared base, with the assumption that the material between cantilever sections acted as distributed spring elements through which energy transfer could occur. The final equation of motion following discretisation is in modal form, and any number of intrinsic cantilever modes (as well as all array modes) can be included. It was demonstrated that the model was capable of capturing the spatial mode shapes for an $M$ beam array at far field for a range of coupling strengths. It was further demonstrated that the model could capture changes in the spatial mode shapes and modal frequencies due to the addition of nonlinear tip forces with a good qualitative match to experimental data. The developed model, incorporating both mechanical coupling and tip-sample forces, is a novel tool for analysing AFM array response, and an equivalent model is not present in the literature prior to the research work of this thesis.

The discontinuous jumps observed in the micro array response were investigated further in Chapter 6 using the developed mathematical and experimental tools. Experimental results demonstrated a strong link between output amplitude and static tip deflection, with sudden changes in static deflection resulting in the observed jumps in amplitude. It was demonstrated using mathematical simulations that saddle node bifurcations occurred in the amplitude response in the region of frequency cross-over when strong

coupling was present in the system. This resulted in discontinuities in the simulated amplitude approach curves. Perturbation analysis was used to link the coupling, damping and excitation amplitude parameters of a two beam array to the creation of multiple solution branches, demonstrating that all three parameters influence the onset of amplitude jumps and that a unique point in parameter space at which bifurcation first occurs does not exist. The model was further used to find the relationship between cantilever gap and frequency separation on the observed level of coupling in the system. It was shown that when cantilevers were closely spaced, increasing the frequency gap was as effective at removing unwanted coupling phenomena as reducing the amount of shared base material, comporting with the results from the micro scale experiments in Chapter 3. It was concluded based on the above results and observations that the best way to ensure unwanted coupling phenomena did not occur during parallel imaging was to separate the resonant frequencies of the individual cantilevers through design by an amount greater than the largest expected resonant frequency shift due to tip forces (roughly 2 kHz). It was demonstrated that a resonant frequency change of 2 kHz could be achieved with a cantilever length change of ≈10 µm, or an addition of a tip mass of 15 ng, corresponding to a gold sphere 6 µm in diameter.

In the final chapter of this thesis (Chapter 7), a new direction for the research was proposed, which was to use the response of an array of coupled cantilevers to enhance the imaging capabilities of standard single point AFM techniques, rather than imaging multiple points in parallel. Specifically, the chapter focused on the use of a mechanically coupled two beam array, with one active scanning cantilever and one passive cantilever, to increase the sensitivity of noncontact FM-AFM imaging. It was proposed that in the vicinity of frequency cross-over, the spatial mode shapes of the system's eigenmodes would undergo a transition, which would result in a change in output resonant frequency that would be a function of the coupling strength. Mathematical simulations proved this concept to be viable, with a simulated increase in the resonant frequency functional gradient in the region of an order of magnitude achieved with a two beam array coupled with 9.5 mm of shared base material over an equivalent single beam system. Experimental investigations on the macro scale confirmed the simulation results that a two beam array could be used for increased sensitivity using FM-AFM, however, the limited precision achievable with the macro scale test rig prevented the measurement of a reliable quantification of the sensitivity increase. It was demonstrated through numerical simulation and perturbation analysis that the achievable functional gradient increase was highly dependent on the coupling strength, with a change in the length of

shared base material of 0.2 mm (on the macro scale) resulting in a drop in the magnitude of maximum achievable sensitivity increase from 90× to 10×. This change in length of shared base material is equivalent to 0.1 % of the cantilever length. It was also demonstrated using the perturbed analytical model that excitation amplitude and system damping influenced the achievable sensitivity increase in addition to coupling strength, meaning that a unique optimal point in parameter space for maximum sensitivity increase does not exist. It was shown that upon fixing the coupling strength (fixed to 9.5 mm of shared base material for the simulations presented), the excitation amplitude could be tuned to further increase the maximum sensitivity increase above 90. This gives the end user a simple method to tune the achievable sensitivity of the array, depending on the application and imaging requirements. The technological implications of the proposed technology were discussed. It was concluded that fine tolerances were required for fabrication to ensure the designed parameter space was achieved. The practicality of achieving the necessary tolerances, particularly with regards to coupling strength and the frequency gap between the cantilevers must be investigated before taking this line of research further.

## 8.2 Future Work

Several research goals have been identified that should be pursued as a continuation of the work presented in this thesis. Some of the necessary future work has already been introduced in early chapters, and will be elaborated here. In addition, areas of improvement to the research conducted in terms of experimental procedure and analysis have been identified. A discussion of these points will also be given here.

The next step of the collaborative research effort between the University of Canterbury and the Technische Universität Ilmenau should be to integrate the compound single beam model developed by Roeser et al. [47] and the array model presented in Chapter 5 of this thesis. The single beam model covers the conversion of an applied voltage signal in the bimorph heater to an actuator force, and accounts for electrical coupling between the actuator and sensor elements. Incorporating these features with the mechanical coupling and nonlinear tip-interaction forces will provide a complete description of the TUI array dynamics in air. This integrated model can be used to fine tune the physical parameters of the TUI array to ensure imaging reliability is not compromised by nonlinear jump phenomena that can occur under certain conditions. Further down the line, the effects of fluidic coupling that is being modelled by other members of the UC research team can be incorporated into the integrated model, creating a full working

model of the TUI arrays in air and liquid environments.

The main outcome of this thesis with direct implications for the TUI research team is the identification of the relative influence of cantilever gap and resonant frequency separation on the level of coupled response, and the identification of the formation of multiple solution branches when frequency cross-over is approached. It was shown that when cantilevers a very closely spaced, the difference in uncoupled resonant frequency between cantilevers has a significant effect on the level of energy transfer that occurs between beams, and that keeping the uncoupled resonant frequencies far apart is the best approach to prevent discontinuous jumps in cantilever response leading to a loss of imaging reliability. Two possible methods were suggested to achieve this; designing each cantilever in the array with different lengths; and applying small, varying masses to the tips of each cantilever. Neither of these methods have been tested or verified for practicality as this was outside the scope of the thesis. The design of the TUI arrays should be reviewed in light of this outcome (Chapter 6) and design considerations implemented to ensure separation of cantilever resonant frequencies. Validation experiments should then be planned and executed to determine if the proposed solution sufficiently solves the reliability problem.

The proposed method of sensitivity enhancement should be investigated further. The method was demonstrated through simulation, but only provisionally validated experimentally on the macro scale. The issues preventing higher precision measurement should be rectified, including obtaining more accurate stepper motors/linear actuators and constructing a more rigid sample structure. The validation experiments can be repeated to confirm the results presented in Chapter 7 and to provide a more accurate measurement of the achievable sensitivity increase over the single beam system. After further experimentation on the macro scale, the next step is to determine if a viable micro scale array can be designed and fabricated, taking into account the implications that were discussed in Section 7.5. Experimentation can then be conducted to determine the true achievable sensitivity increase, practicality and user-friendliness.

In the introduction and literature review chapters, it was stated that array technology could be used for multi-modal and multi-harmonic AFM techniques for the purpose of measuring sample material properties and subsurface features. This was not investigated within the scope of the thesis due to time and resource constraints, but could yield valuable research outcomes. The array model presented in Chapter 5 is capable of capturing higher order array modes, multi-frequency excitation, and harmonic response. As a result, the tools required to simulate multi-modal and multi-harmonic AFM with arrays are already available. This research work can be conducted as

a direct continuation of this thesis.

# Bibliography


[1] H. Rohrer and G. Binnig. United States Patent 4343993, 1982.

[2] G. Binnig, C.F. Quate, and Ch. Gerber. Atomic Force Microscope. *Physical Review Letters*, 56:930–933, 1986.

[3] S. Morita, E. Meyer, and R. Wiesendanger. *Noncontact atomic force microscopy*. Springer, 2002.

[4] G. Meyer and N. M. Amer. Novel optical approach to atomic force microscopy. *Applied Physics Letters*, 53(12):1045–1047, 1988.

[5] D.Y. Abramovitch, S.B. Andersson, L.Y. Pao, and G. Schitter. A Tutorial on the Mechanisms, Dynamics, and Control of Atomic Force Microscopes. In *American Control Conference*, pages 3488–3502. Ieee, jul 2007.

[6] T. Ando, T. Uchihashi, and T. Fukuma. High-speed atomic force microscopy for nano-visualization of dynamic biomolecular processes. *Progress in Surface Science*, 83(7-9):337–437, nov 2008.

[7] Y. Martin, C. C. Williams, and H. K. Wickramasinghe. Atomic force microscope-force mapping and profiling on a sub 100-?? scale. *Journal of Applied Physics*, 61(10):4723–4729, 1987.

[8] T. Ando. High-speed atomic force microscopy coming of age. *Nanotechnology*, 23(6):1–27, mar 2012.

[9] P. Parot, Y. Dufrene, P. Hinterdorfer, C. Le Grimellec, D. Navajas, J. Pellequer, and S. Scheuring. Past, present and future of atomic force microscopy in life sciences and medicine. *Journal of molecular recognition*, 19:299–304, 2007.

[10] T.R. Albrecht, P. Grutter, D. Horne, and D. Rugar. Frequency modulation detection using high-Q cantilevers microscope sensitivity for enhanced force. *Journal of Applied Physics*, 69(2):668–673, 1991.

[11] A. Raman, J. Melcher, and R. Tung. Cantilever dynamics in atomic force microscopy. *Nano Today*, 3(1-2):20–27, 2008.

[12] N. Jalili and K. Laxminarayana. A review of atomic force microscopy imaging systems: Application to molecular metrology and biological sciences. *Mechatronics*, 14:907–945, 2004.

[13] H. G. Hansma. Atomic force microscopy of biomolecules. *Journal of Vacuum Science & Technology B*, 14(2):1390, 1996.

[14] I. Casuso, F. Rico, and S. Scheuring. Biological AFM: where we come from–where we are–where we may go. *Journal of molecular recognition*, 24(3):406–13, 2011.

[15] S. Morita, F. J. Giessibl, E. Meyer, and R. Wiesendanger. *Noncontact atomic force microscopy*. Springer, 2015.

[16] Arturo M. Bar and Ronald G. Reifenberger. *Atomic Force Microscopy in Liquid: Biological Applications*. Wiley-VCH, 2012.

[17] P. K. Hansma, G. Schitter, G. E. Fantner, and C. Prater. High-speed atomic force microscopy. *Science Magazine*, 314(5799):601–602, oct 2006.

[18] T. Ando, T. Uchihashi, N. Kodera, D. Yamamoto, A. Miyagi, M. Taniguchi, and H. Yamashita. High-speed AFM and nano-visualization of biomolecular processes. *European journal of physiology*, 456(1):211–25, apr 2008.

[19] M. Shibata, T. Uchihashi, T. Ando, and R. Yasuda. Long-tip high-speed atomic force microscopy for nanometer-scale imaging in live cells. *Scientific Reports*, 5:8724, 2015.

[20] L. M. Picco, P. G. Dunton, A. Ulcinas, D. J. Engledew, O. Hoshi, T. Ushiki, and M. J. Miles. High-speed AFM of human chromosomes in liquid. *Nanotechnology*, 19(38):384018, 2008.

[21] O. D. Payton, L. M. Picco, and T. B. Scott. High-speed atomic force microscopy for materials science. *International Materials Reviews*, 6608(June):1–22, 2016.

[22] G.S. Shekhawat and V.P. Dravid. Nanoscale imaging of buried structures via scanning near-field ultrasound holography. *Science (New York, N.Y.)*, 310(5745):89–92, oct 2005.

[23] R. Garcia. Probe microscopy: Images from below the surface. *Nature Nanotechnology*, 5(2):101–102, 2010.

[24] G. J. Verbiest, T. H. Oosterkamp, and M. J. Rost. Subsurface-AFM: sensitivity to the heterodyne signal. *Nanotechnology*, 24(36):365701, 2013.

[25] S. Hu, C. Su, and W. Arnold. Imaging of subsurface structures using atomic force acoustic microscopy at GHz Imaging of subsurface structures using atomic force acoustic microscopy at GHz frequencies. *Journal of Applied Physics*, 109(8), 2011.

[26] T. G. Kuznetsova, M. N. Starodubtseva, N. I. Yegorenkov, S. A. Chizhik, and R. I. Zhdanov. Atomic force microscopy probing of cell elasticity. *Micron (Oxford, England : 1993)*, 38(8):824–33, jan 2007.

[27] D. J. Muller. AFM: A nanotool in membrane biology. *Biochemistry*, 47(31):7986–7998, 2008.

[28] A. Alessandrini and P. Facci. AFM: a versatile tool in biophysics. *Measurement Science and Technology*, 16(6):R65–R92, jun 2005.

[29] R. Garcia and E. T. Herruzo. The emergence of multifrequency force microscopy. *Nature Nanotechnology*, 7(4):217–226, 2012.

[30] R. Hillenbrand, M. Stark, and R. Guckenberger. Higher-harmonics generation in tapping-mode atomic-force microscopy: Insights into the tipsample interaction. *Applied Physics Letters*, 76(23):3478, 2000.

[31] A. Raman, S. Trigueros, A. Cartagena, A. P. Z. Stevenson, M. Susilo, E. Nauman, and S. Antoranz Contera. Mapping nanomechanical properties of live ccell using multi-harmonic atomic force microscopy. *Nature Nanotechnology*, 6:809–814, 2011.

[32] J. R. Lozano and R. Garcia. Theory of multifrequency atomic force microscopy. *Physical Review Letters*, 100(7):8–11, 2008.

[33] A. Schuh, I. S. Bozchalooi, I. W. Rangelow, and K. Youcef-Toumi. Multi-eigenmode control for high material contrast in bimodal and higher harmonic atomic force microscopy. *Nanotechnology*, 26(23):235706, 2015.

[34] H. S. Nurul, R. G. Reifenberger, and A. Raman. Enhancing the optical lever sensitivity of microcantilevers for dynamic atomic force microscopy via integrated low frequency paddles. *Nanotechnology*, 27(19):195502, 2016.

[35] B. Zeyen, K. Virwani, B. Pittenger, and K. L. Turner. Preamplifying cantilevers for dynamic atomic force microscopy. *Applied Physics A*, 94(10):103507, 2009.

[36] J. R. Felts, W. P. King, H. Cho, J. R. Felts, and M. Yu. High-sensitivity nanometer-scale infrared spectroscopy using a contact mode microcantilever with an internal resonator paddle. *Nanotechnology*, 21:185705, 2010.

[37] S.C. Minne, S.R. Manalis, and C.F. Quate. Parallel atomic force microscopy using cantilevers with integrated piezoresistive sensors and integrated piezoelectric actuators. *Applied Physics Letters*, 67(26):3918–3920, 1995.

[38] T. Sulchek, R.J. Grow, G. Yaralioglu, S.C. Minne, C.F. Quate, S.R. Manalis, A. Kiraz, A. Aydine, and A. Atalar. Parallel atomic force microscopy with optical interferometric detection. *Applied Physics Letters*, 78(12):1787–1789, 2001.

[39] P. Vettiger, M. Despont, U. Drechsler, U. Durig, W. Haberle, M. Lutwyche, H. Rothuizen, R. Stutz, R. Widmer, and G. Binnig. The "millipede" - more than thousand tips for future afm storage. *IBM Journal of Research and Development*, 44:323–340, 2000.

[40] J. Polesel-Maris, L. Aeschimann, A. Meister, R. Ischer, E. Bernard, T. Akiyama, M. Giazzon, P. Niedermann, U. Staufer, R. Pugin, N.F. Rooij, P. Vettiger, and H. Heinzelmann. Piezoresistive cantilever array for life sciences applications. *Journal of Physics: Conference Series*, 61:955–959, April 2007.

[41] M. Seong, S. Somnath, H. J. Kim, and W. P. King. Parallel nanoimaging using an array of 30 heated microcantilevers. *RSC Advances*, 4:24747–24754, 2014.

[42] D. Endo, H. Yabuno, K. Higashino, Y. Yamamoto, and S. Matsumoto. Self-excited coupled-microcantilevers for mass sensing. *Applied Physics Letters*, 106(22):223105, 2015.

[43] M. Spletzer, A. Raman, A. Q. Wu, X. Xu, and R. Reifenberger. Ultrasensitive mass sensing using mode localization in coupled microcantilevers. *Applied Physics Letters*, 88(25):10–13, 2006.

[44] B. Bhushan, H. Fuchs, and S. Hosaka. *Applied Scanning Probe Methods*. Springer-Verlag, 2004.

[45] D. Roeser, S. Gutschmidt, T. Sattel, and I. W. Rangelow. Coupled Vibrations in a Thermo-Elastic Small Size Scanning Probe Microscopy Array. In *International Conference on Advances in Coupled Systems Mechanics*, 2012.

[46] T. Sattel, D. Roeser, and S. Gutschmidt. Multi-Physics Modeling of an Electro-Thermally Actuated Micro-Cantilever for Scanning Probe Microscopy. In *International Mechanical Engineering Congress & Exposition*, pages 1057–1065, 2010.

[47] D. Roeser, S. Gutschmidt, T. Sattel, and I. W. Rangelow. Tip Motion Sensor Signal Relation for a Composite SPM / SPL Cantilever. *Journal of Microelectromechanical Systems*, 25(1):78–90, 2016.

[48] S. Basak and A. Raman. Hydrodynamic coupling between micromechanical beams oscillating in viscous fluids. *Physics of Fluids*, 19:017105, 2007.

[49] E. Buks and M. L. Roukes. Electrically tunable collective response in a coupled micromechanical array. *Journal of Microelectromechanical Systems*, 11(6):802–807, dec 2002.

[50] R. Lifshitz and M. Cross. Response of parametrically driven nonlinear coupled oscillators with application to micromechanical and nanomechanical resonator arrays. *Physical Review B*, 67(13), apr 2003.

[51] S. Gutschmidt and O. Gottlieb. Nonlinear dynamic behavior of a microbeam array subject to parametric actuation at low, medium and large DC-voltages. *Nonlinear Dynamics*, 67(1):1–36, 2012.

[52] Y. Bromberg, M. Cross, and R. Lifshitz. Response of discrete nonlinear systems with many degrees of freedom. *Physical Review E*, 73(1), jan 2006.

[53] A.J. Dick, B. Balachandran, and C.D. Mote. Localization in Microresonator Arrays: Influence of Natural Frequency Tuning. *Journal of Computational and Nonlinear Dynamics*, 5(1), 2010.

[54] M. Sato, B. E. Hubbard, and A. J. Sievers. Nonlinear energy localization and its manipulation in micromechanical oscillator arrays. *Reviews of Modern Physics*, 78(1):137–157, jan 2006.

[55] S. Ramakrishnan and B. Balachandran. Energy localization and white noise-induced enhancement of response in a micro-scale oscillator array. *Nonlinear dynamics*, 62:1–16, 2010.

[56] M. Spletzer, A. Raman, H. Sumali, and J. P. Sullivan. Highly sensitive mass detection and identification using vibration localization in coupled microcantilever arrays. *Applied Physics Letters*, 92(11):824–833, 2008.

[57] P. Thiruvenkatanathan, J. Woodhouse, J. Yan, and a. a. Seshia. Limits to mode-localized sensing using micro- and nanomechanical resonator arrays. *Journal of Applied Physics*, 109(10), 2011.

[58] A. Glean, J. Judge, J. F. Vignola, and T. J. Ryan. Mode-shape-based mass detection scheme using mechanically diverse, indirectly coupled microresonator arrays. *Journal of Applied Physics*, 117(5):054505, 2015.

[59] I.W. Rangelow, T. Ivanov, K. Ivanova, B.E. Volland, P. Grabiec, Y. Sarov, A. Persaud, T. Gotszalk, P. Zawierucha, M. Zielony, D. Dontzov, B. Schmidt, M. Zier, N. Nikolov, I. Kostic, W. Engl, T. Sulzbach, J. Mielczarski, S. Kolb, Du P. Latimier, R. Pedreau, V. Djakov, S.E. Huq, K. Edinger, O. Fortagne, A. Almansa, and H.O. Blom. Piezoresistive and self-actuated 128-cantilever arrays for nanotechnology applications. *Microelectronic Engineering*, 84(5-8):1260–1264, May 2007.

[60] S. Somnath, H. J. Kim, H. Hu, and W. P. King. Parallel nanoimaging and nanolithography using a heated microcantilever array. *Nanotechnology*, 25(1):014001, jan 2014.

[61] Y. Ahn, T. Ono, and M. Esashi. Micromachined Si cantilever arrays for parallel AFM operation. *Journal of Mechanical Science and Technology*, 22(2):308–311, May 2008.

[62] A. Schneider, R.H. Ibbotson, R.J. Dunn, and S.E. Huq. Arrays of SU-8 microcantilevers with integrated piezoresistive sensors for parallel AFM applications. *Microelectronic Engineering*, 88(8):2390–2393, August 2011.

[63] M. Lutwyche, C. Andreoli, G. Binnig, J. Brugger, U. Drechsler, W. Haberle, H. Rohrer, H. Rothuizen, P. Vettiger, G. Yaralioglu, and C.F. Quate. 5 5 2D AFM cantilever arrays a first step towards a Terabit storage device. *Sensors and Actuators*, 73(1-2):89–94, 1999.

[64] S.C. Minne, G. Yaralioglu, S.R. Manalis, J.D. Adams, J. Zesch, A. Atalar, and C.F. Quate. Automated parallel high-speed atomic force microscopy. *Applied Physics Letters*, 72(18):2340–2342, 1998.

[65] P. Srinivasan, F.R. Beyette, and I. Papautsky. Micromachined arrays of cantilevered glass probes. *Applied optics*, 43(4):776–82, February 2004.

[66] K. Ivanova, Y. Sarov, T. Ivanov, A. Frank, J.P. Zöllner, Ch. Bitterlich, U. Wenzel, B.E. Volland, S. Klett, I.W. Rangelow, P. Zawierucha, M. Zielony, T. Gotszalk, D. Dontzov, W. Schott, N. Nikolov, M. Zier, B. Schmidt, W. Engl, T. Sulzbach, and I. Kostic. Scanning proximal probes for parallel imaging and lithography. *Journal of Vacuum Science & Technology B*, 26(6):2367, 2008.

[67] Y. Sarov, A. Frank, T. Ivanov, J.P. Zöllner, K. Ivanova, B.E. Volland, I.W. Rangelow, A. Brogan, R. Wilson, P. Zawierucha, M. Zielony, T. Gotszalk, N. Nikolov, M. Zier, B. Schmidt, and I. Kostic. Parallel proximal probe arrays with vertical interconnections. *Journal of Vacuum Science & Technology B: Microelectronics and Nanometer Structures*, 27(6):3132, 2009.

[68] T. Zhang, G. Zhao, J. Chu, W. Huang, M. Bartenwerfer, V. Eichhorn, and S. Fatikow. Fabrication and Characterization of Piezoelectric Cantilever Array with Nano-assembly Carbon Nanotube Tips. In *International Conference on Manipulation, Manufacturing and Measurement on the Nanoscale*, pages 292–296, 2012.

[69] M. Despont, J. Brugger, U. Drechsler, U. Durig, W. Haberle, M. Lutwyche, H. Rothuizen, R. Stutz, R. Widmer, G. Binnig, H. Rohrer, and P. Vettiger. VLSI-NEMS chip for parallel AFM data storage. *Sensors and Actuators A ...*, 80(2):100–107, 2000.

[70] M. Tortonese, H. Yamada, R. Barrett, and C.F. Quate. Atomic Force Microscopy Using a Piezoresistive Cantilever. In *International Conference on Solid-State Sensors and Actuators*, pages 448–451, 1991.

[71] O. Hansen and A. Boisen. Noise in piezoresistive atomic force microscopy. *Nanotechnology*, 10:51–60, 1999.

[72] M. Favre, J. Polesel-Maris, T. Overstolz, P. Niedermann, S. Dasen, G. Gruener, R. Ischer, P. Vettiger, M. Liley, H. Heinzelmann, and A. Meister. Parallel AFM imaging and force spectroscopy using two-dimensional probe arrays for applications in cell biology. *Journal of molecular recognition : JMR*, 24(3):446–452, 2011.

[73] T. Akiyama, L. Aeschimann, L. Chantada, N.F. de Rooij, H. Heinzelmann, H.P. Herzig, O. Manzardo, A. Meister, J. Polesel-Maris,

R. Pugin, U. Staufer, and P. Vettiger. Concept and Demonstration of Individual Probe Actuation in Two-Dimensional Parallel Atomic Force Microscope System. *Japanese Journal of Applied Physics*, 46(9B):6458–6462, September 2007.

[74] Y.S. Kim, H.J. Nam, S.M. Cho, and J.W. Hong. PZT cantilever array integrated with piezoresistor sensor for high speed parallel operation of AFM. *Sensors and Actuators A*, 103(1-2):122–129, 2003.

[75] Y. Sarov, T. Ivanov, A. Frank, and I.W. Rangelow. Thermally driven multi-layer actuator for 2D cantilever arrays. *Applied Physics A*, 102(1):61–68, October 2010.

[76] T. Volden, M. Zimmermann, D. Lange, O. Brand, and H. Baltes. Dynamics of CMOS-based thermally actuated cantilever arrays for force microscopy. *Sensors and Actuators A*, 115(2-3):516–522, 2004.

[77] T. Akiyama, U. Staufer, N.F. de Rooij, D. Lange, C. Hagleitner, O. Brand, H. Baltes, A. Tonin, and H.R. Hidber. Integrated atomic force microscopy array probe with metal oxide semiconductor field effect transistor stress sensor , thermal bimorph actuator , and on-chip complementary metal oxide semiconductor electronics Integrated atomic force microscopy arr. *Journal of Vacuum Science & Technology B*, 18(6):2669–2675, 2000.

[78] E. Thielicke and E. Obermeier. Microactuators and their technologies. *Mechatronics*, 10(4-5):431–455, 2000.

[79] S.A. Miller, K.L. Turner, and N.C. MacDonald. Microelectromechanical scanning probe instruments for array architectures. *Review of Scientific Instruments*, 68(11):4155–4162, 1997.

[80] M. Dahleh, B. Bamieh, and M. Napoli. Optimal Control of Arrays of Microcantilevers. In *IEEE conference on Decision and Control*, volume 121, pages 2077–2082, 1999.

[81] M. Napoli, W. Zhang, K. Turner, and B. Bamieh. Characterization of electrostatically coupled microcantilevers. *Journal of Microelectromechanical Systems*, 14(2):295–304, 2005.

[82] M. Lenczner. Multiscale model for atomic force microscope array mechanical behavior. *Applied Physics Letters*, 90(9):091908, 2007.

[83] M. Lenczner and R.C. Smith. A two-scale model for an array of AFMs cantilever in the static case. *Mathematical and Computer Modelling*, 46(5-6):776–805, September 2007.

[84] M. Lenczner and Y. Yakoubi. Semi-decentralized approximation of optimal control for partial differential equations in bounded domains. *Comptes Rendus Mécanique*, 337(4):245–250, 2009.

[85] H. Hui, M. Lenczner, E. Pillet, and S. Cogan. A two-scale model for one-dimensional arrays of cantilevers and its verification. *Mechatronics*, 22(5):538–543, August 2012.

[86] D. Saya, K. Fukushima, H. Toshiyoshi, G. Hashiguchi, H. Fujita, and H. Kawakatsu. Fabrication of single-crystal Si cantilever array. *Sensors and actuators A*, 95(2-3):281–287, 2002.

[87] B. Balachandran and I. Chakraborty. Cantilever Dynamics with Attractive and Repulsive Tip Interactions. In *ASME 2009 International Mechancial Engineering Congress and Exposition*, pages 443–449, Florida, 2009.

[88] I. Chakraborty and B. Balachandran. Near-grazing dynamics of base excited cantilevers with nonlinear tip interactions. *Nonlinear Dynamics*, 70(2):1297–1310, August 2012.

[89] T. Hikihara, Y. Okamoto, and Y. Ueda. An experimental spatio-temporal state transition of coupled magneto-elastic system. *Chaos*, 7(4):810–816, December 1997.

[90] H. Yabuno, Y. Seo, and M. Kuroda. Self-excited coupled cantilevers for mass sensing in viscous measurement environments. *Applied Physics Letters*, 103(6):2011–2016, 2013.

[91] M. Sato, B. E. Hubbard, A. J. Sievers, B. Ilic, D. a. Czaplewski, and H. G. Craighead. Observation of locked intrinsic localized vibrational modes in a micromechanical oscillator array. *Physical review letters*, 90(4), January 2003.

[92] D.G. Yablon. *Scanning Probe Microscopy for Industrial Applications: Nanomechanical Characterization*. John Wiley & Sons, 2013.

[93] S. D. Solares, S. An, and C. J. Long. Multi-frequency tapping-mode atomic force microscopy beyond three eigenmodes in ambient air. *Beilstein Journal of Nanotechnology*, 5(1):1637–1648, 2014.

[94] S. S. Rao. *Mechanical Vibrations*. Pearson Education, 2004.

[95] P. Thota, S. MacLaren, and H. Dankowicz. Controlling bistability in tapping-mode atomic force microscopy using dual-frequency excitation. *Applied Physics Letters*, 91(9), 2007.

[96] P. Hagedorn and A. DasGupta. *Vibrations and Waves in Continuous Mechanical Systems*. John Wiley & Sons, 2007.

[97] D. Sarid. *Scanning Force Microscopy With Applications to electric, Magnetic and Atomic Forces*. Oxford University Press, 1994.

[98] B. Cappella and G. Dietler. Force-distance curves by atomic force microscopy. *Surface Science Reports*, 34(1-3):1–104, jan 1999.

[99] R. Serway, J. Jewett, K. Wilson, and A. Wilson. *Physics Vol. 2*. Cengage Learning, 2013.

[100] H. Dankowicz and F. Schilder. *Recipes for Continuation*. Society for Industrial and Applied Mathematics, 2013.

[101] S. H. Strogatz and I. Stewart. Coupled oscillators and biological synchronization. *Scientific American*, 269(6):102–109, 1993.

[102] S. H. Strogatz. *Nonlinear Dynamics and Chaos*. Perseus Books Publishing, 1994.

[103] R. Garcia and T. R. Rodriguez. Theory of Q control in atomic force microscopy. *Applied Physics Letters*, 82(26):4821–4823, 2003.

[104] A. H. Nayfeh. *Introduction to Perturbation Techniques*. Wiley-VCH, 2004.

[105] P. Shih. Frequency function in atomic force microscopy applied to a liquid environment. *Sensors*, 14(6):9369–9379, 2014.

[106] B. Voigtlander. *Scanning Probe Microscopy: Atomic Force Microscopy and Scanning Tunneling Microscopy*. Springer, 2015.

[107] A. Schuh, M. Hofer, T. Ivanov, and I. W. Rangelow. Active Microcantilevers for High Material Contrast in Harmonic Atomic Force Microscopy. *Journal of Microelectromechanical Systems*, 24(5):1622–1631, 2015.

[108] F. J. Giessibl, H. Bielefeldt, S. Hembacher, and J. Mannhart. Calculation of the optimal imaging parameters for frequency modulation atomic force microscopy. *Applied Surface Science*, 140(3-4):352–357, 1999.

[109] V. Pini, J. J. Ruz, P. M. Kosaka, O. Malvar, M. Calleja, and J. Tamayo. How two-dimensional bending can extraordinarily stiffen thin sheets. *Scientific Reports*, 8(July):1–16, 2016.

APPENDIX A

# EOM Matlab Code

The following MATLAB® code is used to solve for the spatial mode shapes and to conducted the spatial discretisation to find the equations of motion of the array system as a set of coupled ordinary differential equations from the system parameters. The code produces the parameters needed to form the equation of motion in the form of (5.25) or (5.27) from Section 5.3.

```
clear
clc
close all

%%  Setting up model parameters

No_beams = 2; % Define number of beams in the model
No_modes = No_beams; % Define number of modes to be solved
                     %  (at least equal to number of beams)
Coupling_size = 1; % Define nearest neighbour coupling
if Coupling_size>No_beams
    Coupling_size = No_beams;
end

rho1 = 2770; % Density of cantilever material
rho2 = 2770; % Density of base material
h1 = 0.0015; % Thickness of cantilever
h2 = 0.0015; % Thickness of base
b1 = 0.04; % Cantilever width
b2 = 0.04; % Base width
b3 = 0.01; % Coupling width
L1 = 0.16; % Cantilever length
L1_orig = L1; % Save original L1 value for normalisation
L2 = 0.005; % Base length
L1 = L1-L2; % Redefine L1 as length of
            %  cantilever section
Lb_tot = No_beams*b2+(No_beams-1)*b3; % Total width of the array
E1 = 71e9; % Cantilever modulus
E2 = 71e9; % Base modulus
A1 = b1*h1; % Cantilever cross-section area
I1 = (b1*h1^3)/12; % Cantilever second moment of area
A2 = b2*h2; % Base cross-section area
I2 = (b2*h2^3)/12; % Base second moment of area
damp = 0.007; % Damping coefficient
Km = -6e-5; % Magnetic strength

stiffness = zeros(1,Coupling_size);
Kl = zeros(1,No_beams);
for i = 1:Coupling_size
```

```
40      % Coupling stiffness assuming a linear spring between beams
41      stiffness(i) = (E2*L2*h2^3)/(4*(i*b3+(i-1)*b1)^3);
42      Kl(i) = stiffness(i)/L2;
43  end
44
45  if No_beams==1
46      Kl = 0;
47  end
48
49  mass = [0.00035,0.00035]; % Tip masses (vector length should
50                            %  equal number of beams.
51
52  %%  Spatial normalisation of Parameters
53
54  L1_h = L1/L1_orig;
55  L2_h = L2/L1_orig;
56  Lb_tot_h = Lb_tot/L1_orig;
57
58  mu1 = (E1*I1)/(rho1*A1*L1_orig^4)*ones(1,No_beams);
59  mu2 = (E2*I2)/(rho1*A1*L1_orig^4)*ones(1,No_beams);
60  Kl_h = (Kl)/(rho1*A1);
61  mass_h = mass/(rho1*A1*L1_orig);
62
63  %%  Solving the spatial matrix to find the eigenfrequencies
64
65  exit_flag = 0;
66  count = 0;
67  om_start = 10;  om_stop = 200;
68  step_size = (om_stop-om_start)/500;
69  tol_orig = 1e-12;   tol = tol_orig;
70
71  while exit_flag == 0;
72      om = (om_start:step_size:om_stop)*2*pi;
73      p = 1;  flag = 0;
74      out = ones(1,length(om));
75      e = exp(1);
76      for i = 1:length(om)
77          if flag == 0
78              % Initialise frequency for normalisation when
79              %  the first eigenfrequency is yet to be found
80              om1 = om(i);
81          end
82
83          % Temporal normalisation of parameters
84          mu1_n = mu1/(om1^2);
85          mu2_n = mu2/(om1^2);
86          Kl_n = Kl_h/(om1^2);
87          om_n = om(i)/om1;
88
89          O = zeros(4,4);
90          Kc = zeros(4*No_beams,4*No_beams);
91          Kb = zeros(4*No_beams,4*No_beams);
92          for m = 1:No_beams
93              for n = 1:No_beams
94                  if m==n
95                      % Equation of motion (diagonal terms of the combined
                            matrix)
96                      Sb = [0,1,0,0;0,0,1,0;0,0,0,1;((om_n^2)/mu2_n(m))
                            ,0,0,0];
97                      Sb(4,1) = Sb(4,1) - SetSB(m,Kl_n,No_beams,Coupling_size
                            )/mu2_n(m);
98                      Sc = [0,1,0,0;0,0,1,0;0,0,0,1;((om_n^2)/mu1_n(m))
                            ,0,0,0];
```

```
99                      Kb(4*(m-1)+1:4*(m-1)+4,4*(m-1)+1:4*(m-1)+4) = Sb;
100                     Kc(4*(m-1)+1:4*(m-1)+4,4*(m-1)+1:4*(m-1)+4) = Sc;
101                 else
102                     % Off-diagonal coupling terms of the combined matrix
103                     G = zeros(4,4);
104                     G(4,1) = SetG(m,n,Kl_n)/mu2_n(m);
105                     Kb(4*(m-1)+1:4*(m-1)+4,4*(m-1)+1+4*(n-m):4*(m-1)+4+4*(n
                            -m)) = G;
106                 end
107             end
108         end
109         % Eigenvalues/eigenvalues of the combined matrix
110         [vc,ec] = eig(Kc);
111         [vb,eb] = eig(Kb);
112         % Solving the spatial mode shapes at the boundary/transition points
113         Wb0 = (vb*e^(eb*0)*inv(vb));
114         WbL = (vb*e^(eb*L2_h)*inv(vb));
115         Wc0 = (vc*e^(ec*0)*inv(vc));
116         WcL = (vc*e^(ec*L1_h)*inv(vc));
117         O_v = zeros(1,4*No_beams);
118
119         % Computing the boundary and transition conditions
120         K = zeros(8*No_beams,8*No_beams);
121         for j = 1:No_beams
122             K(8*(j-1)+1,:) = [Wb0(4*(j-1)+1,:),O_v];
123             K(8*(j-1)+2,:) = [Wb0(4*(j-1)+2,:),O_v];
124             K(8*(j-1)+3,:) = [WbL(4*(j-1)+1,:),-Wc0(4*(j-1)+1,:)];
125             K(8*(j-1)+4,:) = [WbL(4*(j-1)+2,:),-Wc0(4*(j-1)+2,:)];
126             K(8*(j-1)+5,:) = [WbL(4*(j-1)+3,:),-Wc0(4*(j-1)+3,:)];
127             K(8*(j-1)+6,:) = [WbL(4*(j-1)+4,:),-Wc0(4*(j-1)+4,:)];
128             K(8*(j-1)+7,:) = [O_v,-WcL(4*(j-1)+3,:)];
129             K(8*(j-1)+8,:) = [O_v,-mu2_n(j)*WcL(4*(j-1)+4,:)-mass_h(j)*WcL
                    (4*(j-1)+1,:)];
130         end
131
132         % Computing the determinant of the boundary/transtion conditions.
133         %   The determinant will be zero at a valid eigenfrequency.
134         out(i) = abs(det(K));
135
136         if i >= 3
137             % Find a zero crossing, indicating the precense of an
                    eigenfrequency
138             if out(i-1) < out(i) && out(i-1) < out(i-2)
139                 % Fine tuning the located eigenfrequency
140                 [om_true,exit_flag2,tol_out] = find_om_Ncouple(mu1,mu2,Kl_h
                        ,mass_h,Coupling_size,om(i-2),om(i),om1,L1_h,L2_h,
                        No_beams,flag,tol_orig);
141                 if tol_out>tol
142                     tol = tol_out;
143                 end
144                 if exit_flag2 == 1
145                     % Recording located eigenfrequency
146                     nat_freq(p) = om_true;
147                     p = p+1;
148                     if flag == 0
149                         om1 = om_true;
150                         flag = 1;
151                     end
152                 end
153             end
154         end
155         % Clearing variables for the next iteration
156         clear K;    clear mu1_n;    clear mu2_n;
```

```
157             clear om_n;    clear K1_n;
158             clear Sb;    clear Sc;    clear Sb1;   clear G;
159             clear Kb;    clear Kc;
160             clear vc;    clear ec;    clear vb;    clear eb;
161             clear Wb0;   clear WbL;   clear Wc0;   clear WcL;
162             clear O_v;   clear b;     clear K_n;
163             clear An;
164         end
165         if (rem((p-1),No_beams) ~= 0 || (p-1) == 0)
166             % If an insufficient number of eigenfrequencies are found, the
167             %   step size is reduced and the iteration process is repeated
168             count = count + 1;
169             om_start = min(nat_freq/(2*pi))-step_size*3;
170             om_stop = max(nat_freq/(2*pi))+step_size*3;
171             step_size = (om_stop-om_start)/(2000*count);
172             clear p;     clear nat_freq;
173         else
174             % Exiting loop when all required eigenfrequencies are found
175             exit_flag = 1;
176         end
177     end
178     clear om;
179
180     if length(nat_freq)<No_modes
181         No_modes = length(nat_freq);
182     end
183     J1_b_tot = zeros(1,No_modes);
184     J3_b_tot = zeros(1,No_modes);
185     J1_c_tot = zeros(1,No_modes);
186     J3_c_tot = zeros(1,No_modes);
187
188     %%  Solving the spatial mode shapes
189
190     for k = 1:No_modes
191         om = nat_freq(k);
192         % Normalise parameters
193         mu1_n = mu1/(om1^2);
194         mu2_n = mu2/(om1^2);
195         Kl_n = Kl_h/(om1^2);
196         om_n = om/om1;
197
198         O = zeros(4,4);
199         Kc = zeros(4*No_beams,4*No_beams);
200         Kb = zeros(4*No_beams,4*No_beams);
201         for m = 1:No_beams
202             for n = 1:No_beams
203                 if m==n
204                     % Equation of motion (diagonal terms of the combined matrix
                            )
205                     Sb = [0,1,0,0;0,0,1,0;0,0,0,1;((om_n^2)/mu2_n(m)),0,0,0];
206                     Sb(4,1) = Sb(4,1) - SetSB(m,Kl_n,No_beams,Coupling_size)/
                            mu2_n(m);
207                     Sc = [0,1,0,0;0,0,1,0;0,0,0,1;((om_n^2)/mu1_n(m)),0,0,0];
208                     Kb(4*(m-1)+1:4*(m-1)+4,4*(m-1)+1:4*(m-1)+4) = Sb;
209                     Kc(4*(m-1)+1:4*(m-1)+4,4*(m-1)+1:4*(m-1)+4) = Sc;
210                 else
211                     % Off-diagonal coupling terms of the combined matrix
212                     G = zeros(4,4);
213                     G(4,1) = SetG(m,n,Kl_n)/mu2_n(m);
214                     Kb(4*(m-1)+1:4*(m-1)+4,4*(m-1)+1+4*(n-m):4*(m-1)+4+4*(n-m))
                            = G;
215                 end
216             end
```

```
217     end
218     % Eigenvalues/eigenvalues of the combined matrix
219     [vc,ec] = eig(Kc);
220     [vb,eb] = eig(Kb);
221     % Solving the spatial mode shapes at the boundary/transition points
222     Wb0 = (vb*e^(eb*0))/vb;
223     WbL = (vb*e^(eb*L2_h))/vb;
224     Wc0 = (vc*e^(ec*0))/vc;
225     WcL = (vc*e^(ec*L1_h))/vc;
226     O_v = zeros(1,4*No_beams);
227
228     % Computing the boundary and transition conditions
229     K = zeros(8*No_beams,8*No_beams);
230     for j = 1:No_beams
231         K(8*(j-1)+1,:) = [Wb0(4*(j-1)+1,:),O_v];
232         K(8*(j-1)+2,:) = [Wb0(4*(j-1)+2,:),O_v];
233         K(8*(j-1)+3,:) = [WbL(4*(j-1)+1,:),-Wc0(4*(j-1)+1,:)];
234         K(8*(j-1)+4,:) = [WbL(4*(j-1)+2,:),-Wc0(4*(j-1)+2,:)];
235         K(8*(j-1)+5,:) = [WbL(4*(j-1)+3,:),-Wc0(4*(j-1)+3,:)];
236         K(8*(j-1)+6,:) = [WbL(4*(j-1)+4,:),-Wc0(4*(j-1)+4,:)];
237         K(8*(j-1)+7,:) = [O_v,-WcL(4*(j-1)+3,:)];
238         K(8*(j-1)+8,:) = [O_v,-mu2_n(j)*WcL(4*(j-1)+4,:)-mass_h(j)*WcL(4*(j
                -1)+1,:)];
239     end
240
241     % Converting system to reduced row echelon form
242     K = rref(K,tol);
243     for i = 1:length(K)
244         if K(i,i) == 0
245             % Find row with rank deficiency
246             ind = i;
247             break
248         end
249     end
250     b = -1*K(:,ind);
251     K_n = [K(:,1:ind-1),K(:,ind+1:end)];
252     An = K_n\b;
253     res1 = K_n*An;
254     % Constants of integration
255     An = [An(1:ind-1);1;An(ind:end)];
256     res2 = K*An;
257
258     % Discretised spatial vector along the base/cantilever length
259     x1 = 0:(L1_h*0.0001):L1_h;
260     x2 = 0:(L2_h*0.0001):L2_h;
261
262     Wc{k} = zeros(No_beams,length(x1));
263     Wc_4{k} = zeros(No_beams,length(x1));
264     Wb{k} = zeros(No_beams,length(x2));
265     Wb_4{k} = zeros(No_beams,length(x2));
266
267     % Creating spatial mode shapes of the base section
268     for j = 1:No_beams
269         for i = 1:length(x2)
270             Ab = real(vb*e^(eb*x2(i))*inv(vb)*An(1:4*No_beams));
271             Ab_prime = real(vb*eb*e^(eb*x2(i))*inv(vb)*An(1:4*No_beams));
272             Wb{k}(j,i) = Ab(4*(j-1)+1);
273             Wb_4{k}(j,i) = Ab_prime(4*(j-1)+4);
274         end
275     end
276
277     % Creating spatial mode shapes of the cantilever section
278     for j = 1:No_beams
```

```
279             for i = 1:length(x1)
280                 Ac = real(vc*e^(ec*x1(i))*inv(vc)*An(4*No_beams+1:8*No_beams));
281                 Ac_prime = real(vc*ec*e^(ec*x1(i))*inv(vc)*An(4*No_beams+1:8*
                        No_beams));
282                 Wc{k}(j,i) = Ac(4*(j-1)+1);
283                 Wc_4{k}(j,i) = Ac_prime(4*(j-1)+4);
284             end
285         end
286
287         % Creating and plotting the spatial mode shapes
288         xtot = [x2,x1+L2_h];
289         figure(k*1000);clf;
290         hold on
291         for j = 1:No_beams
292             Wtot{k}(j,:) = [Wb{k}(j,:),Wc{k}(j,:)]/max(abs(Wc{k}(1:No_beams,end
                    )));
293             Wtot_couple{k}(j,:) = [Wb{k}(j,:),0*Wc{k}(j,:)]/max(abs(Wc{k}(1:
                    No_beams,end)));
294             Wtot_4{k}(j,:) = [Wb_4{k}(j,:),Wc_4{k}(j,:)]/max(abs(Wc{k}(1:
                    No_beams,end)));
295             plot3(xtot,((j-1)*(Lb_tot_h*4))*ones(1,length(xtot)),Wtot{k}(j,:))
296         end
297         hold off
298         view(3)
299     end
300
301     %%  Spatial discretisation using Galerkins method
302
303     Taum = Km/(rho1*A1*om1^2*L1_orig^4);          % Normalising the nonlinear
            force coefficient
304     for i = 1:length(Wtot{1}(1,:))
305         for j = 1:No_beams
306             if xtot(i)>(xtot(end)-0.03125*L1_orig)
307                 % Integration vector of the force and nonlinear coefficients
308                 %   at the tip section
309                 F_vec(j,j) = 1;
310                 NL_vec(j,j) = 1;
311             else
312                 % Integration vector of the force and nonlinear coefficients
313                 %   at all other points
314                 F_vec(j,j) = 0;
315                 NL_vec(j,j) = 0;
316             end
317             for k = 1:No_modes
318                 % Coefficient of the inertial term (A_vec), diagonal stiffness
319                 %   term (B_vec) and off-diagonal coupling term (C_vec)
320                 A_vec(j,k) = Wtot{k}(j,i);
321                 if j==1
322                     B_vec(j,k) = mu1_n(j)*Wtot_4{k}(j,i)+Kl_n(j)*Wtot_couple{k
                            }(j,i);
323                     if No_beams>1
324                         C_vec(j,k) = -Kl_n(j)*Wtot_couple{k}(j+1,i);
325                     else
326                         C_vec(j,k) = 0;
327                     end
328                 elseif j==No_beams
329                     B_vec(j,k) = mu1_n(j)*Wtot_4{k}(j,i)+Kl_n(j-1)*Wtot_couple{
                            k}(j,i);
330                     C_vec(j,k) = -Kl_n(j-1)*Wtot_couple{k}(j-1,i);
331                 else
332                     B_vec(j,k) = mu1_n(j)*Wtot_4{k}(j,i)+(Kl_n(j)+Kl_n(j-1))*
                            Wtot_couple{k}(j,i);
```

```
333                     C_vec(j,k) = -Kl_n(j)*Wtot_couple{k}(j+1,i)-Kl_n(j-1)*
                            Wtot_couple{k}(j-1,i);
334                 end
335             end
336         end
337         % Normalising such that the inertial coefficient is 1
338         A_matrix(:,:,i) = A_vec'*A_vec;
339         B_matrix(:,:,i) = A_vec'*B_vec;
340         C_matrix(:,:,i) = A_vec'*C_vec;
341         F_matrix(:,:,i) = A_vec'*F_vec;
342         NL_matrix(:,:,i) = A_vec'*NL_vec;
343     end
344     vec_size=size(A_vec);
345
346     A_matrix_int = zeros(vec_size(2),vec_size(2));
347     B_matrix_int = zeros(vec_size(2),vec_size(2));
348     C_matrix_int = zeros(vec_size(2),vec_size(2));
349     F_matrix_int = zeros(vec_size(2),vec_size(2));
350     NL_matrix_int = zeros(vec_size(2),vec_size(2));
351     for i = 1:vec_size(2)
352         for j = 1:vec_size(2)
353             % Spatial integration using the trapezium method
354             A_matrix_int(i,j) = trapz(xtot,A_matrix(i,j,:));
355             B_matrix_int(i,j) = trapz(xtot,B_matrix(i,j,:));
356             C_matrix_int(i,j) = trapz(xtot,C_matrix(i,j,:));
357             F_matrix_int(i,j) = trapz(xtot,F_matrix(i,j,:));
358             NL_matrix_int(i,j) = trapz(xtot,NL_matrix(i,j,:));
359         end
360     end
361
362     % Normalised modal stiffness matrix
363     system = inv(A_matrix_int)*(B_matrix_int+C_matrix_int);
364     % Normalised modal coefficient of the nonlinear terms
365     NL = inv(A_matrix_int)*NL_matrix_int;
366     % NOrmalised modal coefficient of the forcing terms
367     F = inv(A_matrix_int)*F_matrix_int;
```

APPENDIX B

# COCO Matlab Code

The COCO continuation toolbox was used to find the stable and unstable periodic orbits of array systems throughout this thesis. An example piece of MATLAB® code is presented here to demonstrate how the toolbox was used. This particular example is the code used to conduct the FM-AFM two beam array simulations in Chapter 7.

```
1  clear;
2  close all;
3  clc;
4
5  %% Defining system parameters
6
7  coupling = 8e-3; % Length of shared base to be used for the simulation
8
9  % Initialising the parameters of the two beam array using the user defined
10 % function set_values.  This function utilises Mode_shape_code to calculate
11 % the system parameters
12 consts = set_values(coupling(trial));
13 L1 = consts(end-4);
14 consts = consts(1:end-5);
15 vars = num2cell(consts);
16 [Wc11,Wc12,Wc21,Wc22,Wk11,Wk12,Wk21,Wk22,V1,V2,V3,V4,AC1,AC2,Taum,Taum2] =
       deal(vars{:});
17
18 % Initial and final d0 value over which the continuation will run
19 start = 3.2e-3/L1;
20 stop = 2.6e-3/L1;
21
22 try
23     rmdir('data','s')
24 catch
25 end
26
27 % Initialising continuation parameters excitation frequency (OM) and d0
28 p0 = [1;start];
29 vars = num2cell(consts);
30 [Wc11,Wc12,Wc21,Wc22,Wk11,Wk12,Wk21,Wk22,V1,V2,V3,V4,AC1,AC2,Taum,Taum2] =
       deal(vars{:});
31
32 % Finding the initial static deflection about which the continuation solver
33 % will find periodic orbits.
34 x_h = fsolve(@(u) [Wk11*u(1) + Wk12*u(2) + (V1*Taum)/((p0(2,1) - u(1))^2) +
       (V2*Taum)/((p0(2,1)+10 - u(2))^2),Wk21*u(1) + Wk22*u(2) + (V3*Taum)/((
       p0(2,1) - u(1))^2) + (V4*Taum)/((p0(2,1)+10 - u(2))^2)],[0,0]);
35
```

```
% Fully initialising the continuation parameters
p0 = [p0;consts;x_h'];

%% Initial values for periodic orbit

% Finding the initial periodic orbit from which the continuation solver
% will start.
OPTIONS = odeset('RelTol',1e-6,'AbsTol',1e-6);
[t0, x0] = ode45(@(t,x) Two(x,p0), [0:0.05:1500*pi], [x_h(1)+1e-3/L1;x_h(2)
    +1e-3/L1;0;0],OPTIONS); % Transients

[pks,locs] = findpeaks(x0(:,1));
ind2 = locs(end);
ind1 = locs(end-1);
p0(1) = (2*pi)/(t0(ind2)-t0(ind1));

x0 = x0(ind1:ind2,:);
t0 = t0(ind1:ind2)-t0(ind1);

%% Fixed-period orbit continuation

% Initialising the periodic orbit continuation solver
pnames = 'p';

prob = coco_prob();
prob = coco_set(prob, 'coll');

% Inserting the system functions (see below) and system parameters
funcs = { @Two, @Two_dx, @Two_dp, @Two_dt };
coll_func = { @Two, @Two_dx, @Two_dp, @Two_dt };
coll_args = [ coll_func, { t0, x0, { 'OM' 'd0' 'Wc11' 'Wc12' 'Wc21' 'Whc22'
     'Wk11' 'Wk12' 'Wk21' 'Whk22' 'V1' 'V2' 'V3' 'V4' 'AC1' 'AC2' 'Taum' '
    Taum2' 'xh1' 'xh2'}, p0 }];
prob = ode_isol2po(prob, '', coll_args{:});

%% Frequency response curve

% Defining the boundaries of the contuation
wRange = [stop,start];
cont_args = { 1, { 'd0' }, {wRange} };

% Setting the stepping parameters of the continuation solver
h_max_set = (0.05e-3)/L1;          h_min_set = (1e-5)/L1;        h0_set =
    h_max_set;
prob = coco_set(prob,'cont','h_max',h_max_set,'h_min',h_min_set,'h0',h0_set
    ,'ItMX',10000,'NPR',1,'PtMX',200,'TOL',1e-12);
prob = coco_set(prob,'corr','ItMX',50,'SubItMX',7,'TOL',1e-10,'ResTOL',1e
    -10);

% Run the continuation solver
bd1 = coco(prob, 'run', [], cont_args{:});

% Outputs x (periodic orbits) and d0 (corresponding separation distance)
x  = coco_bd_col(bd1, '||po.orb.x||');
d0  = coco_bd_col(bd1, 'd0');
```

```
% Function Two defines the first order equations of motion governing the
% response of the two beam array

function f = Two(x, p)

% x1 and x2 are the displacement variables, x3 and x4 are the velocity
% variables
```

```
8
9  x1 = x(1,:);
10 x2 = x(2,:);
11 x3 = x(3,:);
12 x4 = x(4,:);
13
14 n = 4;
15
16 f = [x3;
17     x4;
18     -p(3,:).*x3-p(4,:).*x4-p(7,:).*(x1+p(19,:))-p(8,:).*(x2+p(20,:))-(p
           (15,:).*p(11,:)+p(16,:).*p(12,:)).*(-x3./sqrt((x1).^2+x3.^2)) - (p
           (11,:).*p(17,:))./((p(2,:)-(x1+p(19,:))).^2) - (p(12,:).*p(17,:))
           ./((p(2,:)+10-(x2+p(20,:))).^2) + (p(11,:).*p(18,:))./((p(2,:)-(x1+
           p(19,:))).^n) + (p(12,:).*p(18,:))./((p(2,:)+10-(x2+p(20,:))).^n);
19     -p(5,:).*x3-p(6,:).*x4-p(9,:).*(x1+p(19,:))-p(10,:).*(x2+p(20,:))-(p
           (15,:).*p(13,:)+p(16,:).*p(14,:)).*(-x3./sqrt((x1).^2+x3.^2)) - (p
           (13,:).*p(17,:))./((p(2,:)-(x1+p(19,:))).^2) - (p(14,:).*p(17,:))
           ./((p(2,:)+10-(x2+p(20,:))).^2) + (p(13,:).*p(18,:))./((p(2,:)-(x1+
           p(19,:))).^n) + (p(14,:).*p(18,:))./((p(2,:)+10-(x2+p(20,:))).^n)];
20
21 end
```

APPENDIX C

# LabVIEW FPGA Code

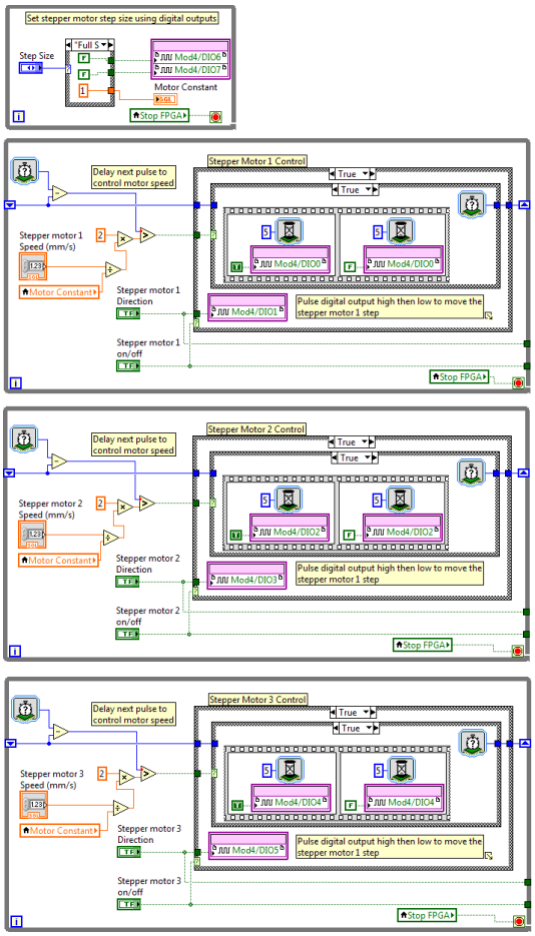


Figure C.1: Labview FPGA code used to run the second macro scale test rig (part 1).

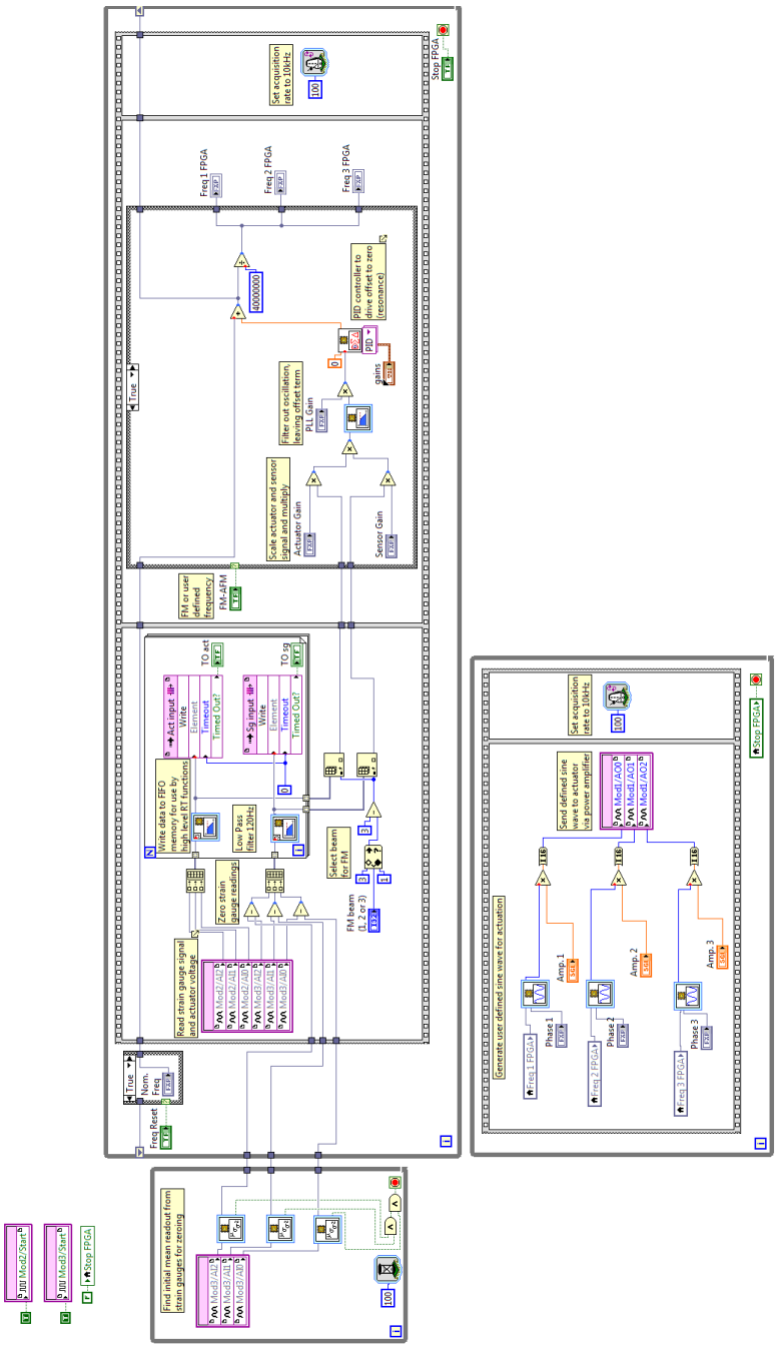


Figure C.2: Labview FPGA code used to run the second macro scale test rig (part 2).

APPENDIX D

# Perterburation B Values

$$\boldsymbol{B_{11}} = R_1^2V_4^2 - 2R_1^2V_4r_1^2 + R_1^2r_1^4 + 2R_1R_3V_2V_4 - 2R_1R_3V_2r_1^2 + R_3^2V_2^2,$$

$$\boldsymbol{B_{12}} = 2R_1S_1V_4^2 + 2R_3S_3V_2^2 + 2R_1S_1r_1^4 + 2R_1S_3V_2V_4 + 2R_3S_1V_2V_4 - 4R_1S_1V_4r_1^2 - 2R_1S_3V_2r_1^2 - 2R_3S_1V_2r_1^2,$$

$$\boldsymbol{B_{13}} = 2R_1V_4\sigma_1 + 2R_3V_2\sigma_1 - 2R_1r_1^2\sigma_1,$$

$$\boldsymbol{B_{14}} = S_1^2V_4^2 - 2S_1^2V_4r_1^2 + S_1^2r_1^4 + 2S_1S_3V_2V_4 - 2S_1S_3V_2r_1^2 + S_3^2V_2^2,$$

$$\boldsymbol{B_{15}} = 2S_1V_4\sigma_1 - 2S_1r_1^2\sigma_1 + 2S_3V_2\sigma_1,$$

$$\boldsymbol{B_{16}} = P_1^2V_4^2 - 2P_1^2V_4r_1^2 + P_1^2r_1^4 + 2P_1P_3V_2V_4 - 2P_1P_3V_2r_1^2 + P_3^2V_2^2 + \sigma_1^2,$$

$$\boldsymbol{B_{17}} = -Q_1^2V_4^2 + 2Q_1^2V_4r_1^2 - Q_1^2r_1^4 - 2Q_1Q_3V_2V_4 + 2Q_1Q_3V_2r_1^2 - Q_3^2V_2^2,$$

$$\boldsymbol{B_{21}} = R_2^2V_3^2 - 2R_2R_4V_3r_2^2 + R_4^2r_2^4 + 2R_2R_4V_1V_3 - 2R_4^2V_1r_2^2 + R_4^2V_1^2,$$

$$\boldsymbol{B_{22}} = 2R_2S_2V_3^2 + 2R_4S_4V_1^2 + 2R_4S_4r_2^4 + 2R_2S_4V_1V_3 + 2R_4S_2V_1V_3 - 4R_4S_4V_1r_2^2 - 2R_2S_4V_3r_2^2 - 2R_4S_2V_3r_2^2,$$

$$\boldsymbol{B_{23}} = 2R_2V_3\sigma_2 + 2R_4V_1\sigma_2 - 2R_4r_2^2\sigma_2,$$

$$\boldsymbol{B_{24}} = S_2^2V_3^2 - 2S_2S_4V_3r_2^2 + S_4^2r_2^4 + 2S_2S_4V_1V_3 - 2S_4^2V_1r_2^2 + S_4^2V_1^2,$$

$$\boldsymbol{B_{25}} = 2S_2V_3\sigma_2 - 2S_4r_2^2\sigma_2 + 2S_4V_1\sigma_2,$$

$$\boldsymbol{B_{26}} = P_2^2V_3^2 - 2P_4^2V_1r_2^2 + P_4^2r_2^4 + 2P_2P_4V_1V_3 - 2P_2P_4V_3r_2^2 + P_4^2V_1^2 + \sigma_2^2,$$

$$\boldsymbol{B_{27}} = -Q_2^2V_3^2 + 2Q_4^2V_1r_2^2 - Q_4^2r_2^4 - 2Q_2Q_4V_1V_3 + 2Q_2Q_4V_3r_2^2 - Q_4^2V_1^2.$$

APPENDIX E

# Micro and Macro Array Parameters

The following tables present the key physical parameters of the TUI micro cantilever arrays, the arrays of the first macro scale test rig and the arrays of the second macro scale test rig for reference.

Table E.1: System parameters of the TUI micro arrays.

| **System Parameter** | **Quality/Quantity** |
|---|---|
| Cantilever Length | 350 µm |
| Cantilever Width | 40 µm |
| Cantilever Thickness | 1.5 mm |
| Cantilever Material | Primarily Silicon |
| Beam Spacing | 5 µm |
| Mode of Actuation | Bimorph heater |
| Mode of Sensing | Piezoresistive bridge and laser vibrometer |
| Young's Modulus | 71 GPa |
| Density | 2330 $\mathrm{kg\,m^{-3}}$ |

Table E.2: System parameters of the macro arrays used on the first test rig.

| **System Parameter** | **Quality/Quantity** |
|---|---|
| Cantilever Length | 105 mm |
| Cantilever Width | 29 mm |
| Cantilever Thickness | 1.5 mm |
| Cantilever Material | Aluminium |
| Beam Spacing | 10 mm |
| Mode of Actuation | Piezo-film |
| Mode of Sensing | Strain gauge bridge |
| Method of Coupling Variation | Length of shared base protruding from clamp |
| Young's Modulus | 120 GPa |
| Density | 2770 $\mathrm{kg\,m^{-3}}$ |

Table E.3: System parameters of the macro arrays used on the second test rig.

| **System Parameter** | **Quality/Quantity** |
|---|---|
| Cantilever Length | 160 mm |
| Cantilever Width | 40 mm |
| Cantilever Thickness | 1.5 mm |
| Cantilever Material | Aluminium |
| Beam Spacing | Various, predominantly 10 mm |
| Mode of Actuation | Piezo-film |
| Mode of Sensing | Strain gauge bridge |
| Method of Coupling Variation | Aluminium sections attached at cantilever base |
| Young's Modulus | 120 GPa |
| Density | 2770 $\mathrm{kg\,m^{-3}}$ |